Physik-Department

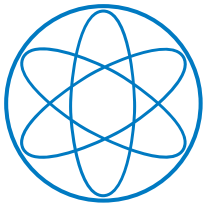

Precision Design and Characterization of DNA Origami Nanostructures Using High-Resolution Cryo-EM

Dissertation by

Fabian Kohler

Technische Universität München

Fakultät für Physik der Technischen Universität München

Labor für Biomolekulare Nanotechnologie

Precision Design and Characterization of DNA Origami Nanostructures Using High-Resolution Cryo-EM

Fabian Kohler

Vollständiger Abdruck der von der Fakultät für Physik der Technischen Universität München zur Erlangung des akademischen Grades eines

Doktors der Naturwissenschaften (Dr. rer. nat.)

genehmigten Dissertation.

Vorsitzende(r): Prof. Dr. Martin Zacharias

Prüfer der Dissertation:

1. Prof. Dr. Hendrik Dietz
2. Prof. Dr. Friedrich C. Simmel

Die Dissertation wurde am 07.07.2021 bei der Technischen Universität München eingereicht und durch die Fakultät für Physik am 14.09.2021 angenommen.

List of peer-reviewed publications

Massimo Kube*, Fabian Kohler*, Elija Feigl*, Baki Nagel-Yüksel, Elena M. Willner, Jonas J. Funke, Thomas Gerling, Pierre Stömmer, Thomas G. Martin, Sjors H. W. Scheres, and Hendrik Dietz°

Revealing the structures of megadalton-scale DNA complexes with nucleotide resolution

Nature Communications 11 (2020), DOI: 10.1038/s41467-020-20020-7

Floris A. S. Engelhardt, Florian Praetorius, Christian H. Wachauf, Gereon Brüggenthies, Fabian Kohler, Benjamin Kick, Karoline L. Kadletz, Phuong Nhi Pham, Karl L. Behler, Thomas Gerling, and Hendrik Dietz°

Custom-Size, Functional, and Durable DNA Origami with Design-Specific Scaffolds.

ACS Nano 13 (2019), DOI: 10.1021/acsnano.9b01025

Brigitte A. K. Kriebisch , Alexander Jussupow, Alexander M. Bergmann, Fabian Kohler, Hendrik Dietz, Ville R. I. Kaila, and Job Boekhoven°

Reciprocal Coupling in Chemically Fueled Assembly: A Reaction Cycle Regulates Self-Assembly and Vice Versa

Journal of the American Chemical Society 142 (2020), DOI: 10.1021/jacs.0c10486

Jia-Jhen Kang, Florian A. Jung, Chia-Hsin Ko, Kaltrina Shehu, Lester C. Barnsley, Fabian Kohler, Hendrik Dietz, Junpeng Zhao, Stergios Pispas, and Christine M. Papadakis°

Thermoresponsive Molecular Brushes with Propylene Oxide / Ethylene Oxide Copolymer Side Chains in Aqueous Solution

Macromolecules 53 (2020), DOI: 10.1021/acs.macromol.0c00263

Caren Wanzke, Alexander Jussupow, Fabian Kohler, Hendrik Dietz, Ville R. I. Kaila, and Job Boekhoven°

Dynamic Vesicles Formed by Dissipative Self-Assembly

ChemSystemsChem 2 (2019), DOI: 10.1002/syst.201900044

(*= These authors contributed equally to this work. °= Corresponding author.)

Contents

Introduction

In nature, DNA serves as a carrier of genetic information. Via the sequence of the four nucleobases, various genes encode the amino acid sequences of proteins. In the field of structural DNA nanotechnology, DNA itself is used as a building material by exploiting the sequence-dependent Watson-Crick base-pairing [1–4]. The methods of structural DNA nanotechnology provide a platform for rational design and bottom-up fabrication of objects with user-defined shapes and functions on the nanoscale. Since the invention of DNA origami by Rothemund in 2006 [4], the field has constantly advanced and put forth a wide range of methods and applications including DNA walkers [5, 6], plasmonic nanostructures [6–9], nanotools [10–19], complex higher-order assemblies [20–23], and advances towards medical applications [24–26] and molecular machines [27–32].

In general, multilayer DNA origami objects are designed by arranging a virtual set of double-stranded DNA (dsDNA) helices with certain lengths parallel to each other on a square or honeycomb lattice to approximate the desired shape [33–36]. A circular M13 bacteriophage genome-based 'scaffold' single-strand is routed through the virtual helices, which are then complemented and connected to each other by a set of chemically synthesized short single-stranded 'staple' oligonucleotides. Connections between helices are implemented via Holliday junction-based motifs [37, 38]. Based on the sequences of the scaffold and staple strands, the objects self-assemble in a one-pot reaction [39–41]. This is striking given this process requires the interaction and precise arrangement of several hundred strand segments in the final object. Design motifs including hinges [42–44], corners [45, 46], shape-complementary stacking contacts [47], curvature- and twist-inducing elements [48, 49], as well as precise modification of individual nucleotides with chemical moieties [50–52] provide a large design toolbox. A more detailed overview over the various methods and applications of DNA origami as well as a practical guide to scaffolded DNA origami design are given in the excellent primers by Dey et al. [53] and Castro et al. [54].

To fully exploit the potential of DNA origami, the structures of the designed objects require precise experimental characterization. However, whereas 3D structures of proteins, including de novo designs [55–57], are regularly solved at near-atomic resolution [58–67], up until recently only a few cryogenic electron microscopy (cryo-EM) 3D structures of DNA

origami objects were available and most were reported at relatively low resolutions[20, 68–71]. Instead, DNA origami structures are commonly analyzed using negative stain electron microscopy (EM). During the preparation of the specimen, the particles are adsorbed on a carbon layer, embedded in a solution containing heavy metal salt, and air-dried. However, this procedure may result in the deformation of the objects [53] and limits the resolution due to the background signal of the carbon layer and the grain size of the staining agent [72]. In cryo-EM, the sample is vitrified inside the holes of a special kind of grid using liquid ethane to embed the particles in a matrix of glass-like free-standing ice. That is, in the holes the particles are hydrated, frozen in the native buffer, and unaffected by the carbon layer [73 pp. 30–34].

Bai et al. presented the first cryo-EM 3D structure of a DNA origami object [68], termed 'the Pointer', characterizing global features and structural details of the square lattice-based design. Contrary to the prior general assumption, Wagenbauer et al. found that honeycomb lattice-based objects exhibit global right-handed twist [20]. With reported values of ranging from 11.5 Å to about 20 Å these cryo-EM reconstructions have revealed valuable insights to improve DNA origami design. We recently published a library of 26 cryo-EM 3D reconstructions of DNA origami objects with resolutions of up to 4.3 Å [74]. Here, we present a selection of this library as well as several new structures and address the important topics of:

1. the extraction of high resolution structural information from cryo-EM data of structural heterogeneous objects,
2. global twist and design motifs in multilayer square lattice-based objects,
3. the characterization of an object created with two scaffolds with orthogonal base sequences,
4. the robust construction and modification of corners.

In the first chapter, we give an introduction to electron microscopy, including the basic components of an electron microscope as well as the principles of image formation and 3D reconstruction. We introduce the models of 3D refinement, 3D classification, and multi-body refinement implemented in the Relion software suite [75–79], as well as the CryoSPARC 3D variability analysis (3DVA) tool [80, 81], which were used in this thesis. In the following chapters, we address the individual research topics and put them into perspective.

Zoom-in reconstruction: An electron density map is reconstructed from many thousands of 2D projections of imperfect copies of the object of interest and represents the average structure of this set of particle snapshots. The heterogeneity of the particle set

is due to structural differences as well as conformational changes based on the underlying energy landscape of the object and causes blurring in the reconstructed map. This was also the case for a multidomain object termed 'Twist-Tower', which we also used to study the global twist in square lattice-based multilayer designs. By treating the object in the reconstruction as a single rigid body, the resolution in the electron density map was increasingly poorer for the smaller domains, to the extent that the domain with a cross section of 2×2 helices is barely recognizable. We addressed this issue and present a zoom-in approach based on the multi-body refinement tool implemented in Relion [78]. We show this approach for the Twist-Tower, where we used two zoom-in steps:

1. an individual refinement of the four domains treated as four rigid bodies
2. a scanning-focused refinement on small regions of interest

Based on the improved resolution of the four-body refinement and a molecular dynamics flexible fitting (MDff) approach, we present a pseudo-atomic model fit of the object. We characterize the object using the fit in combination with the recently reported viewer tool [74]. We show the effectiveness of the approach by presenting priorly poorly resolved regions with resolutions up to 4.3 Å after applying the procedure. Thereby, structural details are revealed, including single-strand and double-strand crossovers, phosphate moieties along the backbone, and discontinuities in the backbone at the nick sites of staple strands.

Global twist and design motifs in multilayer square lattice-based objects: Ke et al. presented a design to create compact multilayer DNA origami objects in 3D by arranging the helices on a square lattice [35]. In this approach, the enclosed angle between a helix and two direct neighbors is a multiple of 90°. The commonly used distance of eight basepairs between two consecutive crossovers along a helix corresponds to an angle of 270° and an effective twist density of 10.67 bp/turn as imposed by the square lattice. This mismatch to the native twist density of 10.5 bp/turn results in an underwinding of the individual helix segments and accumulates to a global right-handed twist of the objects. Using negative stain electron microscopy, the authors showed that global twist can be corrected by reducing the average effective twist density. This is implemented by shortening the distance between consecutive crossovers of some segments, which induces local overwinding and counter-torque. They found that a reduction of the effective twist density to 10.5 bp/turn was not sufficient, but larger values of 10.44 bp/turn to 10.39 bp/turn were required to compensate the global twist. However, the electrostatic interaction between the charged carbon layer and the DNA origami objects and the negative stain solution might have changed the global shape. The first cryo-EM structure of a square lattice-based object, the Pointer, showed a global right-handed twist as well, which, however, was is difficult to quantify due to the asymmetric shape. Here, we present a cryo-EM study of

global twist in square lattice-based multilayer design. We reconstructed and characterized two variants of the Twist-Tower, a multidomain object consisting of four cuboids with cross sections of 2×2, 4×4, 6×6, and 8×8 helices. We designed the first variant with a native effective twist density of 10.67 bp/turn. In the second variant, we reduced the effective twist density to 10.33 bp/turn. We give an analysis of the dependency of the global twist on the cross section and discuss the influence of crossovers on effective twist correction. Additionally, we studied the effect of crossover stacks of different lengths, the omission of crossovers, and the use of similar sequences in neighboring staple segments on the global and local structure of the objects.

Dual-scaffold object: Commonly, DNA origami objects are built using a scaffold of predefined length and sequence. Therefore, the size and properties of a DNA origami object are limited by the scaffold [82, 83]. For the first scaffolded DNA Origami objects, Rothemund used a 7249 nt long circular single-stranded DNA of the bacteriophage M13mp18 [4]. Scaffolds of different sizes have been created including the popular M13-based 7560 nt and 8064 nt scaffolds [36]. Although longer scaffolds have been developed to build increasingly larger objects [84, 85], the production becomes increasingly challenging and scaffold yields tend to decrease [83, 86]. Higher-order assemblies of one or several different types of M13-based scaffolded monomers can be built using base-pairing or base-stacking interactions at shape-complementary interfaces. However, the individual types of monomers require separate folding and purification. Folding different types of M13-based objects simultaneously in a one-pot reaction results in aggregation of the components [83]. Attempting to directly fold large objects from multiple intertwined M13-based scaffolds leads to the same result. To address this issue, Engelhardt et al. developed methods to create custom scaffolds of different lengths and sequences, including four 7560 nt long scaffolds orthogonal to each other and to the M13 derivative [83]. To illustrate the effectiveness of the approach, they built a barrel-like dual-scaffold object, which consists of 126 helices arranged on a honey comb lattice and is folded in a one-pot reaction. Based on gel electrophoresis analysis and negative stain TEM imaging, the object folds at a high monomer yield without major structural defects [83]. Here we report the detailed structural characterization of the 126-helix bundle using cryo-EM methods, including a pseudo-atomic model fit to interpret the electron density map in context of the actual design. Based on the local resolution estimation of the structure, we give a quantitative analysis of the internal interfaces between the two scaffolds to identify potential systematic structural defects caused by the multi-scaffold design approach.

Corner design and characterization: Due to the parallel arrangement of the ds-DNA helices, lattice-based objects have one main direction along the helical axes, which

limits the achievable geometric shapes. Therefore, corners are important design elements to modify the direction of an object. A specific angle is realized by adjusting the lengths of the individual helices at the interface of the two arms of the corner [45]. Given the various possible combinations of backbone orientations of the corresponding helices at the interfaces, the design of the connections remains challenging. Here we first present different design strategies of double-stranded and single-stranded connections independent of the backbone orientation and test the influence of crossovers near the corner site. We perform these tests on variants of a 'Triple-Corner' design featuring three corners with approximately 45°, 90°, and 135°, and characterize the objects using gel electrophoresis and 3D cryo-EM reconstructions. Identifying the 45° corner as the most challenging one, we develop a more sophisticated connection strategy, which takes the backbone orientation of each helix into account, and implement it in a small object with a single 45° corner, which is better suited to obtain a high-resolution cryo-EM structure. We characterize the flexibility of the object using principle component analysis-based methods. Additionally, we present and characterize several variants of the design with modifications, including:

- internal and external angle braces to modify the flexibility of the corner,
- an increased crossover density to reduce the previously reported 3D chickenwire pattern of the helices [68],
- a reduced effective helical twist density to correct for residual global twist

Chapter 1

Electron Microscopy

An electron microscope shares similarities with a light microscope including an illumination source, a system of condenser, objective, and magnification lenses, and a screen or detector to visualize the image. In a light microscope, a beam of light, i.e., photons are focused by lenses via refraction. In electron microscopes, electron lenses with magnetic fields are used to focus a beam of electrons. By accelerating the electrons to a few hundred keV and the corresponding small wavelengths, an electron microscope allows for up to atomic resolution. In this chapter, an overview of bright field electron microscopy is given, including the basic components of an electron microscope and the theory of image formation. The principles of 3D reconstruction and the implementation of the single particle analysis (SPA) approach are explained.

1.1 Basic components of an electron microscope

In an electron microscope, a so-called electron gun serves as the electron source. The emitted electrons are accelerated by a high-voltage potential. A condenser lens system consisting of electron lenses and apertures is used to control the illumination of the sample, which is mounted on an adjustable stage. The electron beam interacts with the thin sample and is focused via the objective lens system. A system of additional lenses magnifies and projects the image onto a detector (Fig. 1.1A). In the following, these basic components of an electron microscope are described in more detail.

1.1.1 Electron gun

The electron gun serves as the emitter of electrons. In conventional electron microscopes, thermionic emission lanthanum hexaboride (LaB_6) cathodes are used. Having a low work function of around 2.7 eV [87], the electrons are boiled over the potential barrier by heating the cathode to about 2×10^3 K [73 p. 17, 88]. The electrons which have enough energy

to overcome the work function, can leave the tip of the cathode and are pulled into the vacuum by an electric field. High-end electron microscopes are equipped with field emission guns (FEG). In a Schottky FEG, a strong electric field is applied to the tip of a zirconiumoxide (ZrO) covered tungsten wire heated to about 1.8×10^3 K to induce field enhanced thermionic emission of electrons. In a cold-FEG, the tip is not heated and emission is achieved via the tunneling effects induced by strong electric fields. FEGs require ultra-high vacuum which makes them more expensive compared to thermionic sources [89]. However, FEGs have increased brightness and a higher degree of coherence of the electron beam due to a lower energy spread and a smaller gun tip [73 p. 17]. The emitted electrons are accelerated to relativistic velocities by a potential. In a 300 kV electron microscope, the electrons of the beam have a wavelength of 2 pm, theoretically allowing for far below atomic resolution.

1.1.2 Condenser system

With a system of condenser lenses including apertures, the illumination of the sample is controlled. An electron lens consists of a coil with the optical axis of the microscope in its center. The current running through the coil produces a magnetic field inside the lens, which deflects the electrons of the beam. On their way through the magnetic field of the lens, the electrons are focused with respect to the optical axis. By changing the current in the coil, the strength of the lens, and by this the position of the back-focal plane can be adjusted.

1.1.3 Specimen

In the specimen plane of the microscope, the electrons interact with the 3D Coulomb potential of the thin sample. The electrons either are scattered or transmitted through the sample unaffected. In the wave description, the incoming plane wave of the beam is distorted by the thin sample and the information of the sample is encoded mainly in the phase modulation of the exit wave [73 pp. 35–38]. In this thesis, transmission electron microscopes were used, in which the forward elastically scattered electrons carry valuable information about the sample. Inelastically scattered electrons lose energy in the scattering process and hence are deflected differently by the electromagnetic lenses than the transmitted or elastically scattered electrons, which leads to image blurring.

There are mainly two methods to prepare the sample to analyze it with an electron microscope. In the negative stain approach, the sample, e.g., a protein in buffer solution, is adsorbed onto a carbon-coated grid, embedded in a layer of heavy metal salts like uranyl formate, and air-dried. Since image formation is based on the atomic number (Z)

dependent scattering cross sections [90], the different atomic numbers of the stain and the sample leads to increased contrast. However, there are a few factors that limit the resolution. The grain size of the negative stain of 4 Å to 5 Å for uranyl-based stains, the adsorption on the carbon support layer, and the drying process limit the resolution of the procedure [73 p. 16]. In cryogenic electron microscopy (cryo-EM), the sample is applied to a carbon-coated grid and plunge-frozen using liquid ethane. Due to the rapid cooling process, the specimen is embedded in glass-like vitreous ice, which is considered a more natural environment compared to the negative stain approach [73 p. 19]. Commonly, holey carbon grids are used, where holes are arranged in a regular pattern in the carbon layer, e.g., with a diameter of 2 µm and a spacing of 1 µm. Thus, the specimen is suspended in so-called free-standing ice unaffected by the carbon support layer.

1.1.4 Objective lens and aberrations

The objective lens forms the first image of the sample in the optical system of the electron microscope. As explained for the condenser lens, the focus of the objective lens is determined by the strength of its magnetic field which is controlled via the current in the coil. However, various types of inhomogeneity of the magnetic field result in optical aberrations, which limit the resolution of the electron microscope [73 pp. 17–18]. In case of imperfect axial symmetry, the image is affected by astigmatism. An inhomogeneity of the field in x- and y-direction (two-fold symmetry) leads to different respective back focal planes and to two-fold axial astigmatism. Spherical inhomogeneity of the electromagnetic field causes rays which pass through the lens further away from the optical axis to be more strongly focused leading to the spherical aberration Cs [91]. This is unavoidable for rotationally symmetric electromagnetic lenses as shown by the Scherzer theorem [92] and reduces the achievable resolution [93]:

$$d_{min} = 0.64 \sqrt[4]{\lambda^3 C_s}. \tag{1.1}$$

The chromatic aberration is another inherent optical error of spherical electron lenses [92]. Since electrons of different velocities are deflected differently strong by the electromagnetic field, the focal length depends on the energy of the electrons. Hence, the energy spread of the gun and inelastic scattering lead to blurring of the image. These imperfections and other higher-order aberrations can be reduced by specific hardware including high-quality electron sources with a narrow energy spread, monochromators, energy filters, and multipole correctors.

1.1.5 Detector

In the image plane of the electron microscope, the projection of the sample can be visualized using a fluorescence screen or an image capturing device. While in the early electron microscopes photographic films or plates were used, they have been replaced by charge coupled devices (CCD) and detectors with complementary metal-oxide-semiconductor monolithic active pixel sensors (CMOS MAPS) [94]. The development of direct electron detectors led to the strong resolution improvement of electron microscopy in recent years. Instead of converting the electrons first into an optical signal using a scintillator, the incident electrons are detected directly. While passing through the active layer of the detector, the high energy incident electrons leave an ionization trail which is collected and directly converted into a digital signal. By using a very thin active layer of only a few micrometers, the lateral spread of the ionization trail is reduced, increasing the localization of the signal. Direct electron detectors can be operated in so-called "counting mode". By setting the average number of electrons detected by each pixel per frame sufficiently below one, individual electron events can be detected. Some devices can detect at a resolution below the physical Nyquist frequency by fitting a 2D Gaussian or similar function to the signal created by a single electron event proportionately detected by neighboring pixels [73 pp. 18–19, 94].

1.2 Image formation and 3D reconstruction

In the following, an overview of the image formation, the contrast transfer function, and approaches in 3D reconstruction is given. For a more detailed description of the underlying theory, the interested reader is encouraged to study the book on Electron microscopy by Joachim Frank [73] and the publications on cryo-EM single particle analysis (SPA) structure determination by Sjors H.W. Scheres [75–79].

1.2.1 Image formation

The electron beam emitted by the gun propagates in z-direction (optical axis). This incoming wave ψ_0 interacts with the 3D Coulomb potential $C(\mathbf{r}, z)$ of the sample resulting in a distortion of the exit wave function $\psi(\mathbf{r})$ in form of a phase shift $\phi(\mathbf{r})$ in x- and y-direction, with $\mathbf{r} = (\mathrm{x}, \mathrm{y})^{\mathrm{T}}$:

$$\psi(\mathbf{r}, \mathbf{z}) = \exp\left[ikz\right] \exp\left[i \int C(\mathbf{r}, z) dz\right] = \psi_0 \exp\left[i\phi(\mathbf{r})\right] \tag{1.2}$$

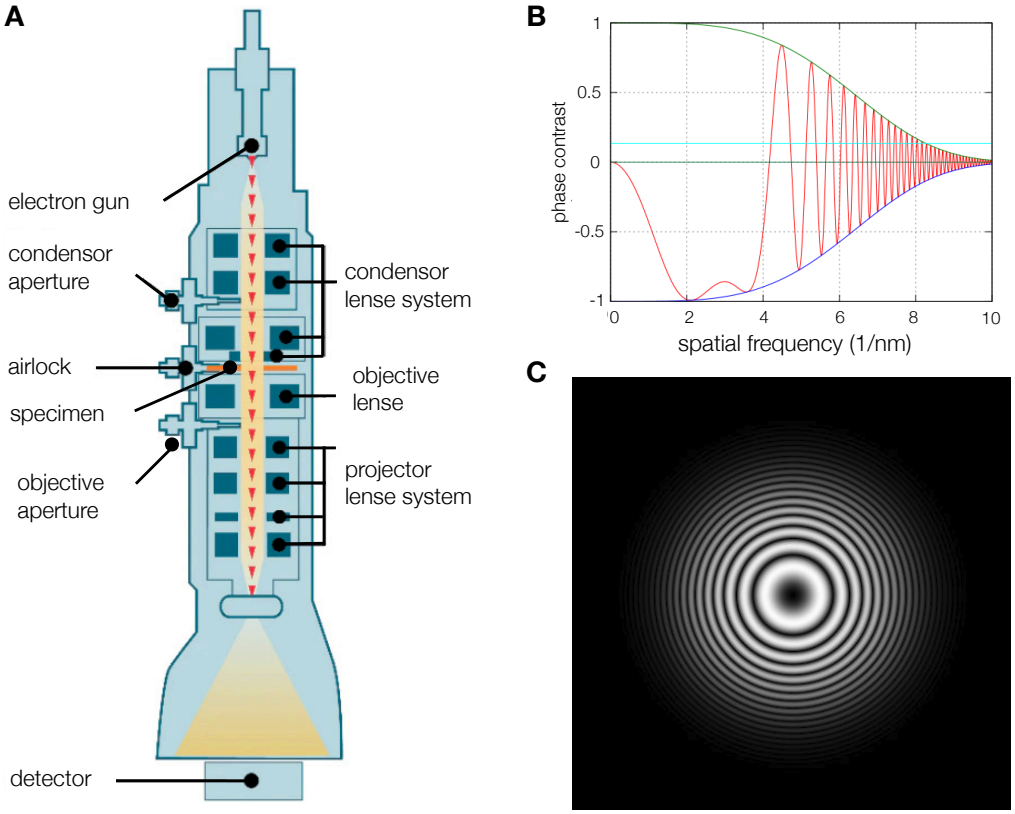

Figure 1.1 Electron Microscope (A) Schematic illustration of the basic components of an electron microscope. **(B)** Line profile of the CTF (red) damped by the envelope function (blue and green). **(C)** 2D contrast transfer function. Adopted from [95] and [96], modified.

For a weak-phase object, assuming $\phi(\mathbf{r}) << 1$, the exit plane wave function can be expanded:

$$\psi(\mathbf{r}, \mathbf{z}) = \psi_0 \left[1 + i\phi(\mathbf{r}) - \frac{1}{2}\phi(\mathbf{r})^2 + ...\right] \tag{1.3}$$

Thus, the exit wave can be expressed as an interference of the unscattered wave (first term) and a scattered wave (second and higher order terms) with the analogy of unscattered and scattered electrons in the particle picture. By neglecting the higher order terms, the scattered wave is shifted by 90 deg. Given the weak 90° phase shift of the scattered wave, the amplitude of the exit wave is unaffected, and the information about the sample is only encoded in the phase shift of the exit wave. Since the detector measures the intensity of the image wave function

$$I(\mathbf{r}) = |\psi_i(\mathbf{r})|^2, \tag{1.4}$$

the information encoded in the phase shift is not detected [97]. However, due to the aberations of the objective lens, the scattered wave is affected by additional phase shits,

described by the contrast transfer function, resulting in the phase contrast being transferred into amplitude variations of the image wave $\psi_i(\mathbf{r})$ [73 pp. 34–38].

1.2.2 Contrast transfer function

The exit wave function is focused by the objective lens. Given a lens which focuses the entire exit wave and is free of aberrations, the wave function in the backfocal plane is, according to Fraunhofer diffraction, the Fourier transform of the exit wave. The coordinates in the Fourier domain, i.e., the spatial frequencies, are proportional to the scattering angles. Depending on the scattering angle, the spatial-frequency-dependent components of the wave pass through different regions of the lens. Thus, the inhomogeneity of the magnetic field of the lens and the corresponding result in additional spatial-frequency-dependent phase shifts, assuming zero axial astigmatism:

$$\gamma(\mathbf{k}) = 2\pi\chi(\mathbf{k}) = -\pi\lambda\Delta z k^2 + \frac{1}{2}\pi\lambda^3 C_s k^4, \tag{1.5}$$

with spatial frequencies $\mathbf{k} = (\mathrm{kx}, \mathrm{ky})$ and $k = |\mathbf{k}|$, the wave aberration function $\chi(\mathbf{k})$, the defocus of the objective lens Δz, and the third-order spherical aberration C_s.

In general, a spherical aperture with radius R and aperture function $A(\mathbf{k})$ is placed in the backfocal plane. The resulting wave in the back focal plane in Fourier domain is then [73 pp. 36–37]:

$$\psi_{bf}(\mathbf{k}) = \mathcal{F}\{\psi\}(\mathbf{k}) \exp[i\gamma(\mathbf{k})] A(\mathbf{k}), \qquad A(\mathbf{k}) = \begin{cases} 1 & \text{if k} \leq \text{R} \\ 0 & \text{else} \end{cases} \tag{1.6}$$

The phase contrast transfer function (pCTF) is defined as $\sin\gamma(\mathbf{k})$ and describes the Fourier transform of the image intensity as a modulation the Fourier transform of the projected potential $\mathrm{O}(\mathbf{k})$, assuming $\phi(\mathbf{r})$ is real and ignoring higher order terms [73 pp. 38–39]:

$$J(\mathbf{k}) = \mathcal{F}\{I(\mathbf{r})\} = O(\mathbf{k}) \sin\gamma(\mathbf{k}) A(\mathbf{k}), \qquad O(\mathbf{k}) = \mathcal{F}\{\phi(\mathbf{r})\}. \tag{1.7}$$

The loss of electrons due to the objective aperture and the removal of inelastically scattered electrons, leads to amplitude contrast. In the contrast transfer function (CTF), this is included by a term describing the imaginary part of the potential:

$$CTF(\mathbf{k}) = O_r(\mathbf{k}) \sin\gamma(\mathbf{k}) - O_i(\mathbf{k}) \cos\gamma(\mathbf{k}), \tag{1.8}$$

with the Fourier transforms of the real and the imaginary part of the potential $O_r(\mathbf{k})$ and $O_i(\mathbf{k})$, respectively. Assuming a homogeneous sample and $O_i(\mathbf{k})/O_r(\mathbf{k})$ to be equal for all

atoms and constant within the frequency range of interest, the CTF can be rewritten to:

$$CTF(\mathbf{k}) = \sin\gamma(\mathbf{k}) - A(\mathbf{k})\cos\gamma(\mathbf{k}), \tag{1.9}$$

with the amplitude contrast ratio A [73 pp. 47–51].

The image is further modulated by a spatial-frequency-dependent envelope function E(**k**) (Fig. 1.1B-C). It describes the decrease contrast for higher frequencies due to the energy spread and the finite tip size of the gun, the objective lens current stability, and other deteriorating effects [73 pp. 39–41]. The envelope function can be approximated by a Gaussian function and the so-called B-factor [98].

$$E(\mathbf{k}) = \exp[-Bk^2], \tag{1.10}$$

To briefly summarize, the intensity profile in the image plane of an electron microscope is a 2D projection of a 3D volume due to the interaction of the incoming electron wave with the Coulomb potential of the sample modulated by the optical system of the microscope. In Fourier space, this modulation is described by a multiplication of the Fourier transforms of the projected potential, the CTF, the aperture function, and the envelope function:

$$J(\mathbf{k}) = O(\mathbf{k})CTF(\mathbf{k})A(\mathbf{k})E(\mathbf{k}) = O(\mathbf{k})H(\mathbf{k}) \tag{1.11}$$

Due to the sinusoidal character of the CTF and the dependency on spatial frequency, the contrast oscillates between positive and negative regions. Between the extrema, the contrast is attenuated, and for spatial frequencies, where the CTF is zero, no contrast is transferred at all, which results in a complete loss of information about the sample.

1.2.3 CTF deconvolution and Wiener filtering

The optical system corrupts the signal described by the spatial-frequency dependent CTF. When the CTF is known, the image can be deconvoluted to partially recover the signal. However, a naive division is not possible, due to the zeros of the CTF and an additional noise term resulting from the acquisition of the image with an imperfect detector:

$$X(\mathbf{k}) = J(\mathbf{k}) + N(\mathbf{k}). \tag{1.12}$$

For spatial frequencies with low signal-to-noise ratio (SNR), a naive division results in an amplification of noise. Commonly, the multiplication of the image with the mathematical

construct of the Wiener filter $W(\mathbf{k})$ is used as a deconvolution approach:

$$W(\mathbf{k}) = \frac{CTF(\mathbf{k})}{|CTF(\mathbf{k})|^2 + \frac{|N(\mathbf{k})|^2}{|S(\mathbf{k})|^2}}, \tag{1.13}$$

with the spatial frequency dependent terms of the noise power spectrum (NPS) $|N(\mathbf{k})|^2$ and the signal power spectrum (SPS) $|J(\mathbf{k})|^2$ [73 pp. 50–51, 73 pp. 58–59]. It "can be described by a 'careful division' by the CTF such that the noise amplification is kept within limits" [73 p. 58]

1.2.4 Fourier Slice Theorem and 3D reconstruction

In a real electron microscope, the detector samples the continuous signal of the image wave intensity into a discrete signal with J pixels in the image space. Therefore, the strategies of 3D reconstruction are presented in the following for the case of discrete signals. As a convention, the terms (inverse) Fourier transform and components refer to the discrete (inverse) Fourier transform and the total number of components in two or three dimensions, respectively. The j-th component of the Fourier transform of the i-th image of a data set is:

$$X_{ij} = J_{ij} + N_{ij} \qquad \text{for i} = 1, ..., \text{I, and j} = 1, ..., \text{J} \tag{1.14}$$

The 3D reconstruction from 2D projections of the volume of interest is based on the Fourier slice theorem stating that the 2D Fourier transform of a projection of a 3D volume represents a 2D slice of the 3D Fourier transform perpendicular to the projection direction:

$$X_{ij} = CTF_{ij} \sum_{l=1}^{L} \mathbf{P}_{jl}^{\phi} V_l + N_{ij}, \tag{1.15}$$

where CTF_{ij} is the j-th component of the CTF of the i-th image, V_l the l-th component of the 3D Fourier transform of the volume of interest, $\sum_{l=1}^{L} \mathbf{P}_{jl}^{\phi} V_l$ extracts a slice from V in the orientation ϕ. With the Fourier transforms of many images of a structure of interest acquired from many different orientations, the 3D Fourier space is filled with the respective slices to reconstruct the Fourier transform of the volume.

In the SPA approach, snapshots of particles of a structure of interest in various unknown orientations are acquired. In an iterative process, each particle snapshot X_i is compared with projections calculated from the 3D volume of a reference structure in orientations ϕ to find the best orientation $\phi_\text{i}^\star$. In the first iteration, an initial guess is used as a reference. A 3D electron density map is calculated by filling the Fourier space with the Fourier transform of the particle snapshots according to the respective orientations.

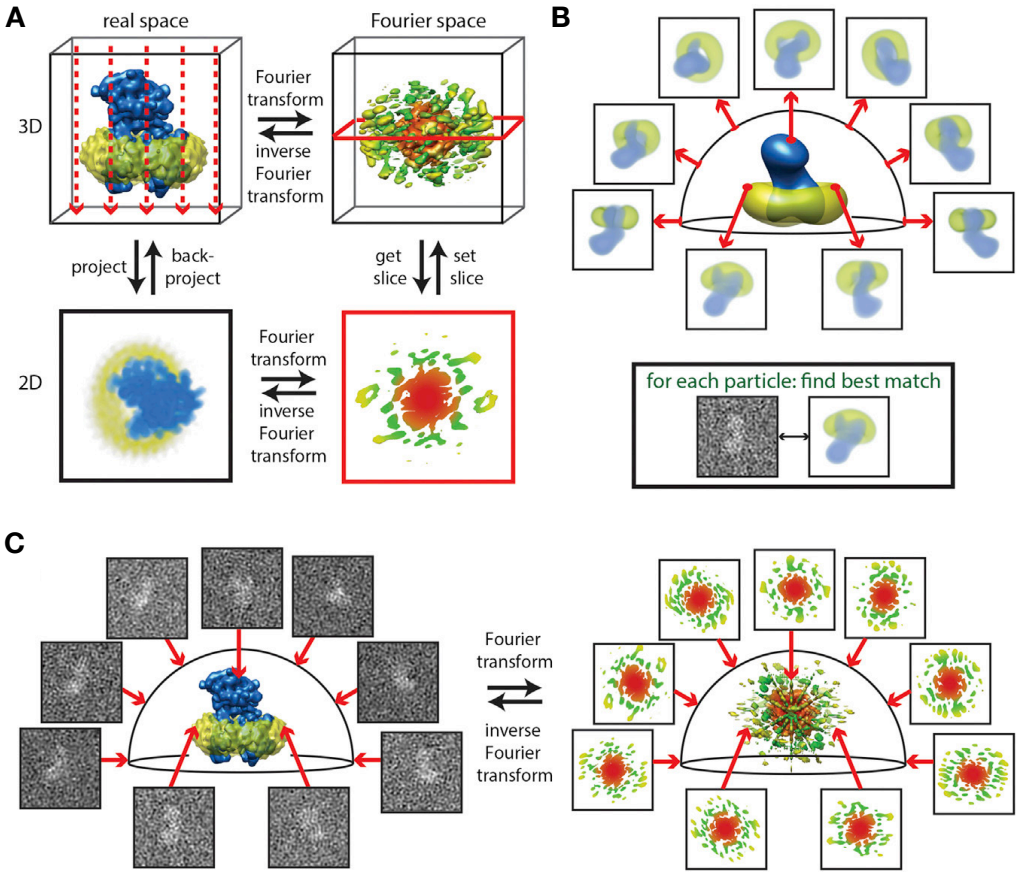

Figure 1.2 Concepts of 3D SPA of electron microscopy data (A) Illustration of the Fourier Slice Theorem. **(B)** Comparison of a particle snapshot with calculated projections of a 3D reference. **(C)** Reconstruction of the 3D structure via many particle snapshots projected from various orientations. Adopted from [99], modified.

This map is used as the new reference in the next iteration:

$$V_l^{(n+1)} = \frac{\sum_{i=1}^{I}\sum_{j=1}^{J} \mathbf{P}_{lj}^{\phi_i^{\star}T}\,\mathrm{CTF}_{ij}X_{ij}}{\sum_{i=1}^{I}\sum_{j=1}^{J} \mathbf{P}_{lj}^{\phi_i^{\star}T}\,\mathrm{CTF}_{ij}^2 + \frac{NPS_{ij}}{SPS_{ij}}}, \tag{1.16}$$

where $\sum_{j=1}^{J} \mathbf{P}_{lj}^{\phi_i^{\star}T} X_{ij}$ places the Fourier transform of the i-th image as a slice into the 3D Fourier transform of the volume according to the optimized orientation parameter $\phi_i^{\star}$. The CTF terms are used to deconvolute the image by Wiener filtering. In many software packages, the inverse SNR in the Wiener filter is approximated by a free parameter C. Commonly, the reference is low-pass filtered during the iterative refinement to compensate for the inaccuracy of the Wiener filtering and to avoid overfitting. However, with the filter shape unknown, this results in additional free parameters "which may ultimately lead to subjectivity in the cryo-EM structure determination process" [77].

1.2.5 Relion

Relion is a software package for SPA using **Re**gularised **Li**kelihood **O**ptimatio**n** and is the implementation of "A Bayesian View on Cryo-EM Structure Determination [77]" by Sjors H.W. Scheres [76]. It is based on the linear image formation model shown in equation 1.15 and the following assumptions:

- The noise in the complex plane N_{ij} is independent and Gaussian distributed with mean equal to zero and variance σ_{ij}.
- The Fourier components of V_l are independent and Gaussian distributed with mean equal to zero and variance τ_l and serves as prior information.

Previous methods used maximum likelihood (ML) optimization where the likelihood $P(X|\Theta, Y)$ of observing the data set X given a certain model with parameter set Θ and a reference Y is maximized by varying the orientations. In contrast, Relion uses maximum a posteriori (MAP) optimization, where the posterior distribution $P(\Theta|X, Y)$ of the model Θ, which includes all V_l, τ_l, and σ_{ij}, being the correct one given the observed data X and the prior information Y, is optimized:

$$P(\Theta|X, Y) \; \alpha \; P(X|\Theta, Y)P(\Theta|Y). \tag{1.17}$$

The assumption of Gaussian distributed signal represents the prior information Y. It is implemented in the prior $P_{prior}(\Theta|Y)$, i.e., the likelihood that the model Θ is correct given the prior information Y:

$$P(\Theta \mid Y) = \prod_{l=1}^{L} \frac{1}{2\pi\tau_l^2} \exp\left(\frac{|V_l|^2}{-2\tau_l^2}\right). \tag{1.18}$$

The parameters τ_l of the prior regularize the optimization process. Inside the framework of Relion, the data are divided into two half-sets which are reconstructed independently. In each iteration, the Fourier shell correlation is calculated to estimate τ_l. Since the correlation drops towards higher frequencies, the resulting smaller values for τ_l represent a low-pass filter and prevent overfitting.

Similar to other approaches, the data are compared to projections of the current model calculated from various orientations. The likelihood terms $P(X_i|\Theta, Y)$ are computed by integrating [1] over the orientations ϕ:

$$P(X_i|\Theta, Y) \; \alpha \; \int P(X_i|\phi, \Theta, Y)P(\phi|\Theta, Y)d\phi = \int \Gamma_{i\phi} d\phi \tag{1.19}$$

[1] "In practice, the integrations over ϕ are replaced by (Riemann) summations over discretely sampled orientations" [76]

In the term $\mathrm{P}(\phi|\Theta,\mathrm{Y})$, prior information about the distribution of $\mathrm{P}(\phi)$ can be included. Due to the Gaussian distributed noise, the term $\mathrm{P}\left(\mathrm{X_i} \mid \phi,\Theta,\mathrm{Y}\right)$, i.e., the likelihood of observing the Fourier transform of an image given the orientation, the model, and the prior, is:

$$P\left(X_{ij} \mid \phi,\Theta,Y\right) = \prod_{j=1}^{J} \frac{1}{2\pi\sigma_{ij}^2} \exp\left(\frac{\left|X_{ij} - CTF_{ij}\sum_{l=1}^{L}\mathbf{P}_{jl}^{\phi}V_l\right|^2}{-2\sigma_{ij}^2}\right), \tag{1.20}$$

where the product is used to combine the likelihoods of observing the independent components.

The MAP estimate is implemented using the expectation-maximization algorithm:

$$V_l^{(\mathrm{n+1})} = \frac{\sum_{i=1}^{I}\int_{\phi}\Gamma_{i\phi}^{(\mathrm{n})}\sum_{j=1}^{J}\mathbf{P}_{lj}^{\phi^\top}\frac{\mathrm{CTF}_{ij}X_{ij}}{\sigma_{ij}^{2\,(n)}}d\phi}{\sum_{i=1}^{I}\int_{\phi}\Gamma_{i\phi}^{(\mathrm{n})}\sum_{j=1}^{J}\mathbf{P}_{lj}^{\phi^\top}\frac{CTF_{ij}^2}{\sigma_{ij}^{2\,(n)}}d\phi + \frac{1}{\tau_l^{2(n)}}}, \tag{1.21}$$

where the likelihood and the prior are represented by the integration term and the Wiener filter, respectively. For further reading, including the details of updating τ_{kl} and σ_{ij}, and the implementation of the algorithm, please refer to the original publications [76, 77].

1.3 Addressing structural Heterogeneity

In the SPA approach, the 2D projections of many thousands of copies of a structure are used to reconstruct an electron density map by iteratively refining the orientations of the particle snapshots. However, these copies are not ideal. Structural differences and thermal motion lead to heterogeneity in the data set. The reconstructed 'consensus' electron density map represents the average structure of the particles, and the local degree of heterogeneity affects the local resolution of the structure. As a convention, the term refinement refers both to the iterative process and the resulting electron density map. In the following, strategies to address the structural heterogeneity of the data are presented, including:

- reconstructing multiple electron density maps from subsets of particles, implemented in Relion and other software in a 3D classification procedure,
- focusing the optimization on one or several subregions,
- fitting a linear subspace model to the data using principal component analysis.

.

1.3.1 3D classification

In an iterative process, the particles are assigned to a user-defined number of classes and the electron densities of these classes are reconstructed. In Relion, the i-th image of the data set is now described as:

$$X_{ij} = CTF_{ij} \sum_{l=1}^{L} \mathbf{P}_{jl}^{\phi} V_{kl} + N_{ij}, \tag{1.22}$$

where V_{kl} is the l-th component of the 3D Fourier transform of the k-th structure [76]. In the modified algorithm, the model is optimized including the assignment of the particles to the classes. The equations describing the algorithm are adjusted accordingly. E.g., the likelihood of observing an image is described by $P\left(X_i \mid \phi, k, \Theta, Y\right)$ given an orientation ϕ, class assignment k, model Θ (including V_{kl}, σ_{ij}, and τ_{kl}), and prior Y.

1.3.2 Focused refinement and multi-body refinement

Focused refinement is an approach to address the conformational heterogeneity of the data set. By using a masked reference, the alignment of the particle snapshots can be focused onto a region of interest. Partial signal subtraction can be used to reduce the effect that the signal outside the masked region effectively acts as noise during the focused refinement. For this, a map is created from the consensus refinement, where the region of interest is removed using a smooth mask. This map is used to calculate 2D projections according to the consensus refined orientations which are then subtracted from the corresponding particle snapshots to create a new set of partial-signal-subtracted particles.

In the multi-body refinement approach by Nakane et al. [78] the 3D volume of the consensus refinement is divided into a user-defined number of subvolumes, termed bodies. These bodies are refined in parallel using focused refinement and partial signal subtraction. For each iteration, the volumes of the previous iteration are used as new references and to create updated sets of subtracted particles. In this approach, the i-th particle snapshot is described as:

$$X_i = CTF_i \sum_{b=1}^{B} \mathbf{P}^{\phi_b} V_b + N_i, \tag{1.23}$$

with the Fourier Transform of the b-th body V_b and the orientation ϕ_b of the b-th body with respect to the particle. Here, the individual Fourier components are not written to facilitate the readability of the equation. The i-th subtracted particle associated with the b-th body is:

$$S_{ib} = X_i - CTF_i \sum_{b' \neq b}^{B} \mathbf{P}_{\phi_{ib'}^{\star}} V_{b'}, \tag{1.24}$$

with the optimal orientations of all bodies of the previous iteration $\phi^{\star}_{\mathrm{ib}'}$. The updated volume of the b-th body is calculated similarly to the consensus refinement:

$$V_b^{(\mathrm{n}+1)} = \frac{\sum_{i=1}^{I} \int_{\phi_b} \Gamma^{(\mathrm{n})}_{i\phi_b} \mathbf{P}^{\mathrm{T}}_{\phi_\mathrm{b}} \frac{\mathrm{CTF}_i S_{ib}}{\sigma_i^i} d\phi_b}{\sum_{i=1}^{I} \int_{\phi_b} \Gamma^{(\mathrm{n})}_{i\phi_b} \mathbf{P}^{\mathrm{T}}_{\phi_\mathrm{b}} \frac{\mathrm{CTF}_i^2}{\sigma_i^2} d\phi_b + \frac{1}{\tau_b^2}}. \tag{1.25}$$

The posterior distribution uses the assumption that ϕ_b is Gaussian distributed, centered on the orientations of the consensus refinement with user-defined standard deviations as a prior $\mathrm{P}\left(\phi_\mathrm{b} \mid \Theta^{(\mathrm{n})}\right)$:

$$\Gamma^{(\mathrm{n})}_{i\phi_b} = \frac{P\left(\mathbf{X}_i \mid \phi_b, \Theta^{(\mathrm{n})}\right) P\left(\phi_b \mid \Theta^{(\mathrm{n})}\right)}{\int_{\phi'_b} P\left(\mathbf{X}_i \mid \phi'_b, \Theta^{(\mathrm{n})}\right) P\left(\phi'_b \mid \Theta^{(\mathrm{n})}\right) d\phi'_b}. \tag{1.26}$$

The optimal orientations for the next iterations $\phi_{ib}^{\star(\mathrm{n}+1)}$ are calculated by optimizing the posterior distribution:

$$\phi_{ib}^{\star(\mathrm{n}+1)} = \max_{\phi_b} \Gamma^{(\mathrm{n})}_{i\phi_b}. \tag{1.27}$$

These orientations can be used to analyse the distribution of the changes in orientation with respect to the consensus refinement using principal component analysis. The analysis is performed on six coordinates per body: three Euler angles and three translational degrees of freedom, converted from the two-dimensional translational changes of the particle snapshots into a uniform three-dimensional Cartesian coordinate system. The orientational changes of the particles can be projected on the set of eigenvectors to analyze the distribution of the amplitudes of the particles along the eigenvector. A multimodal distribution indicates a noncontinuous heterogeneity of the data set and the presence of local minima in the conformational landscape [78].

1.3.3 3D Variability Analysis

The 3DVA tool in the CryoSparc software suite [80, 81] is based on a variant of probabilistic principal component analysis (PCA). In the 3DVA model, each image $\mathrm{X_i}$ is described as a noisy, CTF-corrupted projection of a linear combination of the 3D mean volume V_0 and a user-defined number of M components $\mathrm{V_m}$:

$$X_i = CTF_i \ \mathbf{P}^{\phi} \ V_i + N_i = CTF_i \ \mathbf{P}^{\phi} \left[V_0 + \sum_{m=1}^{M} w_{im} V_m \right] + N_i, \tag{1.28}$$

where $\mathbf{P}^{\phi}$ extracts a Fourier slice as in previous equations, and w_{im} are the weight coefficients of the components. For the I images of the data set, the components span a M dimensional linear subspace. In conventional PCA, the components and the weight coeffi-

cients represent the eigenvectors of the covariance matrix of the data and the amplitudes of the projection of the data onto the set of eigenvectors, respectively. The orthogonal eigenvectors describe the directions of maximal variance. In the model of 3DVA, the mean volume and the particles CTFs and orientations are taken from a previous consensus refinement. The assumption of Gaussian distributed weights are used as a prior. The components, including the mean of the posterior distribution of the weights as well as the components and scale parameters, are iteratively refined by maximum likelihood estimation.

Chapter 2

Zoom-in reconstruction of a multidomain object

Remark: The presented work in this chapter was published in Massimo Kube, Fabian Kohler, Elija Feigl et al., Revealing the structures of megadalton-scale DNA complexes with nucleotide resolution (2020) [74]. Elija Feigl constructed the pseudo-atomic model. Baki Nagel-Yüksel supported sample preparation and data analysis as a working student. Maximilian N. Honemann provided scaffold.

Electron microscopy particle snapshots represent 2D projections of a 3D object. In the SPA approach, a 3D electron density map is reconstructed from the combined 2D-projected information of many particles in different orientations. The underlying assumption is that a set of projections of one particle from different orientations is the same as a set of individual projections from the same projection angles of many exact copies of the particle, and will therefore result in the same reconstructed electron density map. However, in reality, the individual particles are not identical, which decreases the resolution of the reconstructed electron density map. The particles are subjected to structural heterogeneity depending on the underlying energy landscape. While particles in distinct conformations can be relatively easily separated from each other using 3D classification, continuous motion presents a significant challenge. In the following sections, we present strategies to extract high resolution information from heterogeneous single-particle cryo-EM data of DNA nanoobjects. We used a multidomain object as a model, referred to as "Twist-Tower", where the name refers to its additional use in the study of the global twist of multilayered DNA objects, which is presented in chapter 3. The Twist-Tower consists of four cuboids with quadratic cross sections of 2×2, 4×4, 6×6, and 8×8 helices arranged on a square lattice (Fig. 2.1A-B), and each domain has a length of about 64 bp. The three smaller domains are connected to the 8×8 domain, which serves as a platform.

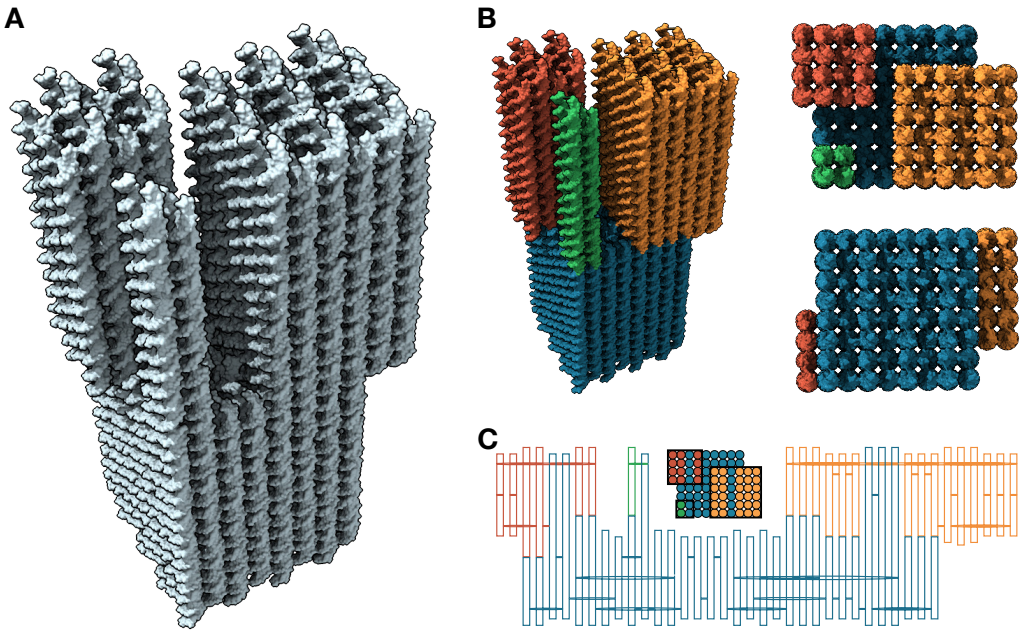

Figure 2.1 Design of the Twist-Tower (A) 3D illustration of the global shape. The objects consists of four domains with quadratic cross sections of 2 × 2, 4 × 4, 6 × 6, and 8 × 8 helices arranged on a square lattice. The illustration is based on oxDNA starting configuration created with tacoxDNA [100] from a caDNAno design diagram [33]. **(B)** Side, top, and bottom view of the Twist-Tower colored by domains. **(C)** Blueprint of the scaffold routing. One column of helices in each of the 2 × 2, 4 × 4, and 6 × 6 domains is directly created by scaffold loops which are part of the 8 × 8 domain (blue). The other helices of the 2 × 2 (green), 4 × 4 (red), and 6 × 6 (orange) domain are created from loops originating from these helices. Inset: top view with the same scaffold color scheme.

The object is designed with the native effective helical twist density of 10.67 bp/turn as imposed by the square lattice design.

The design of the Twist-Tower is explained in detail in section 2.1, which includes the scaffold routing, as well as an analysis of the folding product quality using gel electrophoresis and negative stain electron microscopy. In section 2.2, we show the 3D cryo-EM structure of the object reconstructed via a basic 3D refinement, where the object is treated as a single rigid body. In the sections 2.3 and 2.4, we present the first and second zoom-in step in the form of a domain-based refinement and a scanning-focused refinement strategy, respectively. In the final section, we analyze the heterogeneity of the object using principle component analysis-based methods.

2.1 Design and folding optimization

The scaffold routing of the object is designed such that the individual domains are built from loops of the 8064 nt long circular scaffold (Fig. 2.1C). The helices of one row in each of the smaller domains are created from scaffold extensions from the 8 × 8 domain. The other

helices of the respective domains are created from loops protruding from the helices of these rows. Most of these helices are connected to the 8 × 8 domain via staple oligonucleotides, with scaffold crossovers located at the interfaces. Due to this design strategy, the average distance of segments connected by staple oligonucleotides in the topology of the scaffold is reduced compared to a design where the scaffold is routed back and forth along the entire length of the helices. Based on the findings of previous computational and experimental studies on the folding process [41, 101], we expected that the chosen scaffold routing is beneficial for the folding yield of the Twist-Tower.

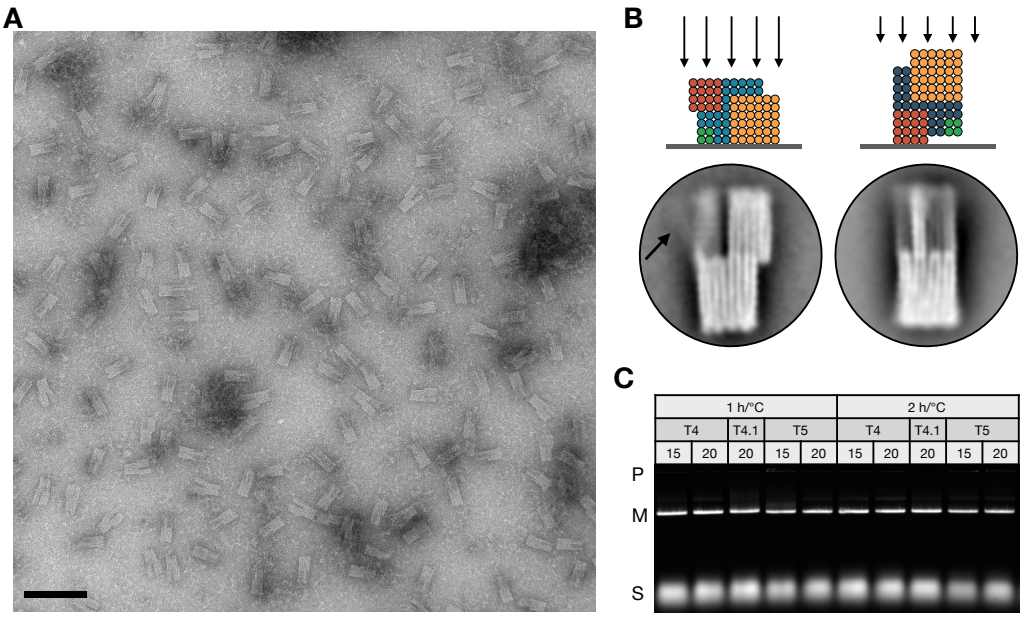

Figure 2.2 Negative stain EM imaging and gel electrophoretic analysis (A) Exemplary negative stain EM micrograph of an unpurified sample of the native Twist-Tower on a carbon coated grid. The particles appear to be well folded. Excess staples are visible in the background. The scale bar is 100 nm. **(B)** 2D class averages, with possible orientations of the particles in the classes illustrated above. The grid and the direction of incident electrons are illustrated as a gray lines and arrows, respectively. The arrow in the left class average image indicates the 2 × 2 domain which appears to be bent to the side. **(C)** Gel electrophoretic analysis of the folding products of different folding conditions. P = pocket, M = approximate migration distance of monomers, S = excess staples. The top row indicates the duration of each 1 °C temperature step in the respective annealing ramps, which are indicated in the second row. T4, T4.1 and T5 represent annealing ramps of 56 °C to 53 °C, 54 °C to 53 °C, and 58 °C to 55 °C, respectively. The third row indicates the concentration of $MgCl_2$.

We analyzed the composition of the folding products using gel electrophoresis and negative stain EM, which revealed high monomer yields for a variety of folding conditions (Fig. C.1). Negative stain EM images show well folded particles with a global shape according to the design (Fig. 2.2A). The Twist-Tower particles have a strong orientational bias and lie almost exclusively on one of the sides. Since the images are 2D projections, the

local brightness within the particles corresponds to the amount of DNA and negative stain which the beam has passed through. We extracted particles from the micrographs and performed reference-free 2D classification (Fig. 2.2B). In the 2D-class averaged images, stripe patterns are visible in the 8 × 8 and 6 × 6 domain which results from the helices of multiple layers being well aligned. The 6 × 6 and the 8 × 8 domain account for over 80 % of the total mass, which results in a strong signal, and thus the particles are aligned predominantly with respect to these domains. The stripes indicate a low amount of twist in these domains. In contrast, the two small domains appear blurred, which indicates global twist or internal or relative structural heterogeneity of the domains, i.e., within the domains or with respect to the larger domains. Interestingly, the 2 × 2 domain seems to be bent towards the side. By optimization of the annealing ramp and folding buffer composition, we achieved monomer yields above 85 % (Fig. 2.2C).

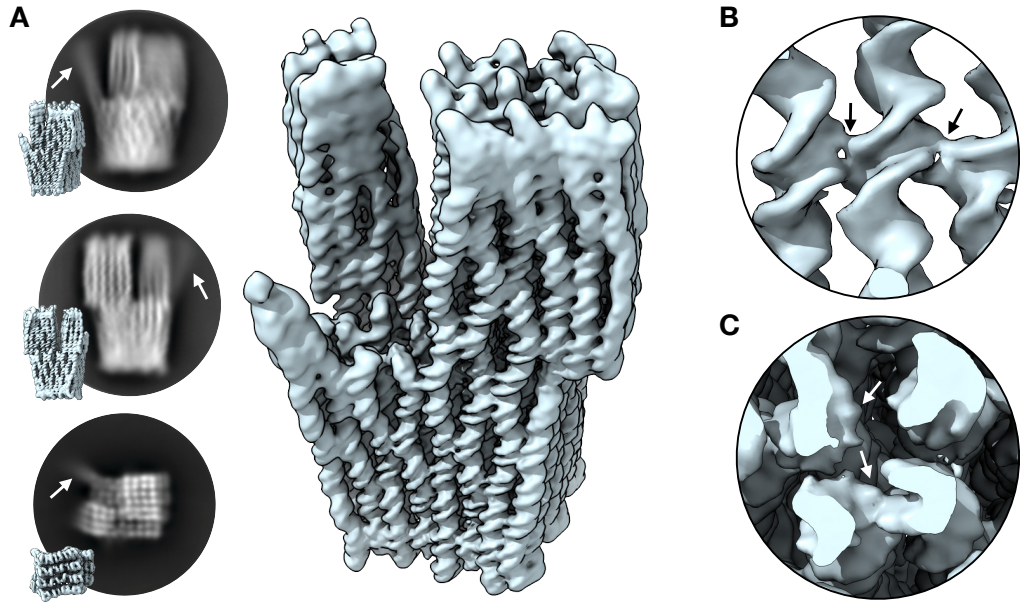

Figure 2.3 Consensus-refined map of the Twist-Tower. (A) Exemplary 2D class averaged images and 3D electron density map. For each 2D class, the approximate orientation of particles contributing to the class are as indicated by the orientation of the adjacent 3D map. White arrows indicate the position of the 2 × 2 domain. **(B)** Exemplary crossover stack extracted from the 8 × 8 domain. Arrows indicate the positions of two crossovers. **(C)** Top view onto a region extracted from the 8 × 8 domain. The arrows indicate the positions of an exemplary phosphate moiety which manifests as bumps (top) and a well-resolved crossover (bottom).

2.2 Consensus refinement

To study the 3D structure of the Twist-Tower in solution, we acquired cryo-EM images of purified and concentrated Twist-Tower particles in free-standing ice using a Titan

Krios 300 kV electron microscope. We reconstructed an electron density map from about 6.8×10^5 particles at a global resolution of 7.4 Å (Fig. D.12). In the electron density map, the 2 × 2 domain is only resolved partly, whereas the global shape of the rest of the object looks as expected (Fig. 2.3A). In low-threshold surface representations (Fig. E.7) and in 2D class average images (Fig. 2.3B) the global shape of the 2 × 2 domain can be recognized and appears to be tilted to the side. The 4 × 4, 6 × 6, and 8 × 8 domains are increasingly well resolved. Individual helices are visible in the 4 × 4 domain. The helices at the corners show a lower resolution, while even the shape of the double helices are recognizable towards the 8 × 8 domain. In the 6 × 6 and 8 × 8 domains, structural details of the helices are resolved, including crossovers (Fig. 2.3B) and the positions of phosphate moieties along the backbone, which manifest as bumps (Fig. 2.3C). Global structural features of the object, including the global twist of the individual domains and the chickenwire-like arrangement of the helices, as well as structural details, including the crossover stack design motifs, will be addressed in chapter 3.

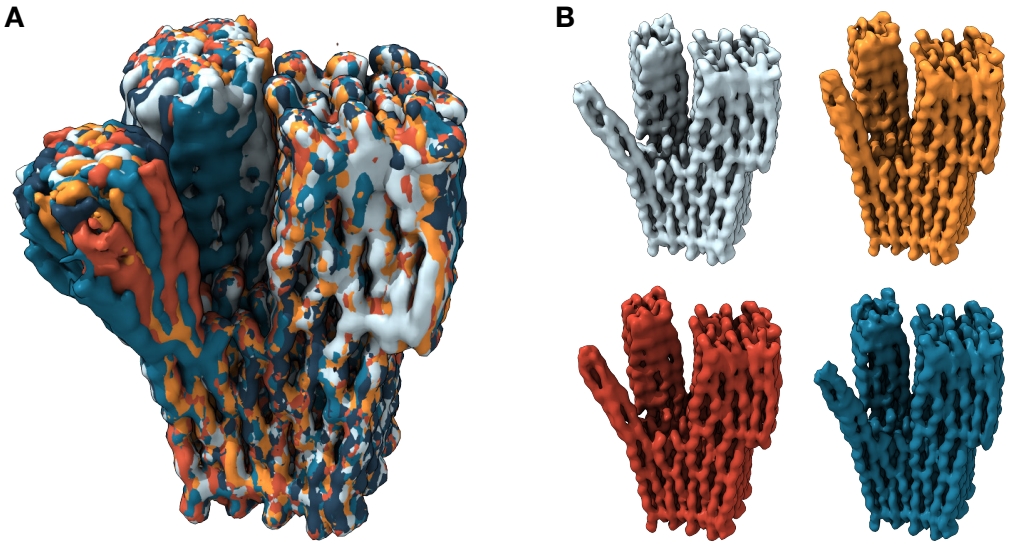

Figure 2.4 Structural heterogeneity of the Twist-Tower. (A) Heterogeneity visualized by 3D classification superimposed maps from a 3D classification. **(B)** Individual maps of exemplary 3D classes.

In accordance with the visual analysis, the local resolution estimation exhibits a wide spectrum within the presented volume (Fig. 2.3A) ranging from 6.0 Å to 14.2 Å (Fig. E.6). To analyze the structural heterogeneity of the object, we performed an extensive 3D classification with 200 classes. The 2 × 2 and 4 × 4 domains show high levels of structural heterogeneity (Fig. 2.4), which is in agreement with the heterogeneity in resolution in the consensus refined map. In the individual maps of the 3D classification the local resolution distribution is more homogeneous, and in most classes, the entire 2 × 2 domain is resolved

at a similar level as the other domains. The estimated values of the global resolution of the individual classes are in the range of 17 Å to 25 Å.

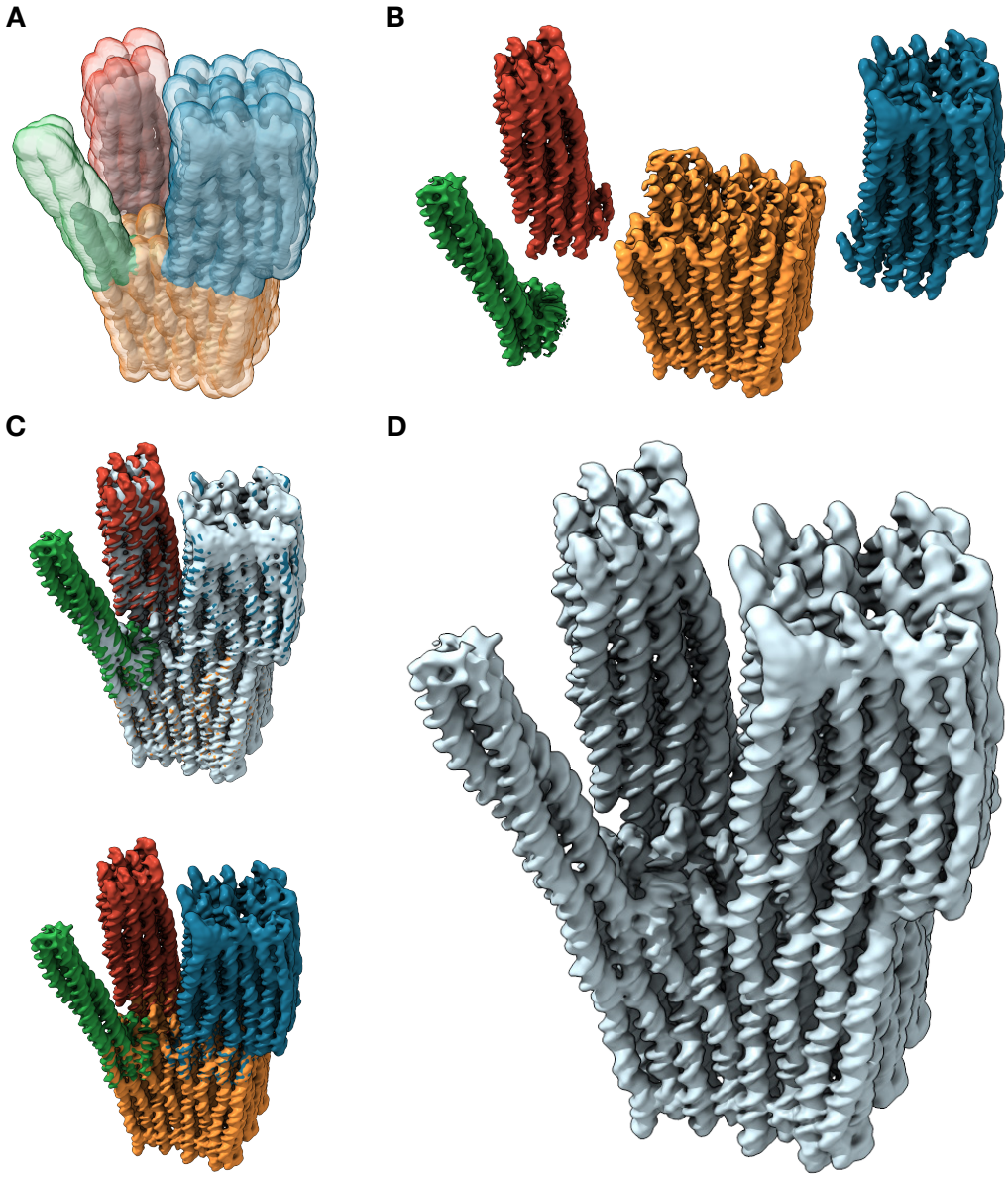

Figure 2.5 Four-body refinement of the Twist-Tower. **(A)** Representation of masks to define the bodies (green, red, orange, blue). The consensus refinement is shown as a reference. **(B)** Maps of the individually refined four bodies. **(C)** Superposition of the refined bodies, aligned to the consensus-refined map. Top: the consensus-refined map is shown at low-threshold as a reference. **(D)** Composite map. [74]

2.3 Refinement of domain-like regions

In the consensus refinement, the entire structure is treated as a single rigid body. However, as revealed by 3D classification, the four domains show different levels of heterogeneity. To extract structural information at higher resolution, we refined the four domains of the Twist-Tower individually by conducting a multi-body refinement [78] (Fig. 2.5A). A description of the underlying theory and implementation of this approach is given in chapter 1. We performed global and local resolution estimations of the four-body-refined maps, and created sharpened and local resolution-filtered maps (Fig. 2.5B). We improved the resolution of the 8×8, 6×6 and 4×4 domains from 7.5 Å, 7.3 Å, and 8.4 Å to 7.1 Å, 6.8 Å, and 6.5 Å, respectively (Fig. D.12, D.13). For the 2×2 domain, we achieved a global resolution of 7.8 Å, which may be compared to the barely recognizable 2×2 domain in the consensus refined map.

We aligned the multi-body refined domains to the consensus refinement (Fig. 2.5C) and created a composite map (Fig. 2.5D), which had a sufficient resolution to perform a pseudo-atomic model fit (Fig. 2.6). To meet the requirements of our DNA origami cryo-EM structures, we used the previously reported fitting protocol, which is based on cascaded relaxation and molecular dynamics flexible fitting (MDff) [74].

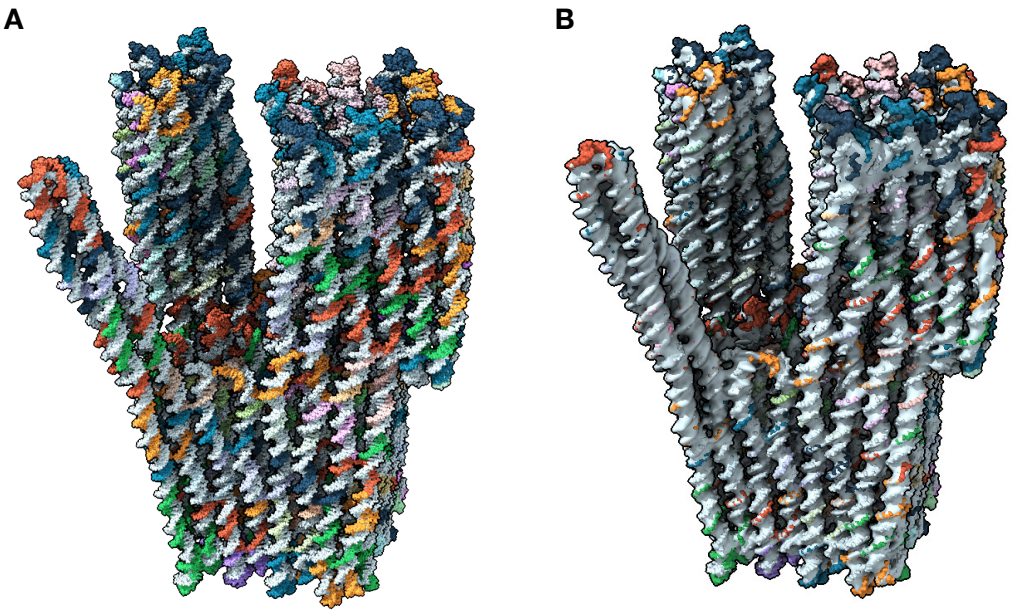

Figure 2.6 Pseudo-atomic model of the Twist-Tower. (A) Pseudo-atomic model. The scaffold is depicted in light blue color. **(B)** Model and electron density map superimposed.

2.4 Scanning-focused refinement

In the first zoom-in step, we improved the resolution of the Twist-Tower, particularly for the smaller domains, by focusing the refinement on the individual domains using the approach of multi-body refinement. We selected one of the best resolved regions, located

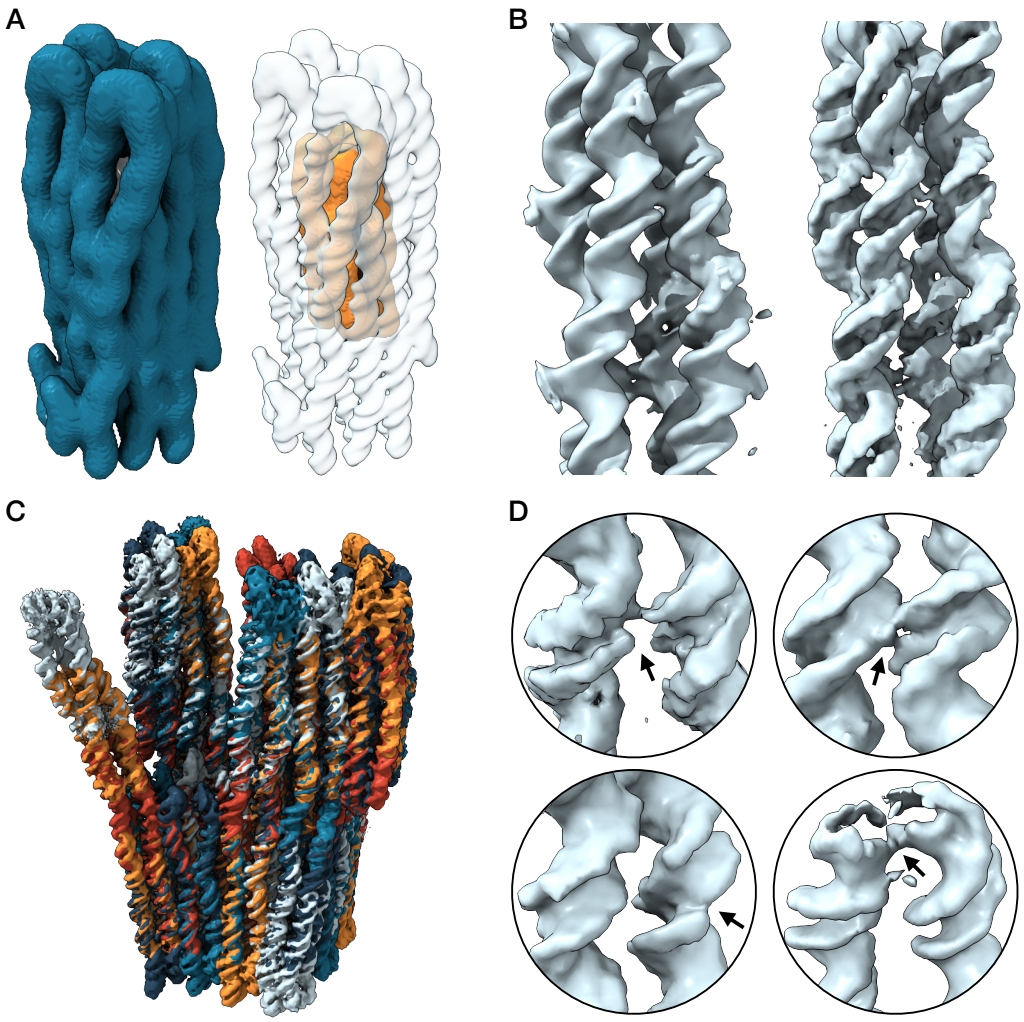

Figure 2.7 Scanning-focused refinement of the Twist-Tower. (A) Masks defining a region of interest (orange) in the center and the rest (blue) of the 4 × 4 domain. **(B)** Comparison of the region of interest cut-out from the four-body refined 4 × 4 domain (left) and the same region after applying the focused refinement using the masks presented in (A). **(C)** Scanning-focused refined Twist-Tower from the iterative application of the focused refinement on many overlapping regions using the same window size as in (A). **(D)** Examples of high-resolution features revealed by the scanning-focused refinement. The arrows indicate the described features. Top left: single-stranded staple crossover with a hole on the terminating staple strand due to the absence of a phosphate moiety. Top right: double-stranded crossover. Bottom left: staple strand break site manifested as a discontinuity in the backbone. Bottom right: single-stranded terminal scaffold connection of two helices. Less defined features at the termini indicate poly-T staple-overhangs. [74]

in the center of the 4 × 4 domain, with a cross section of 2 × 2 and an approximate length of 32 bp, to test if the resolution could be further improved in a second zoom-in step. To reduce the computational effort, we performed the calculations on a set of cropped particle snapshots with the signal of the other domains subtracted. We created two soft masks containing the inside and the outside of the region of interest, respectively, and performed a two-body refinement (Fig. 2.7A-B). With this approach, we achieved a resolution of 4.3 Å for the small region of interest (Fig. D.14). Local resolution estimation yielded a range of 3.8 Å to 4.8 Å, which may be compared to the local resolution estimation of this region of 5.5 Å to 6.5 Å after the first zoom-in step. We attempted to focus on even smaller regions by using smaller windows with a cross section of 2 × 1, or only a single helix. However, this was less successful.

We scanned the entire Twist-Tower with overlapping windows, each with an approximate size of 32 bp times 2 × 2 helices, achieving up to nucleotide resolution (Fig. 2.7C). This is a striking result, particularly for the 2 × 2 domain, considering it was only visible as a poorly defined shape in the consensus refinement. At this resolution, several structural features are revealed, including phosphate moieties of the nucleotides, which manifest as bumps (Fig. 2.7B,D). In double-stranded crossovers, the two connections between the helices are visibly separated. In single-stranded staple crossovers, holes are recognizable at the nick sites of the other staple strands, caused by the lack of phosphate moieties at both termini of the chemically synthesized oligonucleotides. Similarly, discontinuities of the backbone are visible at the nick sites in segments between crossovers. At the helix ends, the terminal scaffold connections of pairs of helices are resolved, and features in the electron density maps indicate single-stranded staple overhangs which are designed to prevent dimerization.

2.5 Flexibility analysis

In the consensus refinement, the particle snapshots are averaged resulting in local resolution differences depending on the structural heterogeneity. In the first zoom-in step, we were able to improve the resolution of the domains, particularly for the 4 × 4 and 2 × 2 domains. In the second zoom-in step, we refined small regions of interest up to nucleotide resolution. The improved resolution reveals valuable and previously hidden structural information. However, the information of local heterogeneity is diminished compared to considering the Twist-Tower as a whole.

To provide information about the heterogeneity, we performed a principle component analysis (PCA) on the results of the four-body refinement, which are the relative rotational and translational changes of each body for each particle. Using the respective tool in Relion, we identified four main components of a total of 24, which account for 43 %

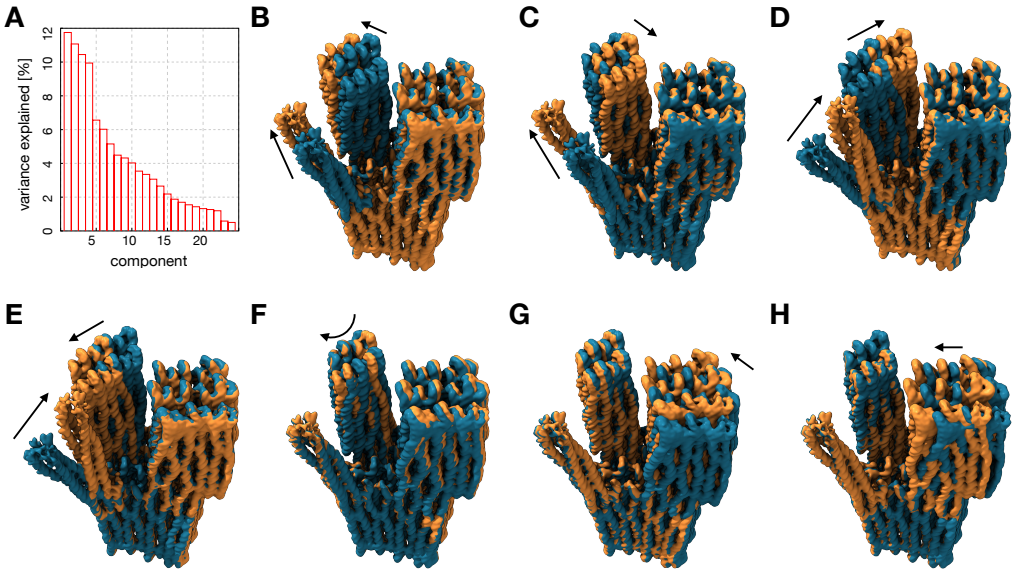

Figure 2.8 Multi-body PCA. (A) Distribution of the percentage of total variance explained by the components. **(B) - (H)** The first seven principal components. For each component, the two overlapped maps (blue and orange) represent the median orientations of the upper and lower 10 % of the particle images in the distribution of the component. Arrows indicate the most prominent movements in the component.

of the total variance of the heterogeneity of the data set, as well as three medium components, which each account for above 5 % of the total variance (Fig. 2.8A). To visualize the changes along the components, we created a series of ten maps for each component by splitting the amplitude distribution of the particles along the component into equally populated bins. The first four components mainly describe movements of the 2×2 and 4×4 domains, and can be categorized into two pairs of orthogonal directions, each pair containing two components with motions in equal and in opposite directions (Fig. 2.8B-E). In the fifth component a rotational movement of the 4×4 domain is dominant (Fig. 2.8F). While in the first five components the motion of the two big domains is only marginal, in the sixth and seventh component primarily changes of the 6×6 domain are visible (Fig. 2.8G-H). The amplitude distributions of the particles along the respective components are monomodal, indicating continuous motion along each of the components.

Multi-body PCA (MB-PCA) describes the heterogeneity as an approximation, with a user-defined number of rigid bodies. By treating the four domains as rigid bodies, discontinuities at the interfaces of the bodies are visible in the maps of the component series. Deformations within each domain and across the interfaces are not resolved. Therefore, we additionally analyzed the heterogeneity of the Twist-Tower using 3DVA [81]. The tool fits a linear 3D subspace model to the data set of particle snapshots, consisting of the mean volume and a user-defined number of weighted eigenvolumes along the direction of the largest variances. We performed 3DVA using ten components and built maps repre-

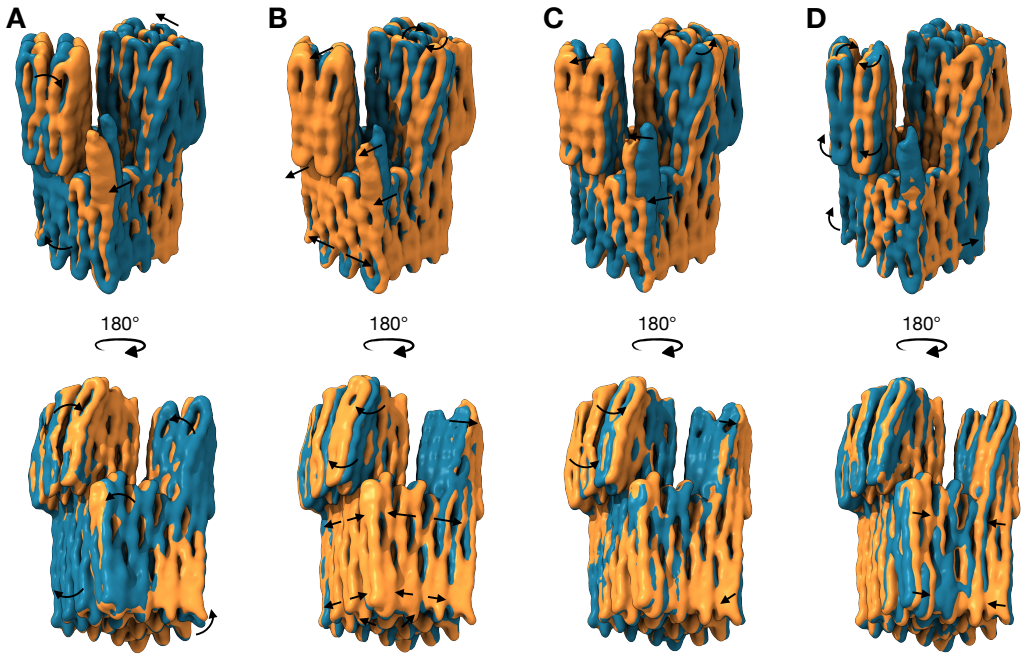

Figure 2.9 3D variability analysis (3DVA). (A) - (D) Exemplary principal components. For each component the motion is represented by two overlapped maps (blue and orange). Arrows indicate the most prominent movements in the component. Top and bottom: front and back view. Complex local motions including translation, rotation, compression, and extension can be observed.

senting the components via linear combinations of the mean volume and the respective eigenvolume of the component (Fig. 2.9). We noticed a heterogeneity in the resolution of these maps, where the 2×2 domain is only partially resolved similar to the consensus refinement. Compared to the simple types of motion we observed in the MB-PCA, the components of the 3DVA describe motion with complex vector fields. They include relative translation and rotation of certain parts relatively to each other similar to the MB-PCA, but also elastic transformation like compression and extension. The latter can be seen particularly in the 8×8 domain. In comparison to the four-body approximation, the maps do not show discontinuities at the interfaces of the domains. We observed coordinated movements in the small domains and the respective parts of the 8×8 that they are connected to.

2.6 Discussion

We described the zoom-in reconstruction and structural heterogeneity analysis of the Twist-Tower multidomain object, in which we:

1. reconstructed the Twist-Tower as a single rigid object using consensus refinement,

2. performed a multi-body refinement by segmenting the object into four bodies,
3. used a scanning-focused refinement approach with a small window to refine the entire object,
4. characterized the structural heterogeneity of the object using MB-PCA and 3DVA.

In the consensus refinement, the resolution of the two smaller domains is considerably lower than the bigger domains. In addition to an increased flexibility of objects with smaller sizes, the heterogeneity in local resolution can be explained by the algorithm of the alignment process. In the consensus refinement, the orientations of the individual particle snapshots are refined iteratively to achieve the best global resolution. Since the 8×8 domain and the 6×6 domain contribute over 53 % and 30 % of the total molecular weight of the object respectively, the snapshots of the particles are aligned predominantly with respect to these two high-signal domains. Using a four-body refinement, we achieved an improvement of each domain. However, the resolution of the 2×2 domain is significantly lower compared to the other domains, but reached similar levels in the subsequent scanning-focused refinement. We attribute this to the very poor initial resolution of the 2×2 domain compared to the other domains. Additionally, it is also possible that the small part of the 8×8 domain within the mask of the 2×2 domain interfered with the proper alignment of the subtracted particle snapshots. Enabled by the improved resolution, we fitted a pseudo-atomic model to the composite map created from the four-body refined domains. For the scanning-focused refinement, we used a window size of about 32 bp times a cross section of 2×2 helices. This window size corresponds to an approximate molecular weight of 100 kDa, below of which the alignment becomes progressively difficult and which presents a limitation of the multi-body refinement as stated by the authors of the multi-body approach [78]. This is in accordance with our observations of smaller windows being less effective.

Analyzing the structural heterogeneity using MB-PCA, based on the four-body refinement, revealed large ranges in the dominant motions of the 2×2 and 4×4 domains relatively to the 8×8 domain. This is in agreement with the observations of the 3D classification. Due to the approximation by four rigid bodies, the maps, which represent the motion along the respective components, exhibit discontinuities at the interfaces. This is not the case in the 3DVA. However, in the 3DVA maps, the 2×2 domain is only resolved in part. We attribute this to the operating principle of the 3DVA, where the 3D volume of each particle is described by a linear combination of the weighted eigenvolumes of the components and the mean volume, where, however, the 2 x 2 domain is poorly resolved. Using 3DVA, we identified motion patterns in the 8×8 domain which continue into the other domains. Whether they originate in the 8×8 domain and are transmitted to the other domains, vice versa, or a combination of both could not be clarified. However, we

assume that the local connectivity in the 8×8 domain, e.g., the omission of crossovers influences the observed motion.

The combination of both high resolution data revealed by focused refinements and information about structural heterogeneity obtained from 3D classification, MB-PCA, and 3DVA provides valuable structural feedback. With over 8000 bp at up to 4.3 Å resolution, the Twist-Tower presents an interesting opportunity for data mining, including the search for deviations from canonical B-DNA, the impact of the DNA sequence on the local resolution in general, and on DNA origami design motifs. We successfully applied zoom-in reconstruction and PCA to a variety of objects presented in this thesis, including a twist-free variant of the Twist-Tower (see chapter 3), a dual-scaffold object (see chapter 4), and several corner objects (see chapter 5).

Chapter 3

Global twist and design motifs in square lattice

Remark: The presented work in this chapter was published in Massimo Kube, Fabian Kohler, Elija Feigl et al., Revealing the structures of megadalton-scale DNA complexes with nucleotide resolution (2020) [74]. Elija Feigl constructed the pseudo-atomic model. Baki Nagel-Yüksel supported sample preparation and data analysis as a working student. Maximilian N. Honemann provided scaffold.

In lattice-based DNA nanoobjects, helices are arranged parallely, and neighboring helices are connected to each other via crossovers arranged in regular patterns. In multilayer square lattice-based DNA nanoobjects, neighboring helices span angles of 90°, 180°, and 270° with direct neighbors. The generally used distance of eight basepairs between two consecutive crossovers along a helix corresponds to an effective twist density of 10.67 bp/turn. This mismatch to the DNA periodicity of 10.5 bp/turn, results in an underwinding of the individual helix segments, and causes a global right-handed twist [35]. By reducing the average effective twist density, the global twist can be corrected. This is implemented by shortening the distance between consecutive crossovers of some segments, which induces compensating local overwinding and countertorque. Via negative stain EM imaging of ribbons polymerized from brick-like objects, Ke et al. showed that a reduction of the effective twist density to 10.5 bp/turn was not sufficient, but lower values of 10.44 bp/turn to 10.39 bp/turn were required to compensate the global twist [35]. Assuming a native twist density of 10.5 bp/turn, the authors speculated that the additional reduction was required due to a two-component global twisting stiffness analogous to the two-component stretching of dsDNA. However, it is possible that the negative staining sample preparation, including the electrostatic interaction with the carbon support layer,

the uranyl formate solution, and the procedure of drying, influenced the structure of the DNA objects.

Bai et al. were the first to solve a cryo-EM 3D structure of a DNA origami object [68]. The asymmetric square lattice-based, non-twist-corrected pointer object showed the expected right-handed twist. To achieve the required particle density in the vitrified ice of the grid, a carbon support layer was used. Advances in methods for the sample preparation of DNA origami objects [45, 102, 103] enabled the reconstruction of support-free cryo-EM structures. Here, we present a study of global twist and design motifs in single-layer (section 3.1) and multilayer (section 3.2) square lattice-based nanoobjects in solution using support-free cryo-EM. We address the influence of the cross section, crossover-based design motifs, and the reduction of the effective helical twist density on the structure of square lattice-based multilayer objects.

3.1 Single-layer DNA origami tiles

Single-layer tiles were part of the first DNA origami objects presented by Paul Rothemund in 2006 [4]. Along a helix, crossovers are placed at regular intervals of 16 bp alternating between the two neighboring helices, resulting in the mismatch and the imposed a twist

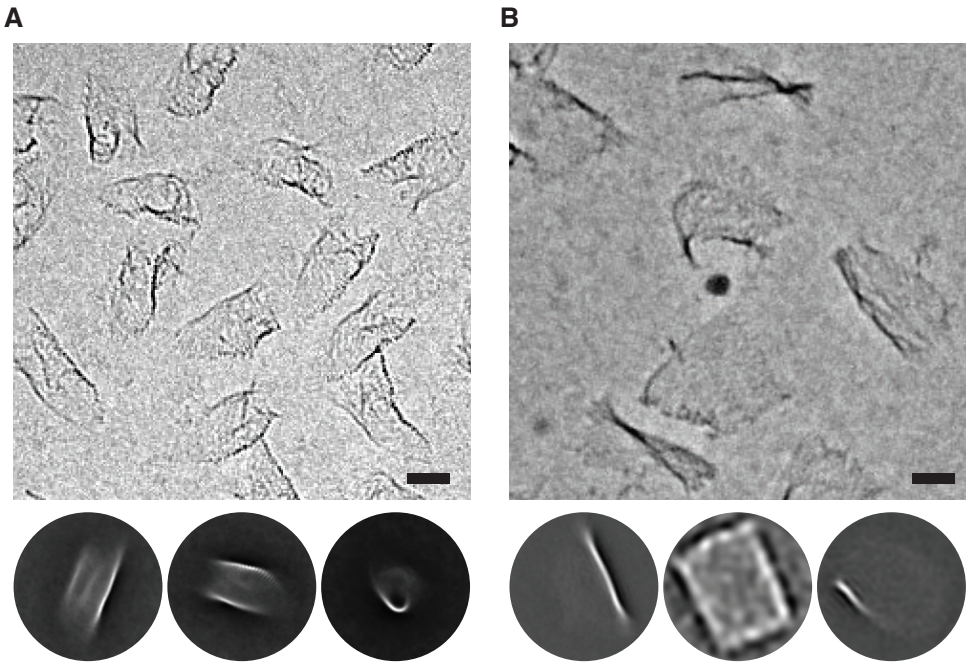

Figure 3.1 Cryo-EM imaging of single-layer DNA origami rectangle variants. **(A)** Exemplary cryo-EM free-standing ice micrograph and 2D particle snapshot averages of a rectangle variant with default crossover spacing corresponding to an effective periodicity of 10.67 bp/turn . **(B)** Like in (A) but for a 10.44 bp/turn-variant. Scale bars are 25 nm [74].

density of 10.67 bp/turn as described above. We imaged two variants of single-layer DNA origami tiles designed with a default and a reduced effective twist density of 10.67 bp/turn and 10.44 bp/turn, respectively (Fig. 3.1). We analyzed the particle snapshots and performed reference-free 2D class averaging. The variant designed with a default crossover spacing shows a strongly curled up global shape. In the 10.44 bp/turn variant, this effect is reduced and the objects appear to be more planar. Both data sets exhibited high degrees of structural heterogeneity, which resulted in unsuccessful attempts of reconstructing 3D electron density maps from the data.

3.2 Multilayer square lattice-based design

To systematically analyze the global twist and design motifs in multilayered square-lattice DNA nanoobjects with various cross sections, we used two variants of a multidomain object termed Twist-Tower (see chapter 2). It consists of four cuboids with quadratic cross sections of 2×2, 4×4, 6×6, and 8×8 helices, of which each has a length of about 64 base pairs. We designed a native variant (Twist-Tower) with default crossover spacing corresponding to a helical periodicity of 10.67 bp/turn imposed by the square lattice design. To create a twist-corrected variant (Twist-Tower-v2), we reduced the helical periodicity imposed by the square lattice to 10.33 bp/turn for each of the four domains. We achieved the reduction of the helical periodicity by introducing so-called ”skips” in the Cadnano [33] design diagram every 32 base pairs. This results in a general pattern of three segments of eight base pairs followed by one segment of seven base pairs between consecutive crossover positions. The local overwinding of the individual helices is expected to create local counter-torques to be transferred to the entire object via the connections between the helices. In addition to global twist, we used the Twist-Tower variants to study crossover stacks and the effect of crossover omission.

3.2.1 Advantages of the multidomain approach

We assumed that the global twist results from an equilibrium between the cumulative torque of the helices and the local twisting stiffness. Therefore, we expected that for each domain the effect of the respective other domains on the global twist would be negligible. The particular design of the Twist-Tower has several advantages compared to building and reconstructing the domains individually.

Asymmetric global shape: We expected that the asymmetric global shape of the Twist-Tower facilitates the reconstruction process. The individual domains themselves each are pseudo-symmetric. Hence, for individual cuboids, there are distinct local minima in the likelihood landscapes of the particle orientations in the reconstruction process,

which might lead to errors in the orientation assignment in the early iterations. Additional asymmetrical features attached to the objects might prevent this, but would result in the object deviating in part from the desired quadratic cross section.

Globular shape: A global shape with an aspect ratio close to one is favorable for a single-particle cryo-EM study. Overlapping particles are detrimental for the reconstruction. Due to the geometry, overlapping can be easily avoided for a globular structure, even in a very highly concentrated sample by imaging regions with sufficiently thin ice. Additionally, globular particles have a superior ratio of particle volume to effective occupied volume compared to particles with rod-like shapes. Here, the occupied volume is defined as the volume each particle occupies in the ice in order that neighboring particles do not overlap, independently of their orientations. Therefore, a higher particle density can be achieved for globular particles, resulting in a higher number of particles acquired per hour and a better use of valuable beam time. However, due to design restrictions an object with a small cross section, like the 2 × 2 cuboid, has a rod-like shape. By combining the cuboids in the Twist-Tower, we achieved a more globular shape.

A platform for the small 2 × 2 cuboid: By attaching the 2 × 2 cuboid to a larger platform, the issues and challenges of reconstructing a small object, which include the extraction and alignment of the low-signal particles from the micrographs and their alignment, are overcome. At a length of 64 bp as it is used in the multidomain object the 2 × 2 object alone would have a molecular weight of only approximately 160 kDa, and would be a very challenging sample. Building a longer 2 × 2 object, however, would result in a less favorable aspect ratio due to the rod-like shape as pointed out above. As part of the Twist-Tower, the 2 × 2 domain itself might be hard to recognize in the micrographs, but the larger domains are a clear reference during the procedures of particle picking and alignment. The same is the case for the 4 × 4 domain, although to a lesser extent.

Better comparability of the domains The resolution of an object depends on several parameters, including the heterogeneity of the particles, the quality of the microscope alignment, the level of background noise induced by different thickness of the particle embedding ice, and the distribution of the orientation of the particles. By combining the four objects of different cross sections in one multidomain object, the imaging parameters and the orientational distribution are kept constant, allowing for a better comparison of the domains.

3.2.2 Global twist

We reconstructed the Twist-Tower by refining the four domains individually using multi-body refinement. A detailed description of the reconstruction procedure is given in

chapter 2. Similarly, we reconstructed the electron density of the Twist-Tower-v2 from 9.5×10^4 particle snapshots, achieving a resolution of 8.5 Å (Fig. D.2). We performed multi-body refinement to separately refine the four domains. Thus, we improved the resolutions of the four domains achieving 10.0 Å, 7.7 Å, 8.0 Å, and 8.1 Å for the 2×2, 4×4, 6×6, and 8×8 domains, respectively (Fig. D.15). We built a composite map from the multi-body-refined domains and fitted a pseudo-atomic model to the electron density (Fig. 3.2).

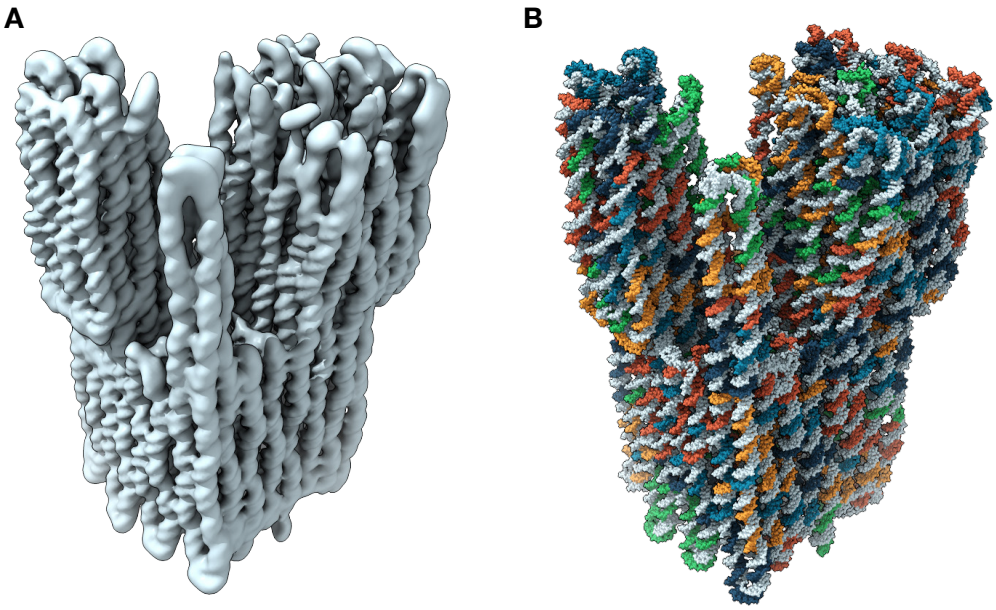

Figure 3.2 Twist-Tower-v2 (A) Composite electron density map built from the multi-body-refined domains. **(B)** Pseudo-atomic model. The scaffold is colored in light blue.

By comparing the composite maps of the two variants, the reduced global right-handed twist is apparent (Fig. 3.3A-C). By aligning the two maps for maximum overlap, the orientation of the 2×2 domain appears to be less bent outwards in the twist-corrected variant. However, we are convinced that the difference in orientation of the 2×2 domain is negligible for the individual twist evaluation of the domains. For both variants of the Twist-Tower, we measured the average global twist in the individual cuboids by comparing slices consisting of helix segments which are at the same base pair positions according to the design. For each cuboid, we extracted two slices at a distance of 40 bp to each other using the viewer tool and the pseudo-atomic model (Fig. 3.3D-E). The measured values are summarized in table 3.1. For the 4×4, 6×6, and the 8×8 domains, the twist correction was successful with close to no residual global twist. For the 2×2 domain, the global twist was reduced by approximately 44 %.

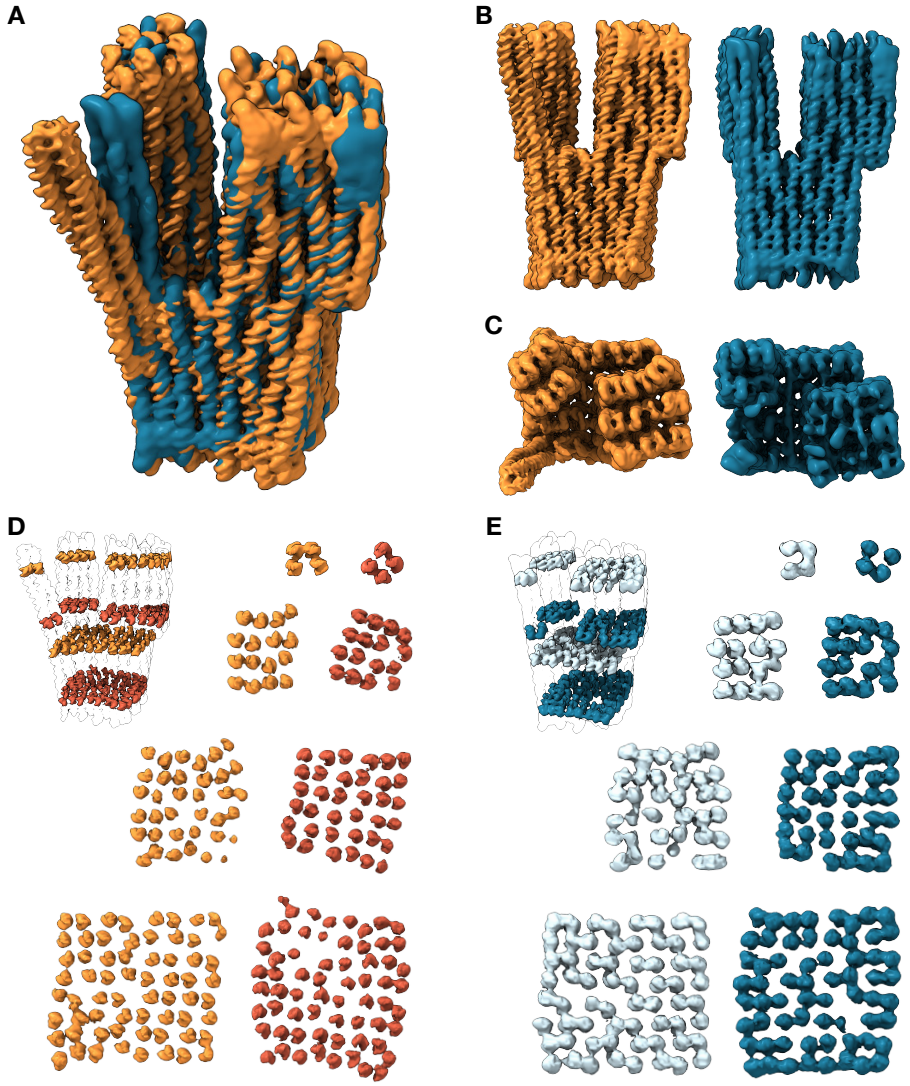

Figure 3.3 Comparison of the Twist-Tower variants. **(A)** Superposition of the electron density maps of the Twist-Tower (orange) and the Twist-Tower-v2 (blue). **(B)** Side view. **(C)** Top view. **(D)** Slices extracted from the Twist-Tower to illustrate the different amounts of global twist in the domains. The slices show nonuniform deviations from quadratic cross section across the object. **(E)** As in (D) but for the twist-corrected variant. The 2 × 2 domain shows a significant amount of residual twist.

	2 × 2	4 × 4	6 × 6	8 × 8
Twist-Tower	-1.24 ± 0.04	-0.39 ± 0.04	-0.19 ± 0.03	-0.14 ± 0.02
Twist-Tower-v2	-0.69 ± 0.03	0.00 ± 0.01	-0.05 ± 0.02	0.03 ± 0.01

Table 3.1 Global twist measurements. Values for the cuboids of the Twist-Tower variants are given in °/bp

3.2.3 Structural features and design motifs

The designs of the Twist-Tower variants contain several interesting features which we will address in the following using electron density maps, pseudoatomic models, and design blueprints.

Omission of crossovers: In the design of the Twist-Tower, we omitted a possible staple crossover, located close to the vertex of the 8 × 8 domain and the interface to 6 × 6 domain. The two outer helices in this outer layer terminate at the base pair level of the omitted crossover and are connected to each other via a terminal scaffold connection. We passivated both ends of the two helices with poly-T overhangs to avoid blunt ends, instead of placing a staple connection at the terminus of the inner one of the two helices. Due to the omission of this crossover, the first crossover between the second and third outer helix is at a distance of 32 bp. In the electron density map, the unconnected group of helices bend away from the main part of the structure (Fig. 3.4A). In the design of the twist-corrected variant of the Twist-Tower, we placed a crossover directly at the helix terminus. This additional crossover is well resolved in the electron density map and connects the two outer helices to the rest of the structure leading to a well-shaped vertex (Fig. 3.4B). Similarly, we omitted a crossover in the Twist-Tower design located at the interface of

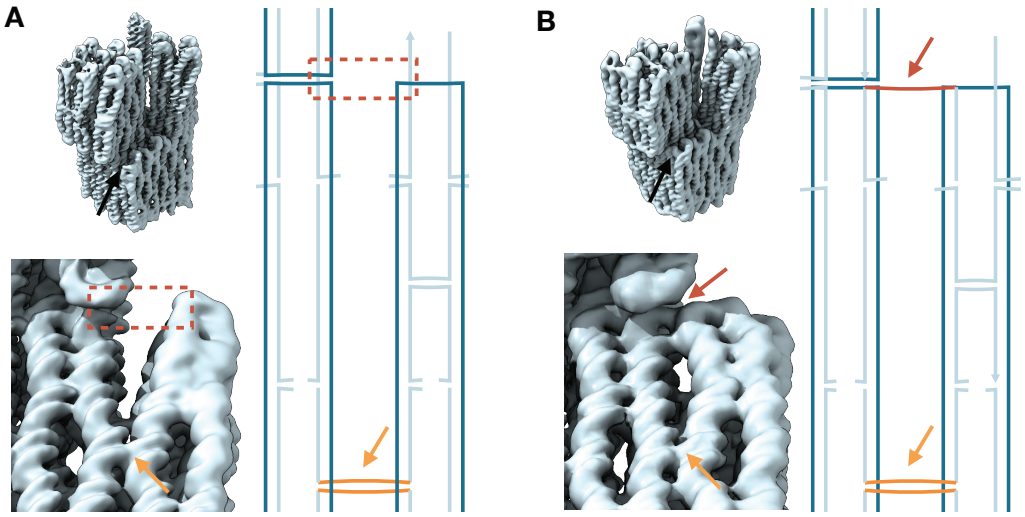

Figure 3.4 Unused crossover position at a vertex of the 8 × 8 domain. (A) Twist-Tower. Top left: Overview. The region of interest is indicated by the arrow. Bottom left: Zoom-in. The two helices on the right are bent away from the other helices. The dashed box and the orange arrow indicate a potential crossover position and the first designed crossover to connect the group of helices to the left, respectively. Right: Schematic connectivity diagram. The scaffold is colored in dark blue. The color code of the highlighted regions is as before. **(B)** Corresponding region in the twist-corrected variant Twist-Tower-v2. An additional staple crossover is placed at the top of the two helices (red arrow).

the 2 × 2 domain and observed outwards bending of the domain. In the Twist-Tower-v2 design, we placed a crossover at this location. In contrast to the first variant, the 2 × 2 domain in the electron density map of the Twist-Tower-v2 is straight and not bent to the side.

Crossover stacks: The square lattice-based 'crossover stack' design motif was first analyzed using cryo-EM in the previously reported Pointer object. The motif consists of an alternating arrangement of staple and scaffold crossovers in a row of helices. It was well resolved in the electron density map of the Pointer object and the authors speculated "that the systematic use of many of these junction stacks in future designs will lead to compaction and confer increased mechanical rigidity". Therefore, we included the crossover stack motif in several regions of the Twist-Tower, including stacks of up to seven crossovers in the 8 × 8 domain. As reported for the Pointer object, the regular arrangement of crossovers without using stacks results in a 3D-chicken-wire-like pattern [68], where helices alternatingly bend towards and away from each other (Fig. 3.5A). In a crossover stack, however, the inner

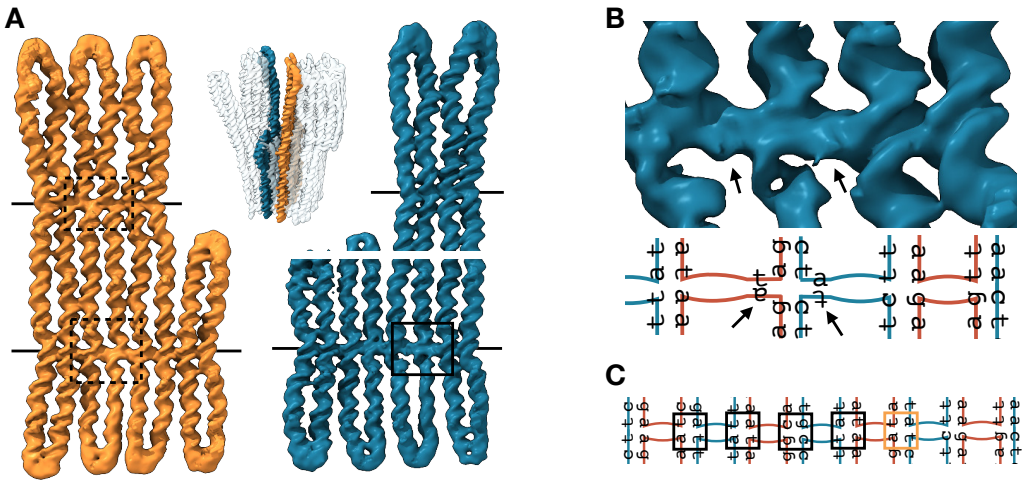

Figure 3.5 Crossover stacks in the Twist-Tower-v1. **(A)** Two slices including crossover stacks in the 8x8, 6 × 6, and 4 × 4 domain. The slice including the 4 × 4 domain (blue) is presented as two parts due to global twist. The positions of crossover stacks are indicated by black lines. In all cases the helices are bent inwards at the crossover stack. Left: compared to the outer helices, the top and bottom parts of the helices in the center of the stacks are shifted relatively to each other (boxed). Right: The highlighted helices (boxed) exhibit a relatively large distance from each other at the crossover stack, compared to the outer helices. **(B)** Zoom-in of of the solid boxed region crossover region in A: In the crossover on the right the helices are closely together. At the two other positions the helices are further spread and additional features in the electron density map are visible at the crossover (arrows). The design diagram shows a possible re-arrangement of base pairs at the central crossover (arrows). Scaffold and staple strands are depicted in red and blue, respectively. **(C)** Design diagram of the entire crossover stack. Multiple positions (black boxes) have a similar sequence pattern as the one highlighted in B (orange box).

helices are connected to both neighboring helices. This results in a constriction and a slightly hourglass-like shape. This can already be observed for a stack of three crossovers, but is more pronounced for larger stacks (Fig. 3.5A).

In the central helices of a large stack of seven crossovers in the 8 × 8 domain and to a lesser extent in a stack of five crossovers in the 6 × 6 domain, we recognized lateral shifts of the two parts of the helices before and after the crossover with respect to the helical direction. These are visible as discontinuities of the helical axes. We attribute this phenomenon to electrostatic repulsion between the helices and the fact that the central crossovers are stabilized by base-stacking interactions only. The helices might shift laterally to adopt a more energetically favorable conformation. Additionally, we observed larger distances between neighboring helices for the central crossovers in stacks of seven crossovers in the 8 × 8 domain, presumably also caused by electrostatic repulsion. The larger distances might even indicate local dehybridization of base pairs. In one stack of seven crossovers, we found two crossovers with additional features in the electron density map indicating a rearrangement of base pairs (Fig. 3.5B). We identified a sequence similarity in the staple and scaffold segments of the helix between these crossovers. The nucleotides of each of the four strand segments (two staples and two segments of the scaffold) at the crossover might not form a pair with its intended partner (scaffold with staple) but with the nucleotide of the other strand of the same type (staple-staple and scaffold-scaffold). In addition to this helix, there are four other helices with a similar sequence pattern at the crossover position (Fig. 3.5C). However, we did not find additional features in the electron density map at these positions as clearly visible as for the other positions.

Sequence similarity in staple segments: An interesting stack of three crossovers is located in the 8 × 8 domain (Fig. 3.6A). Unlike the two other crossovers of this stack, one of the staple crossovers has significantly lower values in the electron density map and becomes only visible at a low threshold (Fig. 3.6B-E). Both staple crossovers in the stack are designed such that the staple strands have a nick site after a segment of eight base pairs behind the crossover on either one of the two helices (Fig. 3.6 F). In the poorly resolved staple crossover, the eight nucleotide-long terminal segments of the staple strands have a common sequence of five nucleotides, allowing for an additional stable conformation. Instead of crossing over to the other helix, the staples continue on the same helix. However, in this conformation, the last three bases of the staples do not match the sequence of the scaffold segments, making it energetically less favorable, and therefore less likely. As it is the case for the crossover position, the electron density map exhibits lower values at the positions of these mismatches.

Deviation from design: A region in the Twist-Tower electron density map located at the periphery of the 6 × 6 domain deviates from the design (Fig. 3.7A). In this outer layer,

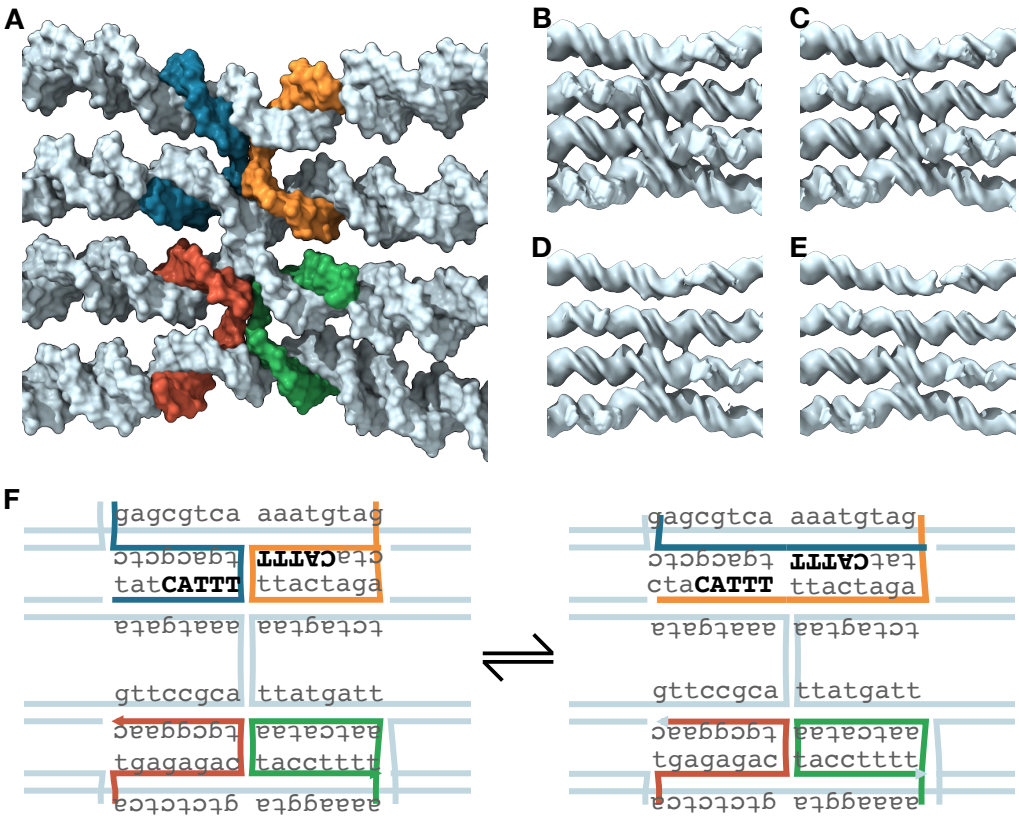

Figure 3.6 Crossover consisting of staples with similar terminal sequences **(A)** Pseudo-atomic model illustrating the designed conformation. Staples contributing to the crossovers are colored. **(B - E)** Electron density map at increasing thresholds. The upper staple crossover disappears. **(F)** Design diagrams of two conformations. Left: Designed conformation. The segments of the staples with identical sequence (orange and blue) are highlighted (bold font). Right: conformation without the top crossover. The three terminal bases of the staples of interest do not match the scaffold sequence.

the helices are designed to be connected by a central stack of five crossovers. However, the second crossover from the left located between helices 2 and 3 (h2 and h3) is poorly resolved and the fourth crossover located between helices 4 and 5 (h4 and h5) are not resolved. Instead, h4 is strongly bent away from h5, leaving gap. In addition, a gap within h4 can be seen close to the designed crossover site. Furthermore, we noticed that the top parts of h1 and h2 are less well resolved. An extensive 3D classification with 200 classes revealed a wide spectrum of conformations (Fig. 3.7A). This includes classes in which the missing crossover between h4 and h5 and the discontinuity in h4 are very distinct, but the rest is well resolved. In other classes, the top parts of h1 and h2 are not resolved at all, including the crossover between h2 and h3, but the crossover between h4 and h5, including the part of h5 below the crossover, is resolved. We designed this outer layer in the 6 × 6 domain from six scaffold loops in order to have additional scaffold crossovers in the center to increase the stability (Fig. 3.7C). Similar to the crossover stack discussed in

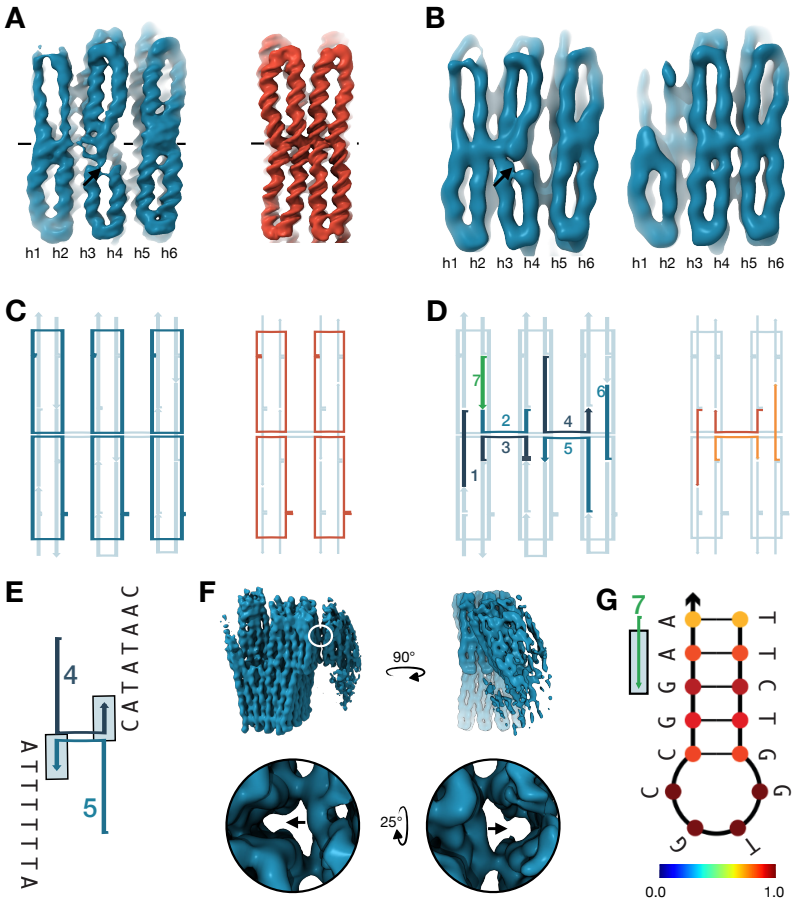

Figure 3.7 Analysis of a region at the periphery of the 6 × 6 domain of the Twist-Tower deviating from design. **(A)** Layers of helices in the 6 × 6 domain (blue) and in the 4 × 4 domain (red) as a comparison with similar design patterns (see C and D) including a central crossover stack (indicated by black lines). The 6 × 6 region deviates from the design: the helices h4 and h5 are not connected, h4 is interrupted below the middle with a visible gap (arrow) and the top part is bent towards left, 3) the crossover between h2 and h3, and the top parts of h1 and h2 are poorly resolved. **(B)** Exemplary classes of a 3D classification. Left: The crossover between h2 and h3 is resolved. H4 is interrupted (arrow). H4 and h5 are not connected. Right: The crossover between h4 and h5 is resolved. The top parts of h1 and h2 including the designed crossover to h3 are not resolved. **(C)** Scaffold routing. The 6 × 6 region and the 4 × 4 region are similarly constructed from six and four scaffold loops, highlighted in dark blue and red, respectively. **(D)** Staples contributing to the designed crossover stacks of the 6 × 6 and the 4 × 4 domains are highlighted in dark blue and red, respectively. **(E)** High AT content in highlighted (boxed) regions of staples 4 and 5. **(F)** Dimer class. The second monomer is visible in parts due to the sizes of the particle extraction box and the applied masks. Monomers are tilted to each other and are formed by connections of h4 to h5 and vice versa instead of forming the designed crossover (white circle). Zoom-ins: Top views onto the position of the connection in helical direction of the first (left) and the second monomer (right). Arrows indicate the not formed crossovers. **(G)** Possible hairpin conformation in the highlighted section (boxed) of staple 7. The color key indicates the probability of each base to adopt the depicted state.

section 3.2.3, each of the staple strands contributing to a crossover of the stack has a nick site after a short segment of eight nucleotides after the crossover (Fig. 3.7D). In one of the outer layers of the 4 × 4 domain, we applied the same strategy for scaffold and staple routing. This region, however, is well resolved (Fig. 3.7A). Hence, we wondered if the particular sequences of the staple and scaffold strands are the root cause of the deviations from the design in the 6 × 6 layer. We found that the short segments of the two staple strands st4 and st5, which are designed to form the crossover between h4 and h5, have a particularly high AT content of 75 % and 100 %, respectively (Fig. 3.7E). The lower binding energy of these segments combined with the stress imposed by the crossover stack might promote conformations where the crossover is not formed. We also found dimer classes containing a small fraction of particles (Fig. 3.7F). The electron density maps of these classes show that the dimers are formed by two monomers which face each other and are connected between h4 and h5 at the position of the designed crossover. In these dimers, both monomers lack the crossover between h4 and h5. These observations indicate that instead of forming the crossover, the short segments of the staples st4 and st5 of each monomer bind to the complementary scaffold segments of the other monomer, forming two connections without unpaired nucleotides. In the poorly resolved upper region of h1 and h2, we found several segments on the staple and scaffold strands which are complementary to themselves. One of the staples has a segment of 14 nucleotides that can form a stable hairpin (Fig. 3.7G). With the scaffold having the reverse complementary sequence of the staple, it can also form a hairpin. Both hairpin conformations compete with the designed conformation, resulting in structural heterogeneity and hence a lower resolution.

3.3 Discussion

We presented a study of global twist and twist correction in square lattice-based objects of various cross sections in solution using cryo-EM. We imaged two variants of single-layer tiles, both exhibiting excessive heterogeneity. Hence, we were not successful in reconstructing a 3D electron density map, but analyzed the object in 2D. Our observations of a strongly rolled-up global shape and a reduced twist for the two variants designed with an effective twist density of 10.67 bp/turn and 10.44 bp/turn, respectively, are in agreement with previous findings derived from studying chains of tiles adsorbed on a support layer using atomic force microscopy (AFM) [104]. Our data of the 10.67 bp/turn-variant are also in accordance with in-solution small angle X-ray scattering (SAXS) measurements of monomeric tiles [105]. However, the SAXS data suggesting a wrapped up conformation of a 10.44 bp/turn-variant in the opposite direction but similar absolute twist are not supported by our data.

We evaluated the global twist and twist correction as well as other design motifs in eight multilayer square lattice-based cuboids with quadratic cross sections using two variants of the Twist-Tower object. For the 4×4, 6×6, and 8×8 domains, the twist correction using a reduced twist density of 10.33 bp/turn was successful with no residual twist remaining. In contrast to the other domains, the global twist correction in the 2×2 domain was only reduced by about half. Due to a lower number of direct neighbors, the 2×2 domain has a lower crossover density than the other domains, resulting in a higher number of 16-bp- and 24-bp long segments. We previously showed that crossovers play a key role to achieve twist correction [74] (Fig. E.8). Hence, we attribute the lower impact of the twist correction on the 2×2 domain to the reduced crossover density in this domain, which results from the lower average number of direct neighbors for each helix compared to the other domains. By aligning the electron density maps of the two variants, the different orientation of the 2×2 domains is apparent. We assume this is due to multiple reasons: First, the two maps have a variety of local structural differences. Since the alignment was conducted by maximization of the overlap, the differences in the 2×2 domain appear particularly large due to its small fraction of the total volume. Second, the mismatch in twist density might cause deformation by twist-bend coupling. Third, we placed an additional crossover in the Twist-Tower-v2 design close to the interface of the 2×2 and the 8×8 domain. Similarly, the omission of a crossover at a vertex of the 8×8 domain resulted in the bending outwards of a group of helices. These deformations by crossover omission are most likely caused by electrostatic repulsion and are in accordance with previous findings [68].

We analyzed the various variants of the crossover stack design motif. In each case, the crossover stack led to a constriction of the helices and local deviation from the chickenwire pattern. Crossover stacks, which span an entire row of helices, affect even the global shape causing an hour glass-like shape. We identified a crossover design motif, which is prone to cause deviations from the designed structure. In this motif, both staple strands terminate eight base pairs after crossing over to the other helix. We identified a stack of three crossovers, for which we assume that this type of crossover in combination with a sequence similarity results in an additional local stable conformation in the particle ensemble where the staples do not form the crossover. In the electron density map, the conformations are averaged, resulting in a lower resolution of the particular crossover. Furthermore, the analysis of an extensive 3D classification indicates that this crossover design contributes to the formation of dimers instead of the intended crossover at the periphery of the 6×6 domain. While there are other regions in the design where this crossover motif did not lead to deviations in the map, we suggest to avoid the motif, in particular at the periphery. If the motif is required, the designer should use a scaffold permutation which yields no sequence similarity in the motif.

Chapter 4

Analysis of a dual-scaffold object

Remark: The presented work in this chapter was published in part in Floris A. S. Engelhardt et al. Custom-Size, Functional, and Durable DNA Origami with Design-Specific Scaffolds (2019) [83], and in Massimo Kube, Fabian Kohler, Elija Feigl et al. Revealing the structures of megadalton-scale DNA complexes with nucleotide resolution (2020) [74]. Christian Wachauf provided the design of the 126-helix bundle. Elija Feigl constructed the pseudo-atomic model. Baki Nagel-Yüksel supported sample preparation and data analysis as a working student. Maximilian N. Honemann provided scaffold.

In scaffolded DNA origami, multiple structures can be folded with the same type of scaffold by using different sets of staple oligonucleotides. However, the length and sequence of the scaffold limit the user in the design, in terms of size and properties of the object. Commonly used scaffolds are based on the genome of the bacteriophage M13mp18 and have lengths of 7249 nt to 8634 nt [4, 36]. Longer scaffolds have the disadvantage of increasingly challenging production at decreasing yields [83, 86]. Designing larger objects with multiple M13-based scaffolds results in aggregation during the folding process [83]. Engelhardt et al. developed methods for custom scaffold production and presented scaffolds of different lengths and sequences, including four 7560 nt long scaffolds, which are orthogonal to each other and to the 7560 nt M13 derivative [83]. Using two orthogonal 7560 nt scaffolds, we built a barrel-like dual-scaffold object. The object consists of 126 helices arranged on a honey comb lattice and is designed as two interlocked parts (Fig. 4.1A). Within each part, the respective scaffold is routed through the helices like in a classical DNA origami design and the helices are connected to each other by scaffold crossovers. This type of scaffold crossover will be referred to as intra-scaffold crossover (Fig. 4.1B). At helix positions within the object where the ends of the two parts meet, 'inter-scaffold' crossovers are located, each of which is formed by the strands of both scaffolds and two staples (Fig. 4.1B). The helices of the 126-helix bundle are connected to each other with 453 staple oligonucleotides forming

staple crossovers, both within each part and between the two parts (Fig. 4.1). Negative stain EM imaging and gel electrophoresis assays confirmed the successful assembly of the object at a high yield [83] indicating efficient assembly. Here, we present a cryo-EM 3D electron density map of the object in solution and a pseudo-atomic model fit. We give a detailed analysis of the structure (section 4.1), including global and local structural heterogeneity (section 4.2), particularly of the inter-scaffold crossovers (section 4.3).

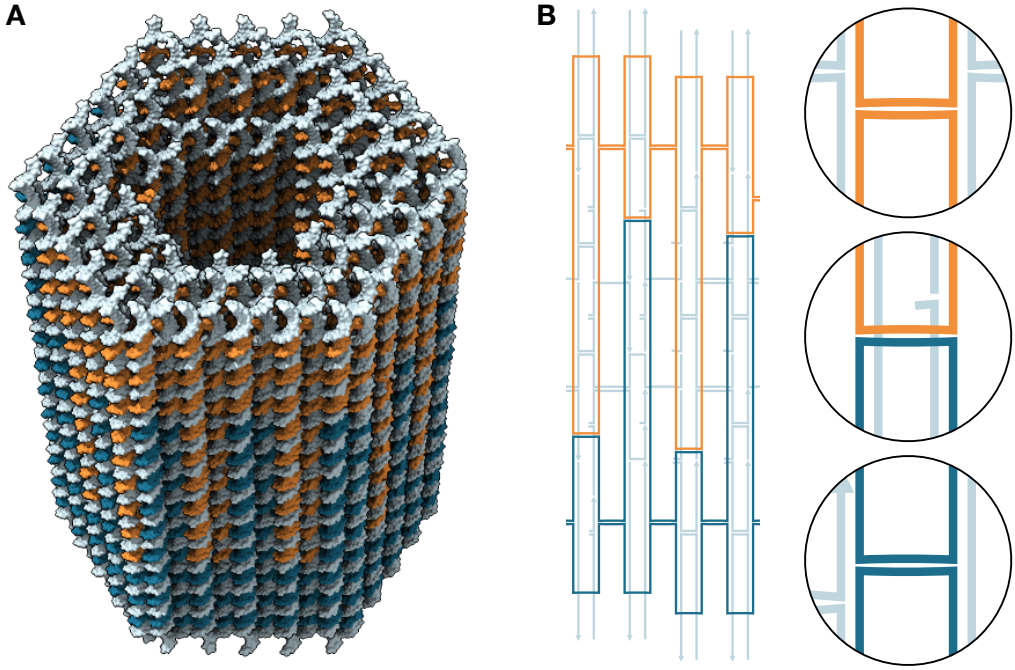

Figure 4.1 Design of the 126-helix bundle. (A) Schematic representation of the design. The two scaffold strands are highlighted in blue and orange. The staple strands are colored in light blue. The representation is based on an oxDNA starting configuration created with tacoxDNA [100]. **(B)** Section of the design blueprint. The color code is like in (A). The zoom-ins show exemplary intra-scaffold crossovers (top and bottom) and inter-scaffold crossovers (middle). Strands which cross over to helices outside the field of view are truncated in the illustration. The design file was created using Cadnano [33].

4.1 Cryo-EM structure analysis

We reconstructed an electron density map from 1.2×10^5 particles (Fig. D.16), which has the the expected barrel-like global shape of the object (Fig 4.2A). The individual helices are well separated and their double helical shape is visible except for the helix ends, towards which the helices become less resolved. For most helices, the ends appear to be truncated and are only resolved in surface representations of the electron density map at very low threshold values, where the structure occupies a multiple of its actual volume (Fig 4.2B). While smaller honeycomb-based objects, designed with the native effective twist density of

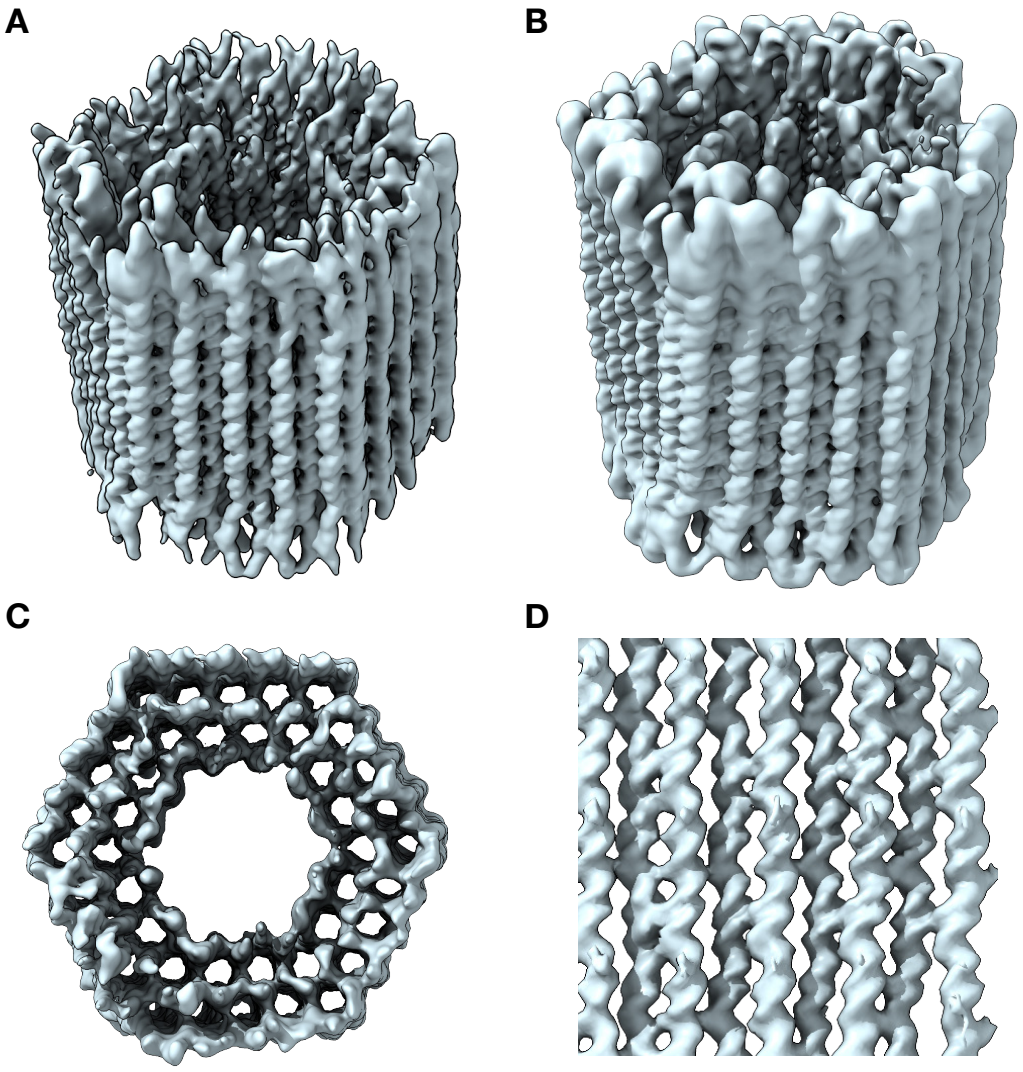

Figure 4.2 Electron density map of the 126-helix bundle object. (A) Consensus-refined map. The global shape of the object and structural details of the helices are resolved. Towards the helix ends the resolution deteriorates and in parts terminal connections between the helices are not resolved. Along the helices which mostly consist of both scaffolds no discontinuities or gaps are visible. **(B)** Map visualized using a lower threshold. **(C)** Top view of (A). **(D)** Slice extracted from (A).

10.5 bp/turn, have a global right-handed twist [20, 74, 106], the 126-helix bundle is straight (Fig. 4.2C) with an average twist of $(-0.01 \pm 0.01)\,°$/bp. Slices along rows of helices show the typical 3D chickenwire-like structure (Fig. 4.2D). At the ends of the 126-helix bundle, the helices slightly bend outwards. The crossovers are well recognizable, especially in the central regions. The different lengths of the helices as well as the crossover pattern allow a clear identification of the orientation of the electron density map, despite the pseudo-hexagonal symmetry, and different regions in the electron density map can be assigned to the corresponding regions in the design file. The object has a global resolution of 9.8 Å.

The local resolution estimation yielded a range of 7.3 Å to 17.9 Å with an average of 10.1 Å and a standard deviation of 1.4 Å. Comparing the layers of helices, one can notice a higher resolution in the helices of the central layer compared to the outer layers, which is apparent by the deeper helical grooves (Fig 4.2A).

4.2 Addressing structural heterogeneity

The 126-helix bundle is a DNA nanoobject with a relatively large cross section and is therefore more rigid than a small object like a 6-helix tube. Nevertheless, it is subjected to structural heterogeneity. We used 3D classification with 32 classes to analyze the heterogeneity of the data set and identified four well-resolved classes. We compared these maps of the classes and used the best resolved class as a reference (Fig. 4.3). The length of the object in helical direction does not differ noticeably across the maps. It should be noted that due to the different levels of resolution of the classes, which affect in particular the ends of the helices, a comparison in this dimension was inconclusive. In planes perpendicular to the helical axis, however, we identified significant differences in global shape. For two classes, the principle changes compared to the reference are approximately constant across

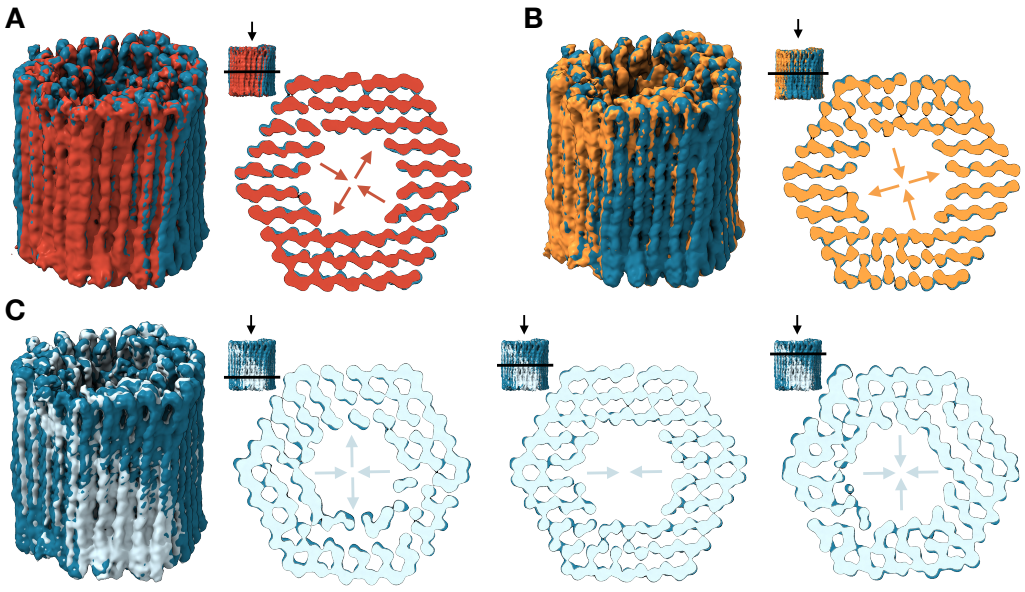

Figure 4.3 Heterogeneity illustrated by 3D classes. In each panel, an exemplary 3D class (red, orange, light blue) is compared to the most populated class (blue). In the top view slices, colored arrows indicate the approximate directions of the largest differences of the map in comparison to the reference. The slices were extracted from the object as indicated by black bars in the small side views. **(A)** Class with two main components approximately constant along the helical direction. **(B)** Class similar to (A), but with components in different directions. **(C)** Class with one approximately constant and one non-constant component.

the entire object and include a relative expansion in one direction and a contraction in approximately perpendicular direction (Fig. 4.3A-B). For the fourth class, the relative contractions and expansions depend on the position along the helical axis (Fig. 4.3C). The differences can be separated into two components: a constant contraction of the map of the class with respect to the reference in one direction across the entire object, and an non-constant component in perpendicular direction, which describes an expansion at the bottom and changes via neutral in the center to a contraction at the top.

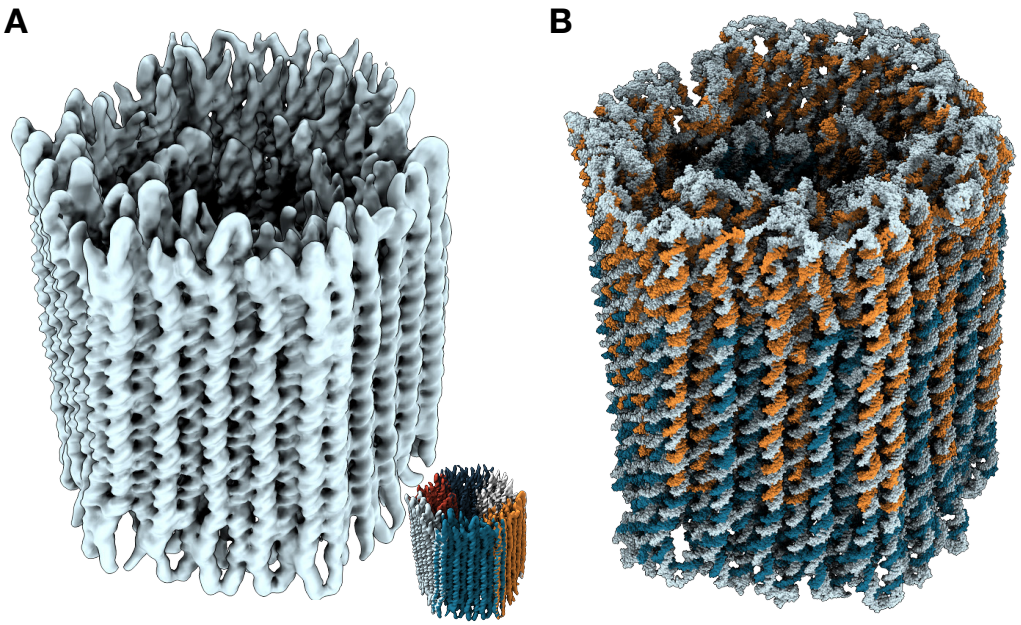

Figure 4.4 Electron density maps and atomic model of the 126-helix bundle object. (A) Composite map built from six bodies separately refined using multi-body refinement. The segmentation is shown in the inset. **(B)** Atomic model fit based on the composite map. The two scaffold strands are colored in orange and blue, the staple strands in light blue.

To address the structural heterogeneity of the particles and to achieve a better resolution, we performed multi-body refinements [78] using different segmentations. For a two-body refinement and a four-body refinement, we cut the object perpendicular to the helical axis into two and four disks, respectively. For both approaches, we did not achieve an improvement in resolution. For a six-body refinement, we separated the object into six slices at the corners through the central axis like cutting pieces from a cake (Fig. 4.4A). The six-body refinement yielded an average resolution improvement of 1.7 Å. We created a composite map from the refined bodies of the six-body refinement, which has an improved resolution across the entire object compared to the consensus refinement. The helices are better separated, the helical details, e.g., the helical grooves are better visible, and the helix ends are better resolved. Particularly due to the improved resolution of the ends of the helices, we were able to fit a pseudo-atomic model to the composite map (Fig. 4.4B),

which facilitated the structure analysis of the object and the comparison to the design. It enabled us to analyze with base pair precision the local resolution estimation of the object and in particular the different types of crossovers.

4.3 Crossover analysis

Since the 126-helix bundle consists of two interwoven scaffolds, the inter-scaffold crossovers are of particular interest. They are distributed around two planes located at one-third and two-thirds of the height of the object (Fig. 4.5A). Based on a visual inspection, they can not

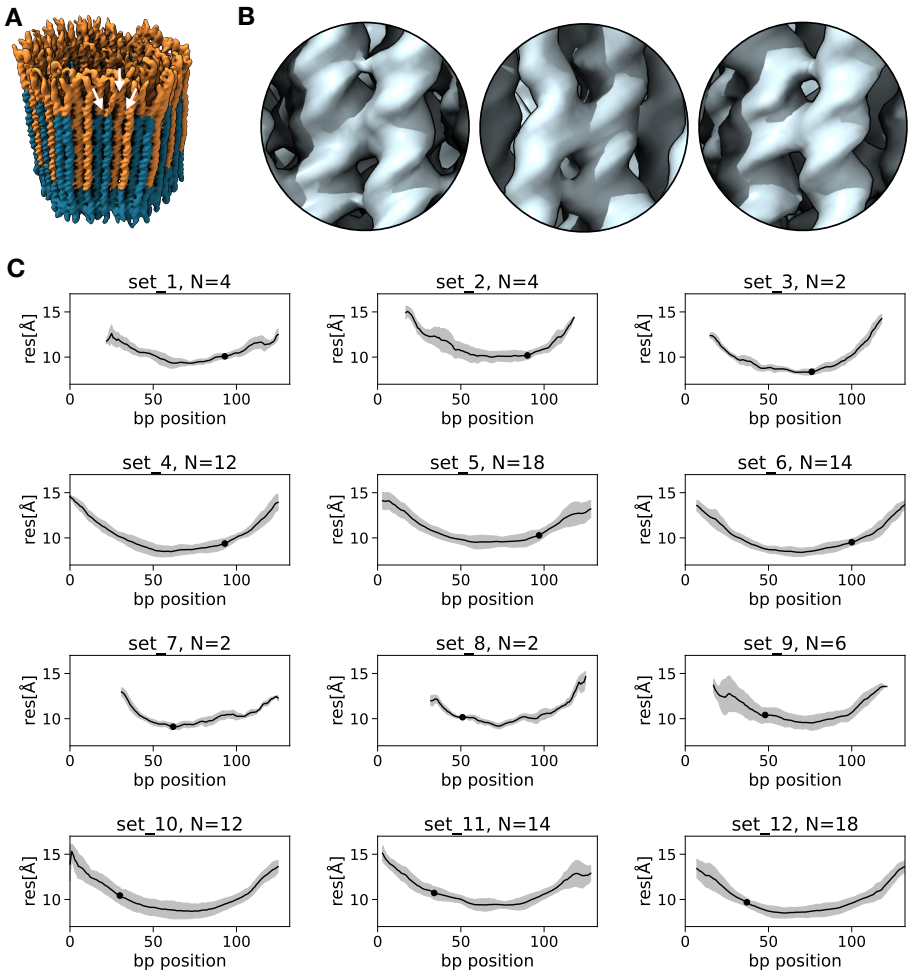

Figure 4.5 Scaffold crossover analysis. (A) Consensus refinement colored by the two scaffolds. Arrows indicate positions of an inter-scaffold crossover (left), an intra-scaffold crossover (center), and staple crossover (right). **(B)** Zoom-ins onto the crossovers highlighted in (A). **(C)** Local resolution plots. For each set of helices, in which the inter-scaffold crossovers are at the same base pair position in the design (black dots), the local base pair resolution, averaged over the helices of the set, is plotted over the base pair position. The shaded area represents the local standard deviation. The number of helices N in a particular set is given in the label of the plot.

be distinguished from other crossovers (Fig. 4.5B). Using the atomic model, we cut out the inter-scaffold crossovers and analyzed their local resolution, yielding an average resolution of 10.0 Å at a standard deviation of 0.7 Å. Hence, the local resolution of the inter-scaffold crossovers is virtually identical to the average local resolution of the object of 10.1 Å. Furthermore, we analyzed the resolution of every base pair in every helix. We grouped the helices into subsets according to the position of the inter-scaffold crossover position, averaged them, and plotted the resolution of the groups over the base pair position in the design (Fig. 4.5C). For each set, we observed a continuous decrease in resolution from the center towards the respective helix ends. We could not identify a local decrease in resolution at the inter-scaffold positions.

4.4 Discussion

We solved and characterized the 3D structure of a dual-scaffold object in solution using cryo-EM single-particle-based methods. We addressed the global shape and structural heterogeneity of the object as well as quantitatively analyzed the inter-scaffold crossover design motif as an indicator of the quality of the multi-scaffold design approach.

We first reconstructed the object using a consensus refinement, treating it as a single rigid body. In contrast to other reported honeycomb lattice-based DNA nanostructures [20, 74, 106], the 126-helix bundle is not globally twisted, which is explained by the high torsional stiffness of the object due to the large cross section. Using 3D classification, we analyzed the structural heterogeneity of the object, revealing relative expansion and contraction perpendicular to the central axis among the classes. To address structural heterogeneity and improve the resolution, we performed focused refinement using the multi-body refinement approach. For the multi-body refinement where we segmented the object into six slices, we achieved an average improvement in resolution of 1.7 Å. Refinements using segmentation into two or four discs did not yield an improvement in resolution. This indicates that the main contributions to the heterogeneity of the particle ensemble are differences in the direction perpendicular to the central axis. This can be explained by the internal structure of the object. Its global shape in axial direction is given by the length of the 126 helices, which are continuous and without gaps or single-stranded segments. In a simplified mechanical description, the energy required to deform the object by stretching or compression is given by:

$$E = \frac{NS}{2L}x^2, \tag{4.1}$$

where N is the number of helices, S is the stretch modulus of an individual DNA double helix, L is the length of the object, and x is the deformation in length. Assuming a stretch

modulus of 1100 pN [54] and focusing the evaluation on the central 87 bp long region consisting of 126 helices, a change in length of 2.8 Å, which is the Nyquist resolution limit of the electron density map, would require about 45 k_BT. Hence, the deformation by stretching and compression of the DNA is unlikely to be resolution limiting. In contrast, the dimensions of the object in the perpendicular directions are determined by the number of parallel helices, which are connected only by the network of crossovers. Due to the electrostatic interaction of the charged DNA, this results in the previously described 3D chicken-wire structure [68] and can be considered as a network of springs. The angles between the central axis and the helical axes at the crossover positions are small. Hence, we reason that a change in angle will result in a relatively small change in the axial direction and large changes in the radial direction. The dominant changes in the radial directions observed for the 126-helix bundle are in accordance with previously reported findings, where we showed that these breathing-like motions are the dominant component in the PCA of the structural heterogeneity of a variant of the Pointer object [74].

The 126-helix bundle shows heterogeneity in local resolution with a higher resolution in the helices of the central layer compared to the inner and outer layer. We attribute this to the different degrees of connectivity. The helices in the central layer have three neighbors each and on average one staple crossover to one of the neighboring helices every seven base pairs. In contrast, the helices in the inner and outer layer have only two neighbors. With one neighboring helix position unoccupied in the honeycomb lattice, the distance between two consecutive staple crossovers along these helices is in general alternating between seven and fourteen base pairs. This likely leads to a higher degree of flexibility and thus a reduced resolution. Similarly, we attribute the lower resolution and outwards bending of the helix ends to the reduced connectivity in these regions. At both ends of the structure, pairs of helices are connected to each other by a terminal scaffold crossover-like connection. The next crossover to a neighboring helix is located up to 16 base pairs away. Hence, these terminal regions are more flexible. The effect of outwards bending is likely caused by electrostatic repulsion. By analyzing the local resolution in the helical direction, we found the best resolution in the center and continuously lower values towards the ends. In addition to the lower connectivity at the ends, we attribute this to heterogeneous bending and stretching deformation along the length of the object as revealed by the 3D classification.

We analyzed the local resolution of the inter-scaffold crossovers by grouping the helices according to the respective positions of inter-scaffold crossovers. We did not find a systematically reduced resolution for the inter-scaffold crossovers in any of the groups. In addition to the absence of discontinuities in the visual analysis, this shows that both scaffolds are well integrated into the structure.

Chapter 5

Design and characterization of corners

Remark: Maximilian Wenig supported sample preparation as a working student. Baki Nagel-Yüksel supported sample preparation and data analysis as a working student and a bachelor student. Floris Engelhardt supported sample preparation. Anna Liedl contributed to the reconstruction and analysis of the cryo-EM data set of the single-corner object CS-v3 as a bachelor student. Maximilian N. Honemann provided scaffold. An overview of the designs presented in this chapter is given in Tab. B.1.

In general, multilayer DNA origami nanostructures are designed by arranging DNA double helices parallel to each other on a honeycomb or a square lattice. Every helix and therefore the entire object have one orientation, which limits the design space. A corner is an important design motif to implement a change in the orientation of an object. The goal is to achieve a sharp, well-defined corner, which folds at a high monomer yield.

A particular angle can be realized by connecting two building blocks, in which the helices have specific lengths. By approximating the helices with cylinders of effective diameter d, the required length of each helix can be determined via simple geometric calculations. Based on previous cryo-EM measurements [68], we used a value of 2.6 nm for the effective helix diameter (Fig. 5.1A). As a convention, we will refer to the outer layer of a corner as the first layer. In a square lattice arrangement, a corner with an angle α can be realized by shortening the helices of the n-th layer on both sides by (Fig. 5.1B):

$$\Delta_n = (n-1) \cdot \frac{d}{\tan\frac{\alpha}{2}}, \quad n \in \mathbb{N}. \tag{5.1}$$

To build for example a 45° corner, the helices of the second and third layer have to be 6.3 nm and 12.6 nm shorter than the first layer, corresponding to 19 bp and 37 bp, respectively.

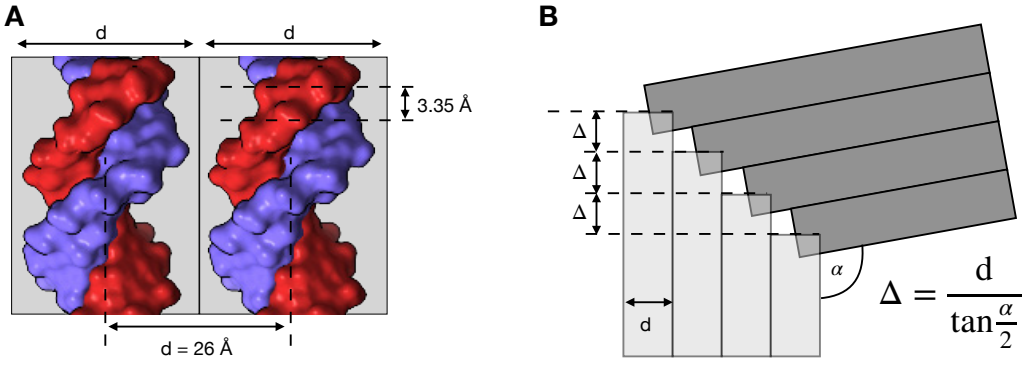

Figure 5.1 Basic concepts of corner design. A) Visualization of approximate geometric properties of DNA in a DNA nanostructure. The helical base pair rise is 3.35 Å. The average distance d between two neighboring helices in the square lattice is approximated with 26 Å. DNA helices are schematically represented by cylinders with effective diameter d (gray rectangles). **(B)** Schematic illustration of the geometry of a corner in a multi-layer square lattice DNA origami object. DNA helices are represented by gray rectangles. The angle α of the corner is determined by the length distance Δ between helices in adjacent layers.

While these geometric calculations are relatively easy, the design of the individual corner sites, where two corresponding helices are connected, remains challenging, given the various combinations of orientations of the backbone at the corner sites. Here, we present different strategies for the design of corner sites including basic double- and single-stranded connections (section 5.1), backbone orientation-specific connections (section 5.2), as well as modifications to influence the global shape and flexibility (section 5.3).

5.1 Coarse screening of corner design strategies

To test multiple angles and design strategies simultaneously, we designed a multidomain object consisting of three corners with approximately 135°, 90°, and 45° (Figure 5.2). As

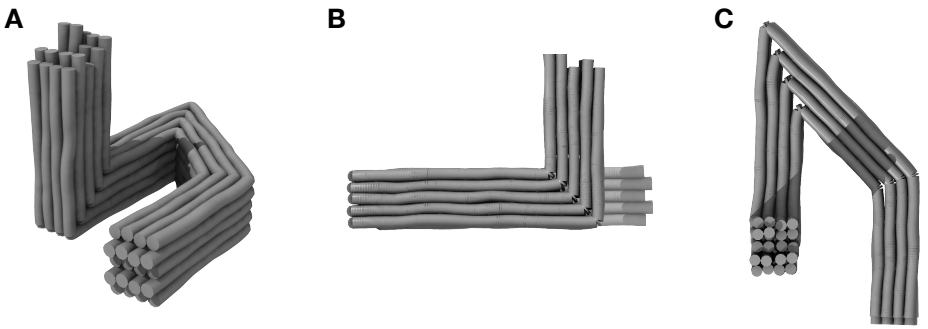

Figure 5.2 Illustration of the TripleCorner design. (A) 3D model based on a CanDo simulation [107]. DNA helices are represented by cylinders. **(B)** Side view. **(C)** Top view.

a convention, we will refer to the three corners as the 135° corner, the 90° corner, and the 45° corner, despite potential deviations from the exact angle. The object consists of 20 helices arranged on a square lattice with a cross section of four by five helices. While the 135° and the 45° corners are arranged in one plane, the 90° corner is positioned perpendicular to this plane. In this arrangement, the object has the most globular aspect ratio, which is beneficial for cryo-EM analysis. In the first variant, which was inspired by a previously reported strategy [45], the corresponding helices at each corner site are connected by the scaffold strand. The staple strands have nicks at the corner sites and hence do not continue to the respective other arm of the corner. However, the helices at the corner sites are entirely double-stranded. To increase the stability and to build sharp, well-defined corners, we positioned interlayer crossovers, i.e., crossovers which connect helices of different layers to each other, as close to the corner sites as possible. The object is designed at an effective helical twist density of 10.44 bp/turn.

5.1.1 Folding and structure analysis

Gel electrophoresis analysis of various folding conditions revealed an overall poor folding quality with a large fraction of dimers and other side products (Fig. 5.3A, Fig. C.2). Negative stain EM images of the folding products show well-folded monomers (Fig. 5.3B)

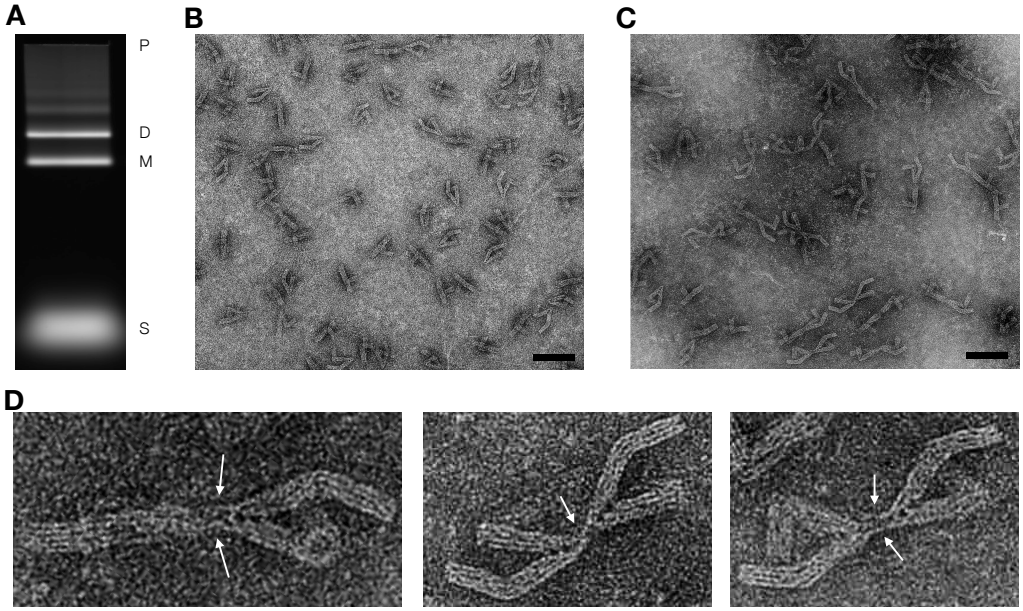

Figure 5.3 Gel electrophoresis and negative stain EM analysis of CS-v1. **(A)** Gel electrophoresis analysis. Gel scan of a folded sample with optimized folding condition. The approximate levels of the pockets (P), dimer bands (D), monomer bands (M) and excess staples (S) are given. **(B)** and **(C)** Exemplary micrographs of gel-purified monomers and dimers, respectively. Scale bars are 100 nm. **(D)** Exemplary dimers. Arrows indicate connections between the monomers.

and dimers, which are formed via connections of the first layer of the 45° corners (Fig. 5.3C-D).

We acquired cryo-EM images of gel-purified monomers and reconstructed an electron density map from about 2.8×10^4 particles and achieved a resolution of 22 Å (Fig. D.5). By using multi-body refinement [78], we improved the resolution of the 135°, 90°, and 45° corner to 20 Å, 19 Å, and 20 Å, respectively, and built a composite map from the three multi-body-refined parts (Fig. D.18). According to the electron density map, the purified monomers are free of mayor structural defects and the global shape is virtually twist-free (Fig. 5.4A-B). However, we note that this in part due to the use of ethidium bromide during the gel purification. In the electron density map, the individual helices and crossovers are

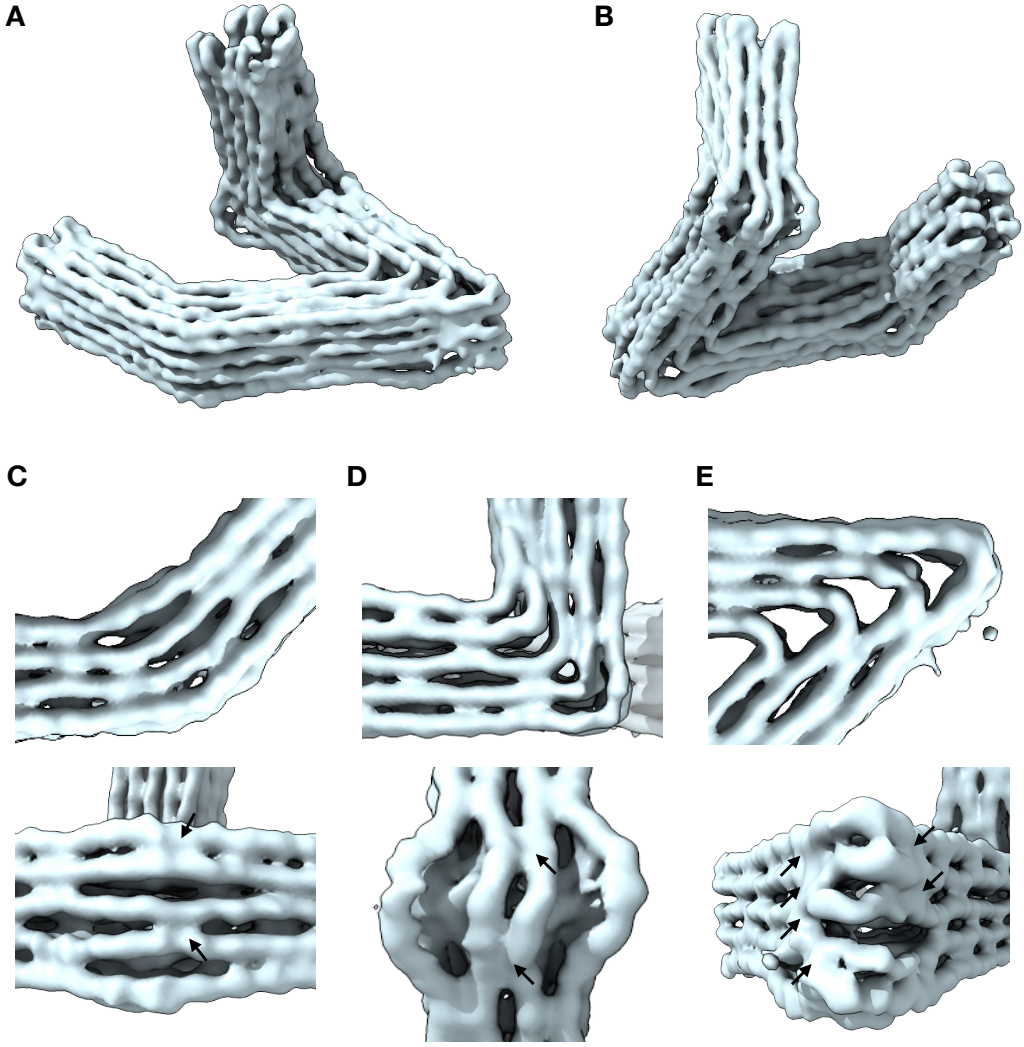

Figure 5.4 Cryo-EM structural analysis of CS-v1. **(A)** Electron density map. **(B)** Rotated view. **(C)** to **(E)** Top and front views of the three corners. Arrows indicate intralayer crossovers close to the corner site.

recognizable, but details, including helical grooves, are not resolved. At the 135° corner, the helices appear to be not kinked directly at the nick sites, but bent in the about 40 bp long segments across the entire corner, between interlayer crossovers (Fig. 5.4C). At the 90° corner and the 45° corner, we observed both curved and kinked helices (Fig. 5.4D-E). An interesting feature in the 90° corner is the outwards bending of two helices of the outer layer which are not connected to their neighboring internal helices in the vicinity to the corner. In contrast, the two inner helices are connected to each other at two positions, each at a distance of 16 bp from the corner site. Outwards bending can not be observed in the outer layers of the two other corners, where we designed crossovers to connect these helices to each other. Additionally, we solved the structure of the object using the same reconstruction approach, but a EtBr-free sample, prepared using polyethylene glycol (PEG) purification and high-performance liquid chromatography (HPLC) purification. The cryo-EM density map shows global right-handed twist (Fig. E.9). Apart from global twist, the 135° and 90° corners are close to identical to their corresponding corners in the EtBr-purified variant. In contrast the 45° corner exhibits folding defects, which might result from the sample preparation.

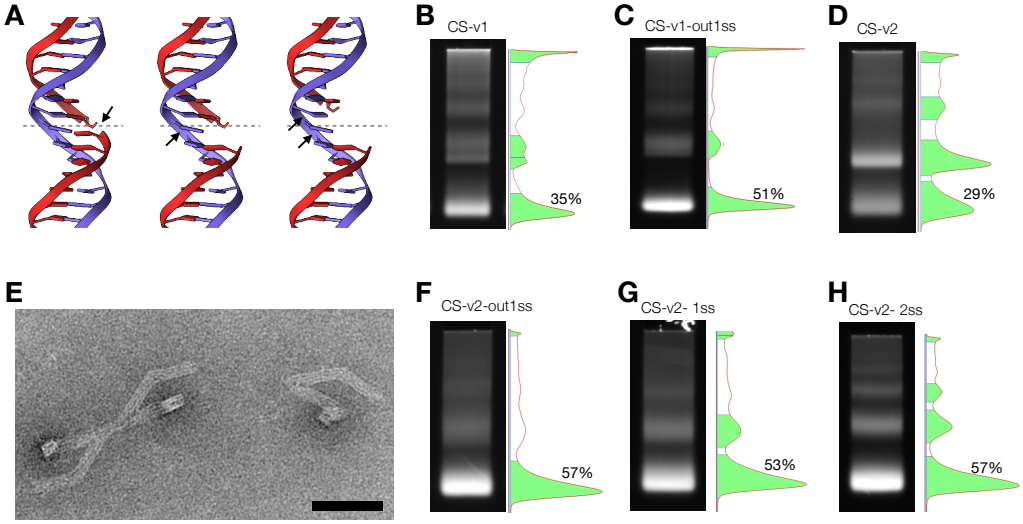

Figure 5.5 Gel electrophoresis and negative stain EM analysis of Triple-Corner variants. **(A)** Schematic illustration of the design variations of the 45° corner sites (dashed line). For simplification, the helices are depicted straight. Staple and scaffold strands are colored in red and blue, respectively. The design features are highlighted by arrows. Left: the helix is double stranded with a staple nick at corner site. Center: one scaffold base is unpaired (1ss). Right: two scaffold bases are unpaired (2ss). **(B)** Gel scan and intensity profile of the best folding condition of CS-v1 **(C)** Variant of CS-v1 with one unpaired scaffold base in the helices of the outer layer. **(D)** CS-v2. **(E)** Exemplary monomer and dimer extracted from a negative stain TEM micrograph. Scale bar is 50 nm. **(F)** Variant of CS-v2 with one unpaired scaffold base in the helices of the outer layer. **(G)** Variant of CS-v2 with one unpaired scaffold base in every helix. **(H)** Variant of CS-v2 with two unpaired scaffold base in every helix.

5.1.2 Design variations

As revealed by negative stain EM analysis, dimers are formed via connections at the 45° corner. We created a modified variant (CS-v1-out1ss) of the CS-v1 Triple-Corner object, where we designed one scaffold base to be unpaired at the corner sites of the first layer of the 45° corner to introduce flexibility (Fig. 5.5A). Comparing the respective best condition of a standardized folding screen with 16 conditions, we achieved an improvement of the monomer yield from 35 % for the unmodified variant to 51 % (Fig. 5.5B-C).

To test the influence of the crossover pattern, we designed a variant with a reduced number of crossovers near the corner sites of the 135° and the 45° corner (CS-v2). The crossover pattern of the 90° corner was kept unmodified. The gel electrophoretic analysis revealed a poor folding quality (Fig. C.3) with a maximum monomer yield of 29 % (Fig. 5.5D). Like in case of the CS-v1 object, the analysis of the folding products of CS-v2

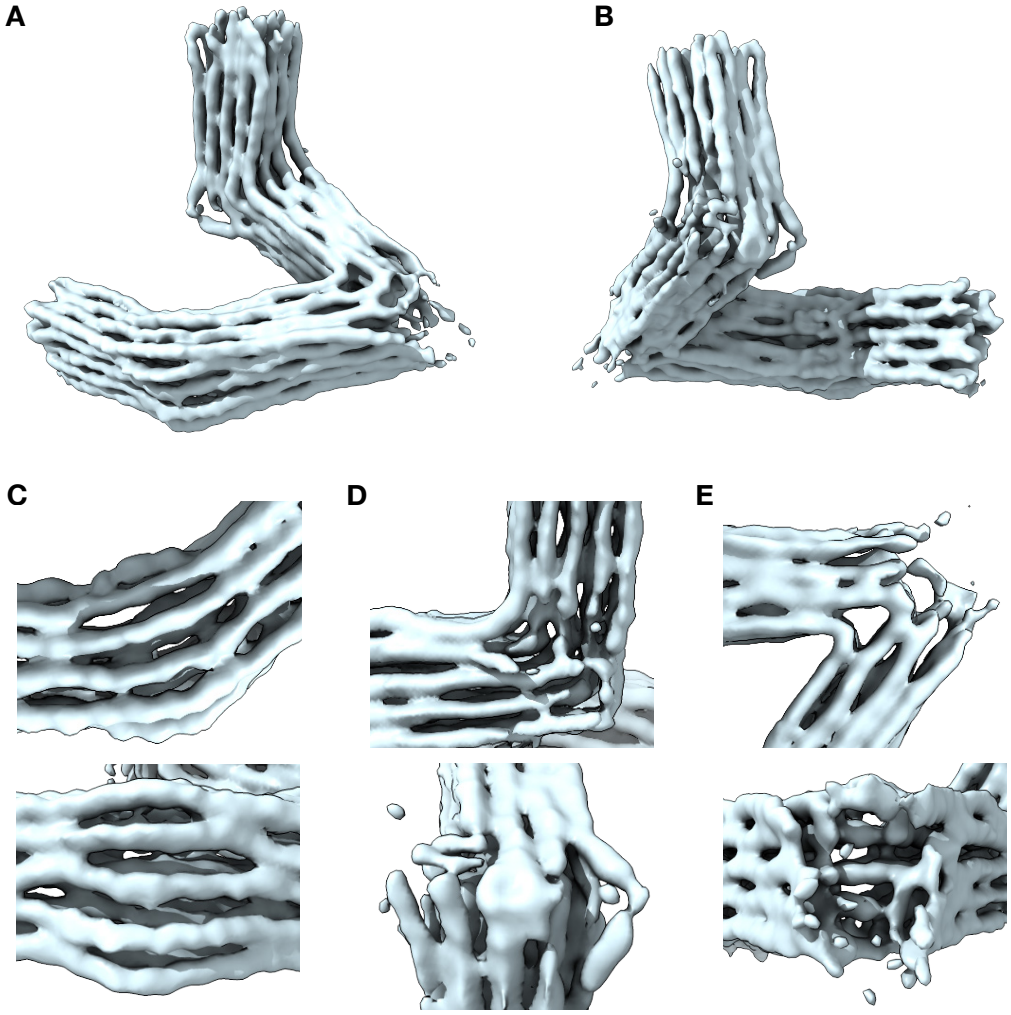

Figure 5.6 Cryo-EM structural analysis of CS-v2-1ss. (A) Electron density map. **(B)** Rotated view. **(C) to (E)** Top and front views of the three corners.

showed, that the dimers form via connections at the 45° corner (Fig. 5.5E). We tested the implementation of one unpaired base at each corner site of the helices of the first layer of the 45° corner (CS-v2-ou1ss), which improved the monomer yield to 57 % (Fig. 5.5F). For two further variants, with one (CS-v2-1ss) and two unpaired bases (CS-v1-2ss) at the corner sites of every helix of the 45° corner, we achieved similar values of 53 % and 57 %, respectively (Fig. 5.5G-H).

Using a PEG-and-HPLC-purified sample, we reconstructed an electron density map for the CS-v2-1ss design from about 2.6×10^4 particles at a resolution of 21 Å (Fig. D.6). Like for the CS-v1 variant, we performed multi-body refinement increasing the resolution to 17 Å, 19 Å, and 19 Å for the 135°, 90°, and 45° corner respectively, and built a composite map from the individually refined corners (Fig. D.19). The object shows global right-handed twist (Fig. 5.6A-B). In the 135° corner, multiple helices bulge outwards, indicating that the additional crossovers in CS-v1 were beneficial to build a corner with a well defined shape (Fig. 5.6C). A poorly resolved region can be found in the 90° corner (Fig. 5.6D), which was well resolved in the CS-v1 variant, although we did not modify the crossover pattern. The defects might have been caused by disadvantageous staple sequences. However, the most striking feature of the map is the outer region of the 45° corner, where almost the entire two outer layers are not resolved (Fig. 5.6E). The helices of these two outer layers are resolved approximately until the positions of intralayer crossover stacks.

5.2 Characterization of a design approach using backbone orientation-specific connections

In the presented variants, the corresponding helices of the two arms are connected via double-stranded helices with continuous scaffold connections and staple strands, which terminate at the corner sites. This design strategy does not take into account the orientations of the backbones at the corner sites. However, depending on the orientation, various scenarios are possible. Given the backbones of the scaffold strands of two connected helices face towards the center of the corner, the nucleotides at the corner could simply unstack to adopt an opened-up conformation. Other orientations, however, might lead to steric hindrance and deformation. The situation, where both scaffold strands face to the outside of the corner, presents the extreme case, in which deformation seems to be inevitable. We showed that the construction of a corner with a small angle is particularly challenging. In the Triple-Corner objects, the 45° corner led to the formation of dimers and exhibited folding defects in the electron density maps. To address these issues, we conducted the further design optimization using a 45° corner object, which is folded with a 2873 nt long scaffold. We present an approach where the individual orientations of the

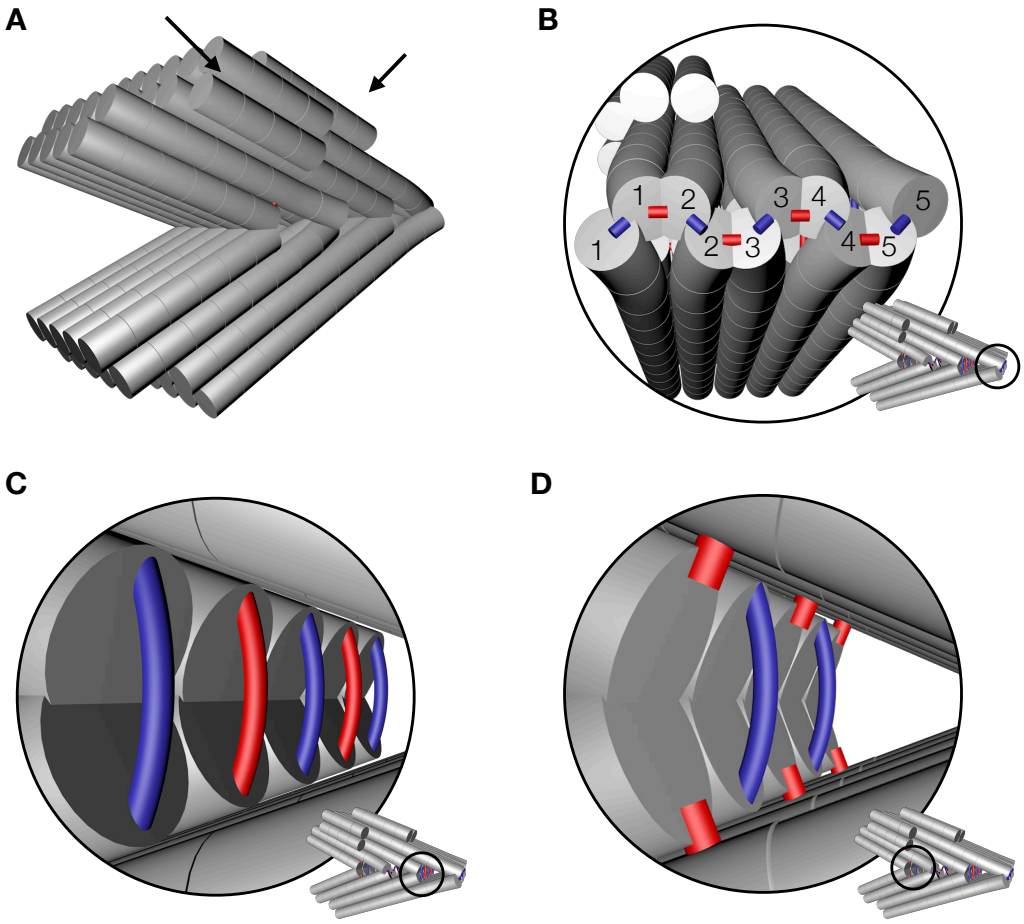

Figure 5.7 Schematic illustrations of the design of CS-v3. (A) Global shape. DNA helices are illustrated as cylinders. Arrows indicate asymmetric features. **(B)** Corner sites of the first layer. Scaffold (blue) and staple (red) crossovers at the corner sites are illustrated as rectangles. Corresponding helices of the two arms (1-1, 2-2, etc) are connected by the scaffold. In each arm, neighboring pairs of helices (1-2, 3-4; 2-3, 4-5) are connected by staples. **(C)** Corner sites of the second layer. Single-stranded scaffold (blue) and staple (red) loops are represented by arcs. **(D)** Corner sites of the forth layer. Representations of loops and crossovers are as above.

backbones of the helices at the corner sites are taken into account. We implemented the insights gained from the Triple-Corner, including the positioning of crossovers and the usage of single-stranded connections, in the new design.

5.2.1 Design approach and folding optimization

The global shape of the new Single-Corner object (CS-v3) is similar to the 45° corner of the Triple-Corner variants. The main body consists of 20 helices arranged on a square lattice with a 4 x 5 cross section. Two flags, each of which is formed by two short helices, are attached to one arm of the structure providing asymmetric features to facilitate the cryo-EM reconstruction process (Fig. 5.7A). In contrast to previous design approaches,

the connections of corresponding helices are designed based on the individual orientations of the backbones of the strands at the corner sites. The majority of staple strands do not terminate at the corner site, but are connected to a neighboring helix of the same layer of the same arm, or to the corresponding helix of the other arm.

First layer: We designed the corner sites of the first layer such that the backbones of the helices face to the sides. In each helix, the scaffold runs across the corner site into the other arm (Fig. 5.7B). In both arms there are two pairs of helices, whose staple backbones point towards each other at the corner site. We connected the respective pairs, resulting in an alternating pattern of intralayer crossovers. Due to this arrangement of crossovers, we assumed to achieve a high stability. We passivated the staple strands of the two helices without a partner using poly-T overhangs. The backbone orientations in the other layers are predetermined by the length differences of the helices.

Second layer: The backbones of the corresponding helices either both point outwards or inwards. For helices whose scaffold backbone points inwards and staple strands point outwards, we connected the scaffold segments directly, without unpaired bases, and the staple segment via single-stranded 6T loops (Fig. 5.7C). Similarly, direct staple connections and loops of six unpaired scaffold bases are used for the helices whose staple backbone points inwards and scaffold points outwards.

Third and fourth layer: The corner sites of the third layer are designed like in the first layer. Layer four is designed similarly to the second layer. However, we exploited that at the corner site of the fourth layer, the backbones of the staple strands of the two outer and central helices of the fourth and third layer point perfectly towards each other. We connected these helices with half-crossovers to increase the stability instead of using the single-stranded staple loop design strategy implemented in the second layer (Fig. 5.7D and Fig. B.27). For the two other helices, we used scaffold loops as described for the second layer.

Gel-electrophoresis analysis of the folding products of various folding conditions yielded high monomer fractions over a wide range of conditions (Fig. 5.8A). By optimizing the folding conditions, we achieved monomer yields above 80 % (Fig. 5.8B-C).

5.2.2 Structural analysis using cryo-EM

We reconstructed an electron density map from about 1.6×10^5 particles and achieved a global resolution of 8.5 Å (Fig. D.7). The global shape of the object is as expected without apparent folding defects (Fig. 5.9A-C). Between crossovers, the helices bend away from each other, particularly at the periphery, forming the previously reported chicken-wire pattern [68]. Structural details including loops, crossovers, helical grooves, and, in the best resolved regions, backbone features are resolved (Fig. 5.9D-F). At the corner sites, the different connection strategies are recognizable. In the first and third layer, the intralayer

staple crossovers located directly at the corner sites are resolved and the helices of the two arms are shifted laterally to each other resulting in a zigzag pattern (Fig. 5.9C,F). In the second and fourth layer, the single-stranded connector loops and interlayer crossovers can be discerned in the well-resolved regions (Fig. 5.9D-E).

Already via visual inspection, the heterogeneity of the resolution across the object is apparent. The helices in the respective centers of the arms are well resolved, including the grooves of the DNA helices and backbone details like phosphates in the form of small bumps. Towards the ends of both arms, first, the double helical shape is decreasingly recognizable, and then the helices are less well separated. Similarly, the two asymmetric features are relatively poorly resolved. Furthermore, the corner sites of the four layers exhibit heterogeneity in resolution, decreasing from the fourth towards the first layer. These observations are in accordance with a quantitative local resolution estimation based on Fourier shell correlation. The distribution of local resolution ranges from 7.0 Å to 14.3 Å with an average of 8.7 Å and a standard deviation of 1.0 Å. The the region around the corner sites of the first layer show an resolution of around 10 Å. With a resolution of of around 9 Å the corner site of the second layer is slightly better resolved. In contrast to the below-average resolution at the first and second layer, the resolution at the corner sites of the third and fourth layer is in the range of 7 Å to 8 Å and parts are among the best resolved regions of the entire structure. This is striking, since the corner sites are the connection points of the two approximately rigid arms and could be regarded as weak spots. Using the previously reported MDff approach [74], we fitted a pseudo-atomic model

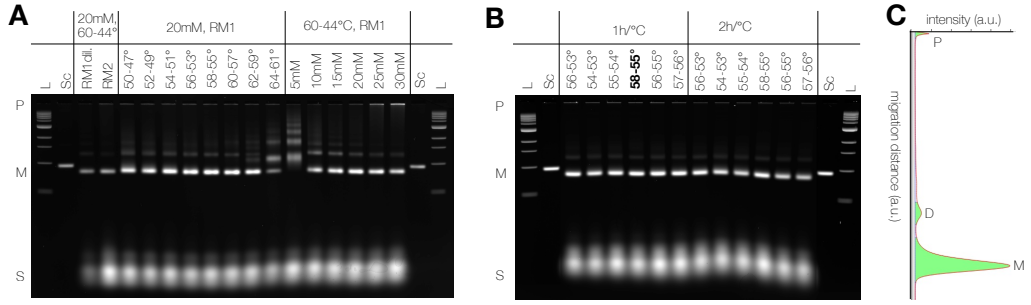

Figure 5.8 Gel electrophoresis analysis of folding conditions of CS-v3. (A) Initial folding screen. L = 1k nt ladder, Sc = 2873 nt scaffold, P = pocket, M = approximate migration distance of monomers, P = excess staples, RM1 = reaction mixture 1 containing 50 nM scaffold and 200 nM staples, RM2 = reaction mixture one containing 20 nM scaffold and 200 nM staples, RM1 dil. = 1:2.5 dilution of RM1, Folding buffers (FOB) contained 5 mM to 30 mM $MgCl_2$ as indicated. Annealing ramps with 1 °C/h were applied using temperature ranges as indicated. **(B)** Finer folding screen. Samples were folded using RM1 and FOB20. Annealing ramps were applied as labeled. The highlighted condition (58 °C to 55 °C, 1 °C/h) was used for cryo-EM sample preparation. **(C)** Intensity profile of the folding condition used for the cryo-EM sample preparation. The monomer yield is 84 %. D = dimer band.

to the electron density map (Fig. 5.10). The model facilitated the structure analysis of the electron density and the comparison with the design.

5.2.3 Addressing structural heterogeneity by focused refinements

In the reconstruction process, the entire structure is treated as one single rigid body and the heterogeneity of the particle ensemble and the resulting electron density map represents the average structure of the particle ensemble. To study the structural heterogeneity of the object, we performed 3D classification using 64 classes. We superimposed and aligned the electron density maps of the best 29 maps which contain 80 % of particles of the data set. We identified an increase in heterogeneity towards the ends of the two arms and towards the corner site of the first layer (Figure E.1A). The comparison of individual classes revealed structural differences including changes in the opening angle of the corner and the amount of global twist in the two arms (Figure E.1B). We used multi-body refinement to focus

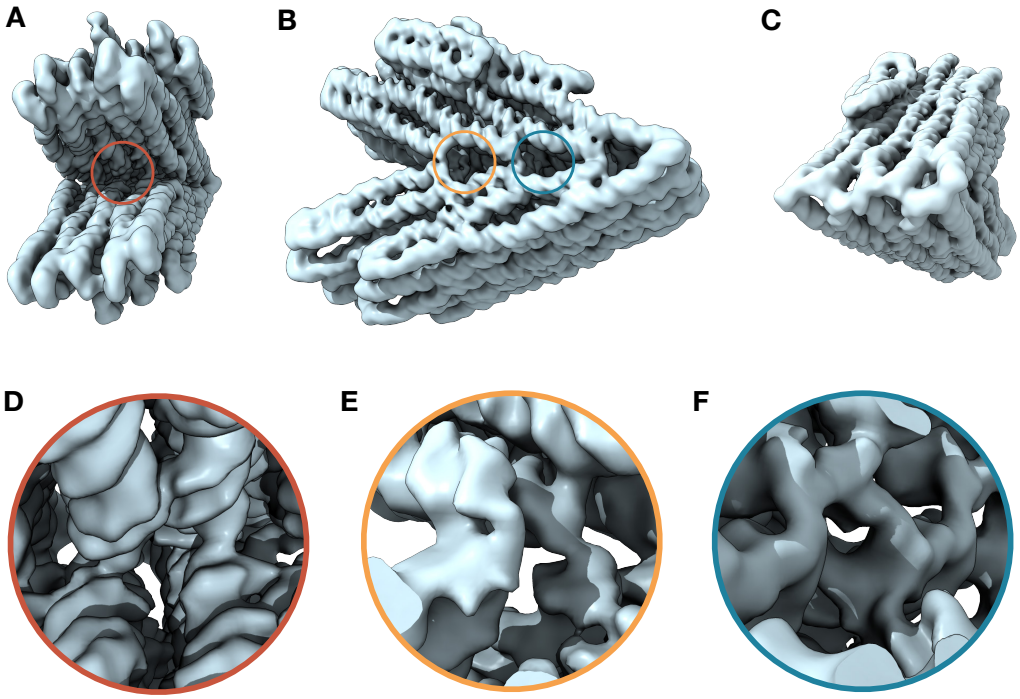

Figure 5.9 Electron density map of the CS-v3 object. **(A)** Front view. A zoomed in view of the section highlighted with the red circle is depicted in panel D. **(B)** Side view. The sections highlighted with an orange and a blue circles are depicted in panel E and F. **(C)** Back view. At the corner site of the first layer, the helices are connected to each other in a zigzag pattern (left to right) and the corresponding helices of the two arms are shifted relatively to each other. **(D)** Zoomed in front view of the corner site of the fourth layer. **(E)** Zoomed in side view of the corner site of the fourth layer. Like in the first layer (C), the intralayer crossovers adopt a zigzag pattern. The two interlayer crossovers (top and bottom center) are resolved. **(F)** Zoomed in side view of the corner site of the third layer.

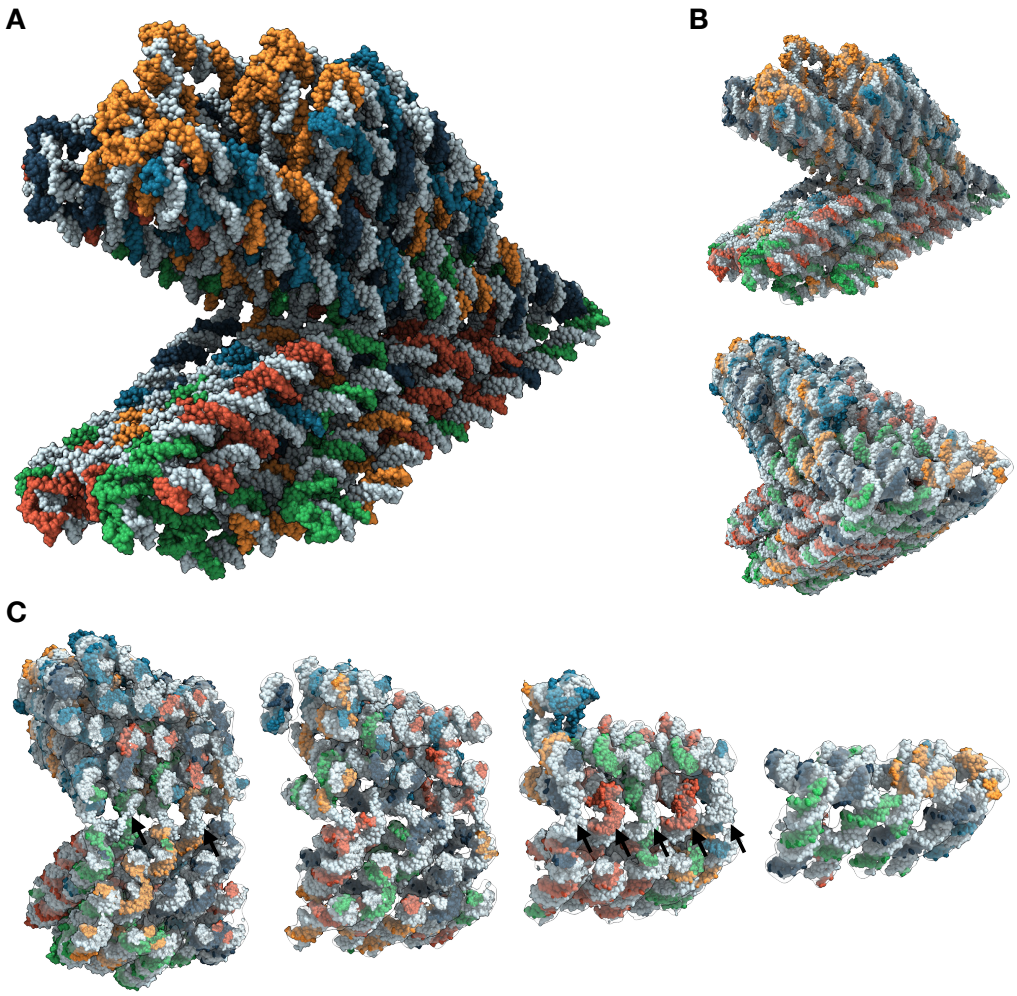

Figure 5.10 Pseudo-atomic model of the CS-v3 object. **(A)** Pseudo-atomic model. The scaffold is colored in light blue. **(C)** Pseudo-atomic model superimposed with the electron density map (transparent). **(C)** Slices of the model and map. Left to right: layer four to one. Arrows indicate single-stranded connector loops.

the alignment onto smaller parts of interest to extract structural information at higher resolution. Using a two-body refinement (Fig. 5.11A), the separate refinements of the two arms yielded a global resolution of 8.1 Å and 8.2 Å for the arm with the asymmetric features and the other arm respectively (Fig. D.20), which may be compared to the global resolution of the consensus refinement of 8.5 Å.

Comparing the map of the consensus refinement with the maps of the two-body refinement, the improvements are visible as deeper grooves in the helices and mainly localized in the previously poorly resolved parts towards the respective ends of the arms. In a quantitative analysis, we calculated the local improvement by taking the voxel-wise difference of the local resolution estimations of the consensus refinement and the two-body refined maps. The calculated average local resolution improvement for both arms is 0.46 Å, and

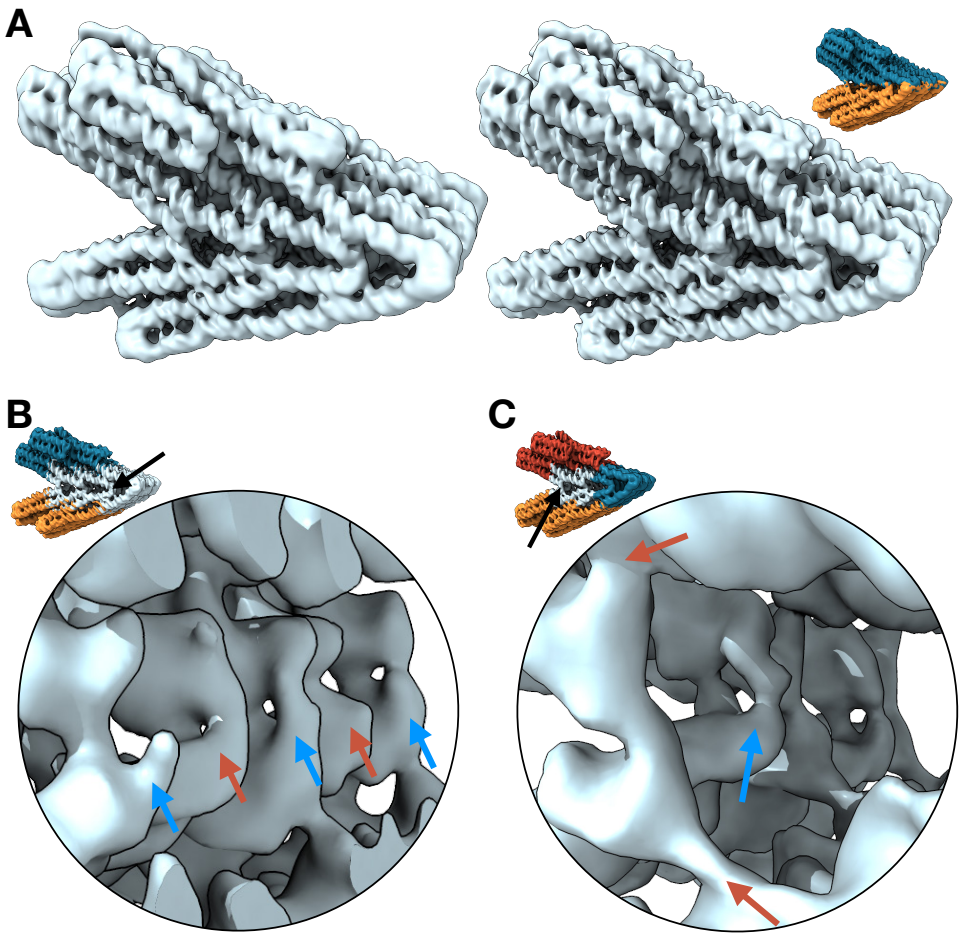

Figure 5.11 Focused refinements. **(A)** Comparison of the consensus refinement (left) and a composite map (right) created from the two-body refined parts (orange and blue). **(B)** Zoom-in onto the corner-sites of the second layer of the three-body refinement (black arrow in overview). Red and blue arrows indicate single-stranded staple and scaffold loops at the corner sites, respectively. The segmentation of the object into three parts is indicated by the differently colored regions in the overview. **(C)** Zoom-in onto the corner-site of the fourth layer of the four-body refinement (arrow in overview). Red and blue arrows indicate exemplary corner-site staple crossovers and scaffold loops, respectively.

the corresponding standard deviations are 0.34 Å and 0.47 Å for the arm with and without asymmetric features, respectively (Fig. E.3). We found the highest improvement in the regions towards the respective ends of the arms. We created a composite map by aligning the maps of the two-body refinement to the consensus refinement and combining the two maps (Fig. 5.11A).

To focus on the corner sites, we performed additional multi-body refinements using different segmentations. In a three-body refinement, we defined the corner sites including the surrounding regions as one body and the remaining parts of the two arms as the second and third body (Fig. D.21). In a four-body refinement, we divided the region of the corner

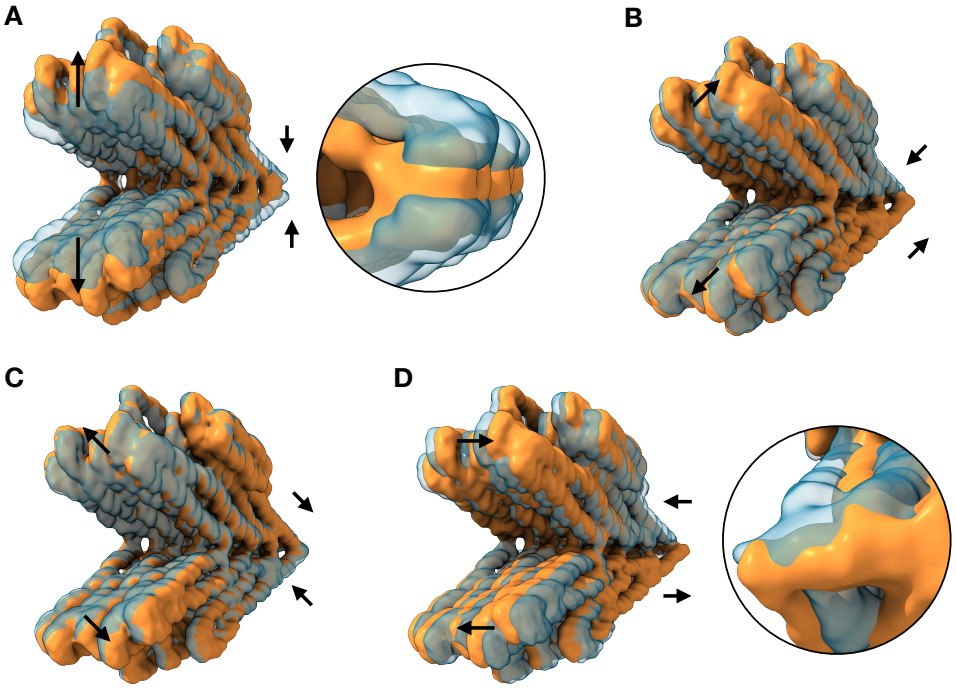

Figure 5.12 PCA of the two-body refinement of the CS-v3 object. Superimposed maps (orange and transparent blue) representing the ranges along the first four components. The arrows illustrate the approximate local changes. **(A)** First component. The zoom-in onto the corner site of the outer layer shows discontinuities in the maps a bulge (orange map) and gaps (blue map). **(B)** Second component. **(C)** Third component. **(D)** Fourth component. The zoom-in onto the corner site viewed from the back shows discontinuities as lateral shifts (orange map).

sites into two parts along a virtual border between the second and third layer (Fig. D.22). With both multi-body refinements, we were able to improve the regions of the arms to an even larger extent than by using the two-body refinement (Fig. E.4, Fig. E.5). In the three-body refined map of the corner site regions, the previously unresolved single-stranded loops of the second layer are visible (Fig. 5.11B). For the corner sites of the fourth layer, we achieved a minor improvement in resolution using the four-body refinement (Fig. 5.11C).

5.2.4 Analysis of structural heterogeneity

In the previous section, the main focus was the improvement of resolution by dividing the structure in multiple parts and refining each part individually using multi-body refinement. Although the higher resolution of the focused-refined maps allows for a more detailed structural analysis, the information about the local heterogeneity of the structure, which is represented in the resolution of the consensus refinement, is diminished. To provide this information and quantify the structural heterogeneity, we analyzed the CS-v3 object using the MB-PCA [78] and 3DVA [81].

With each body having three translational and three rotational degrees of freedom, the motion of a two-body refinement is described by twelve principal components. We identified four main components which explain 23 %, 18 %, 17 %, and 16 % of the total variance of the data set. The histograms of the amplitudes along the components show monomodal distributions (Fig. E.10). For each component, we created maps representing the range of heterogeneity along the components. To visualize the relative deformations of the two bodies to each other, we aligned the maps to the consensus refinement. The first four principle components, viewed from the front, describe:

1. a change in the opening angle (Fig. 5.12A),
2. a diagonal motion of the arms in opposite directions (Fig. 5.12B),
3. a diagonal motion similar to the second component, but in approximately orthogonal direction (Fig. 5.12C),
4. a lateral motion of the arms in opposite directions (Fig. 5.12D).

Corresponding small changes in opposite directions are visible towards the tip of the corner and the least changes are noticeable in the centers of the two arms. At the corner sites, discontinuities in the form of bulges, gaps, and shifts are visible.

We additionally characterized the heterogeneity by fitting a linear 3D subspace model to the data set using 3D variability analysis (3DVA) [81] with three components and calculated maps representing the ranges of motion of the components. In contrast to MB-PCA, the motion patterns of the 3DVA components are more complex and locally diverse (Fig. 5.13A-C). They are described by nonuniform flow fields, where the vectors of local heterogeneity in neighboring regions can differ substantially. We identified global motion patterns similar to the ones described by the components of the MB-PCA. The global deformations described by the first and second components are changes in the opening angle of the corner including diagonal motions of the arms. The dominant deformation of the third component is a lateral motion of the top arm and a rotation of the lower arm. For each of the three components, the deformations are more pronounced towards the ends of the arms. For each component, we fitted the distribution of amplitude values of the particles along the component using kernel density estimation. By taking the negative logarithm of the respective probability density functions, we calculated the energy landscapes along the components (Fig. 5.13D-F). Within the range of the central 94 % of the particle distribution, corresponding to the range of motion presented in the superpositioned maps (Fig. 5.13A-C), the energy landscape of each of the three components is monomodal indicating continuous motion. We additionally performed the analyses in 2D via combinations of two of the three components (Fig. 5.13G-I) and in each case identified a single minimum.

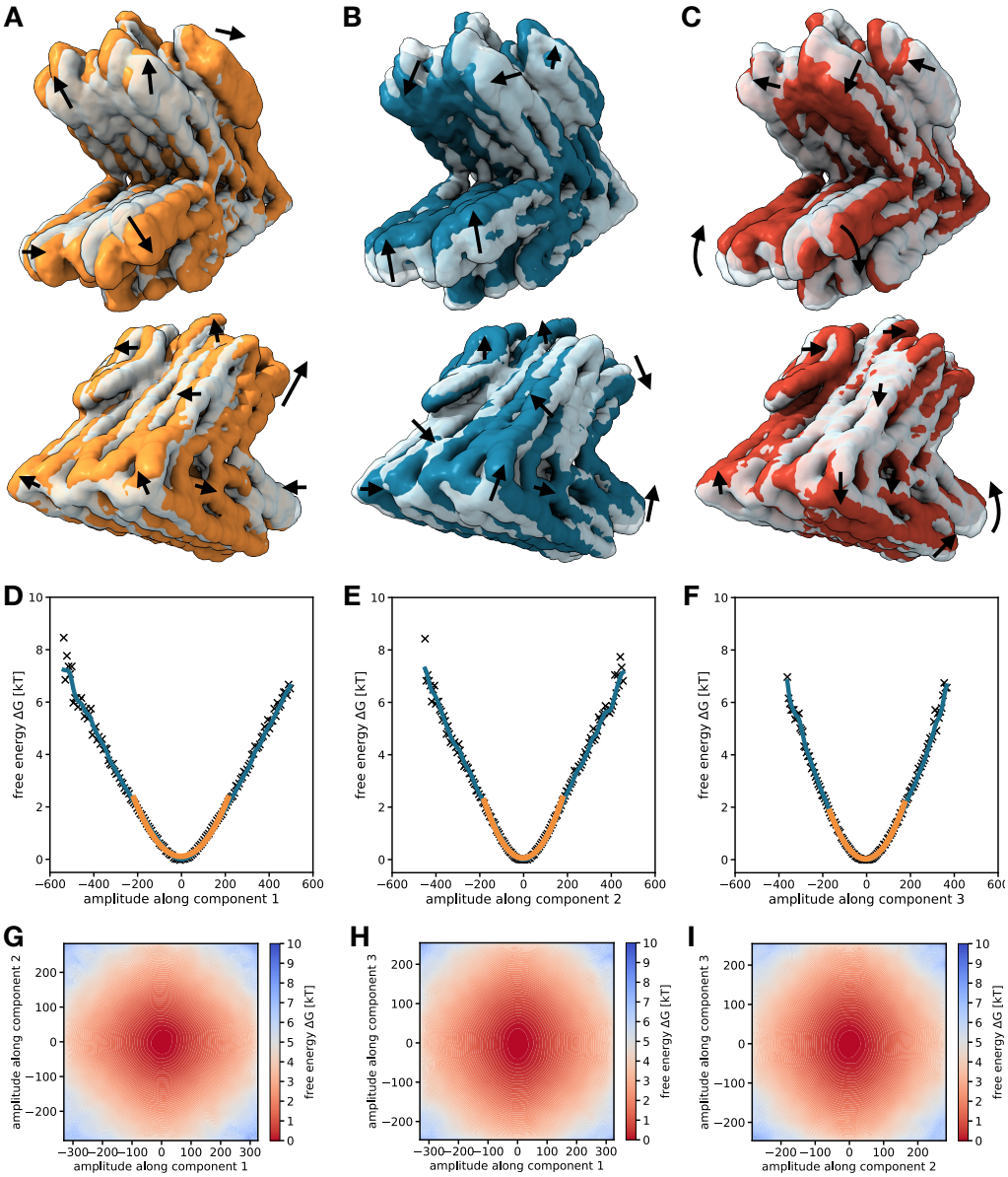

Figure 5.13 3D Variability Analysis (3DVA). (A) - (C) The first three components of the 3DVA are illustrated. For each components two superposed maps (colored and light) represent the 3rd and 97th percentile of deformation along the reaction coordinate. The arrows illustrate the local deformations of the light map towards the colored map along the coordinate. The lengths of the arrows represent the directions and relative ranges of motion of the local deformation. **(D) - (F)** 1D energy landscapes of components 1 to 3 calculated as the negative logarithm of the probability distribution of the particles along the component. The data are fitted using a Gaussian kernel density estimation (KDE) (blue line). Within the central 94 % the data are fitted by a quadratic potential (orange line). The data and fits are shifted vertically that the y-axis describes the difference in free energy from the minimum of the KDE. **(G) - (I)** Central regions of the 2D energy landscapes of combinations of components 1 to 3. The color bar indicate the local difference in free energy from the minimum based on a multivariate Gaussian KDE.

5.3 Design modifications

The analysis of the cryo-EM density map of the 45° corner object showed various structural features which include:

1. structural heterogeneity
2. helices arranged in a chicken wire-like pattern,
3. a global right-handed twist in both arms despite the implementation of an effective helical twist density of 10.33 bp/turn which resulted in a twist-free structure in the Twist-Tower-v2 object (chapter 3).

Based on the design of CS-v3, we created variants to influence these structural features using:

1. angle braces to modify the structural heterogeneity,
2. additional crossovers to achieve a reduced chickenwire pattern,
3. a further reduction of the effective helical twist density to compensate for the residual global twist.

5.3.1 Angle braces

We tested two approaches of implementing angle braces. In the first approach, we placed small helix segments into the gaps between the layers at the corner sites as internal angle braces (Fig. 5.14A). This design will be referred to as CS-v4 in the following. We designed each internal brace from two staple oligonucleotides, one of which originates from one arm, contributes to the brace, and continues into the other arm, and a second one, which originates from one arm and terminates at the end of the brace (Fig. 5.14B). The single-stranded connection is rotationally flexible. Therefore, we assumed that the brace does not introduce torque, which could potentially reduce the stability of the construct, regardless of the length-dependent orientation of its backbones. The attachment sites of the braces are located at helix positions of the main body where the backbone faces towards the associated attachment site of the other arm. Since neighboring helices run antiparallel, the respective brace attachment sites are shifted relatively to each other. To account for the resulting length of neighboring braces and slight structural variations of the attachment sites, we adjusted the length of each brace based on distance measurements in the cryo-EM map of CS-v3. In the second approach, we placed long helices, also entirely formed by staple strands, as external angle braces between the helices of the inner layer (Fig. 5.14C). In the following, this design variant will be referred to as CS-v5. As it is the case for the internal braces, the attachment sites of neighboring external braces are shifted relatively to each other, and we adjusted the length of each brace individually to fit the distances

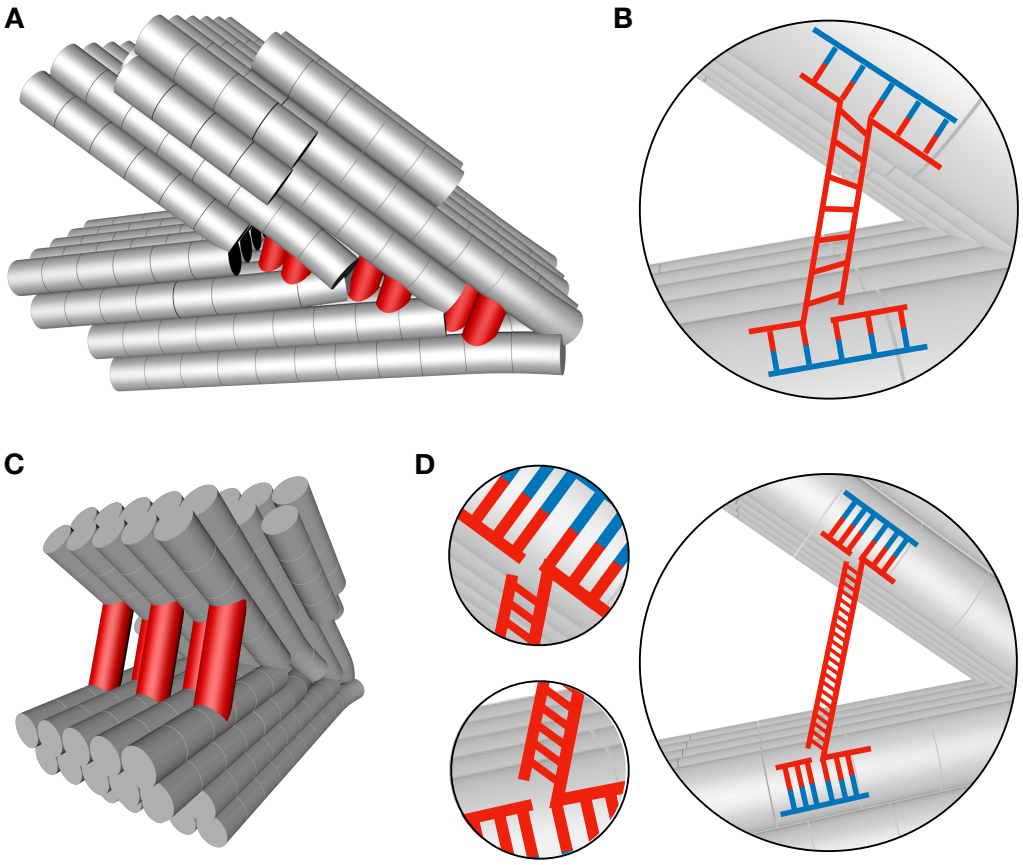

Figure 5.14 Schematic illustrations of the design of corner variants with angle braces. **(A)** Variant with internal angle braces. Double-stranded DNA braces built up entirely from staple strands are illustrated as red cylinders. **(B)** Internal angle brace. Scaffold and staple segments are depicted in blue and red, respectively. **(C)** Variant with external angle braces. **(D)** External angle. Insets: zoom-in views onto the attachments sites

between the corresponding attachment sites. In contrast to the internal braces, each of the external braces is formed by one staple oligonucleotide which protrudes from one arm and continues in the other arm and a second complementary oligonucleotide which is not connected to the arms (Fig. 5.14D). This design strategy was inspired by the design of the previously reported V-brick [20]. We implemented the braces based on CS-v3 without removing crossovers.

The folding screen of CS-v4 revealed poor monomer yields over the entire range of tested conditions with a high fraction of side products (Figure C.5). The highest achieved monomer yield was 29 %. The sample compositions show similarities to the folding screens of the Triple-Corner variants. By removing the internal braces of the first layer and undoing the design changes of this region, we were able to increase the monomer yield of this second version (CS-v4-2) to 77 %, which is a similarly high levels as for the variant

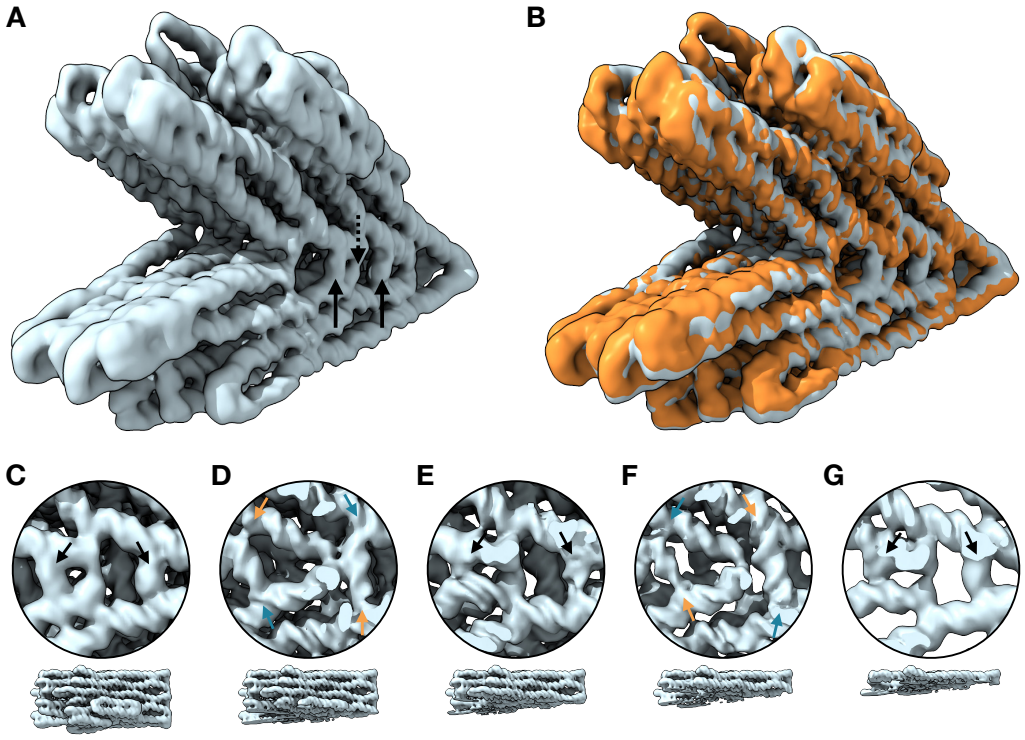

Figure 5.15 Cryo-EM structural analysis of CS-v4-2. (A) Consensus refinement of CS-v4-2. Solid and dotted indicate two internal braces and a corner site. Zoom-ins of slices of the object are given in (C)-(G). **(B)** Comparison of CS-v4-2 (light blue) with the variant without braces CS-v3 (orange). **(C)-(G)** Side views of the braces of slices. The positions of the slices are indicated by the top views below. In each view the corner site of the third layer is visible in the center flanked by the two braces similar to the positions indicated by the arrows in (A). **(C), (E), (G)** Short braces. Brace helices are indicated by black arrows and are poorly resolved. **(D), (F)** Long braces. The double helical shape of the braces is visible. Designed single-stranded and double-stranded attachments are indicated by blue and orange arrows, respectively.

CS-v3 (Figure C.6). The analysis of folding screen of the variant with external struts (CS-v5) revealed a monomer yield of up to 67 % (Figure C.7).

For the variant CS-v4-2, we reconstructed an electron density map from about 2.4×10^5 particles with a global resolution of 8.0 Å (Fig. D.8). The global shape of the object is close to identical to CS-v3 (Fig. 5.16A-B). We analyzed the braces in the five planes of helices using slices of the electron density map (Fig. 5.16C-G). In the first plane, the braces are designed to be close to the corner site and hence are very short (Fig. 5.16C). They are not well resolved and a double-helical shape is not visible. For both braces, the single-stranded versus double-stranded attachment sites can not be distinguished. In the second plane, both braces are positioned further away from the corner sites and are resolved to a degree that the double helical shape is visible (Fig. 5.16D). In the left brace, the designed double-stranded attachment site of the lower arm and the single-stranded attachment site of the upper arm can be distinguished. For the right brace, the types

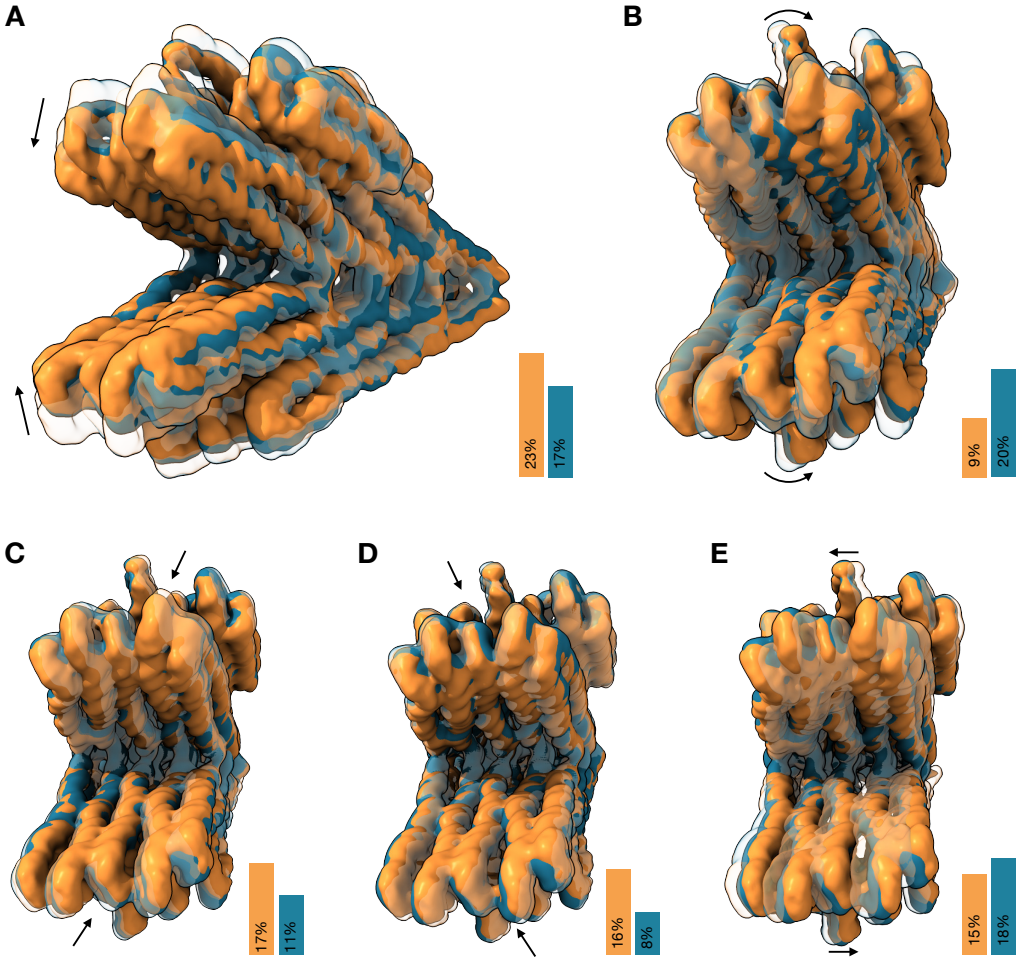

Figure 5.16 Multibody PCA comparison of corresponding components of CS-v4-2 and CS-v3. For each pair of components of CS-v3 (orange) and CS-v4-2 (blue) the range of motion in each variant is represented by two maps (opaque and transparent). Arrows indicate the approximate direction of motion. For each component, the percentage of the total variance of the data set is given and illustrated by bars. **(A)** Dominant component of CS-v3 and third component of CS-v4-2 describing changes in opening angle. **(B)** Dominant component of CS-v4-2 and fifth component of CS-v3 describing rotational motion of the arms. **(C) - (E)** Components two, four, and six of CS-v3 and the corresponding components four, six, and two of CS-v4-2 respectively, describing diagonal and lateral motion patterns.

of connection are opposite and similarly well resolved. The braces of the third and fifth plane are designed like the ones of the first plane and are visible as short and relatively poorly resolved connections (Fig. 5.16E, G). The braces in the fourth plane are similar to the ones of the second plane and the double helical shape is visible (Fig. 5.16F). However, the differences between single-stranded and double-stranded attachments, which by design are arranged at the respective opposite arm compared to plane two, are less clear.

We performed a two-body refinement as we did for CS-v3. We compared the principle components of the data sets of the two objects, and identified corresponding principle com-

ponents of CS-v4-2 describing similar motion patterns. We compared the corresponding components to each other with respect to the percentages of total variance in the respective data sets. The component describing changes in opening angle, which is dominant in CS-v3, is reduced both in terms of range of motion and percentage of total variance in CS-v4-2 (Fig. 5.16A). In CS-v4-2, the dominant component describes a rotational motion of the arms and explains twice as much of the total variance compared to CS-v3, but also has a reduced range of motion (Fig. 5.16B). The percentages of total variance in diagonal motion patterns are reduced in CS-v4-2, whereas the lateral motion of the arms in opposite directions is slightly increased (Fig. 5.16C-E). The diagonal and lateral motion patterns have similar ranges of motion.

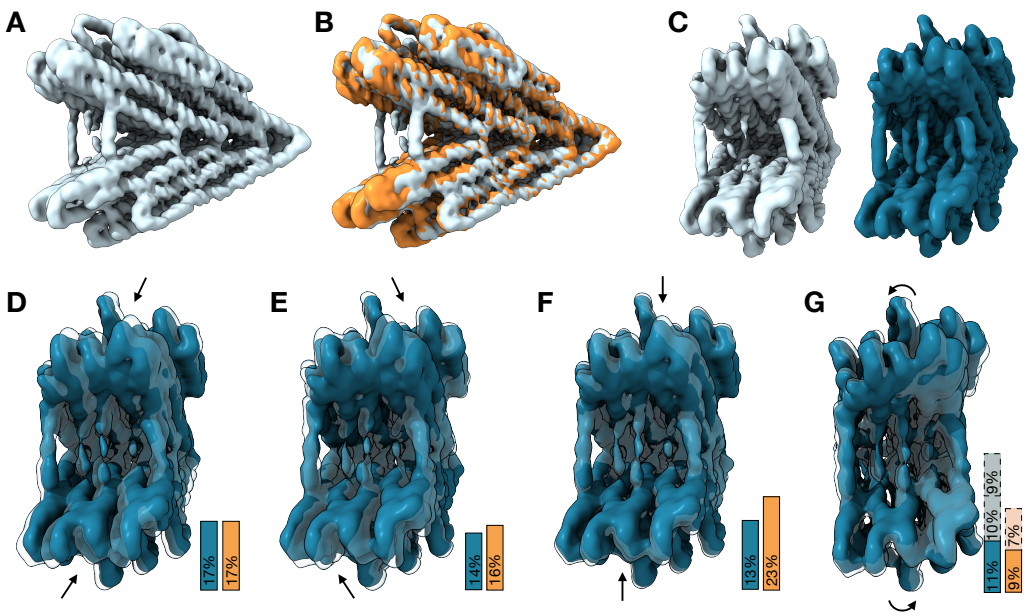

Figure 5.17 Electron density maps of CS-v5 (A) Consensus refinement. **(B)** Comparison with CS-v3 (orange). **(C)** Comparison of the map of the consensus refinement (light blue) and a map reconstructed from a subset containing 2.6×10^4 particles from selected 3D classes (blue). **(D) - (G)** The first four components of a PCA based on a two-body refinement of the particle subset. Arrows show the most prominent direction of variance in the component. Bars show the percentages of the total variance explained by the component of CS-v5 (blue) and a similar component in the data set of CS-v3 (orange). **(G)** Fourth component describing a rotational motion pattern of the arms. Additionally, the variances of components five and six of CS-v5 and an additional component of CS-v3 describing very similar rotational motion patters (dim, dashed boxes) are given.

For CS-v5, the variant with outer braces, we reconstructed an electron density map with a global resolution of 8.1 Å from around 1.3×10^5 particles, and achieved a global resolution of 8.1 Å (Fig. D.9). In most regions of the object, the helices are well resolved and the design features of the corner sites are recognizable (Fig. 5.17A). However, the braces are poorly resolved. Only the outer braces are visible as cylinder-like structures. The central

braces can only be recognized at a low thresholds, where the object occupies a multiple of its actual volume (Fig. E.11). The global shape of CS-v5 is close to identical to CS-v3 (Fig. 5.17B). We performed masked 3D classification focusing on the region of the braces. We reconstructed an electron density map from a subset of 2.6×10^4 particles selected from 3D classes, in which the entire set of braces is resolved to some extent (Fig. 5.17C). Compared to the consensus refinement, the global resolution of object decreased to 9.1 Å. We analyzed the heterogeneity of this subset by two-body refinement (Fig. D.24) and subsequent MB-PCA as described for the previous variants. The first two components of CS-v5 describe diagonal motion patterns and have similar percentages of total variance as we identified for CS-v3 (Fig. 5.17D-E). The third component, which describes a change in opening angle without diagonal components is slightly decreased in CS-v5 compared to the variant CS-v3, in which this motion pattern was dominant (Fig. 5.17F). The percentage of total variance explained by the rotational motion pattern of the fourth component of CS-v5 is slightly decreased (Fig. 5.17G). By combining components in both variants, which describe very similar rotational motion patterns, the difference is more noticeable.

5.3.2 Increase of the number of crossovers

In the electron density map of CS-v3 and the other presented variants based on this design, we observed the arrangement of helices in a 3D chicken-wire pattern which is a result of the helices bending away from each other between crossovers due to electrostatic repulsion [68]. To reduce this effect, we created a variant with an increased number of crossovers, mainly by adding scaffold crossovers (CS-v6). As a result, the scaffold routing is more complex compared to the previous variants. We did not change the effective helical twist density (Fig. B.11).

We reconstructed an electron density map from approximately 2.6×10^5 particle snapshots achieving a resolution of 8.7 Å (Fig. D.10). Similarly to the other variants, two-body refinement improved the resolution, yielding values of 7.3 Å and 6.9 Å for the arm with and without the asymmetric features, respectively (Fig. D.25). We identified a poorly resolved region at the end of the arm with asymmetric features, which originates from a mistake in the design. Apart from this, the object is well resolved, with a similar global shape as CS-v3 (Fig. 5.18A). In CS-v6, the arm without asymmetrical features has a reduced global twist (Fig. 5.18B). We identified regions, where the crossover stacks created by the additional crossovers led to a constriction-like arrangement of the helices (Fig. 5.18C). Due to the additional interlayer crossovers, the chicken-wire pattern is reduced (Fig. 5.18D).

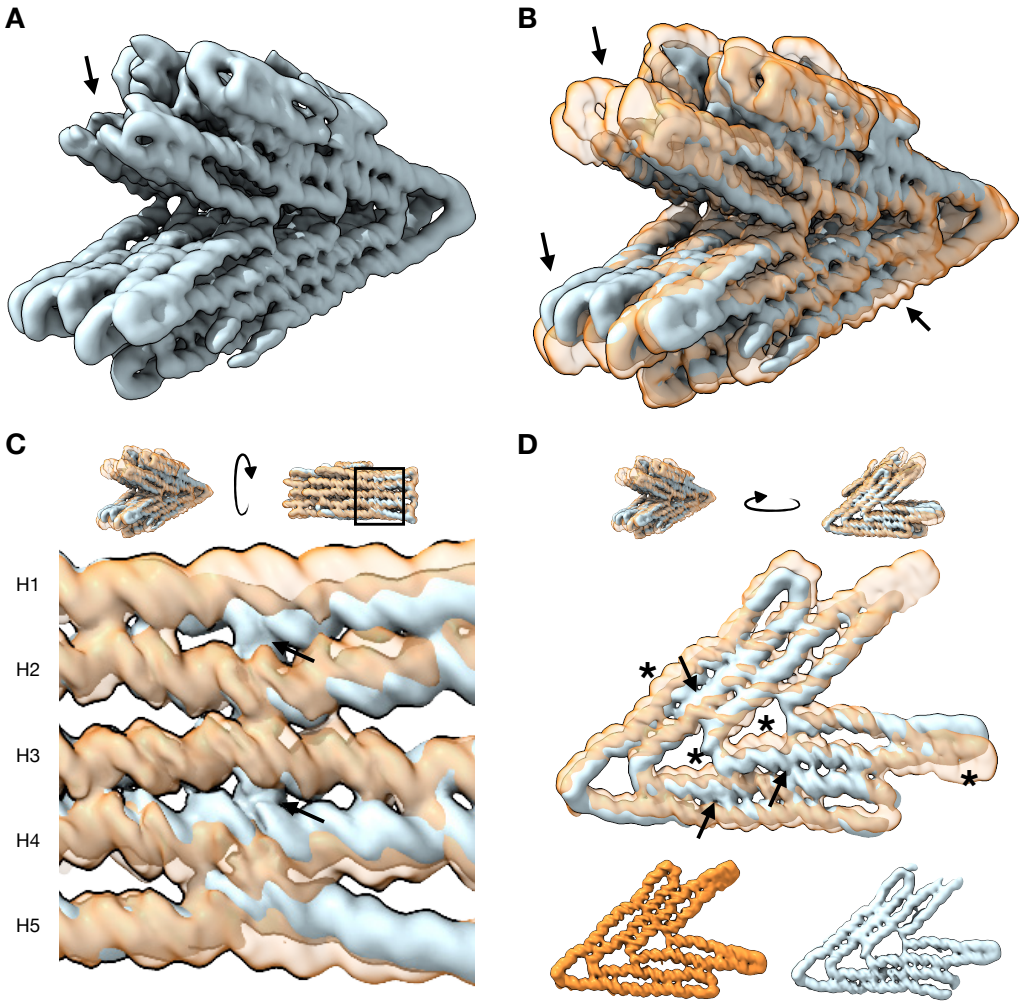

Figure 5.18 Cryo-EM structural analysis of the corner variant with an increased number of crossovers (CS-v6). **(A)** Electron density map of CS-v6. The arrow indicates an unresolved part of the object. **(B)** Comparison of CS-v6 (light blue) and CS-v3 (transparent orange). The arrows highlight deviating regions: the unresolved end of the upper arm of CS-v6 (top left), a reduced global twist of the lower arm (bottom left), and an inwards bending helix at the lower arm (bottom right). **(C)** Comparison of the outer layer of the bottom arm as an exemplary region with different number of crossovers. The maps are colored as described in (B). The five helices are numerated from H1 to H5. Arrows indicate additional crossovers in CS-v6 resulting in a crossover stack where the outer helices H1 and H5 are bent inwards. **(D)** Comparison of the back side of the object. Arrows and stars indicate additional crossovers in CS-v6 compared to CS-v3 and differences between the maps, respectively.

5.3.3 Reduction of the effective helical twist density

Although we designed the corner variant CS-v3 with a reduced effective helical twist density of 10.33 bp/turn, the electron density map showed residual global right-handed twist. To address this, we designed a variant with further reduced effective helical twist density of 1 bp/turn (CS-v7). This required the shortening of most of the helices in each

arm by 10.22 bp. To match the fixed length of the scaffold of 2873 nt within the design rules, we elongated some of the helices, conforming to the rules of square lattice design, and adjusted the crossover pattern (Fig. B.12). The structure folds at high monomer yields over a wide range of the tested conditions in the initial folding screen (Fig. C.9). We further optimized the conditions and achieved a monomer yield of about 94 % (Fig. C.10).

The electron density map, which we reconstructed from about 5.9×10^5 particle snapshots, has a global resolution of 7.1 Å (Fig. D.11). With a two-body refinement, we improved the resolution achieving 7.1 Å and 6.7 Å for the arm with and the arm without asymmetrical features, respectively (Fig. D.26). The structure appears to be well folded without apparent defects (Fig. 5.19A). In the core of the object, the helices are well resolved with their double helical shape clearly visible. Similar to the other variants, the

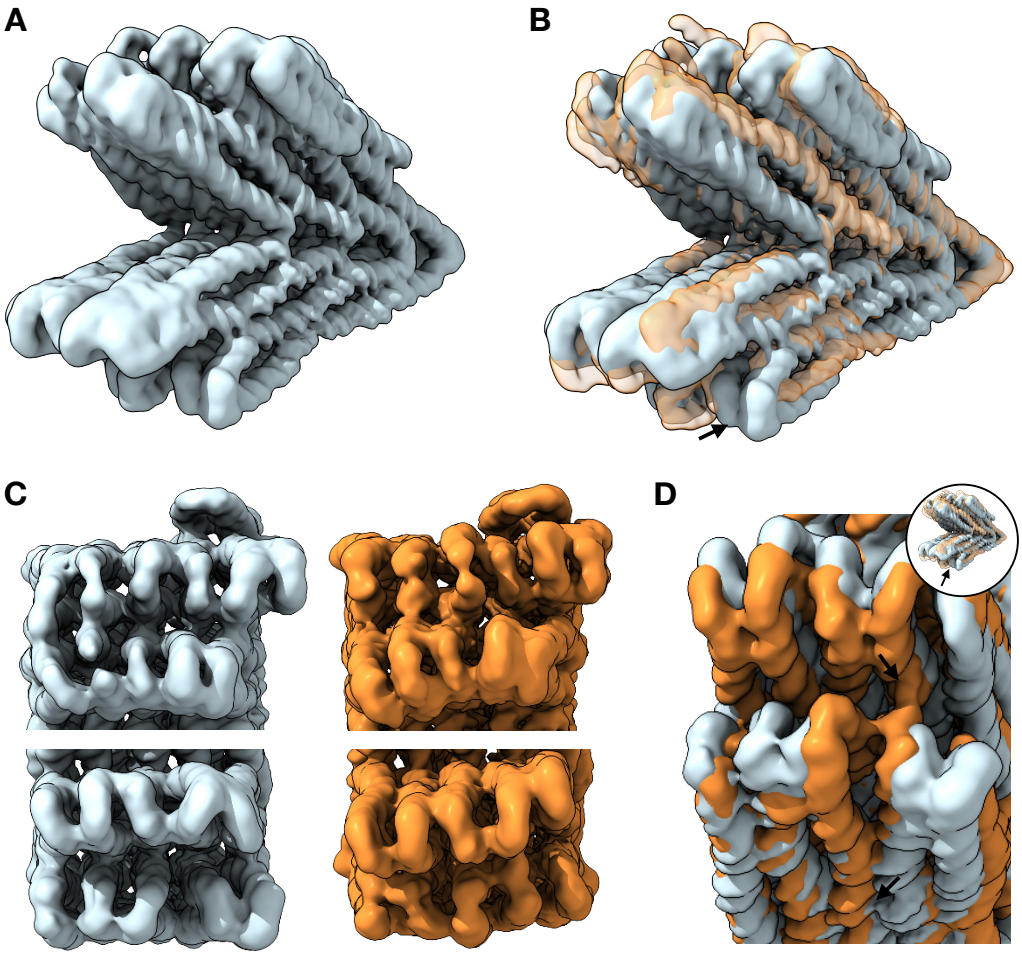

Figure 5.19 Cryo-EM structural analysis of the corner variant with a reduced effective helical twist density (CS-v7). (A) Electron density map. **(B)** Comparison with CS-v3 (orange). The arrow indicates a region in the map of CS-v7, where a group of helices slightly points to the side. **(C)** Front views of the top and bottom arms of the two variants. **(D)** Comparison of the region highlighted in (B). The top and bottom arrows indicate crossovers which are only present in CS-v3 and in CS-v7, respectively.

resolution is lower towards the ends of the arms. Compared to the variant CS-v3, the new variant CS-v7 is free of global twist (Fig. 5.19B-C). We noticed a cluster of helices at the end of the arm without features, which, unlike for CS-v3, slightly points to the side (Fig. 5.19B,D). We attribute this to a crossover which is present at the end of one of the helices in CS-v3, but was removed in the design of CS-v7. Furthermore, an additional crossover in CS-v7, close to the center of the outer layer, results in a crossover stack, which influences the orientation of the helices.

5.4 Discussion

We tested multiple design strategies to build the connections at the corner sites, to adjust the global shape, and to influence the structural heterogeneity, using several variants of Triple-Corner and Single-Corner objects.

Development of an effective design of corner sites: For the Triple-Corner variants CS-v1 and CS-v2 with double-stranded connections and staple nicks at the corner sites, the folding analyses revealed poor monomer yields, as well as dimer formation via the 45° corner. Negative stain EM imaging indicates that the connections are formed by helices of the first layer, which do not form the corner, but branch into the other monomer. Since the staple oligonucleotides terminate at the corner sites, the dimers are most likely formed via scaffold strand swapping. We designed the staple nicks at the corner sites to introduce predefined kink points. However, in the electron density maps, many helices appear to have a bent structure at the corner sites. This effect is particularly pronounced in helices with long segments without crossovers, which additionally resulted in a bloating-like effect, likely due to electrostatic repulsion of the helices. We assume that the bending is caused by the backbone orientations at the nick sites, which are not aligned to the orientation of the corner. At the 45° corner, the largest deformation is required, which might pose a high energetic penalty promoting the formation of dimers via interstrand swapping.

In variants with single-stranded connections at the 45° corner, we achieved higher yields, likely due to the increased flexibility and reduced energetic cost involved in the formation of the corner. However, the 45° corner of the CS-v2-1ss variant showed large structural defects. By design, most of the unresolved part is only connected to the rest of the structure via crossover stacks. It is possible that this design strategy, which was not used in the well-resolved 45° corner of CS-v1, contributed to the defects in CS-v2-1ss. Although, we did not change the connection strategy of the 90° corner, the electron density map of the CS-v2-1ss variant shows deviations from the design, which might have been caused by disadvantageous staple and scaffold sequences. We identified minor defects in

the 45° corner of the CS-v1 electron density map reconstructed from a PEG-and-HPLC purified sample. These defects were not present in the gel purified variant. We assume the defects were formed during folding or purification, due to the use of older and potentially damaged staple oligonucleotides or the exposure to increased temperature in a centrifugation step. The low folding yield and structural defects indicate instabilities and flaws in the used design approaches, particularly for the 45° corner.

We addressed the challenging design of a corner with a small angle by creating and characterizing variants of a Single-Corner object. In gel electrophoretic assays, we achieved monomer yields of up to 94 %. Using high-resolution 3D structural feedback from cryo-EM, we showed that the use of backbone orientation-specific connection strategies, including single-stranded loops and crossovers directly at the corner sites, are beneficial to create sharp, well-shaped corners.

Global shape: Both electron density maps of the PEG- and HPLC-purified Triple-Corner variants CS-v1 and CS-v2-ss, designed with an effective twist density of 10.44 bp/turn, showed a global right-handed twist. In contrast, the electron density map of the CS-v1 sample, which was exposed to EtBr during the gel purification, is close to twist free. This impact of the DNA intercalating agent EtBr on the global twist of DNA origami objects is in accordance with previous findings obtained from AFM measurements [108]. In a study on global twist, we found that for the 4 × 4 cuboid, which has a similar cross section as the corner objects, a reduced effective twist density of 10.33 bp/turn results in a twist-free global shape (see chapter 3). However, despite implementing a reduced twist density of 10.33 bp/turn in the designs of the Single-Corner variants CS-v3, CS-v4-2, CS-v5, and CS-v6, the electron density maps exhibit global right-handed twist. We attribute this to the smaller cross section in most parts of the structure, which may require additional twist correction similar to the 2 × 2 cuboid of the Twist-Tower. In addition, the corner sites might introduce additional torque which also may require a further reduced effective twist density to be compensated. In the variant CS-v7, we achieved a twist-free structure by implementing an effective twist density of 10.22 bp/turn. We showed that by increasing the number of crossovers, without changing the imposed effective helical twist density (CS-v6), straightening of the helices, and therefore a reduction of the chicken-wire pattern can be achieved. We attribute the slightly reduced twist in this variant to the straightening effect.

Characterization of structural heterogeneity: We analyzed extensively the structural heterogeneity of the CS-v3 variant using local resolution estimation, multi-body refinement, MB-PCA, and 3DVA. The local resolution of the asymmetric feature, the corner sites of the outer layer, and the helix ends in both arms is relatively poor. In these regions,

the number of neighboring helices and crossovers is low, which likely results in a higher degree of flexibility. The best resolved parts of the structure are located in the respective centers of the two arms. The helices in these parts are surrounded by neighboring helices, which likely reduce their mobility, and have a high density of crossovers connecting them to other helices. For each multi-body refinement, we achieved large improvements in local resolution in the regions towards the ends of the arms, indicating that these parts exhibit a high structural heterogeneity. This is in accordance with the observations from the 3D classification. In contrast, the resolution of the corner site was only marginally improved. We think that this effect is caused by the pseudosymmetry of the corner. In the consensus refinement, the center of mass is close to the corner site of the inner layer. Hence, the particle snapshots are predominantly well aligned in these regions resulting in a high resolution in these parts and thus lower potential for further improvement by focused refinement. For the corner sites of the first and second layer, we noticed a larger improvement in resolution for the three-body refinement compared to the more focused four-body refinement. It is possible that this is due to the order of processing and weighting of the bodies within the multi-body refinement algorithm.

In the MB-PCA using a two-body approximation, we identified the in-plane change of the opening angle as the direction of the largest variance in the data set. Diagonal and shearing motion patterns account for the second to fourth principle components. The approximation of the heterogeneity with two rigid bodies leads to artifacts in the form of discontinuities in the constructed maps illustrating the direction of heterogeneity of the individual components. Each of these principal components shows monomodal distributed amplitudes indicating continuous motion and the absence of additional local minima. Additionally, we analyzed the heterogeneity of the data set of CS-v3 using 3DVA. The motion patterns of the components are described by complex flow fields. In accordance with the MB-PCA, changes in opening angle including diagonal motion are the dominant motion patterns of the 3DVA components. Based on the distribution of the particle amplitudes along the components, we calculated the energy landscapes, which, in accordance with the MB-PCA, are monomodal indicating continuous motion.

Angle brace modifications: We tested the influence of internal (CS-v4) and external braces (CS-v5), placed in the cavities between the corner sites and the respective centers of the fourth layer, respectively. The variant with internal braces in each of the cavities resulted in a poor monomer yield, whereas we achieved a high folding quality for the variant without internal braces at the first layer (CS-v4-2). We attribute this to the modified staple routing in the first layer of CS-v4 compared to CS-v4-2. Due to additional internal staple braces, the routing of the staple strands is more complex and interwoven, and might cause kinetic traps in the folding landscape resulting in dimerization and other

undesired byproducts. As revealed by the electron density map, the central braces of CS-v5 are poorly resolved, likely caused by the short staple segments at the attachment sites. Using two-body approximation we analyzed the data set of CS-v4-2 as well as a subset of CS-v5 with better resolved braces, and compared each of them to CS-v3. For both sets, we identified components with similar motion patterns as described by the components of CS-v3. Both types of brace modifications changed the percentages of total explained variance of corresponding components. Comparing CS-v4-2 to CS-v3, the percentages of total variance of the components describing changes in opening angle including diagonal motion were reduced. These motion patterns require relatively large deformations of the braces and adjacent helices, like the stretching or contraction of springs. In contrast, the dominant component CS-v4-2 describes a rotational motion pattern, where the two central braces appear to remain virtually neutral. The second component, which describes a lateral motion and is slightly increased in CS-v4-2, requires only small deformation of the braces. We observed a similar trend for the motion patterns in the subset of CS-v5. However, due to the relatively low number of particles in the subset, the analysis is less substantive, and an improved design is required to study the influence of external braces.

Empirical design guide: We developed a highly effective approach to build well-shaped corners with high monomeric folding yield. At the corner sites, single-stranded loops and crossovers are used depending on the orientation of each backbone. Our approach of using an arrangement of alternating intralayer crossovers in the first layer can be implemented in every corner, independently of the desired angle. The strategies for the connections of the following layers are then chosen based on the orientation of the backbones at the corner sites of the individual helices. We note that the use of this design strategy for the first layer results in blunt end-like helix ends at the tip of the corner. If this leads to dimer formation in a particular experiment, e.g., using relatively high concentrations of Mg^{2+}, we suggest to either replace one or more corner-site crossovers with passivating poly-T overhangs or to use the design strategy of corner site loops in the first layer, as implemented in the second and fourth layer of the presented Single-Corner variants. Whereas in cuboids a reduced effective twist density of 10.33 bp/turn was sufficient for effective twist correction, we showed, that the implementation of a value of 10.22 bp/turn led to a twist-free global shape in the presented 45° corners. Depending on the desired shape of the corner design, this value might require slight individual adjustments. Furthermore, the global shape and flexibility of the design can be customized using internal and external angle braces as well as a specific density of crossovers.

Chapter 6

Conclusion and Outlook

The goal of this thesis was the characterization and improvement of design motifs in DNA origami nanostructures via high resolution cryo-EM structural feedback. To this end, we addressed the challenge of extracting detailed structural information from heterogeneous DNA nanoobjects. We solved the 3D structures of eleven DNA nanoobjects with up to nucleotide resolution and fitted pseudoatomic models to four of them. We characterized global twist and square lattice-based design motifs, validated the assembly of dual-scaffold objects, as well as developed effective design strategies for various types of corners.

We presented a zoom-in reconstruction approach to address structural heterogeneity and increase the resolution in regions of interest, using the Twist-Tower object as a model. In the electron density map of the consensus refinement, which was reconstructed by treating the structure as a single rigid body, we observed a wide range of heterogeneity in resolution. In the first zoom-in step, we reconstructed the major domains individually using multi-body refinement and achieved improvements in resolution for each domain, which allowed us to fit a pseudo-atomic model to the electron density map. In an iterative application of a second zoom-in step, we scanned the entire object using a small focused window and achieved resolutions up to 4.3 Å for the focused regions. The step-wise improvement of resolution is particularly striking for the challenging 2×2 domain, which was barely resolved in the consensus refinement. For the the scanning-focused refinement, a previous medium zoom-in step facilitates the creation of localized masks and improves the signal subtraction per particle. Additionally, it allows for a considerable reduction of the computational load by using smaller box sizes as well as cropped and signal-subtracted sets of particles. We could directly transfer the workflow to the reconstruction of the Twist-Tower-v2, the 126-helix bundle, and the corner objects. We used the high-resolution data obtained from one or more zoom-in steps to validate or refine the intended design.

Based on the high resolution of the 3D cryo-EM structures of two variants of the Twist-Tower, we characterize the global twist and the crossover design motif in multilayer

square lattice-based objects. In accordance with previous findings using negative stain EM imaging [35], we showed that the amount of global twist scales inversely with the cross section. Based on our twist measurements and previous findings [74], we conclude that basic square lattice DNA nanoobjects can be twist-corrected by implementing a reduced effective twist density of 10.33 bp/turn, given a sufficient number of crossovers to transmit the counter torque-inducing modifications. However, we note that for more designs with complex motifs like corners and curvatures, slight individual adjustments might be required.

Serving as a model for the multi-scaffold design approach, we solved and characterized the 3D structure of a 126-helix bundle barrel-like object, which is created from two orthogonal scaffolds. The structure is according to the design without structural defects and does not exhibit global twist. We analyzed the inter-scaffold crossover design motif as an indicator for the structural integrity of the object. A qualitative comparison with other types of crossovers, as well as an analysis of the local resolution along the helices yielded no structural defects or systematically reduced resolution in the inter-scaffold crossovers. In addition to the high folding yield [83], these results show the effectiveness of the multi-scaffold design strategy to create large DNA origami objects. It has been successfully applied in previously reported objects, including a penta-scaffold multibrick [83] and the dual-scaffold 'reactive vertex' for gigadalton-scale assemblies [20]. We are convinced that the strategy is a key design tool to build large DNA objects, either as an alternative to multimeric assemblies or as an additional layer for multistep higher-order assemblies.

Applying the zoom-in approach and insights from studying the global twist in square lattice design, we addressed the challenge of building well-shaped corners at a high folding yield. We developed a strategy based on backbone orientation-specific connections using electrophoretic analysis and electron microscopy structural feedback. We demonstrated the effectiveness of this strategy by implementing it in several variants of a corner object with a 45° angle, which we identified as most challenging in previous attempts. We achieved monomer yields of up to 94 % and well-shaped corner sites without structural defects in the high-resolution electron density maps. We showed that the main directions of flexibility of the object can be influenced by internal and external angle braces. Using an increased number of crossovers, without changing the effective twist density, we achieved a reduction of the chickenwire pattern. By means of adjusting the effective twist density in the design, we realized a twist-free variant. Due to the implemented improved attachment sites, the twist-free variant can be used to study the influence of external angle braces, including complex asymmetric and nonparallel arrangements. Our approach of using either an arrangement of alternating intralayer crossovers or, if required, single-stranded loops at the corner sites of the first layer, can be implemented for corners of an arbitrary

angle. The connection strategies for the following layers are then chosen according to the orientation of the individual backbones of the helices.

Recently, the number of published cryo-EM DNA origami structures has been constantly growing [15, 22, 74, 106, 109], providing valuable structural data, which are required for accurate characterization of DNA origami nanostructures. Fitting tools allow the construction of atomic models, which facilitate the interpretation of the maps in light of the actual design [74, 110, 111]. Further development of these tools will enable the fitting of structures with more complex design motifs beyond the boundaries of lattice design. The field of DNA origami structure prediction will benefit from the growing library of maps and atomic models, which provides important experimental data to validate and refine the models and parameters of the prediction tools [112–116]. Furthermore, high resolution maps, particularly the scanning-focused refined Twist-Tower, present an interesting opportunity for data mining, e.g., for the geometric properties of DNA and potential deviations from the native B-form as well as sequence dependencies in terms of local structure and resolution. We are convinced that the results presented in this thesis, and high-resolution cryo-EM characterization of DNA origami objects in general, will drive the field forward by providing valuable structural insights. By improving the design rules and structure prediction tools of DNA-origami nanostructures, we believe to enable the realization of more accurate structures for real-world applications.

Appendix A

Protocols

Remark: The protocols for cryo-EM sample preparation (folding, purification, and concentration), grid preparation, image acquisition, 3D reconstruction, and multi-body refinement were performed in large part as described in Kube, Kohler, Feigl et al. (2020) and were adopted from the methods section of this article [74].

A.1 Buffers

folding buffer (FOBx): 5 mM TRIS, 1 mM EDTA, 5 mM NaCl, and x mM $MgCl_2$ at ph 8. For example, the folding buffer FOB20, contains 20 mM $MgCl_2$.

gel running buffer: 0.5 x TBE, 5.5 mM $MgCl_2$.

polyethylene glycol (PEG) precipitation buffer): 15 % PEG 8000, 5 mM TRIS, 1 mM EDTA, 500 mM NaCl

HPLC buffer: 5 mM TRIS, 1 mM EDTA, 5 mM $MgCl_2$, 200 mM NaCl, pH 8

A.2 Folding

The objects described in this thesis were folded in one-pot reactions. The reaction mixtures contained the the required circular homemade scaffold strand(s) and purchased chemically synthesized oligonucleotides (Eurofins MWG and IDT), suspended in 1xFOBx containing 5 mM to 30 mM $MgCl_2$ depending on the required folding conditions. CS-v5 was folded in a two-step folding procedure. The primary folding step was performed without the five staple oligonucleotides which make the braces double stranded but are not connected to the rest of the structure. In the secondary folding step these oligonucleotides were added to the

folded objects. The folding reactions were performed in a Tetrad thermal cycling device (MJ Research, now Bio-Rad Laboratories). The folding mixture was subjected to a heating step of 15 min at 65 °C to dehybridise secondary structures of the DNA strands. A custom step-wise thermal annealing ramp was applied depending on the object to be folded. After folding, the samples were stored at room temperature. To find the best object-dependent folding conditions, a standardized initial folding screen (IFS) with 16 folding conditions was performed, consisting of a scaffold to staple ratio screen, a temperature screen, and a magnesium screen. The names of the folding conditions, the varying concentrations of the components of the folding mixture, and the applied annealing ramps are summarized in table A.1. Based on the results of the gel electrophoresis analysis, further folding conditions were tested.

folding condition	**c(scaffold)**	**c(staples)**	**c($MgCl_2$)**	**folding ramp**
RM1	50 nM	200 nM	20 mM	60 °C to 44 °C
RM2	20 nM	200 nM	20 mM	60 °C to 44 °C
T1	50 nM	200 nM	20 mM	50 °C to 47 °C
T2	50 nM	200 nM	20 mM	52 °C to 49 °C
T3	50 nM	200 nM	20 mM	54 °C to 51 °C
T4	50 nM	200 nM	20 mM	56 °C to 53 °C
T5	50 nM	200 nM	20 mM	58 °C to 55 °C
T6	50 nM	200 nM	20 mM	60 °C to 57 °C
T7	50 nM	200 nM	20 mM	62 °C to 59 °C
T8	50 nM	200 nM	20 mM	64 °C to 61 °C
M5	50 nM	200 nM	5 mM	60 °C to 44 °C
M10	50 nM	200 nM	10 mM	60 °C to 44 °C
M15	50 nM	200 nM	15 mM	60 °C to 44 °C
M20	50 nM	200 nM	20 mM	60 °C to 44 °C
M25	50 nM	200 nM	25 mM	60 °C to 44 °C
M30	50 nM	200 nM	30 mM	60 °C to 44 °C

Table A.1 Reaction mixtures and folding parameters of the Initial Folding Screen. The reaction mixture of each condition contains folding buffer including the respective concentration of magnesium chloride. Each folding ramp precedes a heating phase of 15 min at 65 °C. The concentration of staple oligonucleotides $c_{staples}$ represents the concentration for each oligonucleotide used in the reaction mixture.

A.3 Gel electrophoresis

The gel was prepared by dissolving 2.5 g of UltraPure™ Agarose (invitrogen™, Thermo Fisher Scientific) in 122.5 g of 0.5 x TBE using microwave heating. Evaporation was compensated by refilling the solution with double distilled water. The agarose solution was cooled under constant shaking to approximately 40 °C. 5.5 mM $MgCl_2$ and 5 drops of aqueous 0.025 % (250 µg/ml ethidium bromide solution in dropper bottle (Carl Roth)

were added. The solution was cured in a gel tray (Owl Easycast^{TM} B2, Thermo Scientific). The tray was filled with running buffer and the wells were loaded with a mixture of sample and loading dye (15 % Ficoll 400, 0.1 % Bromphenol blue, 5 mM TRIS, pH 8) at a ratio of 5:1. A voltage of 90 V was applied for about 2 h. The gel was laser-scanned at a resolution of 50 µm/px using a Typhoon FLA9500 (GE Healthcare) at an excitation wavelength of 532 nm. To facilitate the visual inspection of the gel data, the signal of the gel scan was inverted and the contrast improved using the auto-contrast function in Adobe Photoshop (final inspection: version 21.0.3). Quantitative analysis was performed on the unmodified scan data using the Image Lab software (Bio-Rad Laboratories, Inc., Version 6.1.0). Lanes and bands were auto-detected using the respective functions. The background correction parameter was adjusted per gel to achieve a constant background subtraction and close to zero signal in the blank areas of the gel. The sensitivity parameter of the band detection was adjusted per lane to cover the whole range of the log-normal-distribution-like monomer bands including tails. The best folding conditions were selected based on monomer yield, migration distance, and bandwidth. In case a particular folding condition resulted in a relatively high intensity of the leading band, but had a significantly shorter migration distance or broader bandwidth than the leading bands of other conditions, it was judged to be of minor quality and therefore excluded from the ranking.

A.4 Purification

A.4.1 Gel purification

The preparation steps were as described above. 2.8 g of UltraPure^{TM} Agarose (invitrogen^{TM}, Thermo Fisher Scientific were dissolved in 187.5 g of 0.5 x TBE. 7 drops of EtBr solution and $MgCl_2$ to a final concentration of 5.5 mM were added. After running the gel, the band of interest was cut out and pestled in 1.5 ml tube (Eppendorf, Germany, Hamburg) [45]. For each tube, the tip containing the pestled piece of gel was cut off with a razor blade (Carl Roth, Apollo) and put upside down into a Freeze'N Squeeze^{TM} tube (Biorad). The tube was centrifuged for 5 min at 1000 rcf and the purified sample was collected [45].

A.4.2 PEG purification

The reaction mixture was mixed in a one-to-one ratio (v/v) with PEG buffer and centrifuged for 30 min at 20000 rcf [45]. The supernatant was removed and the pellet dissolved in 1xFOB5 [74].

A.4.3 HPLC purification

Excess staple DNA strands were removed from the reaction mixture by performing one round of PEG purification. The resulting pellets were dissolved in HPLC buffer. For CS-v1 and CS-v2 variants, larger aggregates were removed by filtering the sample using 0.45 µm filters at 13000 rcf for 10 min. We subjected the sample to HPLC (Agilent Technologies 1260/1290 infinity) using the column (Agilent Bio SEC-5: 5 µm, 2000 A, 21.2 x 300 mm) at a flow rate of 2 ml/min and collected the fractions of the monomer peak [45][74].

A.4.4 Filter purification

For the filter purification [45], the sample was diluted with 1 × FOB to a final $MgCl_2$ concentration of 5 mM. Amicon Ultra 0.5-ml, 50-kDa cut-off filters (Millipore) (Cs-v1 w/EtBr with 100 kDa cut-off filters) were rinsed with 500 µl 1 x FOB5 and centrifuged at 5000 rcf for 1 min. 500 µl sample was added to the filters and subjected to a centrifugation step at 5000 rcf for 5 min. Several washing steps were performed consisting of removing the flow-through, refilling the filters to 500 µl with 1 x FOB5, and a centrifugation step. The filters were placed upside-down in fresh tubes and subjected to another centrifugation step. The filtered samples were collected from the tubes and pooled [74].

A.4.5 Filter concentration

Amicon Ultra 0.5-ml 50-kDa cut-off filters (Millipore) were rinsed with 500 µl 1 x FOB5 and centrifuged at 5000 rcf for 1 min. The sample was added to the filter and centrifuged at 5000 rcf for 10 min. In the case of a larger sample volume, multiple steps of adding sample and centrifuging at 5000 rcf for 5 min (10 min for the final step) were performed. The filters were placed upside-down in fresh tubes and centrifuged at 5000 rcf for 5 min [45][74].

A.5 Negative stain EM

A drop of 1 µl of 5 M NaOH was added to the wall of an Eppendorf tube containing 200 µl of in-house prepared 2 % uranyl formate solution. The tube was vortexed for 1 min and centrifuged for 6 min at 16100 rcf. A 5 µl droplet of sample was placed onto a previously glow discharged (Electron Microscopy Sciences) carbon-coated surface of a Cu400 TEM grid (Electron Microscopy Sciences). The grid was blotted with a filter paper. The grid was washed by adding 5 µl of stain solution and subsequent blotting. A droplet of 20 µl stain was incubated for 30 sec on the grid, followed by the final blotting step. The grid was dried for 15 min. TEM imaging was performed on a Philips CM-100 electron microscope operated at an acceleration voltage of 100 kV and equipped with an AMT 2k x 2k CCD camera.

A.6 Cryo-EM

A.6.1 Grid preparation

The purified and concentrated sample was applied to glow-discharged C-Flat grids (Protochips) and plunge-frozen using a Vitrobot Mark IV (FEI, now Thermo Scientific) at the following settings: temperature of 22 °C, humidity of 100 %, 0 sec wait time, 2 sec to 4 sec blot time, -1 blot force, and 0 sec drain time [74]. The composition and treatment of the individual samples are summarized in Tables A.2.

structure	scaffold: type @ concentration	#oligonucleotides, concentration	magnesium in FOB	annealing ramp	purification method	concentration method
CS-v1 w/ EtBr	8064 @ 40nM	222, each @ ~200nM	15mM	54-50°, 2h/°C	Gel	filter
CS-v1 w/o EtBr	8064 @ 50nM	222, each @ ~200nM	20mM	60-44°, 1h/°C	PEG, HPLC	filter
CS-v2-1ss	8064 @ 10nM	225, each @ ~40nM	20mM	60-44°, 1h/°C	PEG, HPCL	filter
CS-v3	2873 @ 50nM	69, each @ ~500nM	20mM	58-55°, 2h/°C	filter	filter
CS-v3-3	2873 @ 50nM	66, each @ 200nM	20mM	60-44°, 1h/°C	filter	filter
CS-v4-2	2873 @ 50nM	72, each @ 200nM	20mM	60-44°, 1h/°C	filter	filter
CS-v5	2873 @ 50nM	69, each @ 200	15mM	60-44°, 1h/°C	filter	filter
CS-v6	2873 @ 50nM	70, each @ 200	15mM	56-53°, 1h/°C	filter	filter
126 helix bundle	7560 @ 20nM, Csv2 @ 20nM	#453, each @200nM	25mM	60-40°C, 3h/°C	filter	filter
TwistTower sample 1 (dataset 1)	8064 @ 50nM	#194, each @ 200nM	20mM	56-53°C, 1h/°C	filter	filter
sample 2 (dataset 2-4)	8064 @ 50nM	#194, each @ 200nM	20mM	54-53°C, 2h/°C	filter	filter
sample 3 (dataset 5)	8064 @ 50nM	#194, each @ 200nM	20mM	54-53°C, 2h/°C	filter	filter
TwistTower-v2	8064 @ 20nM	#191, each @ 200nM	20mM	60-44°C, 1h/°C	filter	filter

Table A.2 Sample preparation.

A.6.2 Image acquisition

The data were acquired on a Titan Krios G2 electron microscope operated at 300 kV equipped with a Falcon 2, later upgraded to a Falcon 3 direct detector, a Volta phase plate (FEI, now Thermo Scientific), and a Cs Corrector (CEOS GmbH) using the EPU software (FEI, now Thermo Scientific). The acquisition parameters for the individual data sets are summarized in Tables A.3 and

A.6.3 3D reconstruction

The image processing was performed in Relion 2[75] and 3[78]. For each data set, the micrographs were motion-corrected and CTF estimated using MotionCor2[117], and CTFFIND3

structure	concentration [µM]	grid type	magnified pixel size [Å]	#micrographs in final refinement	#particles in final refinement
CS-v1 w/ EtBr	0.32	C-Flat 2/1 4C	2.319, phase plate	3,890	27,990
CS-v1 w/o EtBr	0.70	C-Flat 1.2/1.3 4C	2.28	2,056	16,967
CS-v2-1ss	0.85	C-Flat 2/1 4C	2.28	3,513	26,480
CS-v3	2.3	C-Flat 2/1 2C	1.39	18,944	160,094
CS-v3-3	2.4	C-Flat 1.2/1.3 4C	2.28	26,747	261,812
CS-v4-2	2.9	C-Flat 2/1 4C	1.79	26,414	238,269
CS-v5	2.9	C-Flat 1.2/1.3 4C	2.28	13,080	128,847
CS-v6	5.0	C-Flat 2/1 4C	1.39	63,163	589,609
126 helix dataset_1	1.2	C-Flat 2/1 4C	1.39	2,734	67,819
dataset_2	1.2	C-Flat 2/1 4C	1.39	2,271	54,674
Twisttower-v2 dataset 1	0.9	C-Flat 2/1 4C	1.39	876	19,815
dataset 2	0.9	C-Flat 2/1 4C	1.39	5,035	75,019
Twisttower dataset_1	1.5	C-Flat 2/1 4C	1.39	2,050	32,548
dataset_2	1.0	C-Flat 2/1 4C	1.39	4,866	80,415
dataset_3	2.3	C-Flat 2/1 4C	1.39	1,496	46,738
dataset_4	2.0	C-Flat 2/1 4C	1.39	3,623	172,78
dataset_5	1.75	C-Flat 2/1 4C	1.39	9,244	350,111

Table A.3 Cryo-EM acquisition parameters.

and CTFFIND4[118], respectively. The particles were picked using the Relion and Cryolo[119] autopickers. For the autopicking procedure in Relion, several hundred particles were manually picked and subjected to reference-free 2D classification to create templates. The autopicked particles were extracted from the micrographs and subjected to multiple rounds of 2D and 3D classification. Classes were manually selected to remove falsely picked grid contamination and damaged particles, and to address large structural heterogeneity. For the data set of CS-v6, autopicking and 2D/3D classification was performed using TOPAZ[120] and the respective Cryosparc tools[80]. A refined 3D map was reconstructed using a low-resolution initial model created in Relion. The particles were polished (per-particle motion correction and dose weighting), and a polished 3D-refined map was reconstructed. The map was postprocessed using a low-pass filtered mask to calculate the FSCs and estimate the global resolution based on the 0.143 FSC criterion. The map was B-factor sharpened and locally low-pass filtered using the local resolution estimation tool implemented in Relion.

A.6.4 Multi-body refinement

The procedure was performed using the multi-body refinement tool in Relion 3[78]. For the respective data sets, the consensus map was divided into custom parts using the eraser tool in UCSF Chimera [121]. The parts were low-pass filtered, binarized, and multiple layers of soft-edge voxels were added to create masks for multi-body refinement. The multibody-refined maps were postprocessed using low-pass-filtered masks to calculate the FCSs. For the TwistTower, for each body of the previous four-body refinement, sets of particle snapshots were created with subtracted projections of the other bodies, smaller subarea boxes but unchanged pixel size, and the body of interest in the the center to allow for more efficient processing for the subsequent focused scanning refinement described below. From the resulting four partial-signal-subtracted particle sets, 3D-refined maps were reconstructed. The multi-body refined maps were sharpened and locally low-pass filtered based on their estimated local resolution. Composite maps were created by aligning the multi-body-refined maps to the consensus refined map in Chimera [121], and taking the voxel-wise maximum. For the multi-body principal component analysis (PCA), the relative orientational changes of the particles in each body resulting from the multi-body refinement, were analyzed using the relion_flex_analyse program. For each component of PCA, the particles were assigned to nine or ten equally populated bins according to their amplitude values along the component and the center amplitude values of the bins were used to create maps representing the motion of the respective components. To visualize the relative changes of the maps of a component, they were aligned to the consensus refinement. To focus on a small subvolume, the map was divided into a map containing the region of interest (size approximately 40 bp, 2 x 2 helices cross-section) and a second map containing the rest, using the eraser tool in UCSF Chimera [121]). From the two subregion maps, low-pass filtered, soft-edged masks were built and a two-body refinement was performed. The refined region of interest was postprocessed using a low-pass filtered mask to calculate the FSCs and estimate the global resolution. The map was B-factor sharpened and locally low-pass filtered using the local resolution estimation tool implemented in Relion.

A.6.5 Pseudoatomic model fitting

Pseudoatomic model fitting was performed as described in Kube, Kohler, Feigl, et al. (2020) [74].

A.6.6 Electron density map and model visualization

Electron density maps and models were visualized using Chimera (versions up to 1.15) [121] and ChimeraX (versions 0.92 and 1.1.1) [122]. Images were created using ChimeraX.

A.6.7 3D Variability Analysis (3DVA) and energy landscapes

The 3D-refined map and and particles were imported into Cryosparc[80] and a refined map was created using the Relion map as reference. The 3DVA[81] was performed and for each component 10 maps at equally spaced positions between the 4th and 96th percentile of the amplitude values of the particles were created using the respective Cryosparc tools. The energy landscapes were calculated in a self-written Python script using the SciPy and NumPy libraries [123] [124]. For the 1D histogram representation of the probability density, the data (amplitude values of the particles along one component) were binned using the Scott method for automatic bin width determination of the NumPy histogram method. For a continuous probability density function, the data were fitted using the SciPy Gaussian kernel density estimation (KDE) with the Scott method for automatic bin width determination. The energy landscape was calculated by taking the negative logarithm of the probability density function. The energy landscape was shifted along the energy coordinate, so that the minimum is at zero. The data points of the energy landscape (calculated from the histogram) within the range of the 3rd and 97th percentile of the data set, were fitted using a Gaussian function. The 2D energy landscapes were calculated similarly from combinations of two components. The script is available on GitHub: `https://github.com/KohlerF/phd_thesis/releases/tag/v1.0`.

A.6.8 Local resolution analysis

The local resolution analyses were performed with a Python-based Jupyter Notebook[125] using the SciPy [123] and NumPy [124] libraries, as well as the mrcfile 1.1.261 package[126]. Resolution estimation maps were masked using binarized electron density maps of the respective objects. For the 126-helix barrel-like object, the TwistTower, and the small corner objects, the masks were created using a threshold corresponding to an occupied volume of 13.2×10^6 Å^3, 6.7×10^6 Å^3, and 2.4×10^6 Å^3, respectively. Each non-zero voxel of the masked local resolution map contributed as a data point to the statistic. Histogram was created using a bin width of 0.1 Å. The data was fitted using Gaussian kernel density estimation (KDE) at a bin width of 0.01 Å. Both the probability density of the histogram and the KDE were normalized to one. The script is available on GitHub: `https://github.com/KohlerF/phd_thesis/releases/tag/v1.0`.

A.6.9 Twist analysis

Slices with a thickness of 3 bp were extracted from the design at certain positions according to the design using the viewer tool [74], the pseudo-atomic model, and the design file. For each pair of slices, the slices were visualized in ChimeraX [122], aligned in the helical direction, and orthographic top view images of the slices were created. The two images

were superimposed and aligned manually in Keynote. The steps of alignment of the slices, image acquisition, and alignment were repeated ten times for each pair of slices with random initial orientations. The average and standard deviation of the twist angle was calculated in Excel using the respective functions. The uncertainty was calculated as the standard error of the mean at a confidence level of 95.5 % corrected by the factor of 2.32 from the student-T distribution for ten measurements.

A.6.10 126 helix-bundle crossover analysis

The 126 helix-bundle crossover analyses were performed with a Python-based Jupyter Notebook[125] using the SciPy [123] and NumPy [124] libraries, the mrcfile 1.1.261 package[126], and the viewer tool [74]. The regions of the respective crossovers were extracted from the electron density map using the viewer tool and converted into binerized masks using a threshold of 0.08. The corresponding regions in the local resolution map were extracted using the masks. Similarly, the resolutions of slices in the helical direction were calculated. The script is available on GitHub: `https://github.com/KohlerF/phd_thesis/releases/tag/v1.0`.

Appendix B

Supporting information: DNA origami designs

Name	Description
CS-v1	Triple-Corner (45°, 90°, and 135° corners), built from 8064 nt scaffold, double-stranded corner sites with staple nicks
CS-v1-out1ss	Variant of CS-v1, one scaffold base is left unpaired at each corner site of the first layer of the 45° corner
CS-v2	three corners, built from 8064 scaffold, double-stranded corner sites with staple nicks, reduced crossover density at 45° and 135° corner compared to CS-v1
CS-v2-out1ss	variant of CS-v2, one scaffold base is left unpaired at each corner site of the first layer of the 45° corner
CS-v2-1ss	variant of CS-v2, one scaffold base is left unpaired at each corner site of each layer of the 45° corner
CS-v2-2ss	variant of CS-v2, two scaffold bases are left unpaired at each corner site of each layer of the 45° corner
CS-v3	Single-Corner (45° corner), built from a 2873 nt scaffold, backbone orientation-specific designs of corner sites including single stranded loops and crossovers placed directly at the corner sites
CS-v4	variant of CS-v3 with three rows of small internal angle braces in the cavities between the layers
CS-v4-2	variant of CS-v4 without the row of small internal angle braces at the first layer
CS-v5	variant with one row of external angle braces
CS-v6	variant of CS-v3 with increased number of crossovers
CS-v7	variant of CS-v3 with reduced effective twist density

Table B.1 Overview of corner designs.

B.1 Strand diagrams

The designs were prepared with caDNAno [33]. The designs of the Twist-Tower variants, the 126 helix-bundle, the dumbbell variants, and the rectangle variants are reported in Kube, Kohler, Feigl et al. (2020) [74].

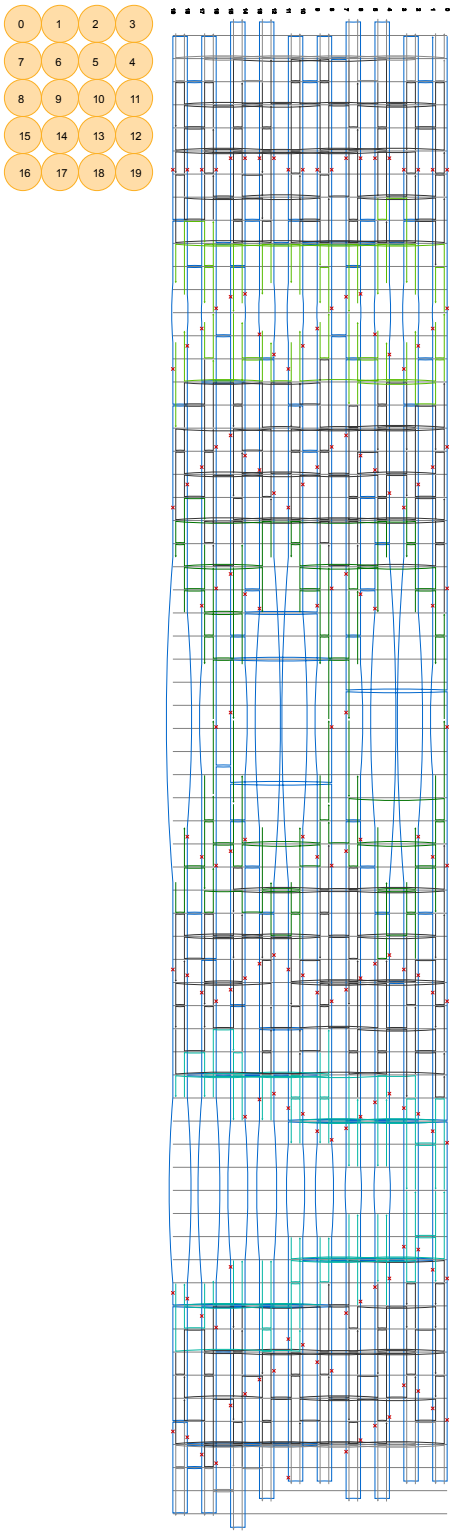

Figure B.1 Strand diagram of CS-v1.

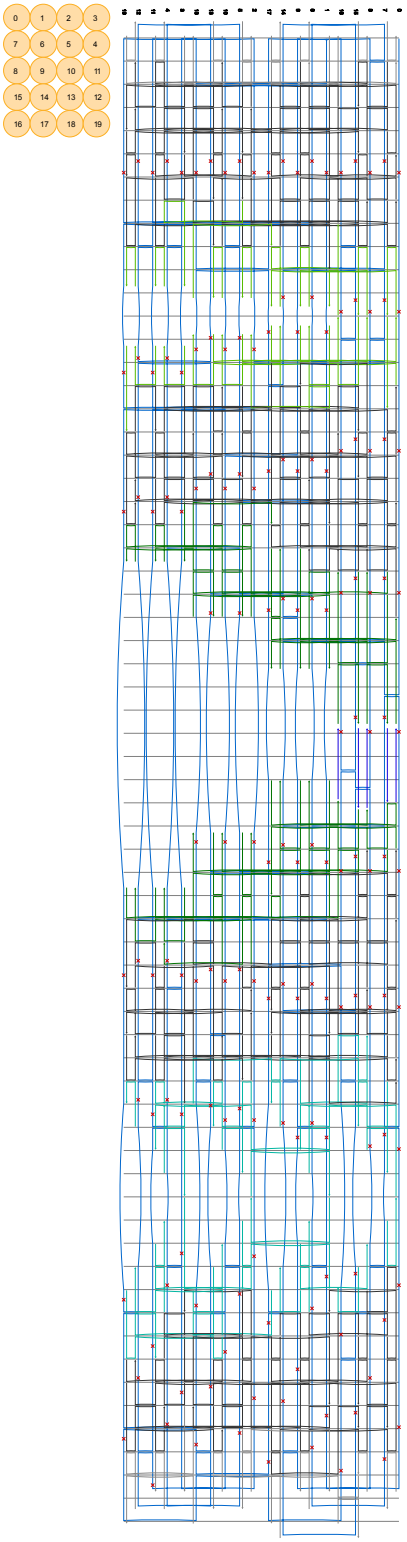

Figure B.2 Strand diagram of CS-v1-out1ss.

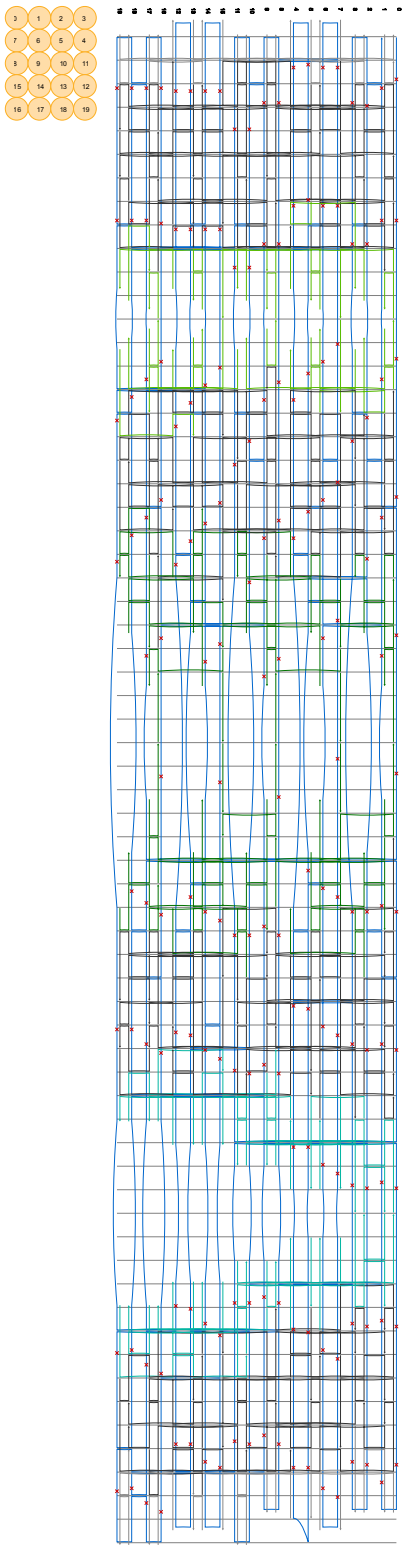

Figure B.3 Strand diagram of CS-v2.

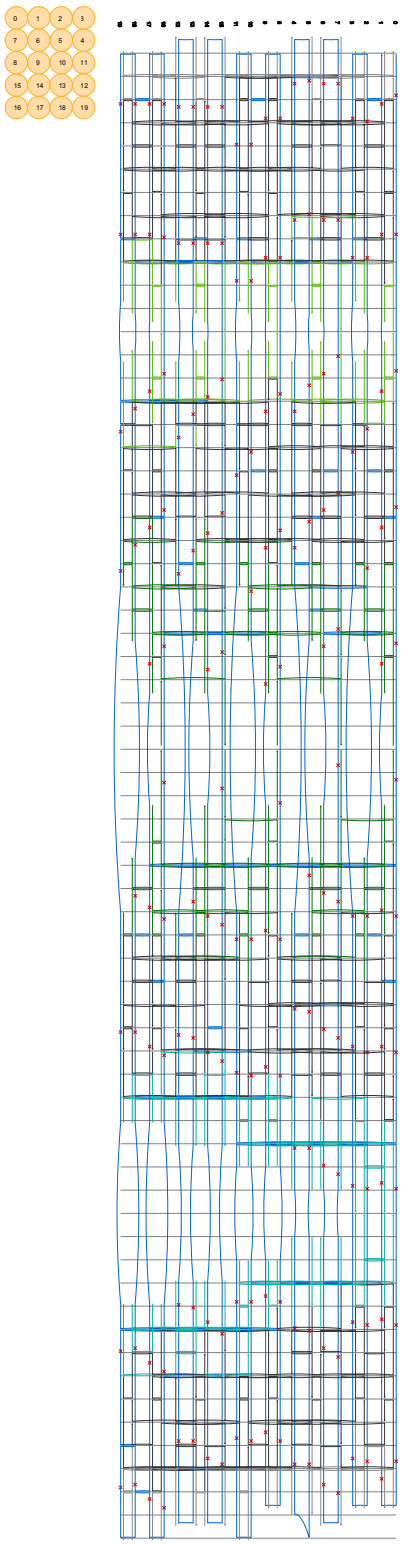

Figure B.4 Strand diagram of CS-v2-out1ss.

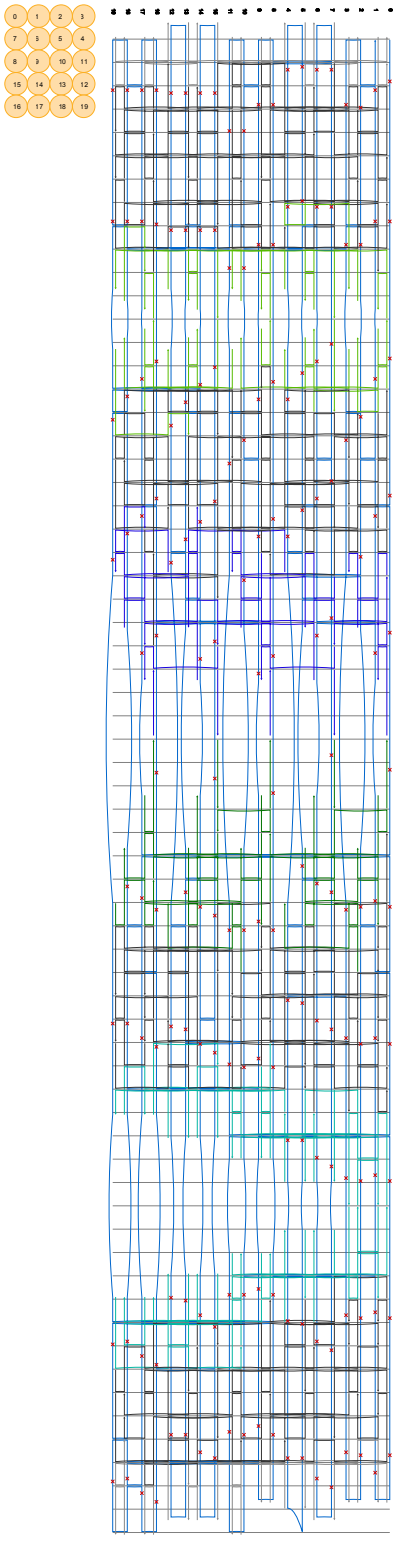

Figure B.5 Strand diagram of CS-v2-1ss.

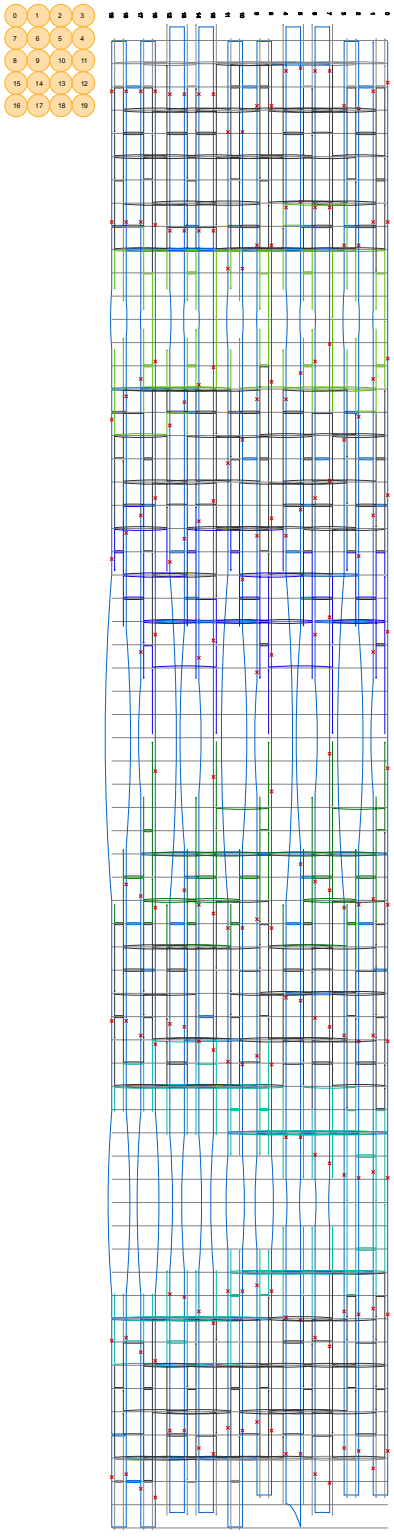

Figure B.6 Strand diagram of a variant of CS-v2-2ss.

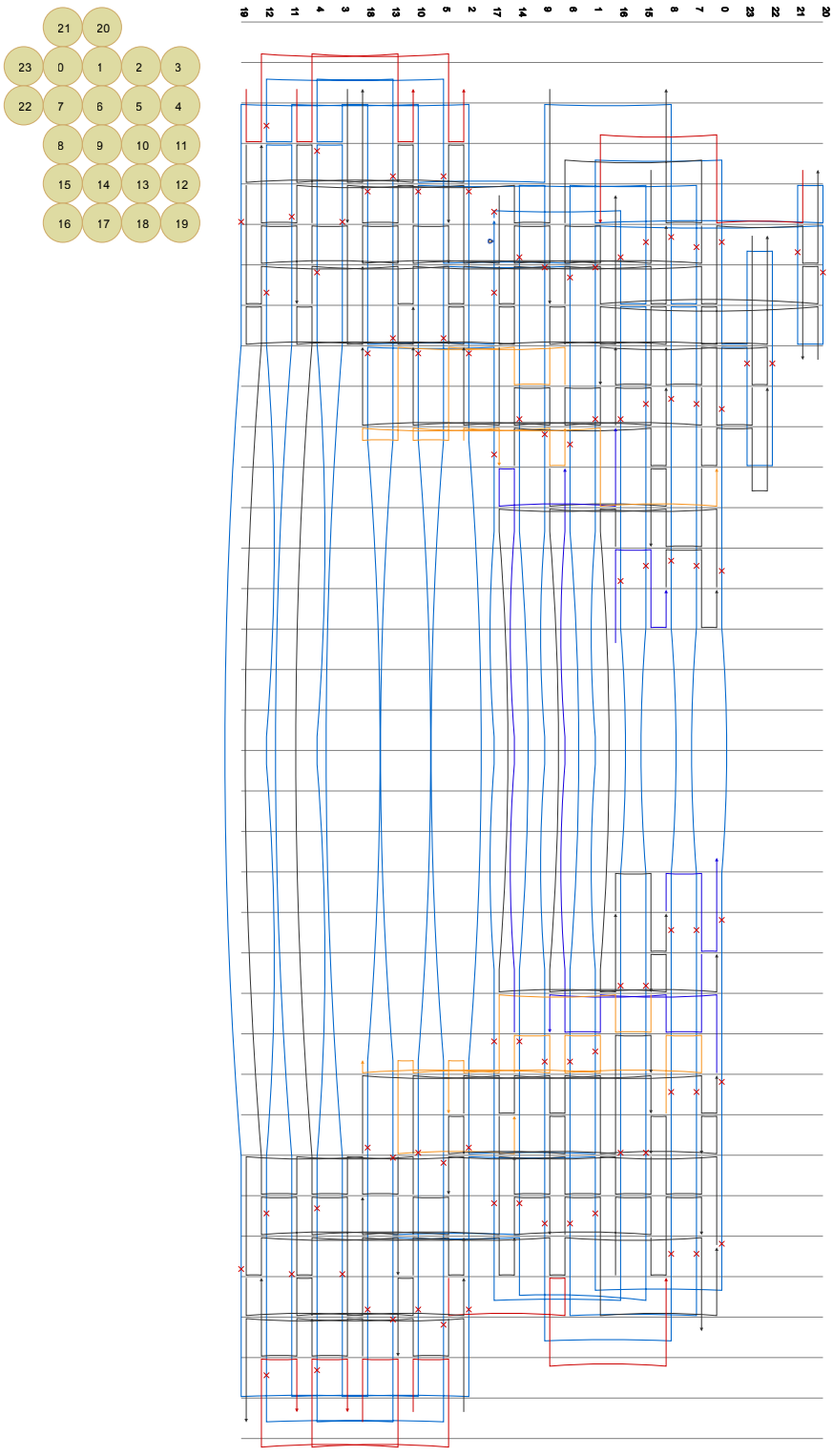

Figure B.7 Strand diagram of CS-v3.

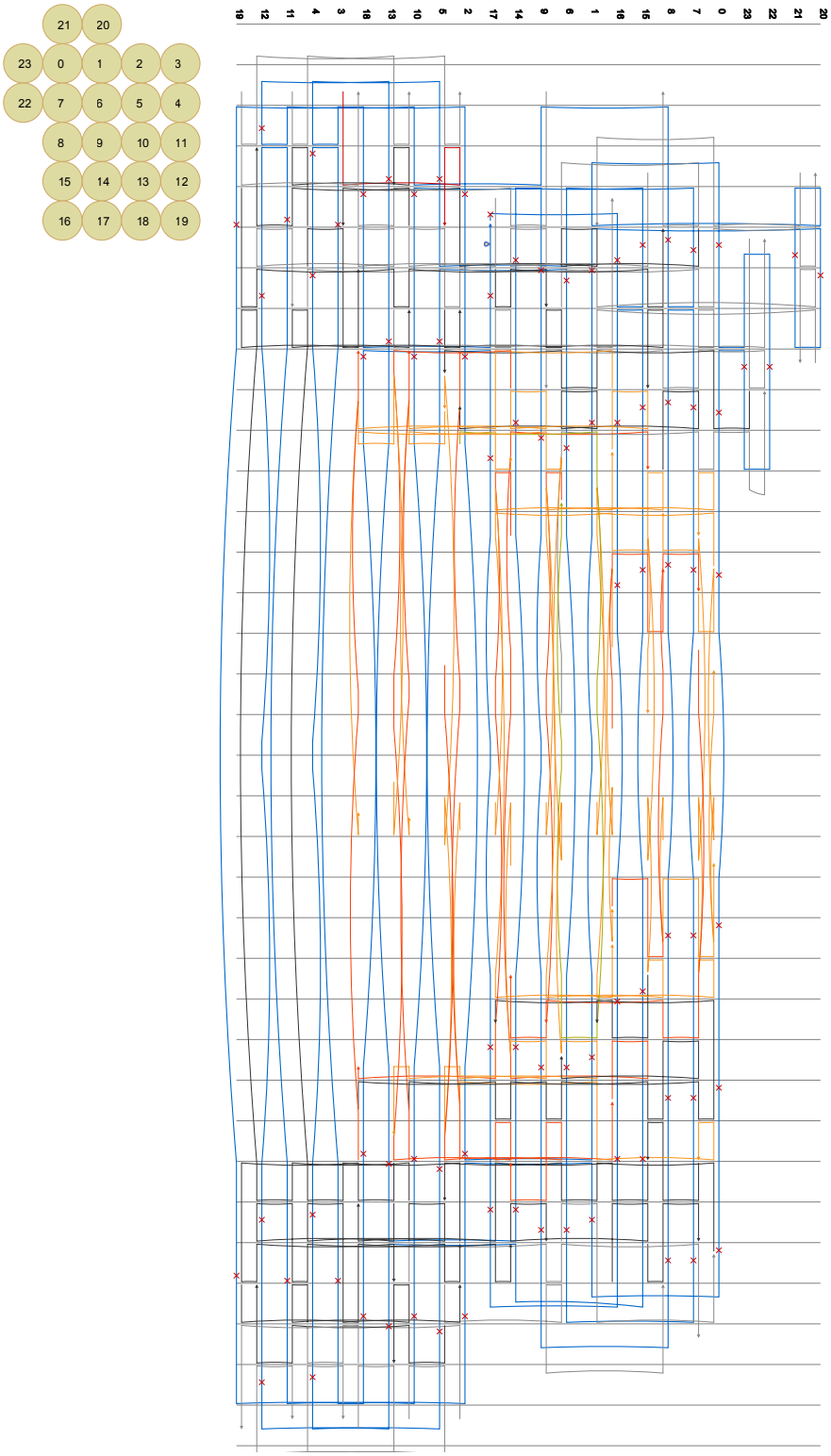

Figure B.8 Strand diagram of CS-v4.

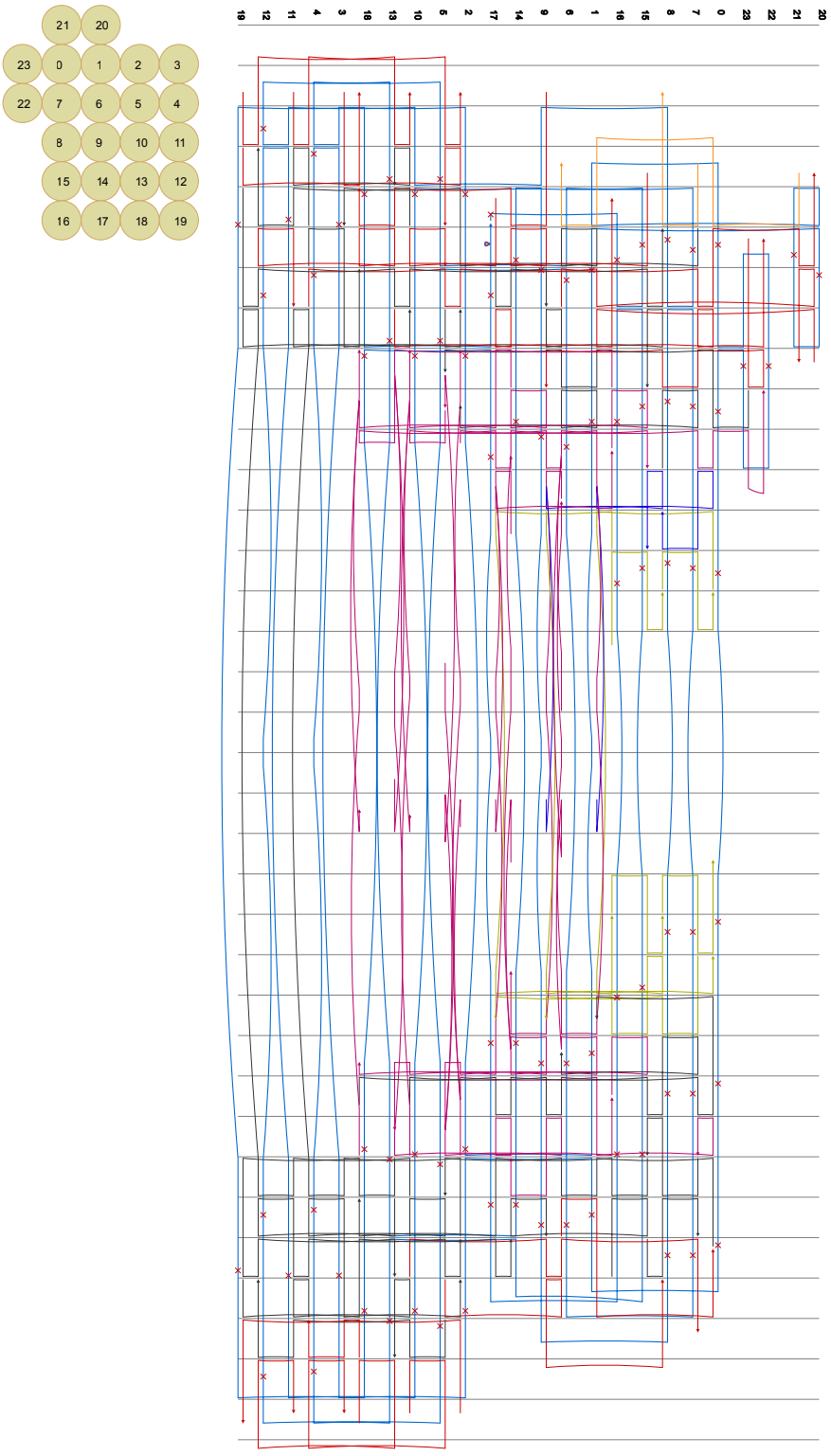

Figure B.9 Strand diagram of CS-v4-2.

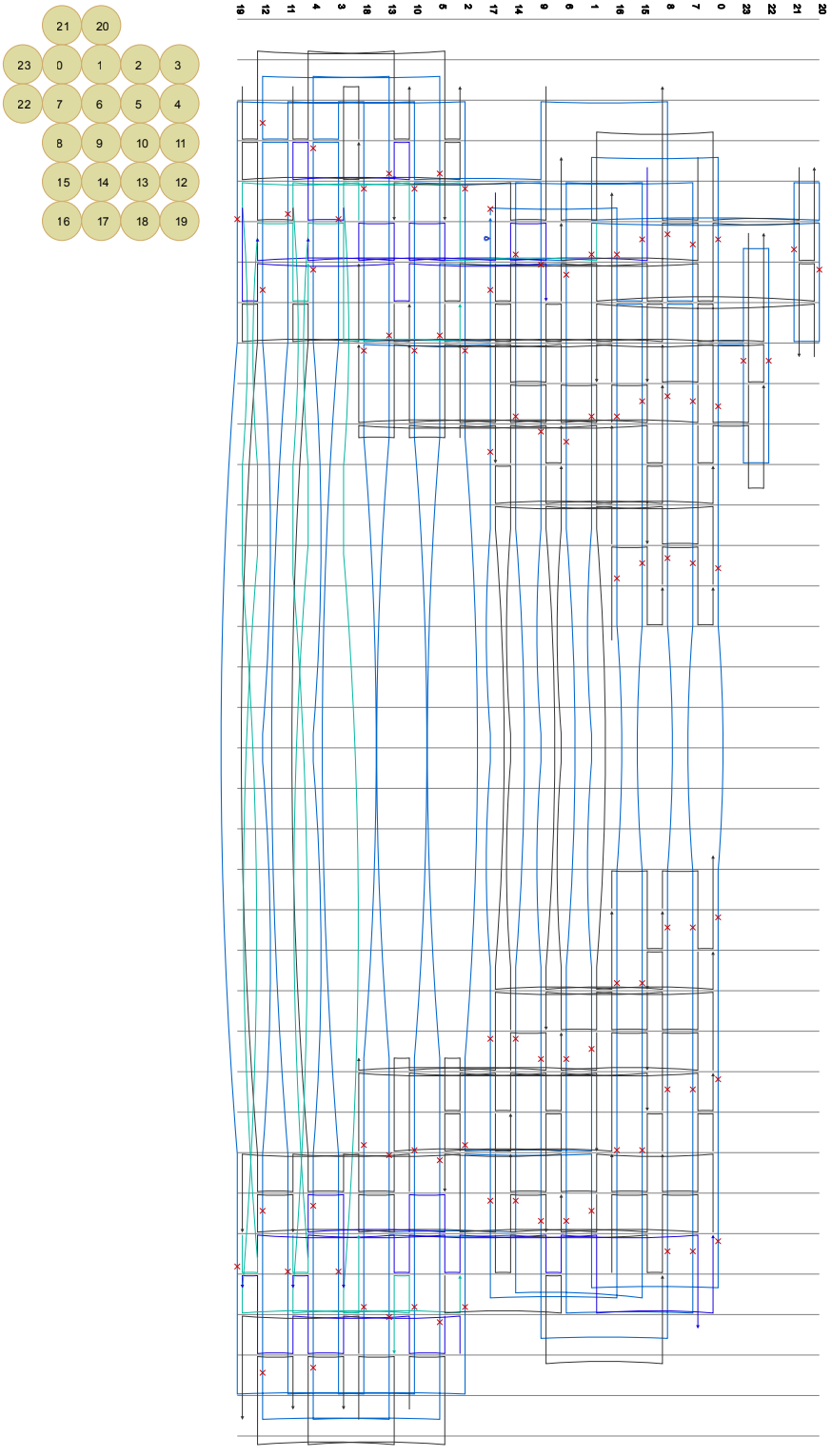

Figure B.10 Strand diagram of CS-v5.

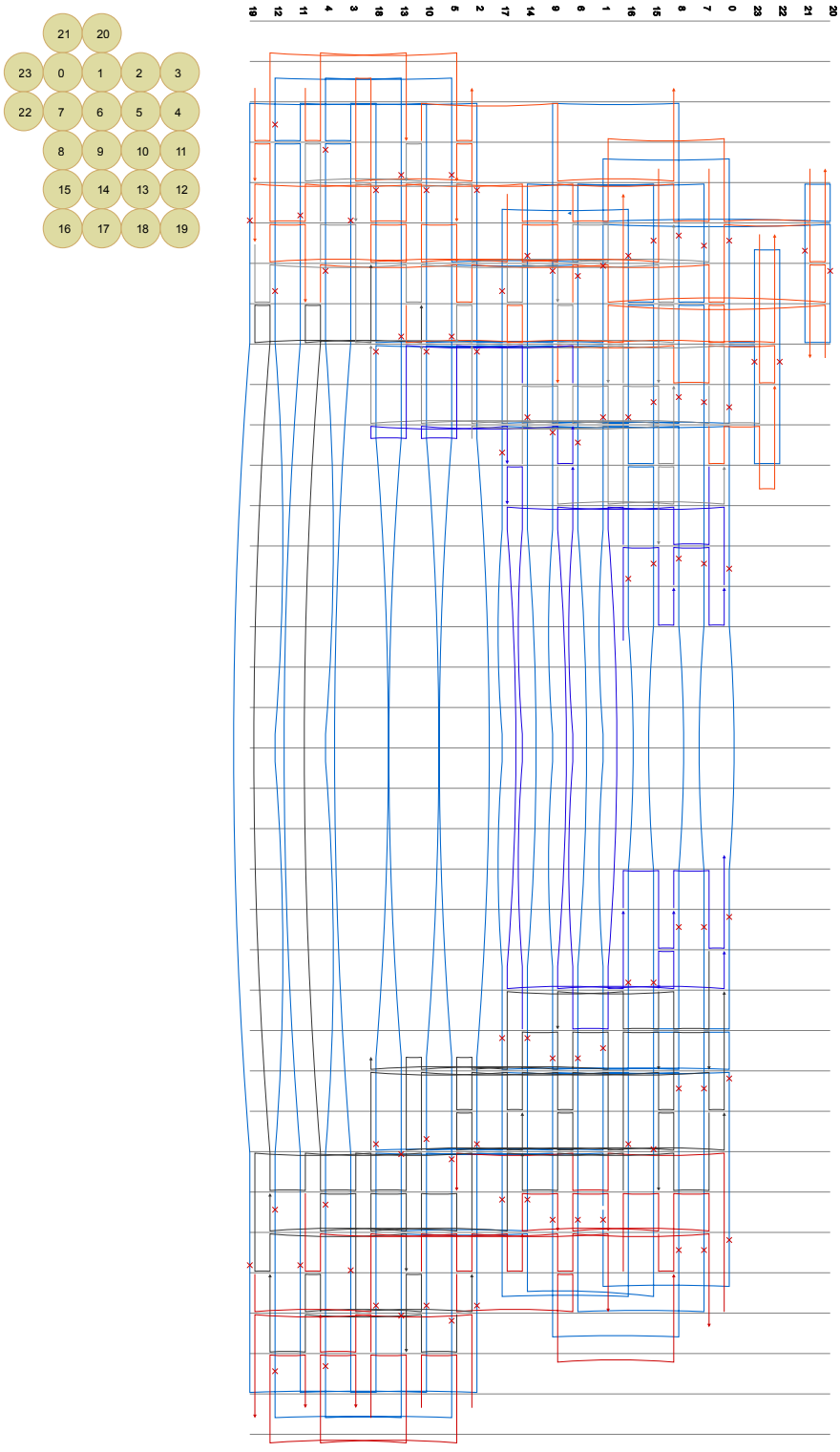

Figure B.11 Strand diagram of CS-v6.

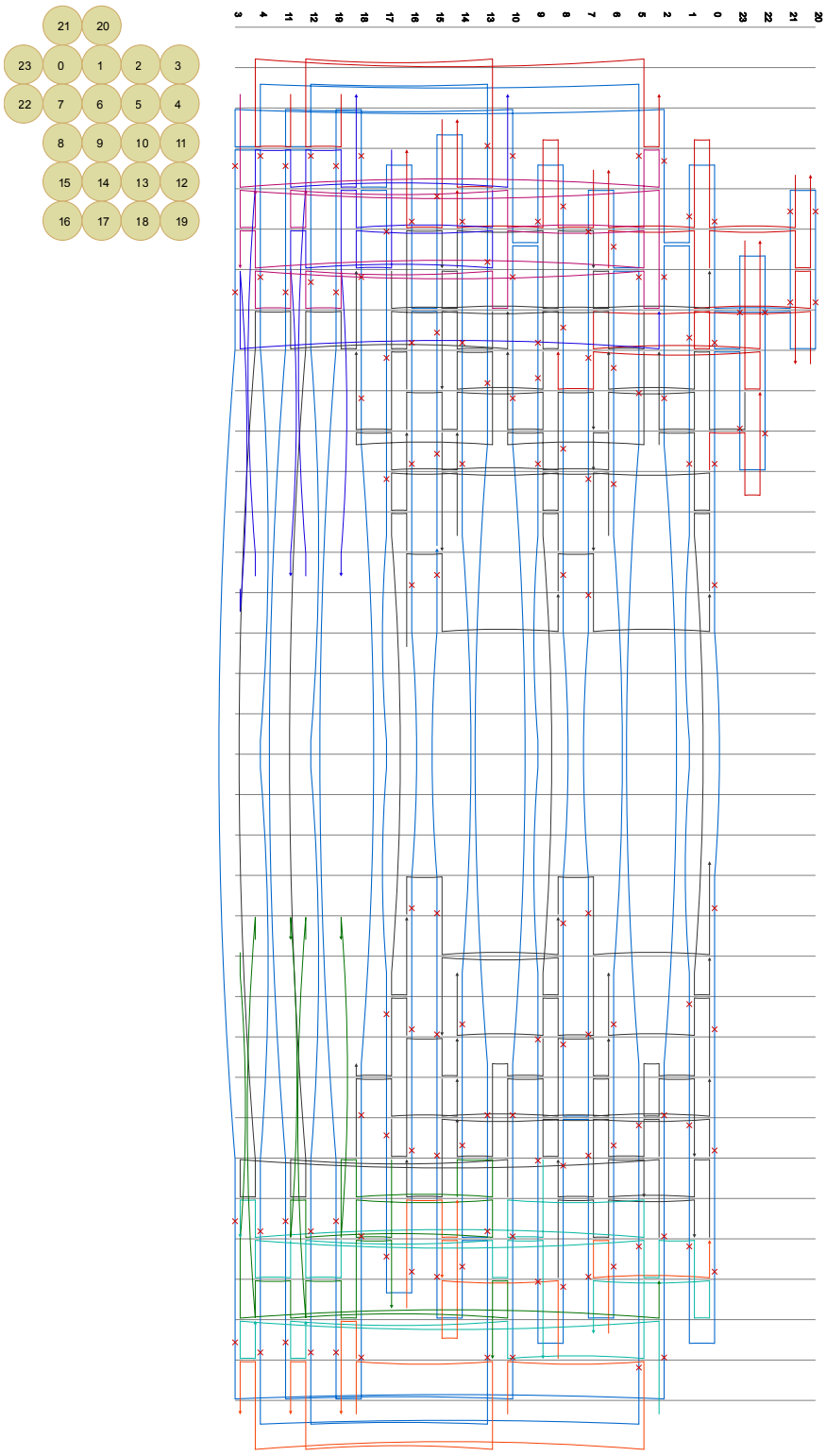

Figure B.12 Strand diagram of CS-v7.

B.2 Sequences

oligoname	sequence
core_1	GTCCACTACGCTGGCAACCGTTGTAGCAATATCTGACC
core_2	AATTACCTATAAATCAATATATGTCATTTTCG
core_3	GCTGAGGCTTGCAGGCGAGCCAGAATACGTA
core_4	ACCTACATTTTGACGCGGAGCTAAAGGCCACC
core_5	GTTTAGACGAATAAGAATTACGAGGCATAGTAAGAGCAATAAAAA
core_6	ATCATTACCGCGCCCATTATTACCAAGAACGACTAACGGATTGTGAA
core_7	AAACGATTAGCTACAACACAAGAAAACTAAAGTACGGTGT
core_8	ACCCTCATGGGTAAAGTTTCTTAAAGTTAGCGTAACGATC
core_9	CCTAAAGGGTTAGAATCAGAGCGTCAATCGCCAGTCACGTAACC
core_10	AGTTGCGCCACCCTCAGAGCCACCCAGAAGATTAAAAATA
core_11	TCGGAACGGGAAAGAGTAAAAGAGTCTG
core_12	TCTGAAATGGATTATTTCTGGCCTATAACGTG
core_13	TTTAGTTATTCTGTAAATCGTCGCCGTAATC
core_14	CATGGTCACATGAAAGCTTTGACCTCCATTAAACGGGTAA
core_15	TTTAATTCCAAATGGTCAATAACCTGTTTAGCCATGTTTT
core_16	TCAGAAACTGTTGGGAAGGGCGTGGCGAAA
core_17	AGTAGCGACAGAATCATTCATCGGGAGTGAATCTGATAGCCGGGGTCA
core_18	AGCCCCAAAAACAGGAGTTAATATATTAGTAAAGCGAAAGCGTGGCGA
core_19	GGTACCGATAAAGCCTGGGGTGCCTAATGAGT
core_20	TAAAACGAATTAGGATTAGCGGGGCCACCAGATACTTTTGTCTGAATA
core_21	AGCAGCACTATTAATTAATTTTCCGAGAAAAGAAGATGACAATAA
core_22	AAGTTGGGTTCTCCGTGGTGAAGGTTGTGAGAGTGTAGATTAACAACC
core_23	TTCGTAATAGCTAAATGGAGGTTGAGGCAGGTCAAAAGAA
core_24	ACGCCAGCATCGGTGCGAGGGGACTAAGAATATACATTGGCAGATTCA
core_25	CCGTACTCACAAAGAAAAATCACCTTTCATAATCAAAATCAGGCCGGA
core_26	AATTCGCATTAAATTGTTGATAATGAAAGCGGACGACAGGTGCATCT
core_27	TATTAAGAGGCTGAGAATTGACACGGTTGT
core_28	AGGCGATTCATTCAGGGATCGCACACAGAGATAGAACCCTCTTCTTTG
core_29	TTGTCGTCTATCAGCTTGCTTTCGAGGTGAAGTTTCTTT
core_30	CGTTAGTAGGTTTGCCGTCACTGCGCGCCTGTAGACAGTC
core_31	CTACCATATCAAAATAAATCCTCATTTACCGGATACAGG
core_32	ACCAAAAACATTATGAGATCCCCGAGAGAAGGAAGAGGCA
core_33	ATAAGAGGTTCATTCGCGCTAATATCAGAG
core_34	AAATTAATGCCGGAGAGGGTAGCTTGCGCGAA
core_35	TTTGTTAAACGTGGACTCCAACGTCAAAGGGCGGGAAGAATAACATCA
core_36	AACAATATTAAGCAAAGCAAAGCGCCATTCGC
core_37	TATTTAAATTGTAAACAGATTGTATCTGGCCATCCAGCCA
core_38	CCTAAAACAATCGTTACGGTGCCGTCCGAAATCGGCAAAA
core_39	ACATTTCGGAGCTTCAAAGCGAACGAATCCCC
core_40	TATATTTCCGAAAGACTTCAAATAAGATTAA
core_41	ATACGAGCCGGAAGCAACACTCAT
core_42	CAGAGCCGTTTTGCTCTCCGTGAGTCACATTAATTGCGT
core_43	AATGACCAGCTTTAAACAGTTCAGATCGCGTTTAATTGCAAATATGC
core_44	TTTGTTAAGCAAATTAAGTGTAGCGATTTAGAGCTTGACG
core_45	GTTCAGCAATCGCCATAGCTGATGTCATAGCCCCCTTA
core_46	GGACAGATGAACGGTGTTACCTTAACCAACGCTTATTTA
core_47	TACAGACCCCTTTTGAAGCAAACTAGATTTAGTTTGACCATTAGATCTGGAAGT
core_48	TATCGGCTCACGGAGGGGGATGTGCTGCA
core_49	TGGTCTGGGGGCCTCTAATCATATGTACCCCG
core_50	ACCTATTATTCTGAAATAGCTGTTCACACAAC
core_51	GAGCTAACCCTCCTCACAGTTGAGCCCTGTAAACCACCACAAGAAATT
core_52	TAATGGAAATTATCATTTTGCGGAAGGAGGTTAGCGCAGTCCAGCAGG
core_53	ACCTTTTTTGCCATCTATCAATATGATATTCAGACGATCCCCCTTACA
core_54	TTTGAATTTCCTTGAAAACGTCACCAATGAAACCATCGATTTAGCGTT
core_55	AGTTGCAGCAAGCGGTCCACGCTAATGAATTGTGTATCA
core_56	TTTCAGGTATTATACTCCGGGAGAGCCTTTA
core_57	ATATTCACAAACAAATTATTTGCATTTTGAT
core_58	ATGGAAGGCACGGAATCATATAAAAGAAACGCTACATAAAAGGTTATC
core_59	GACAAGAACCGAACTGACCAACTTCTTAGAGC
core_60	CATCAAGACCAAATCAATAACCCTTAAATCAAAAATCAGAAAACGAG
core_61	GTTTTTATAGGGACATATGGAAATCGTCGGATTCTCCGTG
core_62	TAATAAGATAGGCAGAGGCATTTTAAAAATCT
core_63	GCGGATGGTGAAGACTCAAATCGTTTACCAGACGACG
core_64	TCATTTTTTGAATCTTTGCGATTTATCGGCTGACCAAGTACCGCACT
core_65	AAAAGAGACGCAGAAACGTACAGCGCCAGTTT
core_66	CGAAAATCCTGTTTGATAAAGTTCTGGTGTGCTCGTC
core_67	TTGCCGTTAACCTTGCCCGTAAAAGCGAATTATTCATTTCCCGAACGA
core_68	TGGTGGTGTGCCCCCTGCATCAACCGTTCTGAGTAACACAGTAC
core_69	TTCCAGTAACCGTCAAAAGACACGTTAGAAC
core_70	TACATGCCGTAAAACAGAAATACAGAGCCG
core_71	AGTGTACTACGCAGTATGTTAGCAAGAAAAG
core_72	ACACTATCACGTAACAAAGCTGCTATAGCAAG
core_73	CATTCAGTAGGCGCATCCAAAATAGTCATAAATATTCATTCAGACCGG
core_74	GAAAGGAAGTCGAGGTCCGATTAAAGGGATTTAAACGCTCTACCGCCA
core_75	CCGGCGAAGAGCGGGCGCTAGGGTTAAAGA
core_76	AGGCTGGCTGACCTTACGTTAACAAATCAG
core_77	CCAGCTTTCATCAACATTAAATGCTCACCG
core_78	ACCTTGCTGAACCTCAACGCCAACCGGCTACA
core_79	AGGAAGTTCCCAGCGATTATACCACACAATTC
core_80	TCGTAGGAATATAGAAGGCTTATCTTCATTACGTAATCTTT
core_81	CCTGTTTAGTATCATAAATATCAAATTAAGACGGAATACC
core_82	TTGAGTTAAGCCCAATCCTTTACA
core_83	CGGATAACTGAGCGAGGGGCGCATCACGACCAGTAATAAA
core_84	TGGTCAGTTAATTACTAACGTAGAAAATACA
core_85	TGGCAAATTAAATATCTTTAGGAGCACTAACTGGCATGACCCTCAA
core_86	AATCAGTGACAGGAGGGCCGTAAAGCACTAAA
core_87	AATTCGCGCGTGGCACGAACGCCAATCAGCTCCCAGTTTGGAACAAGA
core_88	TCAAAAATGCTTTGACGGTCACGCTGCGCGTA
core_89	GAGCAAAACTTTTTCTAAATTTAATGGTTTGAAATACCCGGAGAAA
core_90	CTGGTAATTTTCAGGGCAAACTACACAGCTTGATACCGAT
core_91	ATGAAACAAACGTTATTAATTTTATAAACATGAACCGCCGACAATG
core_92	GCGAAAGATGCCACAAAGAATACACTAAATAAAGTGGCTCGAA
core_93	ACAGCATCGGAACGAGCAACTAATAAAGCATCTCAATATC
core_94	GGTAGCAAATGTAATTGAATATAAAGTACCGACAAAAGGT
core_95	ATTGAGGAGGTGGCAAAATAAGATAAACACCGGAATCA
core_96	TGCTATTTTGCACCCTTTTGTTTGAGAGAAT
core_97	AGATTAGAGCCGTCACCGCCAGCCTCCTCA
core_98	CTTTGAATACCAAGTTAGCATCGAGCCACCAG
core_99	TAAAACGAGGTATTAATCTTTCCTTATCATTCCAGCCATA
core_100	AAAAGTTTAAAACAGACGGATTCGCCTGATTGTTCTGACCAAATATAT
core_101	TACCAGTCCCGGAATGATAGCTCCTCAGGAACTGCGCAA
core_102	CAACAGTAGCCAGCAGCAAATGGAGTTAAA
core_103	AGCGCATTCCCAATCCAAATAAGAATCAATATAAGAACTAAAAATCT
core_104	AACATAAAAACAGGGAAGATAACCTTTTATCC
core_105	GCCATGTTGAAACAATCGGCGAAACCGCCAGCTCCTGTAGTCAGCAGC
core_106	GGTGAGGCGGTCAGTCACCCTCATAGTACCGTATCGGTTTTTCCAGA
core_107	TCACGTTGGATAGACTGGAGCCGCCACGGGAA

oligoname	sequence
135deg_1	CAGAGCACCAGACTGTAGCGCGTTAGTTTGCC
135deg_2	TGGTGCCATCCCCACAGTTGGGCGGTTGT
135deg_3	TCCCTTATCACAGACAAGATGCCGCCCTGCGGTTGCAGGCGCTTTCGCA
135deg_4	GCTGGAGGTGTCCACAAAATCGTCGG
135deg_5	AGCATGTCAACGTCAGCTGGCAGCCTCCGGC
135deg_6	GGTAATCGTAAAACTTTTTTGAATGGCT
135deg_7	GTACATCGACATAAAAAAATCATTTCATC
135deg_8	GTGTTGTTATTTTTTAGAGTCTGGAGCAAAC
135deg_9	CCGAGATAGGGTTGAACCACCACACCCG
135deg_10	TAGGAACCCATGTAGCAACCAGCTTACG
135deg_11	AAGAGAATGAGATCTAGGTTACCTGCAGCCAG
135deg_12	AGGGCGCGTACTATGGTTGCTTTGCGATATCGAGCCGGG
135deg_13	CTTTAGTGATAATTTCTGCTCATTTGCAGCGGAT
135deg_14	ATTAGTCTTTAAATTTTTGACGATGAAC
135deg_15	ACGGCATCGCCCTCATAACGCCTGTAGCATTCCGCCGCTAC
135deg_16	TCCATCACCTTTCCTCGAGCCCCCGAGCACGTCCGTAACACTGAGT
135deg_17	TCACTGTTGCAAAGGCTATCAG
135deg_18	AACGGAACGTGCCGGGAAGGGTAAAGTT
135deg_19	GGCAGCACCCGCGGTCCGTTTT
135deg_20	TTCGTCACCAGTAATAGCAAGCCCAA
135deg_21	AAACGATGCTGATTTAGCGTATCCTCAT
135deg_22	CCGGCAAAGCGCAGAGAAAGCCGCACAGGCGGC
135deg_23	GTCATTGCCTGAACCAATAGAGACAATA
135deg_24	TTCGTCTCGTCGCGTGGTGCCAAACTTAACTTGTAGTCGCTATT
135deg_25	CCGCGCTTAATGAAATCAAAAGAATTAGC
135deg_26	CTCAATCCGCCGGCGCGAACCGCAAGAATGCCAAC
90deg_1	GCTATCTTACCGAAGCACACGGAGATTTGTA
90deg_2	AACCGAGGAGAAAAGTAAGCAGAT
90deg_3	ACAAATTGCCGTTTTTATTTTCACATCGAGATTGGGAAGGGCTCAT
90deg_4	CTGACTATAAAGCGCAGTCTCTGAATTAAAGC
90deg_5	CAGACGATTAATGCCCAAGCAATATATAGTCAGAAGCAAA
90deg_6	AGCCGAACAAAGTTACCAAGAAATGTGTCGAAGCTCAA
90deg_7	CAACGCTCAACAGTATGCGTTAT
90deg_8	TATACCAGTTGAAGCCTAATTTACCTTACCAGTATAAAGC
90deg_9	CATGTTACTTAGCCGGACAAAGTCCTTTTTAAAAGACTAAAGTAATCGCCATA
90deg_10	GCGAGGCGTCCTTATTGGTAATAATGGCCTTGCAGAATGGAAGCCTCAGAGCATAA
90deg_11	GCCCGTATAAACAGTGTTTTAAC
90deg_12	CGACTTGCGGGAGGTTTAAGAAC
90deg_13	CAATAAATCATACAGGTCATTTGGGGCGCGAGCTGAAAAG
90deg_14	CGCAGACGAATCCGCGACCTGCTC
90deg_15	TAAGGGAATGCCTTGAGTAACAGT
90deg_16	GCGGATTGCATCAAAGTCTTTTACC
90deg_17	TCATCGCCTGATAAATCAATGAAATAGCAATA
90deg_18	TTTTCATGGAGGCTTTGAGGACTAAACGCATTGAGAAAACAAGAA
90deg_19	TGAATATAATGCTGTGTCAATCAGAGGAAGCCAAGGCAA
90deg_20	GGGGTCAGCCGGATACGGTATTCTCAGGACGACAAGCAATGCAGTAGAAACC
90deg_21	CAATAGATAAGTCCTGTTCTGTCCAGACGACGACAATAAA
90deg_22	CAACATGTTCAGCTAATGCAGAAAATAGCAGAATAAGAGAGATTAGT
90deg_23	AAATAATACGCGCCTGTTTATCAA
90deg_24	TTTAACAGGGCTTAAATAATAACTTTTAGCGAACCTCC
90deg_25	AGAATTAAGTAGCATTAACATC
90deg_26	TCCTGTGTGAAATTGTGCAAAATTCCTGCCTAAACGAGG
90deg_27	GTGGCATCAATTCTACTAATAGTTATCCGCTAGCGCGAATTTCGGA
90deg_28	AACGTCAAAAATGAATCCCATCCTTAAATCACAGAAGGA
45deg_1	AGTTTCAGCGGAGTGACTGCCGCTATTGGGCTGCCTGTTTTTCAACG
45deg_2	TAAAATAAAAGGGCGACATTCAACCGA
45deg_3	TTGAGGGAGGGAAGGTAAATAGCAACAGCTGAATGAATCGG
45deg_4	ATAACCGATATATAATAATGCGGATAAATCGTCACCCTCAGCAGGCCGCT
45deg_5	CATTTGGGAATTAGAGCCAGCTTGACGGAAATTATTCATTA
45deg_6	TAGTGAATTTATCAAACATATGGTT
45deg_7	ACCGGAACCAGAGCCACCACCGGAATGTGTAAAAATCACGAAGAGTCAA
45deg_8	AGGGTAGAACCGCATTAACACTTTGCCCGAACATCAAGAAAACAAAATCCAATGATAA
45deg_9	ACAACAACCATCGCCTTTAATTGCCACCCTCTGATATAATTAAATCCCGCCT
45deg_10	ACCCTCATCCTGATAGAAAATTATCATAGGTCTGAGATTATATAACTATA
45deg_11	TACCAGCGCCGTCACCGACTTGAGC
45deg_12	CTTCGCGTTCTGCCAAGGAACAGTTGAAAATCTCC
45deg_13	AAGGTGAATTATCACCAAAGACTTTTAGA
45deg_14	GTGGTGCTGCGGCCAGTGAGACGGGGTAAAGAGCCGCCACCC
45deg_15	GCACTCTCGGAATAGTTCTGTATGGCTCCAAAGGAGCCCACGC
45deg_16	GCAACAGTGCCAGGATTTAAGATGAATGCGTAGATTTTAACCAAGTTTATTTGTCAC
45deg_17	TTATCAGATGATGGTTAACGTCGAAGTATT
45deg_18	TTTTCACCAGAATGCGGCGGGCCGT
45deg_19	ATAGATAATACATTTGACGCTGAGTGAAAGGAATACAGTAACA
45deg_20	AATTCGACGAATTATCCCTCAGATTCAAAAGGGTGAGAAAGGCCGG
45deg_21	TGTAAATGAGATTAACATCATAACATTTAACAATTTCA
45deg_22	GTACCTTTTACATGACCGTGTCGCAAGACAAAGAACGCCTTAGAA
45deg_23	ACCACCAGAAGGAGCGAACTCGTAGTATAGCCTTTCACG
45deg_24	TCAGAACCGCCACCCTCAAGGA
45deg_25	AAAAAAAAGGGATTTTGCTAAACCCTGAGAG
45deg_26	CAGAGCCACAATATAATATATTTTAAATGCA
45deg_27	GTCATACCGGGGGTAGTACCAGTTTTTCACACTAAAGGAATTGCGA
45deg_28	TGCGCTCAGAATAGAAGCACGCGGCCAGGGTGGTTTTTC
45deg_29	TTTCCAGTCGGGAAACCTGTCGTGCC
45deg_30	AGCTGCATTATTGCCCTTCACCGCCTGGCAACTTTCAAC
45deg_31	ATGCCTGAGTAACCGCCTGACGCTGACAGTAGCACCATTACCATTAGCA
45deg_32	TACGAAGGCACCAACCATTCGGTCTTTGCGGGGTGCCGTCGAG
45deg_33	AACATAGCGATAGCTTCTGATGCAAATTAATTTTCCTGA
45deg_34	CCAACGCGCGGGGAGAGGCGGTTTGCG
45deg_35	ATAAGGCGTTATCCGGCTTAGGTTGGGGACTACCT
45deg_36	AATCAATTGTTTGGCAATTCATCCACCCTAGACTTTACAAAC
PolyT_1	TTTTAACAGGAATAGACAGGAACGGTTTT
PolyT_2	TTTTATTTAGGAATACCACAAGATTCATCAGTTGAGTTTT
PolyT_3	TTTTCCAGTCACGCACCGCTTCTGTTTT
PolyT_4	TTTTTTCAACTTTAATCTGACGAGA
PolyT_5	TTTTCAGAGGGGGTAATAGTAAAATAACACCAGAACTTTT
PolyT_6	TTTTAAACTATCGGCCTGTCTATCATTTT
PolyT_7	TTTTGATTGACCGTAATGCCATTGCTTTT
PolyT_8	TTTTACAAAGTCAGAGGCCTCTTCCAGAGCCTAATTTTT
PolyT_9	TCAGAGGTAAAACGACGGCCAGTGTTTT
PolyT_10	TTTTCCAAGCTTGGAACAAACGGCGTTTT
PolyT_11	TTTTGAGTAGTAAATTGGGCTTGAGGTAGAAGCTTGCCCAACAACA
PolyT_12	TTTTTGCCGGAAACCAGTGCTGGTATTTT
PolyT_13	TTTTTACGCCAGAATCCATCACCCATTTT
PolyT_14	TAACGAGGTAATTGACATATAACAGTTGATTCCCAATTTT
PolyT_15	TTTTATATCCAGAGTAGAAGAACTCTTTT
PolyT_16	TTTTTTCTGCGAACGAGTCCAACAGGTCAGGATTATTTT
PolyT_17	TTTTGAGAGTACCTTTAATTGCTTGGATAGCGTCCATTTT
PolyT_18	CTTTTGCACCAAAAGGTTCAACTAATGCAGATTTTT
PolyT_19	TAGACGGAGAATTAACTGAACACCCTGATTTT
PolyT_20	TTTTATACTGCGGAATCGCGAGAGG
PolyT_21	TTTTAATCAAGTTTTTTGGGCGTGAACCTGAGAAGTCTTGCCTG
PolyT_22	GGGATAGGGCTTTCCGGACGTTGTTAACGCCAGGGTTTTCTTTT
PolyT_23	TTTTTTTGCCAGTTACAAAATAAAAGAGGTTTAATTTTT
PolyT_24	TTTTGGGCGATGGCCCACTAGAAAAACC
PolyT_25	TTTTACATAACGAAAGAAGTTTTGCTTTT

Figure B.13 Sequences of staple oligonucleotides of CS-v1.

oligoname	sequence
core_1	GTCCACTACGCTGGCAACCGTTGTAGCAATATCTGACC
core_2	AATTACCTATAAATCAATATATGTCATTTTCG
core_3	GCTGAGGCTTGCAGGCGAGCCAGAATACGTA
core_4	ACCTACATTTTGACGCGGAGCTAAAGGCCACC
core_5	GTTTAGACGAATAAGAATTACGAGGCATAGTAAGAGCAATAAAAA
core_6	ATCATTACCGCGCCCATTATTACCAAGAACGACTAACGGATTGTGAA
core_7	AAACGATTAGCTACAACACAAGAAAACTAAAGTACGGTGT
core_8	ACCCTCATGGGTAAAGTTTCTTAAAGTTAGCGTAACGATC
core_9	CCTAAAGGGTTAGAATCAGAGCGTCAATCGCCAGTCACGTAACC
core_10	AGTTGCGCCACCCTCAGAGCCACCCAGAAGATTAAAAATA
core_11	TCGGAACGGGAAAGGAGTAAAAGAGTCTG
core_12	TCTGAAATGGATTATTTCTGGCCTATAACGTG
core_13	TTTAGTTATTCTGTAAATCGTCGCCGTAATC
core_14	CATGGTCACATGAAAGCTTTGACCTCCATTAAACGGGTAA
core_15	TTTAATTCCAAATGGTCAATAACCTGTTTAGCCATGTTTT
core_16	TCAGAAACTGTTGGGAAGGCGTGGCGAAA
core_17	AGTAGCGACAGAATCATTCATCGGAGTGAATCTGATAGCCGGGGTCA
core_18	AGCCCCAAAAACAGGAGTTAATATATTAGTAAAGCGAAAGCGTGGCGA
core_19	GGTACCGATAAAGCCTGGGGTGCCTAATGAGT
core_20	TAAAACGAATTAGGATTAGCGGGCCACCAGATACTTTTGTCTGAATA
core_21	AGCAGCACTATTAATTAATTTTCCGAGAAAAGAAGATGACAATAA
core_22	AAGTTGGGTTCTCCGTGGTGAAGTTGTGAGAGTGTAGATTAACAACC
core_23	TTCGTAATAGCTAAATGGAGGTTGAGGCAGGTCAAAAGAA
core_24	ACGCCAGCATCGGTGCGAGGGGACTAAGAATATACATTGGCAGATTCA
core_25	CCGTACTCACAAAGAAAAATCACCTTTCATAATCAAAATCAGGCCGGA
core_26	AATTCGCATTAAATTGTTGATAATGAAAGCGGACGACAGGTGCATCT
core_27	TATTAAGAGGCTGAGAATTGACACGGTTGT
core_28	AGGCGATTCATTCAGGGATCGCACACAGAGATAGAACCCTCTTCTTTG
core_29	TTGTCGTCTATCAGCTTGCTTTCGAGGTGAAGTTTCTTT
core_30	CGTTAGTAGGTTTGCCGTCACTGCGCGCCTGTAGACAGTC
core_31	CTACCATATCAAAATAAATCCTCATTTACCGGATACAGG
core_32	ACCAAAAACATTATGAGATCCCGAGAGAGGAAGAGGCA
core_33	ATAAGAGGTTCATTCGCGCTAATATCAGAG
core_34	AAATTAATGCCGGAGAGGGTAGCTTGCGCGAA
core_35	TTTGTTAAACGTGGACTCCAACGTCAAAGGCGGGAAGAATAACATCA
core_36	AACAATATTAAGCAAAGCAAAGCGCCATTCGC
core_37	TATTTAAATTGTAAACAGATTGTATCTGGCCATCCAGCCA
core_38	CCTAAAACAATCGTTACGGTGCCGTCCGAAATCGGCAAAA
core_39	ACATTTCGGAGCTTCAAAGCGAACGAATCCCC
core_40	TATATTTCCGAAAGACTTCAAATAAGATTAA
core_41	ATACGAGCCGGAAGCAACACTCAT
core_42	CAGAGCCGTTTTGCTCTCCGTGAGTCACATTAATTGCGT
core_43	AATGACCAGCTTTAAACAGTTCAGATCGCGTTTAATTGCAAATATGC
core_44	TTTGTTAAGCAAATTAAGTGTAGCGATTTAGAGCTTGACG
core_45	GTTCAGCAATCGCCATAGCTGATGTCATAGCCCCCTTA
core_46	GGACAGATGAACGGTGTTACCTTAACCAACGCCTTATTTA
core_47	TACAGACCCCTTTTGAAGCAAACTAGATTTAGTTTGACCATTAGATCTGGAAGT
core_48	TATCGGCTCACGGAGGGGGATGTGCTGCA
core_49	TGGTCTGGGGGCCTCTAATCATATGTACCCCG
core_50	ACCTATTATTCTGAAATAGCTGTTCACACAAC
core_51	GAGCTAACCCTCCTCACAGTTGAGCCCTGTAAACCACCACAAGAAATT
core_52	TAATGGAAATTATCATTTTGCGGAAGGAGGTTAGCGCAGTCCAGCAGG
core_53	ACCTTTTTTGCCATCTATCAATATGATATTCAGACGATCCCCCTTACA
core_54	TTTGAATTTCCTTGAAAACGTCACCAATGAAACCATCGATTTAGCGTT
core_55	AGTTGCAGCAAGCGGTCCACGCTAATGAATTGTGTATCA
core_56	TTTCAGGTATTATACTCGGGAGAAGCCTTTA
core_57	ATATTCACAAACAAATTATTTGCATTTTGAT
core_58	ATGGAAGGCACGGAATCATATAAAAGAAACGCTACATAAAAGGTTATC
core_59	GACAAGAACCGAACTGACCAACTTCTTAGAGC
core_60	CATCAAGACCAAATCAATAACCCTTAAATCAAAAATCAGAAAACGAG
core_61	GTTTTTATAGGGACATATGGAAATCGTCGGATTCTCCGTG
core_62	TAATAAGATAGGCAGAGGCATTTTAAAATCT
core_63	GCGGATGGTGAAAGACTCAAATCGTTTACCAGACGACG
core_64	TCATTTTTTGAATCTTTGCGATTTATCGGCTGACCAAGTACCGCACT
core_65	AAAAGAGACGCAGAAACGTACAGCGCCAGTTT
core_66	CGAAAATCCTGTTTGATAAAGTTCTGGTGTGCTCGTC
core_67	TTGCCGTTAACCTTGCCCGTAAAAGCGAATTATTCATTTCCGAACGA
core_68	TGGTGGTGTGCCCCCTGCATCAACCGTTCTGAGTAACACAGTAC
core_69	TTCCAGTAAGCGTCAAAAGACACGTTAGAAC
core_70	TACATGGCCGTAAAACAGAAATACAGAGCCG
core_71	AGTGTACTACGCAGTATGTTAGCAAGAAAAAG
core_72	ACACTATCACGTAACAAAGCTGCTATAGCAAG
core_73	CATTCAGTAGGCGCATCCAAAATAGTCATAAATATTCATTCAGACCGG
core_74	GAAAGGAAGTCGAGGTCCGATTAAAGGGATTTAAACGCTCTACCGCCA
core_75	CCGGCGAAGAGCGGGCGCTAGGGTTAAAGA
core_76	AGGCTGGCTGACCTTACGTTAACAAATCAG
core_77	CCAGCTTTCATCAACATTAAATGCTCACCG
core_78	ACCTTGCTGAACCTCAACGCCAACCGGCTACA
core_79	AGGAAGTTCCCAGCGATTATACCACACAATTC
core_80	TCGTAGGAATATAGAAGGCTTATCTTCATTACGTAATCTTT
core_81	CCTGTTTAGTATCATAAATATCAAATTAAGACGGAATACC
core_82	TTGAGTTAAGCCCAATCCTTTACA
core_83	CGGATAACTGAGCGAGGGGCGCATCACGACCAGTAATAAA
core_84	TGGTCAGTTAATTACTAACGTAGAAAATACA
core_85	TGGCAAATTAAAATATCTTTAGGAGCACTAACTGGCATGACCCTCAA
core_86	AATCAGTGACAGGAGGGCCGTAAAGCACTAAA
core_87	AATTCGCGCGTGGCACGAACGCCAATCAGCTCCCAGTTTGGAACAAGA
core_88	TCAAAAATGCTTTGACGGTCACGCTGCGCGTA
core_89	GAGCAAAACTTTTTCTAAATTTAATGGTTTGAAATACCCGGGAGAA
core_90	CTGGTAATTTTCAGGGCAAACTACACAGCTTGATACCGAT
core_91	ATGAAACAAACGTTATTAATTTTATAAACATGAACCGCCGACAATG
core_92	GCGAAGATGCCACAAGAATACACTAAATAAAGTGGCTCGAA
core_93	ACAGCATCGGAACGAGCAACTAATAAAGCATCTCAATATC
core_94	GGTAGCAAATGTAATTGAATATAAAGTACCGACAAAAGGT
core_95	ATTGAGGAGGTGGCAAAATAAGAATAAACACCGGAATCA
core_96	TGCTATTTTGCACCCTTTTGTTTGAGAGAAT
core_97	AGATTAGAGCCGTCACCGCCAGCCTCCTCA
core_98	CTTTGAATACCAAGTTAGCATCAGACCACCAG
core_99	TAAAACGAGGTATTAATCTTTCCTTATCATTCCAGCCATA
core_100	AAAAGTTTAAAACAGACGGATTCGCCTGATTGTTCTGACCAAATATAT
core_101	TACCAGTCCCGGAATGATAGCTCCTCAGGAACTGCGCAA
core_102	CAACAGTAGCCAGCAGCAAATGGAGTTAAA
core_103	AGCGCATTCCCAATCCAAATAAGAATCAATATAAGAACTAAAAATCT
core_104	AACATAAAAACAGGGAAGATAACCTTTTATCC
core_105	GCCATGTTGAAACAATCGGCGAACCGCCAGCTCCTGTAGTCAGCAGC
core_106	GGTGAGGCGGTCAGTCACCCTCATAGTACCGTATCGGTTTTCCAGA
core_107	TCACGTTGGATAGACTGGAGCCGCCACGGGAA

oligoname	sequence
135deg_1	CAGAGCACCAGACTGTAGCGCGTTAGTTTGCC
135deg_2	TGGTGCCATCCCACAGTTGGGCGGTTGT
135deg_3	TCCCTTATCACAGACAAGATGCCGCCCTGCGGTTGCAGGCGCTTTCGCA
135deg_4	GCTGGAGGTGTCCACAAAATCGTCGG
135deg_5	AGCATGTCAACGTCAGCTGGCAGCCTCCGGC
135deg_6	GGTAATCGTAAAACTTTTTTGAATGGCT
135deg_7	GTACATCGACATAAAAAAATCATTTCATC
135deg_8	GTGTTGTTATTTTTTAGAGTCTGGAGCAAAC
135deg_9	CCGAGATAGGGTTGAACCACCACACCG
135deg_10	TAGGAACCCATGTAGCAACCAGCTTACG
135deg_11	AAGAGAATGAGATCTAGGTTACCTGCAGCCAG
135deg_12	AGGGCGCGTACTATGGTTGTTGCGGTATGAGCCGGG
135deg_13	CTTTAGTGATAATTTCTGCTCATTTGCAGCGGAT
135deg_14	ATTAGTCTTTAAATTTTTGACGATGAAC
135deg_15	ACGGCATCGCCCTCATAACGCCTGTAGCATTCCGCCGCTAC
135deg_16	TCCATCACCTTTCCTCGACCCCCGAGCCACGTCCGTAACACTGAGT
135deg_17	TCACTGTTTCAAAGGCTATCAG
135deg_18	AACGGAACGTGCCGGGAAGGGTAAAGTT
135deg_19	GGCAGCACCCGCGGTCCGTTTT
135deg_20	TTCGTCACCAGTAATAGCAAGCCCAA
135deg_21	AAACGATGCTGATTTAGCGTATCCTCAT
135deg_22	CCGGCAAAGCGCAGAGAAAGCCGCACAGGCGGC
135deg_23	GTCATTGCCTGAACCAATAGAGACAATA
135deg_24	TTCGTCTCGTCGCGTGGTGCCAAACTTAACTTGTAGTCGCTATT
135deg_25	CCGCGCTTAATGAAATCAAAAGAATAGC
135deg_26	CTCAATCCGCCGGGCGCGAACCGCAAGAATGCCAAC
90deg_1	GCTATCTTACCGAAGCACAACGGAGATTTGTA
90deg_2	AACCGAGGAGAAAAGTAAGCAGAT
90deg_3	ACAAATTGCCGTTTTTATTTTCACATCGAGATTGGGAAGGGCTCAT
90deg_4	CTGACTATAAAGCGCAGTCTCTGAATTAAAGC
90deg_5	CAGACGATTAATGCCCAAGCAATATATAGTCAGAAGCAAA
90deg_6	AGCCGAACAAAGTTACCAAGAAATGTGTCGAAGCTCAA
90deg_7	CAACGCTCAACAGTATGCGTTAT
90deg_8	TATACCAGTTGAAGCCTAATTTACCTTACCAGTATAAAGC
90deg_9	CATGTTACTTAGCCGGACAAAGTCCTTTTTAAAAGACTAAAGTAATCGCCATA
90deg_10	GCGAGGCGTCCTTATTGGTAATAATGGCCTTGCAGAATGGAAGCCTCAGAGCATAA
90deg_11	GCCCGTATAAACAGTGTTTTAAC
90deg_12	CGACTTGCGGGAGGTTTAAGAAC
90deg_13	CAATAAATCATACAGGTCATTTGGGGCGCGAGCTGAAAAG
90deg_14	CGCAGACGAATCCGCGACCTGCTC
90deg_15	TAAGGGAATGCCTTGAGTAACAGT
90deg_16	GCGGATTGCATCAAAGTCTTTACC
90deg_17	TCATCGCCTGATAAATCAATGAAATAGCAATA
90deg_18	TTTTCATGGAGGCTTTGAGGACTAAACGCATTGAGAAAACAAGAA
90deg_19	TGAATATAATGCTGTGTCAATCAGAGGAAGCCAAGGCAA
90deg_20	GGGGTCAGCCGGATACGGTATTCTCAGGACGACAAGCAAGAGCATGTAGAAACC
90deg_21	CAATAGATAAGTCCTGTTCTGTCCAGACGACGACAATAAA
90deg_22	CAACATGTTCAGCTAATGCAGAAAATAGCAGAATAAGAGAGATTAGT
90deg_23	AAATAATACGCGCCTGTTTATCAA
90deg_24	TTTAACAGGGCTTAAATAATAACTTTTAGCGAACCTCC
90deg_25	AGAATTAAGTAGCATTAACATC
90deg_26	TCCTGTGTGAAATTGTGCAAAATTCCTGCCTAAACGAGG
90deg_27	GTGGCATCAATTCTACTAATAGTTATCCGCTAGCGCGAATTTCGGA
90deg_28	AACGTCAAAAATGAATCCCATCCTTAAATCACAGAAGGA
45deg_1	AGTTTCAGCGGAGTGACTGCCCGCTATTGGGCTGCCTGTTTTTCAACG
45deg_3	TTGAGGGAGGGAAGGTAAATAGCAACAGCTGAATGAATCGG
45deg_4	ATAACCGATATATAATAATGCGGATAAATCGTCACCCTCAGCAGGCCGCT
45deg_5	CATTTGGGAATTAGAGCCAGCTTGACGGAAATTATTCATTA
45deg_6	TAGTGAATTTATCAAACATATGGTT
45deg_7	ACCGGAACCAGAGCCACCACCGGAATGTGTAAAAATCACGAAGAGTCAA
45deg_8	AGGGTAGAACCGCATTAACACTTTGCCCCAACATCAAGAAAACAAATCCAATGATAA
45deg_9	ACAACAACCATCGCCTTTAATTGCCCACCCTCGATATAATTAAATCCCGCCT
45deg_10	ACCCTCATCCTGATAGAAAATTATCATAGGTCTGAGATTATATAACTATA
45deg_12	CTTCGCGTTCTGCCAAGGAACAGTTGAAAATCTCC
45deg_14	GTGGTGCTGCGGCCAGTGAGACGGGGTAAAGAGCCGCCACCC
45deg_15	GCACTCTCGGAATAGTTCTGTATGGCTCCAAAAGGAGCCCACGC
45deg_16	GCAACAGTGCCAGGATTTAAGATGAATGCGTAGATTTTAACCAAGTTTATTTGTCAC
45deg_17	TTATCAGATGATGGTTAACGTCGAAGTATT
45deg_18	TTTTCACCAGAATGCGGCGGGCCGT
45deg_19	ATAGATAATACATTTGACGCTGAGTGAAAGGAATACAGTAACA
45deg_20	AATTCGACGAATTATCCCTCAGATTCAAAAGGGTGAGAAAGGCCGG
45deg_21	TGTAAATGAGATTAACATCATAACATTTAACAATTTCA
45deg_22	GTACCTTTTACATGACCGTGTCGCAAGACAAAGAACGCCTTAGAA
45deg_23	ACCACCAGAAGGAGCGAACTCGTAGTATAGCCTTTCACG
45deg_24	TCAGAACCGCCACCCTCAAGGA
45deg_25	AAAAAAAGGGATTTTGCTAAACCCTGAGAG
45deg_26	CAGAGCCACAATATAATATATTTTAAATGCA
45deg_27	GTCATACCGGGGGTAGTACCAGTTTTCACACTAAAGGAATTGCGA
45deg_28	TGCGCTCAGAATAGAAGCACGCGGCCAGGGTGGTTTTTC
45deg_30	AGCTGCATTATTGCCCTTCACCGCCTGGCAACTTTCAAC
45deg_31	ATGCCTGAGTAACCGCCTGACGCTGACAGTAGCACCATTACCATTAGCA
45deg_32	TACGAAGGCACCAACCATTCGGTCTTTGCGGGGTGCCGTCGAG
45deg_33	AACATAGCGATAGCTTCTGATGCAAATTAATTTTCCTGA
45deg_35	ATAAGGCGTTATCCGGCTTAGGTTGGGGACTACCT
45deg_36	AATCAATTGTTTGGCAATTCATCCACCCTAGACTTTACAAAC
Csv1_45_outer1ss_1	TAAAAATAAAAGGCGACATTCAACCG
Csv1_45_outer1ss_2	TTTCCAGTCGGGAAACCTGTCGTGC
Csv1_45_outer1ss_3	AGGTGAATTATCACCAAAGACTTTTAGA
Csv1_45_outer1ss_4	CAACGCGCGGGGAGAGGCGGTTTGCG
Csv1_45_outer1ss_5	TACCAGCGCCGTCACCGACTTGAG
PolyT_1	TTTTAACAGGAATAGACAGGAACGGTTTT
PolyT_2	TTTTATTTAGGAATACCACAAGATTCATCAGTTGAGTTTT
PolyT_3	TTTTCCAGTCACGCACCGCTTCTGGTTTT
PolyT_4	TTTTTTCAACTTTAATCTGACGAGA
PolyT_5	TTTTCAGAGGGGTAATAGTAAAATAACACCAGAACTTTT
PolyT_6	TTTTAAACTATCGGCCTGTCTATCATTTT
PolyT_7	TTTTGATTGACCGTAATGCCATTGCTTTT
PolyT_8	TTTTACAAAGTCAGAGGCGTCTTTCCAGAGCCTAATTTTT
PolyT_9	TCAGAGGTAAAACGACGGCCAGTGTTTT
PolyT_10	TTTTCCAAGCTTGGAACAAACGGCGTTTT
PolyT_11	TTTTGAGTAGTAAATTGGGCTTGAGGTAGAAGCTTGCCCAACAACA
PolyT_12	TTTTTGCCGGAAACCAGTGCTGGTATTTT
PolyT_13	TTTTTACGCCAGAATCCATCACCCATTTT
PolyT_14	TAACGAGGTAATTGACATATAACAGTTGATTCCCAATTTT
PolyT_15	TTTTATATCCAGAGTAGAGAACTCTTTT
PolyT_16	TTTTTTCTCCGAACGAGTCCAACGGTCAGGATTATTTT
PolyT_17	TTTTGAGAGTACCTTTAATTGCTTGGATAGCGTCCATTTT
PolyT_18	CTTTTGCACCAAAAGGTTCAACTAATGCAGATTTTT
PolyT_19	TAGACGGGAGAATTAACTGAACACCCTGATTTT
PolyT_20	TTTTATACTGCGGAATCGCGAGAGG
PolyT_21	TTTTAATCAAGTTTTTTGGGCGTGAACCTGAGAAGTCTTGCCTG
PolyT_22	GGGATAGGGCTTTCCGGACGTTGTTAACGCCAGGGTTTTCTTTT
PolyT_23	TTTTTTGCCAGTTACAAAATAAAAGATGGTTTAATTTTT
PolyT_24	TTTTGGGCGATGGCCCACTAGAAAAACC
PolyT_25	TTTTACATAACGAAAGAAGTTTTGCTTTT

Figure B.14 Sequences of staple oligonucleotides of CS-v1-out1ss.

oligoname	sequence
135deg_1	TTACCAACGCACGCAGAAACAGC
135deg_2	GGATCAAACTTAAATCCTGAATC
135deg_3	AAAAGAGTAACGAGCCTTAAATCAAGATTAGTT
135deg_4	GGCCTTTAGTGATGTACATCGACATAAA
135deg_5	CAAGTTTGCCTTTAAAGGGTAAAGTTA
135deg_6	GACGATTGCCGGAACGAGCCCCCGAACCAGGCGTCAGACTGTAG
135deg_7	AACGGAACGTTTGTATAAGCAA
135deg_8	TGTAGGTAAAGATTCACCGTCGAGAGGGT
135deg_9	AACACCCTGAACAAAGTCAGAGGATGAAAATTCACGGAAATTTGCC
135deg_10	AAAGGGTGCGCATTAGACGGGAGAATTAACTG
135deg_11	ATGAACGGTAATCGTAAAACTAGCATGTCAA
135deg_12	CCCAAAAAACAGGGCGGTCATAGCCCCCTTATTAGCGTTTGC
135deg_13	GAGAATAACATAAAAACTTTCTCCGTGGT
135deg_14	AACGATGCTGATTGAAAGCCGCACAGGC
135deg_15	TGATATAAGTATACAATGCCTGAGTAATG
135deg_16	ATATTTAAATTGTACATCCTCAT
135deg_17	CGCGTTTTCATCGGAGTAGCGACAGAAT
135deg_18	GTCGCTGGCAGCCTCCGACAATTTTATTTCTGCGAGATAGA
135deg_19	GCTATTTTGCACCCAGCTCAGTTGGGATTTGTGA
135deg_20	CATCTTTTCATAATCAAAGCCAGAGCAAACGTTAGATAAGTG
135deg_21	TGTTGTTCAGTCTGGAGCAAACAAGAGAATCG
135deg_22	GCCGCGCTTAATGAATCAAAAGAATAGC
135deg_23	GAAGGGATAGCTCAGCAGCCTTTACAGA
135deg_24	CCCTTATACGCCGCTCAGGAAGAGCCGGACGGTCCGTTTTTTCGTCTC
135deg_25	CCGAGATAGGGTTGAGAACCACCACACCC
135deg_26	AAAATCCCGTAAAAGGGAGGTTCAGAGGCAACCTCCTCGTAGGA
90deg_1	GCGTTATACAAATTCTTACCAGTCCTGAAAGAACGAACCGAAACCTG
90deg_2	CCGAAAGACTTCAAAAAGATAAACAGAGG
90deg_3	AACAGTACATAGCTGTTTCCTGTGTCGTAAT
90deg_4	TGAGGCGGTCAGTATTAAGATTAAGAGGAAGC
90deg_5	TAATGAGTGCACTAACAAAATCTAGATTATCATTTCAACTGTAACAAAGCTGCTCA
90deg_6	ACGGTGTACAGACCAGGCGCATAGTTAGACTGAGCGGATTGAATACCA
90deg_7	TTGCCTGATTCTTTGATTAGTAATGGTCAGGATTGTATCACAAGAACC
90deg_8	TTGCGTTGCGCTCACTGTGGGGTGCC
90deg_9	GCGCGAAACAAAGTACAAACACTCAT
90deg_10	CTTGCTGAAGCTAACTCACATTAA
90deg_11	AATCTAAACTGCAACAGTGCCACG
90deg_12	AAAGCGAACCAGACCGGCATCAAAAACACCGCAATCCAAT
90deg_13	CTCCAACATTTAATTCGAGCTTC
90deg_14	ATATTCCTTCAGTTGAAAATCAACCCAGCGATTATACCAA
90deg_15	CAGGTAGAAAGATTCACGTTAATAA
90deg_16	CAAGAGTAATCTTGACAACTTTGAAAGAGGACAGATGA
90deg_17	TAAATTGTACGGAGATTTAGAGAGACGGAACAACATTATTA
90deg_18	GTAATAGTAAAATGTATTACCCGATTTAGGAAGCAAA
90deg_19	CTGAGAGCCAGCAGCACCAGCAGTATCGCGTAACATCACGAACTGACTCGCCTGA
90deg_20	GCCATATTATAAAGCCAACGCTC
90deg_21	TGTAAATGCTGATGCAGCATCACGTCGCTATGAGAATC
90deg_22	GATAGAACCCTTCTGATAACAACGCCAGTCGGAAATGAAA
90deg_23	AACAGTAGGGCTTAATGAAAAAGCCTGTTTAGTATCATAT
90deg_24	CTCCTCACCCCGCTTTCCAACATGTAAATCAATATATGTGA
90deg_25	CTTTGACCCTTAATCATTGTGAATTGGTTTAAGATGATGGTTATCATC
90deg_26	AACGAACTAATTTTTGCGTAAAGCCAGTTGAGGCATGGTCATAATTTAGGCAGAGG
90deg_27	GTGAATAACCTTGCTTCTTTAATGGA
90deg_28	GGATATTCGCTGGCTGACCTTCAT
PolyT_1	TGAATCCCCCTCAAATGCTTTAAACAGTTTTT
PolyT_2	TTTTCCGTTCCAGTAAGGTCTATCATTTT
PolyT_3	TTTTCAACTCGTATTAAATCCTTTGGAAGGAGTATTATTATACTT
PolyT_4	TTTTCATCAACATTAAATACTGGTATTTT
PolyT_5	TTTTGGGCGATGGCCCACTAAAAAACC
PolyT_6	TTTTCGCCAGCTAGTTTGAGGGGACTTTT
PolyT_7	TTTTAGAAATTGCGTAGATGTAAAACAGAAATAATTTT
PolyT_8	TGTGAGCGCATCTGCCGGCGAAAGGGCCTCTTCGCTATTATTTT
PolyT_9	TTTTTCAGAAAACGAGAGCAACACTATCATAAC
PolyT_10	AGTAAGAATGACCAATTTCATCTTCTGACCTAAATTTT
PolyT_11	ACCAGACGACGATAAATGCCCGAATCATTTTGGACTTTAC
PolyT_12	TTTTTTTAATGGTTGAGAGTTCAATAGTGAATTTATTTT
PolyT_13	TTTTAAGTTACAAAAAAACAATTCGATTTT
PolyT_14	TTTTTCAAAATTATTTGCACGTTAGAACCTACCATATTTT
PolyT_15	TTTTGCGATTAATGTAGCCAGCTTTTTTT
PolyT_16	GTTGGGTAGGGGATGTGCTGCAAGTTTT
PolyT_17	TTTTGACGACAGTATCGCGTCATACTTTT
PolyT_18	TTTTTCAAAATCATAGGTCTGAAGGCGAATTATTCTTTT
PolyT_19	TTTTATAAGTTTCCACCCTCAGAGCTTTT
PolyT_20	TTTTCGCCACCAGAACCATCACCCATTTT
PolyT_21	TTTTAGTTTGAGTAACATTACGTTATTAATTTTAAATTTT
PolyT_22	TTTTAATCAAGTTTTTTGGGCGTGAACCACCACCAAAGCGCA
PolyT_23	TTTTATTTCAATTACCTCCTGATTGCTTTGAATACCTTTT
PolyT_24	TTTTATGGCTTTGTCTCTGAATTTATTTT
45deg_1	GCGCCGACAATAGCATGTGAATAGAAGTTTTCACGGTCATA
45deg_2	AAGGAATTGCGTTCTTAAACGGCCTGGAGGTGTAACGGCATCAGATGCC
45deg_3	AAAATACGTATTCGGTCGCTGAGCACGCATAATTTACGAATAAACA
45deg_4	GGCGCGAGCTGAAAAGGTGGCATC
45deg_5	CGCAAAGATAAGACTCCTTATTACGCAGT
45deg_6	GGGTTACCAGACGATCCAGCGCAGACCGTCACGCCTGGCATTAAAGG
45deg_7	CATAAACATCCCTTACACTGGTGTGTTCAGCATTTACCAGCGCC
45deg_8	TGGGTAAAGGTTTCTTTGCTCGT
45deg_9	CATATAAAAGAAAAAGGCAAATAACATCC
45deg_10	TGCTTTCGAGGTGAATAATAATACGACTTGATGCACTCTGTG
45deg_11	TTTCAACAGTTTCAGGCAAGCCACGATCTAATCAATAA
45deg_12	AAGTAATTCTGTCCAGCGTCTGAACAGAATGCAACCGATTTATTCATTAAA
45deg_13	AGAACAATATTACCGCGACAGGAAAATCAGTGGGCAACAG
45deg_14	GAATTAGCAAAATTAAGCAATAA
45deg_15	AGCCTCAGAGCATAAAGCTAAATC
45deg_16	GTTAAAGGCCGAACCGAGGCAGCTTGAAATGAAATATTATGACCCTGTAAT
45deg_17	GTGCTGCGGCTTTCACCAACGGAAATGAGGGAGGGAAGGTA
45deg_18	ACCCAAAAGAACTAATTCTGCGAACGAGTAGATTTAGTTTGACC
45deg_19	CAGGGATACGGAGTGAAGAAACCACCATCCTAACCGATAGAAGTTTCATTCCAT
45deg_20	TCATTTGGAATAACCTTAATAACGGAAT
45deg_21	CTGATTGCATTAGCACCACCACCACCAGTTGAAATATAGAACCAAGTACCGCACT
45deg_22	AAAGACAAAAGGGGCTGGTAAGAGCCGGGTCACTGTTATACAGGC
45deg_23	CGACATTCCACCACGGAATAAGTTTATTT
45deg_24	AATAAATCTGATTCCCGGCATGATCCATCGCCGCTTGCAGGGA
45deg_25	TCGGCTGAGGCTTATTTCCATTAACCCTCAGCAGCGAAAGCAGAT
45deg_26	AATTCTACTAATAGTAGTAGCAT
45deg_27	AAAGTTACCAGAAGGACTTTTGCGTATCATTCTACCGATAGTT
45deg_28	GGTGAATTATCTGTCACTGTCATATGGAATCGTTCCAGCATC
45deg_29	CAAGAACGGGTATTAATCTTTCCTGGATCGTCAACGGGT
45deg_30	AGCGGGGTGGTTGTATAAAGGTGGCAA
45deg_31	TACGGCTGGCCATTTGGGAATTAGCCTTCACCATTTTTCCTCATTTT
45deg_32	ATGTTAGCAAACGTAGAAAAAAACGCAA
45deg_33	ATTAGATACATTTCGCAAATGGTC
45deg_34	GATTTTAAATATTGGTGAGACGCAGGGTGGTTTTTCTATGGATT
45deg_35	ATAACAGTACGACGACGACAACAAGGCGGGCCAGGAACAACTA
45deg_36	CATTGCAGGCGCTTTCGCACTCAA
45deg_37	TCCGCCGGGCGCGGTTGCGGTAT
45deg_38	TGTCACAATCAATAGAAAATTACATACACCAAAAACTATATTT

oligoname	sequence
Core_1	TTGGGCGCAGGCCACCGAGTAAAAGTTTTTAT
Core_2	GGCCAACGCGCGGGGGCCTGTTCAGCCAGTA
Core_3	CACACGACATTAGTCTAAAAACGCTCATGGAACAGCCATT
Core_4	TCGTGCCAGCTGCATTCCAACAGATACGTGGC
Core_5	CATTCTGGAATGAATCAAAACATCACTCAAACTATCGGC
Core_6	CCTCCGGCAGGAATTAACCAGAAGATAAGGCTTAAATTGGGCTTGAGA
Core_7	TAGAATCACAATGAAACCATCGATAGCACCGTCAGCGACGTATA
Core_8	GCTAAACAGGAGGCCGCCTGAGAGCCATTACCAGCCAGCA
Core_9	ATCGGAACGGGAAAGCGGTTGAGGCAGGTCA
Core_10	TTGAAAAATAAGAATAAACACCGGAATCATCGCAAGA
Core_11	GCCAGCATCAGAACCGTGCCGTAAAGCACTAA
Core_12	CGAGGCGTGCTCCATGTTACTTACCGTAAC
Core_13	TTAAAATTATCACCGCGGTCACGCTGCGCGT
Core_14	AGGTCATGCCTTGAAGTGTAGGATTTAGAGCTTGACG
Core_15	TTAGGTTGCCTCAATCAACATCAATTTTACATCGGGAGAA
Core_16	TGGTGCTGTGATAATCACTCAGGAAAATTTTTATCAGAGAGATAACCC
Core_17	GTAGAAGAGCCATTAAAAATACCGCGTAAGAA
Core_18	TAATGCCGGAGAGGGTTCTAGCGAGACTCAACCGTG
Core_19	CGGTACGCCAGAATCCAGCCGGAACTTGCTGG
Core_20	ATATTCATAGGCTTTTGCAAAAGATTCAGTGAGAGCGGAACAATTCAT
Core_21	CGGCGAACGGAGCGGGCGCTAGGGTTAAAGAA
Core_22	AAAGGAAGTCGAGGCCACCCTCAGAGCCATAACGGGGCAGGAGTG
Core_23	CCTGCATCTGCAGCCATCCCACGCAACCAGCTACTTTTGC
Core_24	TGAGAAGTGAGTCTGTTAATATCCTTAATGCGCGAACTGA
Core_25	CCGCGACCCAGACGGTCAATCATAAGGGAACC
Core_26	CTTTTTAATTTAGTTATAAATCAAAAATCAGG
Core_27	CCTAAAGGCGCCTCCCTCAGAGCCCGTATAAATTATTCTGGTGGGAAC
Core_28	GAGCCGCCAAGAGGCTTCAGTGCCCGCGTCTGGCCTTCC
Core_29	AGTTTTGCGATACATACTGACTATGCGAGAAACTTTTTC
Core_30	CAGCAGGCCAAGCGGTCCACGCTGTGACGAGC
Core_31	ATATGATATTCAACCGTAGCTATTTTAAAGCCAAGCGAAAGTGGCGAG
Core_32	CACCATCACCGGCACCGCTTCTGGATTCAGGC
Core_33	TGCGGAATCGTCATAATCTTTACCACGCCAAA
Core_34	CGTACTATGGTTGCTTTGGTGGTTACCCCGGTCGGCAGC
Core_35	AGAACCCTCATATATTTTAAATGGCCCGGAA
Core_36	AAGGATAAAGGAGCCTACAAGCAAGCCGTTTTTTATTTTCAGCGCTAAT
Core_37	GGCGTTAACATAGCGATAGCTTAGATGAAACA
Core_38	AATTACTATTAATTAATTTTCCCTTGTAAATC
Core_39	ACAGACAATTATTTTTTAGCCCT
Core_40	AAAAGGTAACATGTTCAGCTAATGGTGTCTGGTTTTAAA
Core_41	ATAAGAGAATATAAAGTCACCAGTTTTGCGTAGCAACAGG
Core_42	TTGTAGAACGTAATCCATTTTCGACGTGCTTTCCTCGT
Core_43	TATAGTCAGAAGCAAGATAGCG
Core_44	ATCTACAAAGGCTATCAGTCAAATGGGGTTTTATAGGTCAAAACGGCG
Core_45	TGATGATATGATAAATGCCTCAGGAAGATCG
Core_46	GAATGGCTCAGTAATAAAAGGGACATTTTCG
Core_47	GTCCACTACGCTGGCATATTCACAAACAAATAGGATTAGC
Core_48	ATCAGCTGGGAGAAGAGCCCAATAATAAGAGCCGAAGCC
Core_49	ATACCTAATTTACATTGGCAGATTACCGACCCGGGGGT
Core_50	CATTTTGACGCTCAATGCCCTGCG
Core_51	GCGGTGCCGAAAATCCTGTTTGAGTTTGCCCAATGCCAAGTCTGGTC
Core_52	TTCGCGTCCGTGAGCAATTGCTCACCGTTGT
Core_53	TTTGAGAGCGTGGACTCCAACGTCAAAGGCGGGGAAGAAGAATGGA
Core_54	CCATCACGCAAATTACTGTATGGACTGAGTTCATTCCA
Core_55	CATTCAACTAATGCACAGAGGGGTCCAATAC
Core_56	AATATCTGGTCAGTTAGAAACCCGAGGCATATAGCGAG
Core_57	GGCAAATCGAGACTACGCTGAGAAAATACCGACCGTGTGATAAATAAAAATATAT
Core_58	CGCATTAACCAGGCGATATTTTGTGCCTGAGCAGTTTGGAACAAGA
Core_59	TTAATTGTATCGGTTTAAATCACCTGGTGCCA
Core_60	TACCGCCAATCACCGTAGAAAAGCTCATATGTCCGAAATCGGCAAAAT
Core_61	GGTTTAGATCATTACCGCGCCCATCGGAACG
Core_62	GCTCCAAACCTCAGAGCGAGGCGTTTTAGCGTTTGAGGAAGGGTAGC
Core_63	GCTCATTTTTTAACCAATAGGAACACGTTGTA
Core_64	GTCCTGAACAAGAAAATTCTGCCA
Core_65	GATTTTGCTAAACAACGCACGCGTAGAGGCGG
Core_66	GCGATTTTAAGAACTCCTGAATAACACCAGAATGTTTGGACGGAACAA
Core_67	TACCTTATAGGACGTTGGGAAGAAACTAATAAAAATATC
Core_68	CAAAAGAATACACTAAACTACAACAAGAGGTCTACCTTT
Core_69	CTAAAGACTTTTTCATGAGGAAGTCCGGTATT
Core_70	TTGAGTAACAGTGCCGCCACCCTTGACAGGA
Core_71	CAGTTAATGCCCCCTGATTTTTGTAGCCACCA
Core_72	GGTTATCTGATTAGAGACAGTACCATTTGAATTACCTTTACATTTA
Core_73	ACCGCCACCCTCAGAGAGGCCGGAAGTAGCAAGTTGCAGGGTGCCC
Core_74	GAAAGGAATTGAGGAACAATATAATACCAGTC
Core_75	TCGTCACCAGTACAAGTCGAAATAGCAATAC
Core_76	TCGCGCAGGATTTAGATTTCAGGTTTAACGTCAGATGAATACAATAAC
Core_77	CAGTCACGGCCATCAAGATTCTCCAAACATGAAAGTATT
Core_78	CATTTGAGAACAGTTGGATTCGGAGCAAAAGAAGATGATTAAGAC
Core_79	TTGAGTTACCTTTATTTCAACGCACCGTCGGCCGCAAG
Core_80	AACGGCTAGTTTACAAAATAAACAACGATTTT
Core_81	CATAAAGTGGATGGCTTAGAGCTAAAGAGG
Core_82	TTGAAGCGTCTTTCCGACTTGCCCGTTCCGCCCTCAGAACCGCCAC
Core_83	TATGCAACTGCTGTAGTCGTCTTTTTAGCGTACAATAGGAACCCATGT
Core_84	CGCCTGTTTATCAACAGCTCGAATTGAAATTGCCGGAAG
Core_85	AGTAACACCTCACCACGCCAGGGTTTTCC
Core_86	ACAATTTCGAAAACAAAATTAATTTAGAATCCAACTATACAAAGAAC
Core_87	CGTTGGTGGCGCCATGTGCGCAACTGTTGGGA
Core_88	GTAATGGGGCTCAGTACCTATTTCGGAACCTA
Core_89	TCATTTGACCAGGCAGAAAGGCCGGAGAC
Core_90	CAAATCAGAATCTCCAAAAAAAAGAGCAGCAAAACGTCACGAGCGGGA
Core_91	GTTTAGCAGCAATAGCTATCTTACAAGAAAC
Core_92	TTCAGAGGAAACGACGGCCAGTGCGGTTGTGTAAATCACCGCCAG
Core_93	TGGAGCCGCCACGGGAAACGTACATAGATGGGCCAGCTTT
Core_94	ATAATATCAAGTTTTGCTCAACATTAATGCCACTACGAAGGACCAAC
Core_95	TTATCCGCTCACAATTTAAAGTACGCAGAACG
Core_96	ATCCCCGGGTACCGAATAGATAACATACGAG
Core_97	TCCTGATCGAGTAGTGCCCTGACGAGAAAAACCAAA
Core_98	TTTAGGAGACCTCAAATATCAAACGGTTATAT
Core_99	CAGGGAAGAAAGCGCCATTCGCCTGCCGGAA
Core_100	AGGGCGATCACTCCAGCGCATCGTCTCAAGAGAAGGATTAAATCCTCA
Core_101	TTGTTTAACGTCAAAAGTAATTGACAGAGCCTTAGGTGTGCAAACGC
Core_102	ATACAGTACCGTCAATAGATAATAGCTCATTA
Core_103	TTTACCAGTCCCGGACCAAGCTGATTGACC
Core_104	CGGTGCGGGAAACAATCGGCGAACGGATAAACCCGTCGAAATAATT
Core_105	CCTCATAGCCAGACGTTAGTAAATGAATTTTCTTTGATGCCTGTAG
Core_106	AGCCGAACCTTTTTAAGAAAGTACAATCCAACAAGAACATCGAGA
Core_107	CAGACAGCCTAAAACGTAATTGCTGAATATAACCACACAA
Core_108	AATAAGAAGCCATATTATTTATCCAGACAGCAATAGCAAGCTAAGAAC

Figure B.15 Sequences of staple oligonucleotides of CS-v2.

oligoname	sequence
135deg_1	TTACCAACGCACGCAGAAACAGC
135deg_2	GGATCAAACTTAAATCCTGAATC
135deg_3	AAAAGAGTAACGAGCCTTAAATCAAGATTAGTT
135deg_4	GGCCTTTAGTGATGTACATCGACATAAA
135deg_5	CAAGTTTGCCTTTAAAGGGTAAAGTTA
135deg_6	GACGATTGCCGGAACGAGCCCCCGAACCAGGCGTCAGACTGTAG
135deg_7	AACGGAACGTTTGTATAAGCAA
135deg_8	TGTAGGTAAAGATTCACCGTCGAGAGGGT
135deg_9	AACACCCTGAACAAAGTCAGAGGATGAAAATTCACGGAAATTTGCC
135deg_10	AAAGGGTGCGCATTAGACGGGAGAATTAACTG
135deg_11	ATGAACGGTAATCGTAAAACTAGCATGTCAA
135deg_12	CCCAAAAAACAGGGCGGTCATAGCCCCCTTATTAGCGTTTGC
135deg_13	GAGAATAACATAAAAACTTTCTCCGTGGT
135deg_14	AACGATGCTGATTGAAAGCCGCACAGGC
135deg_15	TGATATAAGTATACAATGCCTGAGTAATG
135deg_16	ATATTTAAATTGTTACATCCTCAT
135deg_17	CGCGTTTTCATCGGAGTAGCGACAGAAT
135deg_18	GTCGCTGGCAGCCTCCGACAATTTATTTCTGCGAGATAGA
135deg_19	GCTATTTTGCACCCAGCTCAGTTGGGATTTGTGA
135deg_20	CATCTTTTCATAATCAAAGCCAGAGCAAACGTTAGATAAGTG
135deg_21	TGTTGTTCAGTCTGGAGCAAACAAGAGAATCG
135deg_22	GCCGCGCTTAATGAATCAAAAGAATAGC
135deg_23	GAAGGGATAGCTCAGCAGCCTTTACAGA
135deg_24	CCCTTATACGCCGCTCAGGAAGAGCCGGACGGTCCGTTTTTTCGTCTC
135deg_25	CCGAGATAGGGTTGAGAACCACCACACCC
135deg_26	AAAATCCCGTAAAAGGGAGGTTCAGAGGCAACCTCCTCGTAGGA
90deg_1	GCGTTATACAAATTCTTACCAGTCCTGAAAGAACGAACCGAAACCTG
90deg_2	CCGAAAGACTTCAAAAAGATAAAACAGAGG
90deg_3	AACAGTACATAGCTGTTTCCTGTGTCGTAAT
90deg_4	TGAGGCGGTCAGTATTAAGATTAAGAGGAAGC
90deg_5	TAATGAGTGCACTAACAAAATCTAGATTATCATTTCAACTGTAACAAAGCTGCTCA
90deg_6	ACGGTGTACAGACCAGGCGCATAGTTAGACTGAGCGGATTGAATACCA
90deg_7	TTGCCTGATTCTTTGATTAGTAATGGTCAGGATTGTATCACAAGAACC
90deg_8	TTGCGTTGCGCTCACTGTGGGGTGCC
90deg_9	GCGCGAAACAAAGTACAAACACTCAT
90deg_10	CTTGCTGAAGCTAACTCACATTAA
90deg_11	AATCTAAACTGCAACAGTGCCACG
90deg_12	AAAGCGAACCAGACCGGCATCAAAAACACCGCAATCCAAT
90deg_13	CTCCAACATTTAATTCGAGCTTC
90deg_14	ATATTCCTTCAGTTGAAAATCAACCCAGCGATTATACCAA
90deg_15	CAGGTAGAAAGATTCACGTTAATAA
90deg_16	CAAGAGTAATCTTGACAACTTTGAAAGAGGACAGATGA
90deg_17	TAAATTGTACGGAGATTTAGAGAGACGGAACAACATTATTA
90deg_18	GTAATAGTAAAATGTATTACCCGATTTAGGAAGCAAA
90deg_19	CTGAGAGCCAGCAGCACCAGCAGTATCGCGTAACATCACGAACTGACTCGCCTGA
90deg_20	GCCATATTATAAAGCCAACGCTC
90deg_21	TGTAAATGCTGATGCAGCATCACGTCGCTATGAGAATC
90deg_22	GATAGAACCCTTCTGATAACAACGCCAGTCGGAAATGAAA
90deg_23	AACAGTAGGGCTTAATGAAAAAGCCTGTTTAGTATCATAT
90deg_24	CTCCTCACCCGCTTTCCAACATGTAAATCAATATATGTGA
90deg_25	CTTTGACCCTTAATCATTGTGAATTGGTTTAAGATGATGGTTATCATC
90deg_26	AACGAACTAATTTTTGCGTAAAGCCAGTTGAGGCATGGTCATAAATTTAGGCAGAGG
90deg_27	GTGAATAACCTTGCTTCTTTAATGGA
90deg_28	GGATATTCGCTGGCTGACCTTCAT
PolyT_1	TGAATCCCCCTCAATGCTTTAAACAGTTTTT
PolyT_2	TTTTCCGTTCCAGTAAGGTCTATCATTTT
PolyT_3	TTTTCAACTCGTATTAAATCCTTTGGAAGGAGTATTATTATACTT
PolyT_4	TTTTCATCAACATTAAATACTGGTATTTT
PolyT_5	TTTTGGGCGATGGCCCACTAAAAAACC
PolyT_6	TTTTCGCCAGCTAGTTTGAGGGGACTTTT
PolyT_7	TTTTAGAAATTGCGTAGATGTAAAACAGAAATAATTTT
PolyT_8	TGTGAGCGCATCTGCCGGCGAAAGGGCCTCTTCGCTATTATTTT
PolyT_9	TTTTTCAGAAAACGAGAGCAACACTATCATAAC
PolyT_10	AGTAAGAATGACCAATTTCATCTTCTGACCTAAATTTT
PolyT_11	ACCAGACGACGATAAATGCCCGAATCATTTTGGACTTTAC
PolyT_12	TTTTTTTAATGGTTTGAGAGTCAATAGTGAATTTATTTT
PolyT_13	TTTTAAGTTACAAAAAACAATTCGATTTT
PolyT_14	TTTTTCAAAATTATTTGCACGTTAGAACCTACCATATTTT
PolyT_15	TTTTGCGATTAATGTAGCCAGCTTTTTTT
PolyT_16	GTTGGGTAGGGGATGTGCTGCAAGTTTT
PolyT_17	TTTTGACGACAGTATCGCGTCATACTTTT
PolyT_18	TTTTTCAAAATCATAGGTCTGAAGGCGAATTATTCTTTT
PolyT_19	TTTTATAAGTTTCCCACCCTCAGAGCTTTT
PolyT_20	TTTTCGCCACCAGAACCATCACCCATTTT
PolyT_21	TTTTAGTTTGAGTAACATTACGTTATTAATTTTAAATTTT
PolyT_22	TTTTAATCAAGTTTTTTGGGCGTGAACCACCACCAAAGCGCA
PolyT_23	TTTTATTTCAATTACCTCCTGATTGCTTTGAATACCTTTT
PolyT_24	TTTTATGGCTTTGTCTCTGAATTTATTTT
45deg_1	GCGCCGACAATAGCATGTGAATAGAAGTTTTCACGGTCATA
45deg_2	AAGGAATTGCGTTCTTAAACGGCCTGGAGGTGTAACGGCATCAGATGCC
45deg_3	AAAATACGTATTCGGTCGCTGAGCACGCATAATTTACGAATAAACA
45deg_5	CGCAAAGATAAGACTCCTTATTACGCAGT
45deg_6	GGGTTACCAGACGATCCAGCGCAGACCGTCACGCCTGGCATTAAAGG
45deg_8	TGGGTAAAGGTTTCTTTGCTCGT
45deg_9	CATATAAAAGAAAAAGGCAAATAACATCC
45deg_10	TGCTTTCGAGGTGAATAATAATACGACTTGATGCACTCTGTG
45deg_11	TTTCAACAGTTTCAGGCAAGCCACGATCTAATCAATAA
45deg_12	AAGTAATTCTGTCCAGCGTCTGAACAGAATGCAACCGATTTATTCATTAAA
45deg_13	AGAACAATATTACCGCGACAGGAAAATCAGTGGGCAACAG
45deg_14	GAATTAGCAAAATTAAGCAATAA
45deg_16	GTTAAAGGCCGAACCGAGGCAGCTTGAAATGAAATATTATGACCCTGTAAT
45deg_17	GTGCTGCGCTTTCACCAACGGAAATGAGGGAGGGAAGGTA
45deg_18	ACCCAAAAGAACTAATTCTGCGAACGAGTAGATTTAGTTTGACC
45deg_19	CAGGGATACGGAGTGAAGAAACCACCATCCTAACCGATAGAAGTTTCATTCCAT
45deg_20	TCATTTGGAATAACCTTAATAACGGAAT
45deg_21	CTGATTGCATTAGCACCACCACCACGTTGAAATATAGAACCAAGTACCGCACT
45deg_22	AAAGACAAAAGGGGCTGGTAAGAGCCGGGTCACTGTTATACAGGC
45deg_23	CGACATTCCACCACGGAATAAGTTTATTT
45deg_24	AATAAATCTGATTCCCGGCATGATCCATCGCCGCTTGCAGGGA
45deg_25	TCGGCTGAGGCTTATTTCCATTAACCCTCAGCAGCGAAAGCAGAT
45deg_26	AATTCTACTAATAGTAGTAGCAT
45deg_27	AAAGTTACCAGAAGGACTTTTGCGTATCATTCTACCGATAGTT
45deg_28	GGTGAATTATCTGTCACTGTCATATGGAATCGTTCCAGCATC
45deg_29	CAAGAACGGGTATTAATCTTTCCTGGATCGTCAACGGGT
45deg_30	AGCGGGGTGGTTGTATAAAGGTGGCAA
45deg_31	TACGGCTGGCCATTTGGGAATTAGCCTTCACCATTTTTTCCTCATTTT
45deg_32	ATGTTAGCAAACGTAGAAAAAAACGCAA
45deg_34	GATTTTAAATATTGGTGAGACGCAGGGTGGTTTTTCTATGGATT
45deg_35	ATAACAGTACGACGACGACAACAAGGCGGGCCAGGAACAACTA
45deg_37	TCCGCCGGGCGCGGTTGCGGTAT
45deg_38	TGTCACAATCAATAGAAAATTACATACACCAAAAACTATATTT
CSv2_ssDNA_45deg_1	CATTGCAGGCGCTTTCGCACTCA
CSv2_ssDNA_45deg_2	TTAGATACATTTCGCAAATGGTC
CSv2_ssDNA_45deg_3	GCCTCAGAGCATAAAGCTAAATC
CSv2_ssDNA_45deg_4	ATAAACATCCCTTACACTGGTGTGTTCAGCATTTACCAGCGCC
CSv2_ssDNA_45deg_5	GGCGCGAGCTGAAAAGGTGGCAT

oligoname	sequence
Core_1	TTGGGCGCAGGCCACCGAGTAAAAGTTTTTAT
Core_2	GGCCAACGCGCGGGGGCCTGTTCAGCCAGTA
Core_3	CACACGACATTAGTCTAAAAACGCTCATGGAACAGCCATT
Core_4	TCGTGCCAGCTGCATTCCAACAGATACGTGGC
Core_5	CATTCTGGAATGAATCAAAACATCACTCAAACTATCGGC
Core_6	CCTCCGGCAGGAATTAACCAGAAGATAAGGCTTAAATTGGGCTTGAGA
Core_7	TAGAATCACAATGAAACCATCGATAGCAGCACCGTCAGCGACGTATA
Core_8	GCTAAACAGGAGGCCGCCTGAGAGCCATTACCAGCCAGCA
Core_9	ATCGGAACGGGAAAGCGGTTGAGGCAGGTCA
Core_10	TTGAAAAATAAGAATAAACACCGGAATCATCGCAAGA
Core_11	GCCAGCATCAGAACCGTGCCGTAAAGCACTAA
Core_12	CGAGGCGTGCTCCATGTTACTTACCGTAAC
Core_13	TTAAAATTATCACCGCGGTCACGCTGCGCGT
Core_14	AGGTCATGCCTTGAAGTGTAGGATTTAGAGCTTGACG
Core_15	TTAGGTTGCCTCAATCAACATCAATTTTACATCGGGAGAA
Core_16	TGGTGCTGTGATAATCACTCAGGAAATTTTTATCAGAGAGATAACCC
Core_17	GTAGAAGAGCCATTAAAAATACCGCGTAAGAA
Core_18	TAATGCCGGAGAGGGTTCTAGCGAGACTCAACCGTG
Core_19	CGGTACGCCAGAATCCAGCCGGAACTTGCTGG
Core_20	ATATTCATAGGCTTTTGCAAAAGATTCAGTGAGAGCGGAACAATTCAT
Core_21	CGGCGAACGGAGCGGGCGCTAGGGTTAAAGAA
Core_22	AAAGGAAGTCGAGGCCACCCTCAGAGCCATAACGGGGCAGGAGTG
Core_23	CCTGCATCTGCAGCCATCCCACGCAACCAGCTACTTTTGC
Core_24	TGAGAAGTGAGTCTGTTAATATCCTTAATGCGCGAACTGA
Core_25	CCGCGACCCAGACGGTCAATCATAAGGGAACC
Core_26	CTTTTTAATTTAGTTATAAATCAAAAATCAGG
Core_27	CCTAAAGGCGCCTCCCTCAGAGCCCGTATAAATTATTCTGGTGGGAAC
Core_28	GAGCCGCCAAGAGGCTTCAGTGCCCGCGTCTGGCCTTCC
Core_29	AGTTTTGCGATACATACTCACTATGCGAGAAAACTTTTTC
Core_30	CAGCAGGCCAAGCGGTCCACGCTGTGACGAGC
Core_31	ATATGATATTCAACCGTAGCTATTTTAAAGCCAAGCGAAAGTGGCGAG
Core_32	CACCATCACCGGCACCGCTTCTGGATTCAGGC
Core_33	TGCGGAATCGTCATAATCTTTACCACGCCAAA
Core_34	CGTACTATGGTTGCTTTGGTGGTTACCCCGGTCGGCAGC
Core_35	AGAACCCTCATATATTTTAAATGGCCCGGAA
Core_36	AAGGATAAAGGAGCCTACAAGCAAGCCGTTTTTATTTTCAGCGCTAAT
Core_37	GGCGTTAACATAGCGATAGCTTAGATGAAACA
Core_38	AATTACTATTAATTAATTTTCCCTTGTAAATC
Core_39	ACAGACAATATTTTTTAGCCCT
Core_40	AAAAGGTAACATGTTCAGCTAATGGTGTCTGGTTTTAAA
Core_41	ATAAGAGAATATAAAGTCACCAGTTTTGCGTAGCAACAGG
Core_42	TTGTAGAACGTAATCCATTTTCGACGTGCTTTCCTCGT
Core_43	TATAGTCAGAAGCAAGATAGCG
Core_44	ATCTACAAAGGCTATCAGTCAAATGGGGTTTTATAGGTCAAAACGGCG
Core_45	TGATGATATGATAAATGCCTCAGGAAGATCG
Core_46	GAATGGCTCAGTAATAAAAGGGACATTTTCG
Core_47	GTCCACTACGCTGGCATATTCACAAACAAATAGGATTAGC
Core_48	ATCAGCTGGGAGAAGAGCCCAATAATAAGAGCCGAAGCC
Core_49	ATACCTAATTTACATTGGCAGATTACCGACCCGGGGGT
Core_50	CATTTTGACGCTCAATGCCCTGCG
Core_51	GCGGTGCCGAAAATCCTGTTTGAGTTTGCCCAATGCCAAGTCTGGTC
Core_52	TTCGCGTCCGTGAGCAATTGCTCACCGTTGT
Core_53	TTTGAGAGCGTGGACTCCAACGTCAAAGGGCGGGGAAGAAGAATGGA
Core_54	CCATCACGCAAATTACTGTATGGACTGAGTTCATTCCA
Core_55	CATTCAACTAATGCACAGAGGGGTCCAATAC
Core_56	AATATCTGGTCAGTTAGAAACCCGAGGCATATAGCGAG
Core_57	GGCAAATCGAGACTACGCTGAGAAAATACCGACCGTGTGATAAATAAAAATATAT
Core_58	CGCATTAACCAGGCGATATTTTGTGCCTGAGCAGTTTGGAACAAGA
Core_59	TTAATTGTATCGGTTTAAATCACCTGGTGCCA
Core_60	TACCGCCAATCACCGTAGAAAAGCTCATATGTCCGAAATCGGCAAAAT
Core_61	GGTTTAGATCATTACCGCGCCCATCGGAACG
Core_62	GCTCCAAACCTCAGAGCGAGGCGTTTTAGCGTTTGAGGAAGGGTAGC
Core_63	GCTCATTTTTTAACCAATAGGAACACGTTGTA
Core_64	GTCCTGAACAAGAAAATTCTCGCCA
Core_65	GATTTTGCTAAACAACGCACGCGTAGAGGCGG
Core_66	GCGATTTAAGAACTGCTGAATAACACCAGAATGTTTGGACGGAACAA
Core_67	TACCTTATAGGACGTTGGGAAGAACTAATAAAATATC
Core_68	CAAAAGAATACACTAAACTACAACAAGAGGTCTACCTTT
Core_69	CTAAAGACTTTTTCATGAGGAAGTCCGGTATT
Core_70	TTGAGTAACAGTGCCGCCACCCTTGACAGGA
Core_71	CAGTTAATGCCCCCTGATTTTTGTAGCCACCA
Core_72	GGTTATCTGATTAGAGACAGTACCATTTGAATTACCTTTACATTTA
Core_73	ACCGCCACCCTCAGAGAGGCCGGAAGTAGCAAGTTGCAGGGTGCCC
Core_74	GAAAGGAATTGAGGAACAATATAATACCAGTC
Core_75	TCGTCACCAGTACAAGTCGAAATAGCAATAC
Core_76	TCGCGCAGGATTTAGATTTCAGGTTTAACGTCAGATGAATACAATAAC
Core_77	CAGTCACGGCCATCAAGATTCTCCAAACATGAAAGTATT
Core_78	CATTTGAGAACAGTTGGATTCGGAGCAAAGAAGATGATTAAGAC
Core_79	TTGAGTTACCTTTATTTCAACGCACCGTCGGCCGCAAG
Core_80	AACGGCTAAGTTACAAAATAAACAACGATTTT
Core_81	CATAAAGTGGATGGCTTAGAGCTAAAGAGG
Core_82	TTGAAGCGTCTTTCCGACTTGCCCGTTCCGCCCTCAGAACCGCCAC
Core_83	TATGCAACTGCTGTAGTCGTCTTTTTAGCGTACAATAGGAACCCATGT
Core_84	CGCCTGTTTATCAACAGCTCGAATTGAAATTGCCGGAAG
Core_85	AGTAACACCTCACCACGCCAGGGTTTTCC
Core_86	ACAATTTCGAAAACAAAATTAATTTAGAATCCAACTATACAAAGAAC
Core_87	CGTTGGTGGCGCCATGTGCGCAACTGTTGGGA
Core_88	GTAATGGGGCTCAGTACCTATTTCGGAACCTA
Core_89	TCATTTGACCAGGCAGAAAGGCCGGAGAC
Core_90	CAAATCAGAATCTCCAAAAAAAAGAGCAGCAAAACGTCACGAGCGGGA
Core_91	GTTTAGCAGCAATAGCTATCTTACAAGAAAC
Core_92	TTCAGAGGAAACGACGGCCAGTGCGGTTGTGTAAATCACCGCCAG
Core_93	TGGAGCCGCCACGGGAAACGTACATAGATGGGCCAGCTTT
Core_94	ATAATATCAAGTTTTGCTCAACATTAATGCCACTACGAAGGCACCAAC
Core_95	TTATCCGCTCACAATTTAAAGTACGCAGAACG
Core_96	ATCCCCGGGTACCGAATAGATAATAACATACGAG
Core_97	TCCTGATCGAGTAGTGCCCTGACGAGAAAAACCAAA
Core_98	TTTAGGAGACCTCAAATATCAAACGGTTATAT
Core_99	CAGGGAAGAAAGCGCCATTCGCCTGCCGGAA
Core_100	AGGGCGATCACTCCAGCGCATCGTCTCAAGAGAAGGATTAAATCCTCA
Core_101	TTGTTTAACGTCAAAAGTAATTGACAGAGCCTTAGGTGTGCAAACGC
Core_102	ATACAGTACCGTCAATAGATAATAGCTCATTA
Core_103	TTTACCAGTCCCGGACCAAGCTGATTGACC
Core_104	CGGTGCGGGAAACAATCGGCGAACGGATAAACCCGTCGAAATAATT
Core_105	CCTCATAGCCAGACGTTAGTAAATGAATTTTCTTTTGATGCCTGTAG
Core_106	AGCCGAACCTTTTTAAGAAAAGTACAATCCAACAAGAACATCGAGA
Core_107	CAGACAGCCTAAAACGTAATTGCTGAATATAACCACACAA
Core_108	AATAAGAAGCCATATTATTTATCCAGACAGCAATAGCAAGCTAAGAAC

Figure B.16 Sequences of staple oligonucleotides of CS-v2-out1ss.

oligoname	sequence
135deg_1	TTACCAACGCACGCAGAAACAGC
135deg_2	GGATCAAACTTAAATCCTGAATC
135deg_3	AAAAGAGTAACGAGCCTTAAATCAAGATTAGTT
135deg_4	GGCCTTTAGTGATGTACATCGACATAAA
135deg_5	CAAGTTTGCCTTTAAAGGGTAAAGTTA
135deg_6	GACGATTGCCGGAACGAGCCCCCGAACCAGGCGTCAGACTGTAG
135deg_7	AACGGAACGTTTGTATAAGCAA
135deg_8	TGTAGGTAAAGATTCACCGTCGAGAGGGT
135deg_9	AACACCCTGAACAAAGTCAGAGGATGAAAATTCACGGAAATTTGCC
135deg_10	AAAGGGTGCGCATTAGACGGGAGAATTAACTG
135deg_11	ATGAACGGTAATCGTAAAACTAGCATGTCAA
135deg_12	CCCAAAAACAGGGCGGTCATAGCCCCCTTATTAGCGTTTGC
135deg_13	GAGAATAACATAAAAACTTTCTCCGTGGT
135deg_14	AACGATGCTGATTGAAAGCCGCACAGGC
135deg_15	TGATATAAGTATACAATGCCTGAGTAATG
135deg_16	ATATTTAAATTGTACATCCTCAT
135deg_17	CGCGTTTTCATCGGAGTAGCGACAGAAT
135deg_18	GTCGCTGGCAGCCTCCGACAATTTTATTTCTGCGAGATAGA
135deg_19	GCTATTTTGCACCCAGCTCAGTTGGGATTTGTGA
135deg_20	CATCTTTTCATAATCAAAGCCAGAGCAAACGTTAGATAAGTG
135deg_21	TGTTGTTCAGTCTGGAGCAAACAAGAGAATCG
135deg_22	GCCGCGCTTAATGAATCAAAAGAATAGC
135deg_23	GAAGGGATAGCTCAGCAGCCTTTACAGA
135deg_24	CCCTTATACGCCGCTCAGGAAGAGCCGCACGGTCCGTTTTTTCGTCTC
135deg_25	CCGAGATAGGGTTGAGAACCACCACACCC
135deg_26	AAAATCCCGTAAAAGGGAGGTTCAGAGGCAACCTCCTCGTAGGA
90deg_1	GCGTTATACAAATTCTTACCAGTCCTGAAAGAACGAACCGAAACCTG
90deg_2	CCGAAAGACTTCAAAAAGATAAAACAGAGG
90deg_3	AACAGTACATAGCTGTTTCCTGTGTCGTAAT
90deg_4	TGAGGCGGTCAGTATTAAGATTAAGAGGAAGC
90deg_5	TAATGAGTGCACTAACAAAATCTAGATTATCATTTCAACTGTAACAAAGCTGCTCA
90deg_6	ACGGTGTACAGACCAGGCGCATAGTTAGACTGAGCGGATTGAATACCA
90deg_7	TTGCCTGATTCTTGATTAGTAATGGTCAGGATTGTATCACAAGAACC
90deg_8	TTGCGTTGCGCTCACTGTGGGGTGCC
90deg_9	GCGCGAACAAAGTACAAACACTCAT
90deg_10	CTTGCTGAAGCTAACTCACATTAA
90deg_11	AATCTAAACTGCAACAGTGCCACG
90deg_12	AAAGCGAACCAGACCGGCATCAAAAACACCGCAATCCAAT
90deg_13	CTCCAACATTTAATTCGAGCTTC
90deg_14	ATATTCCTTCAGTTGAAAATCAACCCAGCGATTATACCAA
90deg_15	CAGGTAGAAAGATTCACGTTAATAA
90deg_16	CAAGAGTAATCTTGACAACTTTGAAAGAGGACAGATGA
90deg_17	TAAATTGTACGGAGATTTAGAGAGACGGAACAACATTATTA
90deg_18	GTAATAGTAAAATGTATTACCCGATTTAGGAAGCAAA
90deg_19	CTGAGAGCCAGCAGCACCAGCAGTATCGCGTAACATCACGAACTGACTCGCCTGA
90deg_20	GCCATATTATAAGCCAACGCTC
90deg_21	TGTTAAATCGTAGCAGCATCGTCACGTGCGTATGAGAATC
90deg_22	GATAGAACCCTTCTGATAACAACGCCAGTCGGAAATGAAA
90deg_23	AACAGTAGGGCTTAATGAAAAAGCCTGTTTAGTATCATAT
90deg_24	CTCCTCACCCCGCTTTCCAACATGTAAATCAATATATGTGA
90deg_25	CTTTGACCCTTAATCATTGTGAATTGGTTTAAGATGATGGTTATCATC
90deg_26	AACGAACTAATTTTTGCGTAAAGCCAGTTGAGGCATGGTCATAATTTAGGCAGAGG
90deg_27	GTGAATAACCTTGCTTCTTTAATGGA
90deg_28	GGATATTCGCTGGCTGACCTTCAT
PolyT_1	TGAATCCCCCTCAAATGCTTTAAACAGTTTTT
PolyT_2	TTTTCCGTTCCAGTAAGGTCTATCATTTT
PolyT_3	TTTTCAACTCGTATTAAATCCTTTGGAAGGAGTATTATTATACTT
PolyT_4	TTTTCATCAACATTAAATACTGGTATTTT
PolyT_5	TTTTGGGCGATGGCCCACTAAAAAACC
PolyT_6	TTTTCGCCAGCTAGTTTGAGGGGACTTTT
PolyT_7	TTTTAGAAATTGCGTAGATGTAAAACAGAAATAATTTT
PolyT_8	TGTGAGCGCATCTGCCGGCGAAAGGGCCTCTTCGCTATTATTTT
PolyT_9	TTTTTCAGAAAACGAGAGCAACACTATCATAAC
PolyT_10	AGTAAGAATGACCAATTTCATCTTCTGACCTAAATTTT
PolyT_11	ACCAGACGACGATAAATGCCCGAATCATTTTGGACTTTAC
PolyT_12	TTTTTTTAATGGTTTGAGAGTCAATAGTGAATTTATTTT
PolyT_13	TTTTAAGTTACAAAAAAACAATTCGATTTT
PolyT_14	TTTTTCAAAATTATTTGCACGTTAGAACCTACCATATTTT
PolyT_15	TTTTTGCGATTAATGTAGCCAGCTTTTTTT
PolyT_16	GTTGGGTAGGGATGTGCTCCAAGTTTT
PolyT_17	TTTTGACGACAGTATCGCGTCATACTTTT
PolyT_18	TTTTTCAAAATCATAGGTCTGAAGGCGAATTATTCTTTT
PolyT_19	TTTTATAAGTTTCCACCCTCAGAGCTTTT
PolyT_20	TTTTCGCCACCAGAACCATCACCCATTTT
PolyT_21	TTTTAGTTTGAGTAACATTACGTTATTAATTTTAAATTTT
PolyT_22	TTTTAATCAAGTTTTTTGGGCGTGAACCACCACCAAAGCGCA
PolyT_23	TTTTATTTCAATTACCTCCTGATTGCTTTGAATACCTTTT
PolyT_24	TTTTATGGCTTTGTCTCTGAATTTATTTT
45deg_1	GCGCCGACAATAGCATGTGAATAGAAGTTTTCACGGTCATA
45deg_3	AAAATACGTATTCGGTCGCTGAGCACGCATAATTTACGAATAAACA
45deg_5	CGCAAGATAAGACTCCTTATTACGCAGT
45deg_8	TGGGTAAGGTTTCTTGCTCGT
45deg_9	CATATAAAAGAAAAAGGCAAATAACATCC
45deg_11	TTTCAACAGTTTCAGGCAAGCCACGATCTAATCAATAA
45deg_12	AAGTAATTCTGTCCAGCGTCTGAACAGAATGCAACCGATTTATTCATTAAA
45deg_13	AGAACAATATTACCGCGACAGGAAAATCAGTGGGCAACAG
45deg_14	GAATTAGCAAAATTAAGCAATAA
45deg_17	GTGCTGCGGCTTTCACCAACGGAAATGAGGGAGGGAAGGTA
45deg_18	ACCCAAAAGAACTAATTCTGCGAACGAGTAGATTTAGTTTGACC
45deg_19	CAGGGATACGGAGTGAAGAAACCACCATCCTAACCGATAGAAGTTTCATTCCAT
45deg_22	AAAGACAAAAGGGGCTGGTAAGAGCCGGGTCACTGTTATACAGGC
45deg_23	CGACATTCCACCACCGAATAGTTTATTT
45deg_24	AATAAATCTGATTCCCGGCATGATCCATCGCCGCTTGCAGGGA
45deg_25	TCGGCTGAGGCTTATTTCCATTAACCCTCAGCAGCGAAAGCAGAT
45deg_26	AATTCTACTAATAGTAGTAGCAT
45deg_34	GATTTTAAATATTGGTGAGACGCAGGGTGGTTTTTCTATGGATT
45deg_35	ATAACAGTACGACGACGACAACAAGGCGGGCCAGGAACAACTA
45deg_37	TCCGCCGGGCGCGGTTGCGGTAT
45_ss_links_1	TCATTTGGAATAACCTTAATAACGGAA
45_ss_links_2	TGTTAGCAAACGTAGAAAAAAACGCAA
45_ss_links_3	GCCTCAGAGCATAAAGCTAAATC
45_ss_links_4	AGGAATTGCGTTCTTAAACGCGCCTGGAGGTGTAACGGCATCAGATGCC
45_ss_links_5	AAAGTTACCAGAAGGACTTTTGCGTATCATTCTACCGATAGT
45_ss_links_6	GGGTTACCAGACGATCCAGCGCAGACCGTCACGCCTGGCATTAAAG
45_ss_links_7	TTAAAGCCCGAACCGAGGCAGCTTGAAATGAAATATTATGACCCTGTAAT
45_ss_links_8	GGCGCGAGCTGAAAAGGTGGCAT
45_ss_links_9	TGCTTTCGAGGTGAATAATAATACGACTTGATGCACTCTGT
45_ss_links_10	AGCGGGGTGGTTGTATAAAGGTGGCA
45_ss_links_11	TACGGCTGGCCATTTGGGAATTAGCCTTCACCATTTTTTCCTCATTT
45_ss_links_12	ATAAACATCCCTTACACTGGTGTGTTCAGCATTTACCAGCGC
45_ss_links_13	CAAGAACGGGTATTAATCTTTCCTGGATCGTCAACGGG
45_ss_links_14	GTCACAATCAATAGAAAATTACATACACCAAAAACTATATTT
45_ss_links_15	CATTGCAGGCGCTTTCGCACTCA
45_ss_links_16	TGATTGCATTAGCACCACCACCACGTTGAAATATAGAACCAAGTACCGCACT
45_ss_links_17	CGGCTGAGGCTTATTTCCATTAACCCTCAGCAGCGAAAGCAGAT
45_ss_links_18	TTAGATACATTTCGCAAATGGTC
45_ss_links_19	GTGAATTATCTGTCACTGTCATATGGAATCGTTCCAGCATC

oligoname	sequence
Core_1	TTGGGCGCAGGCCACCGAGTAAAAGTTTTTAT
Core_2	GGCCAACGCGCGGGGGCCTGTTCAGCCAGTA
Core_3	CACACGACATTAGTCTAAAAACGCTCATGGAACAGCCATT
Core_4	TCGTGCCAGCTGCATTCCAACAGATACGTGGC
Core_5	CATTCTGGAATGAATCAAAACATCACTCAAACTATCGGC
Core_6	CCTCCGGCAGGAATTAACCAGAAGATAAGGCTTAAATTGGGCTTGAGA
Core_7	TAGAATCACAATGAAACCATCGATAGCAGCACCGTCAGCGACGTATA
Core_8	GCTAAACAGGAGGCCGCCTGAGAGCCATTACCAGCCAGCA
Core_9	ATCGGAACGGGAAAGCGGTTGAGGCAGGTCA
Core_10	TTGAAAAATAAGAATAAACACCGGAATCATCGCAAGA
Core_11	GCCAGCATCAGAACCGTGCCGTAAAGCACTAA
Core_12	CGAGCGTGCTCCATGTTACTTACCGTAAC
Core_13	TTAAAATTATCACCGCGGTCACGCTGCGCGT
Core_14	AGGTCATGCCTTGAAGTGTAGGATTTAGAGCTTGACG
Core_15	TTAGGTTGCCTCAATCAACATCAATTTTACATCGGGAGAA
Core_16	TGGTGCTGTGATAATCACTCAGGAAAATTTTTATCAGAGAGATAACCC
Core_17	GTAGAAGAGCCATTAAAAATACCGCGTAAGAA
Core_18	TAATGCCGGAGAGGGTTCTAGCGAGACTCAACCGTG
Core_19	CGGTACGCCAGAATCCAGCCGGAACTTGCTGG
Core_20	ATATTCATAGGCTTTTGCAAAAGATTCAGTGAGAGCGGAACAATTCAT
Core_21	CGGCGAACGGAGCGGGCGCTAGGGTTAAAGAA
Core_22	AAAGGAAGTCGAGGCCACCCTCAGAGCCATAACGGGGCAGGAGTG
Core_23	CCTGCATCTGCAGCCATCCCACGCAACCAGCTACTTTTGC
Core_24	TGAGAAGTGAGTCTGTTAATATCCTTAATGCGCGAACTGA
Core_25	CCGCGACCCAGACGGTCAATCATAAGGGAACC
Core_26	CTTTTTAATTTAGTTATAAATCAAAAATCAGG
Core_27	CCTAAAGGCGCCTCCCTCAGAGCCCGTATAAATTATTCTGGTGGGAAC
Core_28	GAGCCGCCAAGAGGCTTCAGTGCCCGCGTCTGGCCTTCC
Core_29	AGTTTTGCGATACATACTGACTATGCGAGAAAACTTTTTC
Core_30	CAGCAGGCCAAGCGGTCCACGCTGTGACGAGC
Core_31	ATATGATATTCAACCGTAGCTATTTTAAAGCCAAGCGAAAGTGGCGAG
Core_32	CACCATCACCGGCACCGCTTCTGGATTCAGGC
Core_33	TGCGGAATCGTCATAATCTTTACCACGCCAAA
Core_34	CGTACTATGGTTGCTTTGGTGGTTACCCCGGTCGGCAGC
Core_35	AGAACCCTCATATATTTTAAATGGCCCGGAA
Core_36	AAGGATAAAGGAGCCTACAAGCAAGCCGTTTTTTATTTTCAGCGCTAAT
Core_37	GGCGTTAACATAGCGATAGCTTAGATGAAACA
Core_38	AATTACTATTAATTAATTTTCCCTTGTAAATC
Core_39	ACAGACAATATTTTTTAGCCCT
Core_40	AAAAGGTAACATGTCAGCTAATGGTGTCTGGTTTTAAA
Core_41	ATAAGAGAATATAAAGTCACCAGTTTTGCGTAGCAACAGG
Core_42	TTGTAGAACGTAATCCATTTTCGACGTGCTTTCCTCGT
Core_43	TATAGTCAGAAGCAAGATAGCG
Core_44	ATCTACAAAGGCTATCAGTCAAATGGGGTTTTATAGGTCAAAACGGCG
Core_45	TGATGATATGATAAATGCCTCAGGAAGATCG
Core_46	GAATGGCTCAGTAATAAAAGGGACATTTTCG
Core_47	TGTCACTATGGTTGCTATTCACAAACAAATAGGATTAGC
Core_48	ATCAGCTGGGAGAAGAGCCCAATAATAAGAGCCGAAGCC
Core_49	ATACCTAATTTACATTGGCAGATTACCGACCCGGGGGT
Core_50	CATTTTGACGCTCAATGCCCTGCG
Core_51	GCGGTGCCGAAAATCCTGTTTGAGTTTGCCCAATGCCAAGTCTGGTC
Core_52	TTCGCGTCCGTGAGCAATTGCTCACCGTTGT
Core_53	TTTGAGAGCGTGGACTCCAACGTCAAAGGGCGGGGAAGAAGAATGGA
Core_54	CCATCACGCAAATTACTGTATGGACTGAGTTCATTCCA
Core_55	CATTCAACTAATGCACAGAGGGGTCCAATAC
Core_56	AATATCTGGTCAGTTAGAAACCCGAGGCATATAGCGAG
Core_57	GGCAAATCGAGACTACGCTGAGAAAATACCGACCGTGTGATAAATAAAAATATAT
Core_58	CGCATTAACAGGCGATATTTGTGCCTGAGCAGTTTGGAACAAGA
Core_59	TTAATTGTATCGGTTTAAATCACCTGGTGCCA
Core_60	TACCGCCAATCACCGTAGAAAAGCTCATATGTCCGAAATCGGCAAAAT
Core_61	GGTTTAGATCATTACCGCGCCCATCGGAACG
Core_62	GCTCCAAACCTCAGAGCGAGGCGTTTTAGCGTTTGAGGAAGGGTAGC
Core_63	GCTCATTTTTTAACCAATAGGAACACGTTGTA
Core_64	GTCCTGAACAAGAAAATTCTGCCA
Core_65	GATTTTGCTAAACAACGCACGCGTAGAGGCGG
Core_66	GCGATTTTAAGAACTGCTGAATAACACCAGAATGTTTGGACGGAACAA
Core_67	TACCTTATAGGACGTTGGGAAGAAACTAATAAAAATATC
Core_68	CAAAAGAATACACTAAACTACAACAAGAGGTCTACCTTT
Core_69	CTAAACACTTTTCATGAGGAAGTCCGGTAATT
Core_70	TTGAGTAACAATGCGCCACCCTTCACAGGA
Core_71	CAGTTAATGCCCCCTGATTTTTGTAGCCACCA
Core_72	GGTTATCTGATTAGAGACAGTACCATTTGAATTACCTTTACATTTA
Core_73	ACCGCCACCCTCAGAGAGGCCGGAAGTAGCAAGTTGCAGGGTGCCC
Core_74	GAAAGGAATTGAGGAACAATATAATACCAGTC
Core_75	TCGTCACCAGTACAAGTCGAAATAGCAATAC
Core_76	TCGCGCAGGATTTAGATTTCAGGTTTAACGTCAGATGAATACAATAAC
Core_77	CAGTCACGGCATCAAGATTCTCCAAACATGAAAGTATT
Core_78	CATTTGAGAACAGTTGGATTCGGAGCAAAAGAAGATGATTAAGAC
Core_79	TTGAGTTACCTTTATTTCAACGCACCGTCGGCCGCAAG
Core_80	AACGGCTAAGTTACAAAATAAACAACGATTTT
Core_81	CATAAAGTGGATGGCTTAGAGCTAAAGAGG
Core_82	TTGAAGCGTCCTGCGACTTCACCAGTCCCGTTCGCCCTCAGAACCGCCAC
Core_83	TATGCAACTGCTGTAGTCGTCTTTTTAGCGTACAATAGGAACCCATGT
Core_84	CGCCTGTTTATCAACAGCTCGAATTGAAATTGCCGGAAG
Core_85	AGTAACACCTCACCACGCCAGGGTTTTCC
Core_86	ACAATTTCGAAAACAAAATTAATTTAGAATCCAACTATACAAAGAAC
Core_87	CGTTGGTGGCGCCATGTGCGCAACTGTTGGGA
Core_88	GTAATGGGGCTCAGTACCTATTTCGGAACCTA
Core_89	TCATTTGACCAGGCAGAAAGGCCGGAGAC
Core_90	CAAATCAGAATCTCCAAAAAAAAGAGCAGCAAAACGTCACGAGCGGGA
Core_91	GTTTAGCAGCAATAGCTATCTTACAAGAAAC
Core_92	TTCAGAGGAAACGCGCCAGTGCGGTTGTGTAAATCACCGCCAG
Core_93	TGGAGCCGCCACGGGAAACGTACATAGATGGGCCAGCTTT
Core_94	ATAATATCAAGTTTTGCTCAACATTAATGCCACTACGAAGGCACCAAC
Core_95	TTATCCGCTCACAATTTAAAGTACGCAGAACG
Core_96	ATCCCCGGGTACCGAATAGATAACATACGAG
Core_97	TCCTGATCGAGTAGTGCCCTGACGAGAAAAACCAAA
Core_98	TTTAGGAGACCTCAAATATCAAACGGTTATAT
Core_99	CAGGGAAGAAAGCGCCATTCGCCTGCCGGAA
Core_100	AGGGCGATCACTCCAGCGCATCGTCTCAAGAGAAGGATTAAATCCTCA
Core_101	TTGTTTAACGTCAAAAGTAATTGACAGAGCCTTAGGTGTGCAAACGC
Core_102	ATACAGTACCGTCAATAGATAATAGCTCATTA
Core_103	TTTACCAGTCCCGGACCAAGCTGATTGACC
Core_104	CGGTGCGGGAAACAATCGGCGAACGGATAAACCCGTCGAAATAATT
Core_105	CCTCATAGCCAGACGTTAGTAAATGAATTTTCTTTTGATGCCTGTAG
Core_106	AGCCGAACCTTTTTAAGAAAAGTACAATCCAACAAGAACATCGAGA
Core_107	CAGACAGCCTAAAACGTAATTGCTGAATATAACCACACAA
Core_108	AATAAGAAGCCATATTATTTATCCAGACAGCAATAGCAAGCTAAGAAC

Figure B.17 Sequences of staple oligonucleotides of CS-v2-1ss.

oligoname	sequence
135deg_1	TTACCAACGCACGCAGAAACAGC
135deg_2	GGATCAAACTTAAATCCTGAATC
135deg_3	AAAAGAGTAACGAGCCTTAAATCAAGATTAGTT
135deg_4	GGCCTTTAGTGATGTACATCGACATAAA
135deg_5	CAAGTTTGCCTTTAAAGGGTAAAGTTA
135deg_6	GACGATTGCCGGAACGAGCCCCCGAACCAGGCGTCAGACTGTAG
135deg_7	AACGGAACGTTTGTATAAGCAA
135deg_8	TGTAGGTAAAGATTCACCGTCGAGAGGGT
135deg_9	AACACCCTGAACAAAGTCAGAGGATGAAAATTCACGGAAATTTGCC
135deg_10	AAAGGGTGCGCATTAGACGGGAGAATTAACTG
135deg_11	ATGAACGGTAATCGTAAAACTAGCATGTCAA
135deg_12	CCCAAAAAACAGGGCGGTCATAGCCCCCTTATTAGCGTTTGC
135deg_13	GAGAATAACATAAAAACTTTCTCCTGGT
135deg_14	AACGATGCTGATTGAAAGCCGCACAGGC
135deg_15	TGATATAAGTATACAATGCCTGAGTAATG
135deg_16	ATATTTAAATTGTACATCCTCAT
135deg_17	CGCGTTTTCATCGGAGTAGCGACAGAAT
135deg_18	GTCGCTGGCAGCCTCCGACAATTTTATTTCTGCGAGATAGA
135deg_19	GCTATTTTGCACCCAGCTCAGTTGGGATTTGTGA
135deg_20	CATCTTTTCATAATCAAAGCCAGAGCAAACGTTAGATAAGTG
135deg_21	TGTTGTTCAGTCTGGAGCAAACAAGAGAATCG
135deg_22	GCCGCGCTTAATGAATCAAAAGAATAGC
135deg_23	GAAGGGATAGCTCAGCAGCCTTTACAGA
135deg_24	CCCTTATACGCCGCTCAGGAAGAGCCGGACGGTCCGTTTTTTCGTCTC
135deg_25	CCGAGATAGGGTTGAGAACCACCACACCC
135deg_26	AAAATCCCGTAAAAGGAGGTTCAGAGGCAACCTCCTCGTAGGA
90deg_1	GCGTTATACAAATTCTTACACAGTCCTGAAAGAACGAACCGAAACCTG
90deg_2	CCGAAAGACTTCAAAAAGATAAAACAGAGG
90deg_3	AACAGTACATAGCTGTTTCCTGTGTCGTAAT
90deg_4	TGAGGCGGTCAGTATTAAGATTAAGAGGAAGC
90deg_5	TAATGAGTGCACTAACAAAATCTAGATTATCATTTCAACTGTAACAAAGCTGCTCA
90deg_6	ACGGTGTACAGACCAGGCGCATAGTTAGACTGAGCGGATTGAATACCA
90deg_7	TTGCCTGATTCTTTGATTAGTAATGGTCAGGATTGTATCACAAGAACC
90deg_8	TTGCGTTGCGCTCACTGTGGGGTGCC
90deg_9	GCGCGAAACAAAGTACAAACACTCAT
90deg_10	CTTGCTGAAGCTAACTCACATTAA
90deg_11	AATCTAAACTGCAACAGTGCCACG
90deg_12	AAAGCGAACCAGACCGGCATCAAAAACACCGCAATCCAAT
90deg_13	CTCCAACATTTAATTCGAGCTTC
90deg_14	ATATTCCTTCAGTTGAAAATCAACCCAGCGATTATACCAA
90deg_15	CAGGTAGAAAGATTCACGTTAATAA
90deg_16	CAAGAGTAATCTTGACAACTTTGAAAGAGGACAGATGA
90deg_17	TAAATTGTACGGAGATTTAGAGAGACGGAACAACATTATTA
90deg_18	GTAATAGTAAAATGTATTACCCGATTTAGGAAGCAAA
90deg_19	CTGAGAGCCAGCAGCACCAGCAGTATCGCGTAACATCACGAACTGACTCGCCTGA
90deg_20	GCCATATTATAAAGCCAACGCTC
90deg_21	TGTAAATGCTGATGCAGCATCACGTCGCTATGAGAATC
90deg_22	GATAGAACCCTTCTGATAACAACGCCAGTCGGAAATGAAA
90deg_23	AACAGTAGGGCTTAATGAAAAAGCCTGTTTAGTATCATAT
90deg_24	CTCCTCACCCCGCTTTCCAACATGTAAATCAATATATGTGA
90deg_25	CTTTGACCCTTAATCATTGTGAATTGGTTTAAGATGATGGTTATCATC
90deg_26	AACGAACTAATTTTTGCGTAAAGCCAGTTGAGGCATGGTCATAATTTAGGCAGAGG
90deg_27	GTGAATAACCTTGCTTCTTTAATGGA
90deg_28	GGATATTCGCTGGCTGACCTTCAT
PolyT_1	TGAATCCCCCTCAAATGCTTTAAACAGTTTTT
PolyT_2	TTTTCCGTTCCAGTAAGGTCTATCATTTT
PolyT_3	TTTTCAACTCGTATTAAATCCTTTGGAAGGAGTATTATTATACTT
PolyT_4	TTTTCATCAACATTAAATACTGGTATTTT
PolyT_5	TTTTGGGCGATGGCCCACTAAAAAACC
PolyT_6	TTTTCGCCAGCTAGTTTGAGGGGACTTTT
PolyT_7	TTTTAGAAATTGCGTAGATGTAAAACAGAAATAATTTT
PolyT_8	TGTGAGCGCATCTGCCGGCGAAAGGGCCTCTTCGCTATTATTTT
PolyT_9	TTTTTCAGAAAACGAGAGCAACACTATCATAAC
PolyT_10	AGTAAGAATGACCAATTTCATCTTCTGACCTAAATTTT
PolyT_11	ACCAGACGACGATAATGCCCGAATCATTTGGACTTTAC
PolyT_12	TTTTTTAATGGTTTGAGAGTCAATAGTGAATTTATTTT
PolyT_13	TTTTAAGTTACAAAAAAACAATTCGATTTT
PolyT_14	TTTTTCAAAATTATTTGCACGTTAGAACCTACCATATTTT
PolyT_15	TTTTGCGATTAATGTAGCCAGCTTTTTTT
PolyT_16	GTTGGGTAGGGGATGTGCTGCAAGTTTT
PolyT_17	TTTTGACGACAGTATCGCGTCATACTTTT
PolyT_18	TTTTTCAAAATCATAGGTCTGAAGGCGAATTATTCTTTT
PolyT_19	TTTTATAAGTTTCCACCCTCAGAGCTTTT
PolyT_20	TTTTCGCCACCAGAACCATCACCCATTTT
PolyT_21	TTTTAGTTTGAGTAACATTACGTTATTAATTTTAAATTTT
PolyT_22	TTTTAATCAAGTTTTTTGGGCGTGAACCACCACCAAAGCGCA
PolyT_23	TTTTATTTCAATTACCTCCTGATTGCTTTGAATACCTTTT
PolyT_24	TTTTATGGCTTTGTCTCTGAATTTATTTT
45_ss_rechts_1	AGAACAATATTACCGCGACAGGAAATCAGTGGGCAACA
45_ss_rechts_2	CGCCGACAATAGCATGTGAATAGAAGTTTTCACGGTCATA
45_ss_rechts_3	ATTTTAAATATTGGTGAGACGCAGGGTGGTTTTTCTATGGATT
45_ss_rechts_4	AAGACAAAAGGGGCTGGTAAGAGCCGGGTCACTGTTATACAGGC
45_ss_rechts_5	CGCCGGGCGCGGTTGCGGTAT
45_ss_rechts_6	AATAAATCTGATTCCCGGCATGATCCATCGCCGCTTGCAGGG
45_ss_rechts_7	ATTCTACTAATAGTAGTAGCAT
45_ss_rechts_8	CCCAAAAGAACTAATTCTGCGAACGAGTAGATTTAGTTTGAC
45_ss_rechts_9	ATAACAGTACGACGACGACAACAAGGCGGGCCAGGAACAACT
45_ss_rechts_10	TGGGTAAAGGTTTCTTTGCTCG
45_ss_rechts_11	AGGGATACGGAGTGAAGAAACCACCATCCTAACCGATAGAAGTTTCATTCCAT
45_ss_rechts_12	TTTCAACAGTTTCAGGCAAGCCACGATCTAATCAATA
45_ss_rechts_13	TGCTGCGGCTTTCACCAACGGAAATGAGGAGGAAGGTA
45_ss_rechts_14	CGCAAAGATAAGACTCCTTATTACGCAG
45_ss_rechts_15	AAATACGTATTCGGTCGCTGAGCACGCATAATTTACGAATAAACA
45_ss_rechts_16	ATATAAAAGAAAAAGGCAAATAACATCC
45_ss_rechts_17	CGACATTCCACCACGGAATAAGTTTATT
45_ss_rechts_18	AAGTAATTCTGTCCAGCGTCTGAACAGAATGCAACCGATTTATTCATTAA
45_ss_rechts_19	GAATTAGCAAAATTAAGCAATA
45_ss_links_1	TCATTTGGAATAACCTTAATAACGGAA
45_ss_links_2	TGTTAGCAAACGTAGAAAAAAACGCAA
45_ss_links_3	GCCTCAGAGCATAAAGCTAAATC
45_ss_links_4	AGGAATTGCGTTCTTAAACGCGCCTGGAGGTGTAACGGCATCAGATGCC
45_ss_links_5	AAAGTTACCAGAAGGACTTTTGCGTATCATTCTACCGATAGT
45_ss_links_6	GGGTTACCAGACGATCCAGCGCAGACCGTCACGCCTGGCATTAAAG
45_ss_links_7	TTAAAGCCGAACCGAGGCAGCTTGAAATGAAATATTATGACCCTGTAAT
45_ss_links_8	GGCGCGAGCTGAAAGGTGGCAT
45_ss_links_9	TGCTTTCGAGGTGAATAATAATACGACTTGATGCACTCTGT
45_ss_links_10	AGCGGGGTGGTTGTATAAAGGTGGCA
45_ss_links_11	TACGGCTGGCCATTTGGGAATTAGCCTTCACCATTTTTTCCTCATTT
45_ss_links_12	ATAAACATCCCTTACACTGGTGTGTTCAGCATTTACCAGCGC
45_ss_links_13	CAAGAACGGGTATTAATCTTTCCTGGATCGTCAACGGG
45_ss_links_14	GTCACAATCAATAGAAAATTACATACACCAAAAACTATATTT
45_ss_links_15	CATTGCAGGCGCTTTCGCACTCA
45_ss_links_16	TGATTGCATTAGCACCACCACCACGTTGAAATATAGAACCAAGTACCGCACT
45_ss_links_17	CGGCTGAGGCTTATTTCCATTAACCCTCAGCAGCGAAAGCAGAT
45_ss_links_18	TTAGATACATTTCGCAAATGGTC
45_ss_links_19	GTGAATTATCTGTCACTGTCATATGGAATCGTTCCAGCATC

oligoname	sequence
Core_1	TTGGGCGCAGGCCACCGAGTAAAAGTTTTTAT
Core_2	GGCCAACGCGCGGGGGCCTGTTCAGCCAGTA
Core_3	CACACGACATTAGTCTAAAAACGCTCATGGAACAGCCATT
Core_4	TCGTGCCAGCTGCATTCCAACAGATACGTGGC
Core_5	CATTCTGGAATGAATCAAAACATCACTCAAACTATCGGC
Core_6	CCTCCGGCAGGAATTAACCAGAAGATAAGGCTTAAATTGGGCTTGAGA
Core_7	TAGAATCACAATGAAACCATCGATAGCAGCACCGTCAGCGACGTATA
Core_8	GCTAAACAGGAGGCCGCCTGAGAGCCATTACCAGCCAGCA
Core_9	ATCGGAACGGGAAAGCGGTTGAGGCAGGTCA
Core_10	TTGAAAAATAAGAATAAACACCGGAATCATCGCAAGA
Core_11	GCCAGCATCAGAACCGTGCCGTAAAGCACTAA
Core_12	CGAGGCGTGCTCCATGTTACTTACCGTAAC
Core_13	TTAAAATTATCACCGCGGTCACGCTCGCGCGT
Core_14	AGGTCATGCCTTGAAGTTAGAGATTTAGAGCTTGACG
Core_15	TTAGGTTGCCTCAATCAACATCAATTTTACATCGGGAGAA
Core_16	TGGTGCTGTGATAATCACTCAGGAAAATTTTATCAGAGAGATAACCC
Core_17	GTAGAAGAGCCATTAAAAATACCGCGTAAGAA
Core_18	TAATGCCGGAGAGGGTTCTAGCGAGACTCAACCGTG
Core_19	CGGTACGCCAGAATCCAGCCGGAACTTGCTGG
Core_20	ATATTCATAGGCTTTTGCAAAAGATTCAGTGAGAGCGGAACAATTCAT
Core_21	CGGCGAACGGAGCGGGCGCTAGGGTTAAAGAA
Core_22	AAAGGAAGTCGAGGCCACCCTCAGAGCCATAACGGGGCAGGAGTG
Core_23	CCTGCATCTGCAGCCATCCCACGCAACCAGCTACTTTTGC
Core_24	TGAGAAGTGAGTCTGTTAATATCCTTAATGCGCGAACTGA
Core_25	CCGCGACCCAGACGGTCAATCATAAGGGAACC
Core_26	CTTTTTAATTTAGTTATAAATCAAAAATCAGG
Core_27	CCTAAAGGCGCCTCCCTCAGAGCCGTATAAATTATTCTGGTGGGAAC
Core_28	GAGCCGCCAAGAGGCTTCAGTGCCCGCGTCTGGCCTTCC
Core_29	AGTTTTGCGATACATACTGACTATGCGAGAAAACTTTTTC
Core_30	CAGCAGGCCAAGCGGTCCACGCTGTGACGAGC
Core_31	ATATGATATTCAACCGTAGCTATTTTAAAGCCAAGCGAAAGTGGCGAG
Core_32	CACCATCACCGGCACCGCTTCTGGATTCAGGC
Core_33	TGCGGAATCGTCATAATCTTTACCACGCCAAA
Core_34	CGTACTATGGTTGCTTTGGTGGTTACCCCGGTCGGCAGC
Core_35	AGAACCCTCATATATTTTAAATGGCCCGGAA
Core_36	AAGGATAAAGGAGCCTACAAGCAAGCCGTTTTTATTTTCAGCGCTAAT
Core_37	GGCGTTAACATAGCGATAGCTTAGATGAAACA
Core_38	AATTACTATTAATTTAATTTTCCCTTGTAAATC
Core_39	ACAGACAATATTTTTTAGCCCTT
Core_40	AAAAGTAACATGTTCAGCTAATGGTGTCTGGTTTTAAA
Core_41	ATAAGAGAATATAAAGTCACCAGTTTTGCGTAGCAACAGG
Core_42	TTGTAGAACGTAATCCATTTTCGACGTGCTTTCCTCGT
Core_43	TATAGTCAGAAGCAAGATAGCG
Core_44	ATCTACAAAGGCTATCAGTCAAATGGGGTTTTATAGGTCAAAACGGCG
Core_45	TGATGATATGATAAATGCCTCAGGAAGATCG
Core_46	GAATGGCTCAGTAATAAAAGGGACATTTTCG
Core_47	GTCCACTACGCTGGCATATTCACAAACAAATAGGATTAGC
Core_48	ATCAGCTGGGAGAAGAGCCCAATAATAAGAGCCGAAGCC
Core_49	ATACCTAATTTACATTGGCAGATTACCGACCCGGGGGT
Core_50	CATTTTGACGCTCAATGCCCTGCG
Core_51	GCGGTGCGAAAAATCCTGTTTGAGTTTGCCCAATGCCAAGTCTGGTC
Core_52	TTCGCGTCCGTGAGCAATTGCTCACCGTTGT
Core_53	TTTGAGAGCGTGGACTCCAACGTCAAAGGGCGGGGAAGAAGAATGGA
Core_54	CCATCACGCAAATTACTGTATGGACTGAGTTCATTCCA
Core_55	CATTCAACTAATGCACAGAGGGGTCCAATAC
Core_56	AATATCTGGTCAGTTAGAAACCCGAGGCATATAGCGAG
Core_57	GGCAAATCGAGACTACGCTGAGAAAATACCGACCGTGTGATAAATAAAAATATAT
Core_58	CGCATTAACCAGGCGATATTTTGTGCCTGAGCAGTTTGGAACAAGA
Core_59	TTAATTGTATCGGTTTAAATCACCTGGTGCCA
Core_60	TACCGCCAATCACCGTAGAAAAGCTCATATGTCCGAAATCGGCAAAAT
Core_61	GGTTTAGATCATTACCGCGCCCATCGGAACG
Core_62	GCTCCAAACCTCAGAGCGAGGCGTTTTAGCGTTTGAGGAAGGGTAGC
Core_63	GCTCATTTTTTAACCAATAGGAACACGTTGTA
Core_64	GTCCTGAACAAGAAAATTCTGCCA
Core_65	GATTTGCTAAACAACGCACGCTAGAGGCGG
Core_66	GCGATTTTAAGAACTGCTGAATAACACCAGAATGTTTGGACGGAACAA
Core_67	TACCTTATAGGACGTTGGGAAGAAACTAATAAAAATATC
Core_68	CAAAAGAATACACTAAACTACAACAAGAGGTCTACCTTT
Core_69	CTAAAGACTTTTTCATGAGGAAGTCCGGTATT
Core_70	TTGAGTAACAGTGCCGCCACCCTTGACAGGA
Core_71	CAGTTAATGCCCCCTGATTTTTGTAGCCACCA
Core_72	GGTTATCTGATTAGAGACAGTACCATTTGAATTACCTTTACATTTA
Core_73	ACCGCCACCCTCAGAGAGGCCGGAAGTAGCAAGTTGCAGGGTGCCC
Core_74	GAAAGGAATTGAGGAACAATATAATACCAGTC
Core_75	TCGTCACCAGTACAAGTCGAAATAGCAATAC
Core_76	TCGCGCAGGATTTAGATTTCAGGTTTAACGTCAGATGAATACAATAAC
Core_77	CAGTCACGGCCATCAAGATTCTCCAAACATGAAAGTATT
Core_78	CATTTGAGAACAGTTGGATTCGGAGCAAAGAAGTGATTAAGAC
Core_79	TTGAGTTACCTTATTTCAACGCACCGTCGGCCGCAAG
Core_80	AACGGCTAAGTTACAAAATAAACAACGATTTT
Core_81	CATAAAGTGGATGGCTTAGAGCTAAAGAGG
Core_82	TTGAAGCGTCTTTCCGACTTGCCCGTTCCGCCCTCAGAACCGCCAC
Core_83	TATGCAACTGCTGTAGTCGTCTTTTTAGCGTACAATAGGAACCCATGT
Core_84	CGCCTGTTTATCAACAGCTCGAATTGAAATTGCCGGAAG
Core_85	AGTAACACCTCACCACGCCAGGGTTTTCC
Core_86	ACAATTTCGAAAACAAAATTAATTTAGAATCCAACTATACAAAGAAC
Core_87	CGTTGGTGGCGCCATGTGCGCAACTGTTGGGA
Core_88	GTAATGGGGCTCAGTACCTATTTCGGAACCTA
Core_89	TCATTTGACCAGGCAGAAAGGCCGGAGAC
Core_90	CAAATCAGAATCTCCAAAAAAAAGAGCAGCAAAACGTCACGAGCGGGA
Core_91	GTTTAGCAGCAATAGCTATCTTACAAGAAAC
Core_92	TTCAGAGGAAACGACGGCCAGTGCGGTTGTGTAAATCACCGCCAG
Core_93	TGGAGCCGCCACGGGAAACGTACATAGATGGGCCAGCTTT
Core_94	ATAATATCAAGTTTTGCTCAACATTAATGCCACTACGAAGGCACCAAC
Core_95	TTATCCGCTCACAATTTAAAGTACGCAGAACG
Core_96	ATCCCCGGGTACCGAATAGATAACATACGAG
Core_97	TCCTGATCGAGTAGTGCCCTGACGAGAAAAACCAAA
Core_98	TTTAGGAGACCTCAAATATCAAACGGTTATAT
Core_99	CAGGGAAGAAAGCGCCATTCGCCTGCCGGAA
Core_100	AGGGCGATCACTCCAGCGCATCGTCTCAAGAGAAGGATTAAATCCTCA
Core_101	TTGTTTAACGTCAAAAGTAATTGACAGAGCCTTAGGTGTGCAAACGC
Core_102	ATACAGTACCGTCAATAGATAATAGCTCATTA
Core_103	TTTACCAGTCCCGGACCAAGCTGATTGACC
Core_104	CGGTGCGGGAAACAATCGGCGAACGGATAAACCCGTCGAAATAATT
Core_105	CCTCATAGCCAGACGTTAGTAAATGAATTTTCTTTTGATGCCTGTAG
Core_106	AGCCGAACCTTTTTAAGAAAAGTACAATCCAACAAGAACATCGAGA
Core_107	CAGACAGCCTAAAACGTAATTGCTGAATATAACCACACAA
Core_108	AATAAGAAGCCATATTATTTATCCAGACAGCAATAGCAAGCTAAGAAC

Figure B.18 Sequences of staple oligonucleotides of CS-v2-2ss

Name	Sequence
Oligo_1	CTGACTCCCCGTCGTGAGCTCCTTACAGGATTAGCAGTTTTTTAGCGAGGTATGTA
Oligo_2	TTTTGCGCCGCTACAGGGGCTGCAAGGCGATTACCCTGGAA
Oligo_3	GCGTTTCCGTGTAGGTCGTTCGCTACGATACGGGAGGGTTT
Oligo_4	TCCAAGCTGGGCTGTGCGACAGGATGTGAGCA
Oligo_5	CCTTTTTCAATATTTTTTTTATTGAAGCATTTAAGCACTAATTCGCCATTCAGGCT
Oligo_6	TTATCAGCCCCACGCTCACCGGCGATCAAGG
Oligo_7	CTGGCCCCAGTGCTGGTGCACGGTTTAGATAAC
Oligo_8	TTTTATCCGCCTCCATCCAGTCTCCAGATCGAGCGCCCTTCGGGACCGGATA
Oligo_9	GCGATCTGTCTATTTCGGTTACCAAGACTTATCCCTTCGG
Oligo_10	GTAAGTTGCCAGTTAGCCACTGGGCCAGGAACCGTAAAACGACACGG
Oligo_11	TAAACTTGGTCTGACAAGATTATCAAAAAAAGAAGAAGATGTGAGCTACTCACTGA
Oligo_12	GGCCGCAGCCGATCGTTGTCAGAATTCATCCATTCAGCCC
Oligo_13	TTTTCTGTGACCAGTGGAAATCCGTAAGAGAATAGTGTATGC
Oligo_14	CGGGATAAGTTGCTCTTCATTCATCTTACTGTCATGCCCGAAAAC
Oligo_15	AAGCGTGCTACAGAGCGAGTTACACTCATGGTTATGG
Oligo_16	GCGCTTTCCCGCGTGAAATAAACCTTTTTTTTTTAGCCAGCCGGAAGGGC
Oligo_17	TCATAGCTCACGCTGTCGTGCGCTAACGCGAACACTATAAAGGGTTTTC
Oligo_18	TTTAAGTTTTAAATCAATCTTTTAAATTTTTTGTT
Oligo_19	GACCGCTGAATCGACGCTCAAGTCGGCCAGT
Oligo_20	TTGCCCGGTTTTTTTTTTCGTCAATATTAAAAGTGCTCATCATTGGAAAATTT
Oligo_21	CTAACTAATACCGCGGTTGCCGGGAAGCTACCATTGCGGTATGGCTTGCGCAATTT
Oligo_22	GTGGTGGCTCAAAGGCCCTGTCCGCGGTGCGGGCCTCTTCTGTTGGGA
Oligo_23	TTTTCACGCTCTTCCCAACTATTAATTCCTTTCTCAGAAGTGGTCCTGCAACTTTTT
Oligo_24	AAGACACTGCTTAATCAGTGAGGCATTTTTTTTTTCCTATCTCA
Oligo_25	GTTTGGAAACGTCAAAGGGCGAAGAGAAAGGGCGTAATC
Oligo_26	CGGCAAATGCCAGCTGCTTTCCAGCGCTTGGCGTAATCA
Oligo_27	ACGGGGTCTGACGCTCATAAAGTAACTCTCATCGTGCA
Oligo_28	TCTTTTCTTCACGTTAAGGGATTTTGGTCATGCAGCACTGCTAGAAG
Oligo_29	CCTTTGACGGCTACACATAATTCGCTCCGGGTCGTTTTACAGGCATCGTGGTGTTT
Oligo_30	TGCAAGCACACTGCCCGCATTAAAAACGACGGCCAGTG
Oligo_31	GCTCCCTAGGTATCTCAGTTCGCTTACCAT
Oligo_32	AAAAGGGAGCTGTTTTAATTGCGTTGCGCTGCAGATTATTGGTAGCTATATGAG
Oligo_33	ATCAGGGTCGCCAGCTCCGACCCTGCCGCTT
Oligo_34	TTTCGTTCTTCGGGGCGAATGCGGCGAGAAAAATACCCAACTGTAAATCA
Oligo_35	GGACTCCACAAGAGTCCACTATTATTTTT
Oligo_36	CAGGGGATCTCCTGTTGGCGAAAGGGGGATGT
Oligo_37	GTTCGGCGTAAAGCACATACGAGCCGGAAG
Oligo_38	GGCGGTTTGCGTATTAGCAAAAGCAGCAGCCCCCCCCGTAGTTGC
Oligo_39	CGGGGAGAACTCACATCCTGTGTGTTATCCGCATAGACCGTTAAAATTCGCGTTAA
Oligo_40	CCAACGCGAAAAAGAGCGCGCAGAAAAAGGATCTTCACCTAGATCCTAAAGTA
Oligo_41	TGAATCGGGTTGCTGGAACCCGGTCCGGTAACTATCGTCTTT
Oligo_42	TTTAACAAATAGGGGTTCGTATTTAGCGGTATCGCTCGGTCGGCGACCG
Oligo_43	AGCGTTAATTTGAATCGCGCACACCACATAGCAGAACT
Oligo_44	TTTCCTAAATTGTAATTTTTGTATCTTCAGTCCACACACTGGGGTGCCTAATGA
Oligo_45	AAATCGGCGCTCATTTTTTAACCATTT
Oligo_46	AAAATCCCTTATAAATCAAAAGATCACAATCATCTTTTCTCGCTGCAGCTCAC
Oligo_47	CGGGGAAAGCTGGCAAGTGTAGCGGTCACGCGACGTTGT
Oligo_48	ACTTTCAGGATACATATATTTTGAGGGCGATTTTCCCCGAAAAGTGCCATTT
Oligo_49	GCCGCAATATCAGGGAGATAGGGTTGAGTGTTGTTCCATGGTCATAATGGTGTA
Oligo_50	TTTTTTGGGGTCGAGGATCACCCTAATCAAG
Oligo_51	CGATGGCCCACTACGGAGCTTGAAATACTCAAAAACGAC
Oligo_52	TGGAGAATGACGAGCATCACAAACGCCTTAT
Oligo_53	GAGCGAATGCTAGGGCGCCGGCGAACGTGGCAAACCGTC
Oligo_54	AGCGAAAGGAGCGGGCTCTAAGCCATAAGGGAGGCCGC
Oligo_55	GCGCTTAAAGTTGGGTAACGCCAGATACCAG
Oligo_56	CGCGTCCCAATCGTAAAGACCACCACACCCGCC
Oligo_57	GCGCAACGCTATTATATTGTCGGTTATCCTCTTCCGCTTCCTCG
Oligo_58	TCTTGATCTTGAGTCCCGTTTTTCCATAGTTTTTTTTTTGCTCCGCCCCCCT
Oligo_59	TTTATAGGCCGTGAGATCCAGTTTTTTTTTTTTTCGATGTAACCCACAGGATCTTTTT
Oligo_60	TTTCGTTGTTGGAGTAAGTAGTTCTTTTTTTTTTGCCAGTTAATAGT
Oligo_61	TTTTTAAGAACGTAGCGAATTCTAAGTTTTTTTTTTCCTGGAGAATTCGTCGGGAATTT
Oligo_62	TTTACCGCTGTTGGTGAGTACTCATTTTTTTTTTTACCAAGTCATTCTGATGCTTTTTT
Oligo_63	TTTACCTGTCGCAAACCACCGCTGTTTTTTTTTTTGTAGCGGTGGTTTAAAAATGTTT
Oligo_64	TACTCTTAAAGGCCGGGAAAAACAGGAAGGCAAAATAAATGTTG
Oligo_65	TTCTTGAAAACAGTATTTGGTATCTGCCGCACAGAATGGCGGTG
Oligo_66	CCAGTCACTGCGCGTAGGAGCCCCCGATTTATGA
Oligo_67	AGAGGTGGCGAAACCTGCACGAAACTGGTACGGTCCTTGTGCTCTGCTGAA
Oligo_68	TATCATGATCCCCCATGTTCAATGATA
Oligo_69	GGTAATACTCATGAGCCCAGCGTTTCTGGGTGAGCACCTGCCGTA

Figure B.19 Sequences of staple oligonucleotides of CS-v3.

Name	Sequence
Core_1	TTTTCTGTGACCAGTGGAAATCCGTAAGAGAATAGTGTATGC
Core_2	TTTTCACGCTCTTCCCAACTATTAATTCCTTTCTCAGAAGTGGTCCTGCAACTTTTT
Core_3	TTTCGTTGTTGGAGTAAGTAGTTCTTTTTTTTTTGCCAGTTAATAGT
Core_4	TTTTATCCGCCTCCATCCAGTCTCCAGATCGAGCGCCCTTCGGGACCGGATAGGTAATAC
Core_5	TTTAACAAATAGGGGTTCGTATTTAGCGGTATCGCTCGGTCGGCGACCG
Core_6	TTGCCCGGTTTTTTTTTTCGTCAATATTAAAAGTGCTCATCATTGGAAAATTT
Core_7	CTAACTAATACCGCGGTTGCCGGGAAGCTACCATTGCGGTATGGCTTGCGCAATTT
Core_8	AAGACACTGCTTAATCAGTGAGGCATTTTTTTTTTTCCTATCTCA
Core_9	TTTCGTTCTTCGGGGCGAATGCGGCGAGAAAAATACCCAACTGTAAATCA
Core_10	TTTCCTAAATTGTAATTTTTGTATCTTCAGTCCACACACTGGGGTGCCTAATGA
Core_11	TTTAAGTTTTAAATCAATCTTTTAAATTTTTTGTT
Core_12	TCTTGATCTTGAGTCCCGTTTTTCCATAGTTTTTTTTTTTGCTCCGCCCCCCT
Core_13	TGAATCGGGTTGCTGGAACCCGGTCCGGTAACTATCGTCTTT
Core_14	TTTACCTGTCGCAAACCACCGCTGTTTTTTTTTTTGTAGCGGTGGTTTAAAAATGTTT
Core_15	ACTTTCAGGATACATATATTTTGAGGGCGATTTTCCCCGAAAAGTGCCATTT
Core_16	GGACTCCACAAGAGTCCACTATTATTTTT
Core_17	TTTTTAAGAACGTAGCGAATTCTAAGTTTTTTTTTTCCTGGAGAATTCGTCGGGAATTT
Core_18	CCTTTGACGGCTACACATAATTCGCTCCGGGTCGTTTTACAGGCATCGTGGTGTTT
Core_19	TTTACCGCTGTTGGTGAGTACTCATTTTTTTTTTTACCAAGTCATTCTGATGCTTTTTT
Core_20	TTTATAGGCCGTGAGATCCAGTTTTTTTTTTTTTCGATGTAACCCACAGGATCTTTTT
Core_21	AAATCGGCGCTCATTTTTTAACCATTT
Core_22	TTATCAGCCCCACGCTCACCGGCGATCAAGGTTCTTGAAAACAG
Core_23	GCGATCTGTCTATTTCGGTTACCAAGACTTATCCCTTCGG
Core_24	CGGGATAAGTTGCTCTTCATTCATCTTACTGTCATGCCCGAAAAC
Core_25	GACCGCTGAATCGACGCTCAAGTCGGCCAGT
Core_26	CCGACCCTGCCGCTTAAGCGTGCTACAGAGCGAGTTACACTC
Core_27	TTTCCCAGTCACTGCGCGTGGAGC
Core_28	GAGCGAATGCTAGGGCGCCGGCGAACGTGGCAAACCGTC
Core_29	TGGAGAATGACGAGCATCACAAACGCCTTAT
Core_30	AGCGAAAGGAGCGGGCTCTAAGCCATAAGGGAGGCCGC
Core_31	AGCGTTAATTTGAATCGCGCACACCACATAGCAGAACT
Core_32	TAAACTTGGTCTGACAAGATTATCAAAAAAAGAAGAAGATGTGAGCTACTCACTGA
Core_33	CTAGAAGGTGGTGGCTCAAAGGCCCTGTCCGCGGTGCGGGCCTCTTC
Core_34	CGGCAAATGCCAGCTGCTTTCCAGCGCTTGGCGTAATCA
Core_35	GTTCGGCGTAAAGCACATACGAGCCGGAAG
Core_36	CGTATTAGCAAAAGCAGCAGCCCCCCCCGTAGTTGCCTGACTCCCCGTCGTGAGCTC
Core_37	CGGGGAGAACTCACATCCTGTGTGTTATCCGCATAGACCGTTAAAATTCGCGTTAA
Core_38	CCAACGCGAAAAAGAGCGCGCAGAAAAAGGATCTTCACCTAGATCCTAAAGTA
Core_39	GCCGCAATATCAGGGAGATAGGGTTGAGTGTTGTTCCATGGTCATAATGGTGTA
Core_40	AAAAGGGAGCTGTTTTAATTGCGTTGCGCTGCAGATTATTGGTAGCTATATGAG
Core_41	ACTACGGAGCTTGAAATACTCAAAAACGACAGAGGTGGCGAAACCTGCACGAAACTG
Core_42	ACGGGGTCTGACGCTCATAAAGTAACTCTCATCGTGCA
Core_43	TCTTTTCTTCACGTTAAGGGATTTTGGTCATGCAGCACTG
Core_44	TGCAAGCACACTGCCCGCATTAAAAACGACGGCCAGTG
Core_45	AAAATCCCTTATAAATCAAAAGATCACAATCATCTTTTCTCGCTGCAGCTCAC
Core_46	GTTTGGAAACGTCAAAGGGCGAAGAGAAAGGGCGTAATC
Strut_1	CCCCAGTGCTGGTGCACGGTTTAGATAACTCCAGCGACCCTGACATGTCGTGCGCT
Strut_2	TCAGTTCGCTTACCATCTGGCCAGCGTAAGATACGGGAGGGTTT
Strut_3	AGCCTTAAGCCAGGCGTTTCCGTGTAGGTCGTTCGCTACTTACGCTGG
Strut_4	TGTTGGGATTTTTTGGGGTCGAGGATCACCGTTGG
Strut_5	GGCTGCGCAACGCTATTATATTGTCGGTTATCCTCTTCCCGTG
Strut_6	TTTTGCGCCGCTACACGATCCCAGGCCGCCGC
Strut_7	ACACCCAATGTTCAATGATATCATAGCTCACGC
Strut_8	AGAAGCCGGGATCTCCTGTTGGCGAAAGGGGGATTGCGGGTAAATC
Strut_9	CCTGGCTCCTAAGTTAAAGGCCGGGAAAAACAGGAAGGC
Strut_10	GGAAGGACACTAATTCGCCATTCA
Strut_11	TGACAGCGCAGCCGATCGTTGTCAGAATTCATCCATTCAGCCC
Strut_12	AGAACGCATACGTTTCTGGGTGAGCACCTGCCGTAATC
Strut_13	TGTCAGGGTCGCTAAGCTGGGCTGTGCGACAGGATGTGA
Strut_14	CCTGGGATCGGGGGCTGCAAGGCGATTACCCTGGAAGCTCC
Strut_15	GCTTAAAGTTGGGTAACGCCAGATACTTAAGGCTCTAGGTATC
Strut_16	TAGCGGTCACGCGACGTTGTTACTCCTTAGGAGCCAGGAGGGTCGCCAGCT
Strut_17	TATGTACAGGGCTTCTGCACCTTTTTCAATAT
Strut_18	TCATGAGCCCAGCGTATGCGTTCTAAAATAAATGTTGCGGGGAAAGCTGGCAAGTG
Strut_19	TATTGAAGCATTTAAGTCCTTCCCCCCGATTTATGA
Strut_20	GTAAGTTGGCCTGTCAATGGTTATGG
Strut_21	AGGTACGCTAAGTTAGCCACTGGGCCAGGAACCGTAAAACGACACGG
Strut_22	GGCGGTTTGCACGGCTTCCTCG
Strut_23	CGATGGCCCCCAACCTAATCAAG
Strut_24	TATCATGATCCCCCTGGGTGTCTTACAGGATTAGCAGTTTTTTAGCGAGG
Strut_25	AACGCGAACACTATAAAGGGTGATTTACCCGCAATGTCGCGTCCCAATCGTAAAGAACCACCACAC
Strut_26	TATCTGCCGCACAGAATGGCGGAGACGCATGTGTACGGTCCTTGTGCTCTGCTGAAGCCTAGCGTACCTTATTTGG
Strut_27	ACATGCGTCTCCGGTGGCGCTTTCCCGCGTGAAATAAACCTTTTTTTTTTAGCCAGCCGGAAGGGC

Figure B.20 Sequences of staple oligonucleotides of CS-v4.

Name	Sequence
Old_Core_1	CCAACGCGAAAAAGAGCGCGCAGAAAAAGGATCTTCACCTAGATCCTAAAGTA
Old_Core_2	AAAATCCCTTATAAATCAAAAGATCACAATCATCTTTTCTCGCTGCAGCTCAC
Old_Core_3	ACGGGGTCTGACGCTCATAAAGTAACTCTCATCGTGCA
Old_Core_4	GCGATCTGTCTATTTCGGTTACCAAGACTTATCCCTTCGG
Old_Core_5	TTATCAGCCCCACGCTCACCGGCGATCAAGGTTCTTGAAAACAG
Old_Core_6	CGGGATAAGTTGCTCTTCATTCATCTTACTGTCATGCCCGAAAAC
Old_Core_7	ACTACGGAGCTTGAAATACTCAAAAACGACAGAGGTGGCGAAACCTGCACGAAACTG
Old_Core_8	GACCGCTGAATCGACGCTCAAGTCGGCCAGT
Old_Core_9	CCGACCCTGCCGCTTAAGCGTGCTACAGAGCGAGTTACACTC
Old_Core_10	TGCAAGCACACTGCCCGCATTAAAAACGACGGCCAGTG
Old_Core_11	GCCGCAATATCAGGGAGATAGGGTTGAGTGTTGTTCCATGGTCATAATGGTGTA
Old_Core_12	TCTTTTCTTCACGTTAAGGGATTTTGGTCATGCAGCACTG
Old_Core_13	GAGCGAATGCTAGGGCGCCGGCGAACGTGGCAAACCGTC
Old_Core_14	TGGAGAATGACGAGCATCACAAACGCCTTAT
Old_Core_15	CGGCAAATGCCAGCTGCTTTCCAGCGCTTGGCGTAATCA
Old_Core_16	CGTATTAGCAAAAGCAGCAGCCCCCCCCGTAGTTGCCTGACTCCCCGTCGTGAGCTC
Old_Core_17	CGGGGAGAACTCACATCCTGTGTGTTATCCGCATAGACCGTTAAAATTCGCGTTAA
Old_Core_18	TAAACTTGGTCTGACAAGATTATCAAAAAAAGAAGAAGATGTGAGCTACTCACTGA
Old_Core_19	GTTTGGAAACGTCAAAGGGCGAAGAGAAAGGGCGTAATC
Old_Core_20	AAAAGGGAGCTGTTTTAATTGCGTTGCGCTGCAGATTATTGGTAGCTATATGAG
Old_Core_21	AGCGTTAATTTGAATCGCGCACACCACATAGCAGAACT
Old_Core_22	CTAGAAGGTGGTGGCTCAAAGGCCCTGTCCGCGGTGCGGGCCTCTTC
Old_Core_23	GTTCGGCGTAAAGCACATACGAGCCGGAAG
Old_Core_24	AGCGAAAGGAGCGGGCTCTAAGCCATAAGGGAGGCCGC
Old_PolyT_1	TTTTTAAGAACGTAGCGAATTCTAAGTTTTTTTTTTCCTGGAGAATTCGTCGGGAATTT
Old_PolyT_2	TGAATCGGGTTGCTGGAACCCGGTCCGGTAACTATCGTCTTT
Old_PolyT_3	TTTTCACGCTCTTCCCAACTATTAATTCCTTTCTCAGAAGTGGTCCTGCAACTTTTT
Old_PolyT_4	ACTTTCAGGATACATATATTTTGAGGGCGATTTTCCCCGAAAAGTGCCATTT
Old_PolyT_5	TTTACCTGTCGCAAACCACCGCTGTTTTTTTTTTTGTAGCGGTGGTTTAAAAATGTTT
Old_PolyT_6	TTTCCTAAATTGTAATTTTTGTATCTTCAGTCCACACACTGGGGTGCCTAATGA
Old_PolyT_7	TTTCGTTCTTCGGGGCGAATGCGGCGAGAAAAATACCCAACTGTAAATCA
Old_PolyT_8	AAGACACTGCTTAATCAGTGAGGCATTTTTTTTTTCCTATCTCA
Old_PolyT_9	GGACTCCACAAGAGTCCACTATTATTTTT
Old_PolyT_10	TCTTGATCTTGAGTCCCGTTTTTCCATAGTTTTTTTTTTGCTCCGCCCCCCT
Old_PolyT_11	AAATCGGCGCTCATTTTTTAACCATTT
Old_PolyT_12	TTTAAGTTTTAAATCAATCTTTTAAATTTTTTGTT
Old_PolyT_13	CTAACTAATACCGCGGTTGCCGGGAAGCTACCATTGCGGTATGGCTTGCGCAATTT
Old_PolyT_14	TTTAACAAATAGGGGTTCGTATTTAGCGGTATCGCTCGGTCGGCGACCG
Old_PolyT_15	CCTTTGACGGCTACACATAATTCGCTCCGGGTCGTTTTACAGGCATCGTGGTGTTT
Old_PolyT_16	TTTTATCCGCCTCCATCCAGTCTCCAGATCGAGCGCCCTTCGGGACCGGATAGGTAATAC
Old_PolyT_17	TTTACCGCTGTTGGTGAGTACTCATTTTTTTTTTTACCAAGTCATTCTGATGCTTTTTT
Old_PolyT_18	TTTATAGGCCGTGAGATCCAGTTTTTTTTTTTTCGATGTAACCCACAGGATCTTTTT
Old_PolyT_19	TTTTCTGTGACCAGTGGAAATCCGTAAGAGAATAGTGTATGC
Old_Strut_1	TATTGAAGCATTTAAGTCCTTCCCCCCGATTTATGA
Old_Strut_2	TATGTACAGGGCTTCTGCACCTTTTTCAATAT
Old_Strut_3	GGAAGGACACTAATTCGCCATTCA
Old_Strut_4	TGACAGCGCAGCCGATCGTTGTCAGAATTCATCCATTCAGCCC
Old_Strut_5	TAGCGGTCACGCGACGTTGTTACTCCTTAGGAGCCAGGAGGGTCGCCAGCT
Old_Strut_6	TATCTGCCGCACAGAATGGCGGAGACGCATGTGTACGGTCCTTGTGCTCTGCTGAAGCCTAGCGTACCTTATTTGG
Old_Strut_7	AGGTACGCTAAGTTAGCCACTGGGCCAGGAACCGTAAAACGACACGG
Old_Strut_8	GGCTGCGCAACGCTATTATATTGTCGGTTATCCTCTTCCCGTG
Old_Strut_9	TGTTGGGATTTTTTGGGGTCGAGGATCACCGTTGG
Old_Strut_10	GTAAGTTGGCCTGTCAATGGTTATGG
Old_Strut_11	CGATGGCCCCCAACCTAATCAAG
Old_Strut_12	CCTGGCTCCTAAGTTAAAGGCCGGGAAAAACAGGAAGGC
Old_Strut_13	TCATGAGCCCAGCGTATGCGTTCTAAAATAAATGTTGCGGGGAAAGCTGGCAAGTG
Old_Strut_14	ACATGCGTCTCCGGTGGCGCTTTCCCGCGTGAAATAAACCTTTTTTTTTTAGCCAGCCGGAAGGGC
Old_Strut_15	GGCGGTTTGCACGGCTTCCTCG
Old_Strut_16	TATCATGATCCCCCTGGGTGTCTTACAGGATTAGCAGTTTTTTAGCGAGG
Old_Strut_17	AGAACGCATACGTTTCTGGGTGAGCACCTGCCGTAATC
Csv4-2_Corner_1	GCGTTTCCGTGTAGGTCGTTCGCTACGATACGGGAGGGTTT
Csv4-2_Corner_2	TCCAAGCTGGGCTGTGCGACAGGATGTGA
Csv4-2_Corner_3	CGCGTCCCAATCGTAAAGAACCACCACACCCGCC
Csv4-2_Corner_4	GCTCCCTAGGTATCTCAGTTCGCTTACCAT
Csv4-2_Corner_5	CTGGCCCCAGTGCTGGTGCACGGTTTAGATAAC
Csv4-2_Corner_6	GCGCTTAAAGTTGGGTAACGCCAGATACCAG
Csv4-2_Corner_7	TTTTGCGCCGCTACAGGGGCTGCAAGGCGATTACCCTGGAA
Csv4-2_Corner_8	AACGCGAACACTATAAAGGGTTTTCCCAGTCACTGCGCGTGGAGC
Csv4-2_PolyT_1	TTTTTCGTCAATATTAAAAGTGCTCATCATTGGAAAATTT
Csv4-2_PolyT_2	TTTCGTTGTTGGAGTAAGTAGTTCTTTTTTTTTTTGCCAGTTAATAGTTTGCCCGGTTTTT
Csv4-2_Strut_1	ACACCCAATGTTCAATGATATCATAGCTCACGCTGTCGTGCGCT
Csv4-2_Strut_2	AGAAGCCGGGATCTCCTGTTGGCGAAAGGGGGATGT

Figure B.21 Sequences of staple oligonucleotides of CS-v4-2.

Name	Sequence
Core-Oligo_1	CCCTTATAAATCAAAAGATCACAATCATCTTTTCTCGCTGCAGCTCAC
Core-Oligo_2	GATTATTGGTAGCTATATGAGTCAGTGAGGCATTTTTTTTTTCCTATCTCAG
Core-Oligo_3	ACACGGGGTCTGACGCTCATAAAGTAACTCTCATCGTGCA
Core-Oligo_4	TCATAATGGTGTATGAATCGGGTTGCTGGAACCCGGTCCGGTAACTATCGTCTTT
Core-Oligo_5	CGGCAAATGCCAGCTGCTTTCCAGCGCTTGGCGTAATCAGTT
Core-Oligo_6	TTTCCTAAATTGTAATTTTTGTATCTTCAGTCCAC
Core-Oligo_7	AATCAATCTTTTAAATTTTTTGTTTGCAAGCACAC
Core-Oligo_8	TTTAACAAATAGGGGTTCGTATTTAGCGGTATCGCTCGGTCGGCGACCGTCTTT
Core-Oligo_9	CCAACGCGAAAAAGAGCGCGCAGAAAAAGGATCTTCACCTA
Core-Oligo_10	CCAGTCACTGCGCGTAGGAGCCCCCGATTTATGA
Core-Oligo_11	AGAGGTGGCGAAACCTGCACGAAACTGGTA
Core-Oligo_12	CTCAAGTCGGCCAGTGAGCGAATGCTAGGGC
Core-Oligo_13	GCTCCCTAGGTATCTCAGTTCGCTTACCAT
Core-Oligo_14	GCGTTTCCGTGTAGGTCGTTCGCTACGATACGGGAGGGTTT
Core-Oligo_15	TGTTGGGATTTTTTGGGGTCGAGGATCACCCTAATCAAG
Core-Oligo_16	GCGCAACGCTATTATATTGTCGGTTATCCTCTTCCGCTTCCTCG
Core-Oligo_17	CGCGTCCCAATCGTAAAGACCACCACACCCGCC
Core-Oligo_18	CGGGGAAAGCTGGCAAGTGTAGCGGTCACGCGACGTTGT
Core-Oligo_19	TTTTGCGCCGCTACAGGGGCTGCAAGGCGATTACCCTGGAA
Core-Oligo_20	AGCGAAAGGAGCGGGCTCTAAGCCATAAGGGAGGCCGC
Core-Oligo_21	TTTATAGGCCGTGAGATCCAGTTTTTTTTTTTTTCGATGTAACCCACAGGATCTTTTT
Core-Oligo_22	CGGTCCTTGTGCTCTGCTGAAGGCCGCAGCCGATCGTTGTCAGAA
Core-Oligo_23	CTAACTAATACCGCGGTTGCCGGGAAGCTACCATTGCGGTATGGCTTGCGCAATTT
Core-Oligo_24	TTCTTGAAAACAGTATTTGGTATCTGCCGCACAGAATGGCGGTG
Core-Oligo_25	TTTCGTTCTTCGGGGCGAATGCGGCGAGAAAAATACCCAACTG
Core-Oligo_26	GGTAATACTCATGAGCCCAGCGTTTCTGGGTGAGCACCTGCCGTA
Core-Oligo_27	CAGGGGATCTCCTGTTGGCGAAAGGGGGATGT
Core-Oligo_28	GCGCTTAAAGTTGGGTAACGCCAGATACCAG
Core-Oligo_29	GCGCTTTCCCGCGTGAAATAAACCTTTTTTTTTTTAGCCAGCCGGAAGGGC
Core-Oligo_30	TACTCTTAAAGGCCGGGAAAAACAGGAAGGCAAAATAAATGTTG
Core-Oligo_31	TCTTGATCTTGAGTCCCGTTTTTCCATAGTTTTTTTTTTTGCTCCGCCCCCCT
Core-Oligo_32	AGCGTTAATTTGAATCGCGCACACCACATAGCAGAACTCGGGATAAGTTGCTC
Core-Oligo_33	TTTTTAAGAACGTAGCGAATTCTAAGTTTTTTTTTTTCCTGGAGAATTCGTCGGGAATTT
Core-Oligo_34	GCCGGCGAACGTGGCAAACCGTCAAAAGGGAGCTGTTTTAATTGCG
Core-Oligo_35	GAGAAAGGGCGTAATCTGGAGAATGACGAGCATCACAAACGCCTTATAAGACAC
Core-Oligo_36	TATCATGATCCCCCATGTTCAATGATA
Core-Oligo_37	GTAAGTTGCCAGTTAGCCACTGGGCCAGGAACCGTAAAACGACACGG
Core-Oligo_38	CGGGGAGAACTCACATCCTGTGTGTTATCCGCATAGACCGTTAAAATTCGCGTTAA
Core-Oligo_39	CGGCTACACATAATTCAGCTCCGGGTCGTTTTACAGGCATCGTGGTGTTT
Core-Oligo_40	CTAGAAGGTGGTGGCTCAAAGGCCCTGTCCGCGGTGCGGGCCTCTTC
Core-Oligo_41	CGATGGCCCACTACGGAGCTTGAAATACTCAAAAACGAC
Core-Oligo_42	GGACTCCACAAGAGTCCACTATTATTTTT
Core-Oligo_43	GCACATACGAGCCGGAAGAAATCGGCGCTCATTT
Core-Oligo_44	GGCGGTTTGCGTATTAGCAAAAGCAGCAGCCCCCCCCGTAGTTGC
Core-Oligo_45	ACTTTCAGGATACATATATTTTGAGGGCGATTTTCCCCGAAAAGTGCCATTT
Core-Oligo_46	GCCGCAATATCAGGGAGATAGGGTTGAGTGT
Core-Oligo_47	TTTACCTGTCGCAAACCACCGCTGTTTTTTTTTTGTAGCGGTGGTTTAAAAATGTTT
Core-Oligo_48	TTTAACCATTTTTTTCTGTGACCAGTGGAAATCCGTAAGAGAATAGTGTATGC
Core-Oligo_49	TTTACCGCTGTTGGTGAGTACTCATTTTTTTTTTACCAAGTCATTCTGATGCTTTTTT
Core-Oligo_50	TCCAAGCTGGGCTGTGCGACAGGATGTGAGCA
Core-Oligo_51	TCATAGCTCACGCTGTCGTGCGCTAACGCGAACACTATAAAGGGTTTTC
Core-Oligo_52	CGATCTGTCTATTTCGGTTACCAAGACTTATCCCTTCGG
Core-Oligo_53	AAGCGTGCTACAGAGCGAGTTACACTCATGGTTATGG
Core-Oligo_54	TTTTTCGTCAATATTAAAAGTGCTCATCATTGGAAAATTT
Core-Oligo_55	CTGGCCCCAGTGCTGGTGCACGGTTTAGATAAC
Core-Oligo_56	TTCATCCATTCAGCCCGACCGCTGAATCGACG
Core-Oligo_57	CTGACTCCCCGTCGTGAGCTCCTTACAGGATTAGCAGTTTTTTAGCGAGGTATGTA
Core-Oligo_58	TTTCGTTGTTGGAGTAAGTAGTTCTTTTTTTTTTGCCAGTTAATAGTTTGCCCGGTTTTT
Core-Oligo_59	TTATCAGCCCCACGCTCACCGGCGATCAAGG
Core-Oligo_60	TTTTATCCGCCTCCATCCAGTCTCCAGATCGAGCGCCCTTCGGGACCGGATA
Core-Oligo_61	ATCAGGGTCGCCAGCTCCGACCCTGCCGCTT
Core-Oligo_62	CCTTTTTCAATATTTTTTTTTATTGAAGCATTTAAGCACTAATTCGCCATTCAGGCT
Core-Oligo_63	TTTTCACGCTCTTCCCAACTATTAATTCCTTTCTCAGAAGTGGTCCTGCAACTTTTT
Core-Oligo_64	TGCTTAATAAACTTGGTCTGACAAGATTATCAAAAAAAGAAGAAGATGTGAGCTACTCACTGA
Csv5.2_Strut_3	TTCATTCTCTTACTGTCATGCCCGAAACATTTAAGAGCCGCACGAACCGATCCTAAAGTA
Csv5.2_Strut_11	GTTCGGCGTAAAACGTATTCCTCTGGCCACATCTGCCCGCATTAAAAACGACGGCCAGTG
Csv5.2_Strut_12	TGTTCCATGGTTTATCTCACCAAATTAACACTGGGGTGCCTAATGACCTTTGA
Csv5.2_Strut_4	TTGCGCTGCAATCTTAAGTCATATCACTCTTCACGTTAAGGGATTTTGGTCATGCAGCACTG
Csv5.2_Strut_19	TAAATCAAAAATAGCCGCCATTCCATAGTGAGTTGGAAACGTCAAAGGGCGAA
Csv5.2_Strut_3_compl	GGTTCGTGCGGCTCTTAAATG
Csv5.2_Strut_11_compl	GATGTGGCCAGAGGAATACGT
Csv5.2_Strut_12_compl	TAATTTGGTGAGATAAA
Csv5.2_Strut_4_compl	GTGATATGACTTAAGAT
Csv5.2_Strut_19_compl	ACTCACTATGGAATGGCGGCT

Figure B.22 Sequences of staple oligonucleotides of CS-v5.

Name	Sequence
Corner_01	AGTGTAAAGCCTGTTTTTTGGGTGCCTAATGATCTCAGTT
Corner_02	CTACGGCTGTTGCCATTGCTACCAAGGCGA
Corner_03	AGAAGTAATATGCGGCGACCGTTTTTTAGTTGCTCTTGCC
Corner_04	TTAATTGCTCGCGCTTGGCGTAATCATCCCGTAGGTA
Corner_05	GTTACATGATCCCCCTCCTCTTGTCATTCAGCT
Corner_06	CTCCCCGTAAACTTGGGATTTTGGGATTATCACGGTTATCGCTCTTCCGCTTCCTC
Corner_07	GTGAAATCGTTTTTCCACAGAATCAGGGGATAACGCAGAAACTCACGAAAAAAA
Corner_08	AATAGTGGTTGGCCCAACGGGGCGAAAAGAAATCGGGCTCATTTTTTAACCAATTTTTGT
Corner_09	ATAATACCATCATTGGAAAACGTTCTTGAGATCTGCGCGGCGTC
Corner_10	AGCATAAGTTGGTAGCCGGTCATAGCTGTTTCCTGTCAACATAC
Corner_11	ATAGTTTGCGCAACGTTACACTAGAAGCCCTTCGGTGCTACATAGCAGA
Corner_12	GCGAGGTAAACCCCCCCTCCAAGCTGGGCTGGCT
Corner_13	TGCGCCTTCCACTGGTAACAGGATGAGTTCT
Corner_14	TGAAGTGGAGGCATCGTGGTGTCCCGGTTCCCAACGATTTT
Corner_15	TTTATCCGGTAACTATCGCGCCACTGGCAGCAGTGGCCTAA
Corner_16	TCTTGAGTCGGTGGTTCGGTTCAGCCCGACCGC
Corner_17	CGCGCACATTTCCCCGGAAGCATTGCAAAAACGCAAAATGATATGAGTCCAGTCAC
Right_Core_01	CGTTTCCCCCTGGAACTATAAAGGAGCCGGAACAAACCACTCCAGAGCTCTTGAATCACTCA
Right_Core_02	ACGCTCGTCGTTTGGTTGTAGGCGGAAAAAGA
Right_Core_03	CTTTCACCTGCTTAATTTCGTTCGGATCTCAAGAAGAT
Right_Core_04	TTGCCTGACCGCTGTTTGGGTGATATCAGGGTTATTGTCTCATGAGAACAAAT
Right_Core_05	ATACCAGGCGAAACCCGACAGGATGTGCACGTCCGGCAA
Right_Core_06	AGAGGTGGCATAGGCTCCGCCCCGTTGCTGGTGTTATCCGTTAAGG
Right_Core_07	TAACCCACTGTCTATCAGTGAGGACGCTCAGTGGAACGA
Right_Core_08	CAGCCAGCCGGAAGGTTTATCAGATTCTGAGTGGTTATTAAATCAGCAGTGTTATGGCTTC
Right_Core_09	ATAGGCCCTCTCAAGACCAAGTCCAATAAACCTCACCGGCCGCTGGTAGCGGTG
Right_Core_10	GGCAGCACTGCATAATGACCCACGCGTGTAGAATTCCACA
Left_Core_01	GCGCCACAGGGTTTTCATTGTTGCTCCCTTCGGGAAGCGT
Left_Core_02	GTAGTTCAATACGGGCCGAGATCCCTTATAAATCAAA
Left_Core_03	TGTTGGGCATTCGCCGAACGTGGGGGCGCTAGGGCGCTATACTCA
Left_Core_04	CCAACCCGCTCACGCTTACCGGAGGCGCTTACTCACAATCCGCCTCGCAGAAGTGGTCCT
Left_Core_05	TGGAACAAAGGGTTGAGTGTTGTAGAATAGA
Left_Core_06	AAGGCGGTAATAAAAAGGACTAAGCCTGACGTTGTAACGCCA
Left_Core_07	CTCTGCTGAAGAACAGGTAAGACACGACTTAT
Left_Core_08	TACCTGTCTTCCGACCCTGCCGCTTCGTGCGCTCTCCTG
Left_Core_09	GTGAGCTATCTCATAGTATTTGGTCCATCCA
Left_Core_10	GTTTGCGCACTGCCCCTGCATTATCGGTGCGGGCCTCT
Left_Core_11	AAAGGGAATACTCTTCCTTTTTCAATATTATTAGAAAGCGAGTGCTC
Left_Core_12	AATCGGTTAGCTCCTTCGGATGTTGTG
Left_Core_13	TAAGGGCGACACGGAAAAAATGAGAGCGAATAAACGAC
Right_End_01	TTTTGTATTTAGAAAAATACGGATACAATCTTTTA
Right_End_02	GAAAGAACCCGTAAAAAGGCCGCCCTGACGATACGCGCA
Right_End_03	GTTCGATGAAGATGCTAGGGCTTACCATCTTTTTTTTTTTGGCCCCAGTGCT
Right_End_04	AATCGACGCTCAAGTCGTTTTTTTGCTCACATAACTAC
Right_End_05	TTTTCAGCGATCTCGTGCACCCAATTTTTTTTTTTCTGATCTTCAGCTATTTGAATTT
Right_End_06	TTTTTTAATATTTTGTTAAAATTCGCGTTAAAAAAGTGCAGTACTCAGATCTTA
Right_End_07	GTTTGCAAGCAATGATACCGCGTTCTCTTACACTGGTGCACCTAA
Right_End_08	GCCAGGAAATGTGAGCAAAAGGCCTTTTT
Right_End_09	TTTTTAGCAAAAGCCTTTGATCTTTTTTTTTTTTTTTCTACGGGGTCTGCACCTATCTTT
Right_End_10	ATCCATAGGATACGGGTTTCTGTGTGTCATGCCATCCGTTTT
Right_End_11	TCTGACAGTTACCAAAGCGTTTCGAGATCCAAGGGGTTCATTGTAAGCGTTTTTT
Left_End_01	GGAGAATGTTGCGCTTATTGGGCCGCCTTTCATGAATCGGCCAACGCGCTTT
Left_End_02	TTTTGCGCAACTCGCTATTGGCGATTAAGTCGGGAGGCCAGTGACTCGCTCAGCTCACTCA
Left_End_03	GCGCTCGGTCGTTCGGTTTTTTTTTTTACGCTGCGAATGTTGAGGCAAGTGATGCGCC
Left_End_04	GGCCAGTAGTTTTATAGATCCTTTTAAATTAGCGGTAT
Left_End_05	TTTAACCTGTCGTGCCAGGCTTTCCAGTTGGGTAAAACGACGCGCGTCC
Left_End_06	GCCAGTTACAAAAAAGGAGTCCACTTTTTTTTTTTATTAAAGAACGTGGA
Left_End_07	TTTGGGGAGAGGCGGCTCACTGAGCGAATTTCTTCACCAATCAATCTAAAGTAT
Left_End_08	TAGCAGAAAGGGCGAAACCATCACCCTAATACCCTAAAAGCCGGCAAAGCACTTTT
Left_End_09	CCGCAAAACTTTAAAAAAGGAGCCGAGAAAACGGGGAAGGGAGCCCCCGATTTTTT
Left_End_10	TTTTCTATCAGGGCGATGGCCCTCCAGTTCTCCAACTAGAGTAAGTCTATTAGCAACTTT
Left_End_11	TTTTGGAGAATCGTAACCACCACATTTTTTTTTTCCCGCCGCGCTTATAGCGGTCTTT
Left_End_12	TCTAAGCCGGGGGATGTGCTGCAAACGCCAGCTGGCGAAATTT
Left_End_13	TTTCTGCGGCGTCGCGCTTGGCGTTTTTTTTTTTTAATCATGGTGTA
Left_End_14	TTTAAATCGGACAAGTTTTTTGGGTTTTTTTTGTCGAGGTGCCGTATTCAGGCGCTACAGG
Left_End_15	TTTAGAGCTTGGGAAGGGAACTACGTGCGGGAAGCGTCAAAGGGCGAAAAACCGTTT

Figure B.23 Sequences of staple oligonucleotides of CS-v6.

Name	Sequence
PolyT_right_01	TTTAAGGCAAAATGCCGCAAACCGAAATCCGGGAAGC
PolyT_right_02	CATTCTGGACTGGTGAGTACTCTTT
PolyT_right_03	TTTCTTGGCGTAATCATGCCTGGAGCTCCCTT
PolyT_right_04	TTTTTGGGTAACGCCTCCCTTATTTTTTTTTAAATCAAAAGAATAGGGCAAAA
PolyT_right_05	TTTAACCAAGTTCCAGTTTGGAACTTTTTTTTTTAAGAGTCCACTATGGAAAGCCTTT
PolyT_right_06	TTTGGCGAACGACTGCCCGCTTTTTTTTTTTTTTCCAGTCGGGAAACCACAGAATTTT
PolyT_left_01	TTTTAACAGGATTAGCAGAGCGTAACTATTTATCGCCCTGACGCCGTTCATC
PolyT_left_02	AGAAAAAGAACTGACGAGCATCAAGTTCTTAAGAACAGTAGGCGGTTT
PolyT_left_03	TTTGCGAGTTACATGATCCCCGTCCTCCGATCGTTT
PolyT_left_04	TTTATACCGCGCACCGCTGGTAGCTTTTTTTTTTTGGTGGTTTTTTTGGATCCGGCTTT
PolyT_left_05	TATCTGCGTACACTAGGAAGTGGTGGCCTAATTT
PolyT_left_06	TTTTCAAGAAGATGTAGATAACTATTTTTTTTTTCGATACGGGAGGCGGTTCC
PolyT_left_07	GCCCGACAGTCCAACTTTTTTTTTTCCGGTAAGACACGAC
PolyT_left_08	TTTCTACGGCCTCTGCTGAAGCTTTTTTTTTTCAGTTACCTTCGAAGGATCTTTTT
PolyT_left_09	TTTGCAGTGTTTGACCCACGCTCATTTTTTTTTTCCGGCTCCAGATTTATCAGCCAACGATCAAGTTT
PolyT_left_10	TTTTGCTACAGCAAAAATGAGGTATTACGGGGTACTGGCAGCAGCCACTGGTTT
StrutAdj_le_1	TGCATAATGGCCCACGGAAGGGCACACCCGCCGCTACTTACGCGCTGGGCGCTGCTCGGTC
StrutAdj_le_2	GTAAAGCTGCGTATAATTCCAGGCTCCGCCCCCAAAGAGTTGGTCTCGCTGCCTTCCGCT
StrutAdj_le_3	TTTAAACAAACTCACTGAAGCTCTTTTTGCAAGCAGCAGACATCTGGCTTGGGGTCACCATCAC
Core_01	CACAACATATTGTTATCTACAGGCATAGTTATAAACAAATAGGGG
Core_02	TGTTTCCTAAGTCAGACGCGTTGCTGGCGTT
Core_03	GGCGGTGGCGAAACCCGACCCGTTCATCACGTTAAGGGATT
Core_04	ACGAGCCGGAAGCATAAAGTACATTCAGGTCATAGCACGAAAAC
Core_05	GGCGTAATCATGGCTGCGCACTATCTCACCCGAAAAGTGCCACC
Core_06	ACCTAGATCCTTTTAGTATATATATCGGTGCCGCAACGTTGTT
Core_07	TGAGGCACACTGTGGGCGGAGTAAACTTCGCGTTAAATTTT
Core_08	TTTCCCCCAAAGTGTAAAGCCTACCGTAATGGAAGCTCCCTCGT
Core_09	TAATCAGTTGGTCATGAGATTAAGCTGGGC
Core_10	AGGGTTTTCCCAGTCAATTCTAAGGTGTAAAACTGTTCCG
Core_11	ACATTTCGCGATCTGTCTATTTTCAGTGGA
Core_12	GCGCGTCGCTCGTCGAGAAGTGGTCCTGCAACTGATATCCAGTTGCATCGT
Core_13	GGGCCTCAGTTTATCCGCCTCCATCCAGGTAGTTC
Core_14	CGGGAAGCGTGGCGCTGCGCTCTCCGACGGCCCTAATGAG
Core_15	GCTAGGGCGCTGGCATTCGCTATGAATTCTAATGAAGTTAGCTCACG
Core_16	GAGCGGGCGGAACCCTGAAAAACCCAGGGCGATTCTCTTAAGCAGAACTTTAAAA
Core_17	AAAAGGCCAGCAAAAGCGGTATCCAACGCGCAGGCGGTTACTAAATCGTAACCAC
Core_18	TTCTCATACGGCCAGTGAGCGACGACGTT
Core_19	CCGAGCGCTTTGGTATCAAGGATTAGAAAAGCGGTTAGCTCCTTCGCATGTTGT
Core_20	TTCAGCTCGCTGCTTAATGCGCCGCCGCTCACATCTTTTCGTATTTGG
Core_21	GCCATTGCTACAGCGATGTATCTCATGAGCGGATA
Core_22	CTGTAGGTATCTCAGCCAGGCGGAATTCGCGCTT
Core_23	TGCCCGGCGTCAATATCTTTTACGCCAGTTA
Core_24	GGCCAGGAGGGGTGCAGTGAGCTACGCCAGGTAAAACGTTTTTAACCAATAGGAAAGGGAA
Core_25	CAGCTCATTTAAATCAATCTAAAAATTAAAAAGCCTGGA
Core_26	AATGTATTCTTACCGCTGTTGAGAATACCGCGCCACAT
Core_27	CATATTTGTTCCGCGCGGTGTCACCCATTCGCGCGGTCACGCTGCGC
Core_28	GGTTATTGACCCACACCCTACTCTTCCTTTTTCA
Core_29	TTTTGAAGCATTTATCAGTAAATTGTAAGCGTTCCAATGCT
Core_30	ATATTATAATATTTTGTTAAAATTGGTCT
Core_31	ATACTCAAACTGATCTTCAGCACGG
Core_32	TGTGTGCACGAACCCCAGGAAGATATTCGGTGT
Core_33	CGTCTTGCGCTGCGCCTTATCCGCGACGCTCGTGTGAA
Core_34	GAAAACTCTGGCTTCAGCAAAAAAGCCTGACTCCCCGTCGTCCTTTG
Core_35	GACAGTTATCAAAAAGGATCTTCAGGTCGTTCGCTCCATTT
Core_36	TTTCACCTAAGGGCGACACGGAAATGTTGATGTTAAATATAGTTTG
Strut-left_1	TTTTTCCTAATCATCACTCAGAAGTAAGTTGGCCTTT
Strut-left_2	TTTTTGTTCGGCTGCGGCGATTTCCATA
Strut-left_3	AATAAACCCATTGGAAATGGTTATGGCAGCACTTTTT
Strut-left_4	TTTTTGTCAACGTTCTTCGGGGCGTGCTCATAGCCAGCCTACGTGAGAGGTGCCTTTTT
Strut-left_5	TTTTTTCCTCGCAAGTTTTCCCAGTGCTGCAATGTTT
StrutAdj_ri_1	TAATTGCGTTGCGCTCTGGCGAGTTGACGGTAAAGAA
StrutAdj_ri_2	CTGGCGAAAGGGGGAGCGAAAGTGAGCTAAAATCGGCAGCTCAC
StrutAdj_ri_3	TTTCAGGGGATAACGCAGGGTTATCCTGTCGT
StrutAdj_ri_4	TAAGATGCCCAACGTCACCGAGATGGAAGAAATGTGCTGCAAGGCGATTAAGTTT
StrutAdj_ri_5	GCCCCCGACATTAATGCTCACATATGTGAGCACCCTGCCGCTTACCCCGCCTTTAATTCGCGTTT
Strut-right_1	TTTTTCGTGGACTTTTTCTGTAGAATAGTGTATGCGGCAAAAACAGGTTT
Strut-right_2	TAGAGTAATCTATTAAGTTGCTCTCTGTCATGCCATCCGTTTTT
Strut-right_3	AGCGTTTCTGGGTGAGCGACCGATTGTTGCAAAGGGCAAAGGGATTTTT
Strut-right_4	TTTTTGCCAGCTGTTTAGAGCAAAGGAAGAGGGTTGAGTGTTGT
Strut-right_5	TTTTTTCAAAGGCGGTAATACGAAAGAAC

Figure B.24 Sequences of staple oligonucleotides of CS-v7.

GTGGCACTTTTCGGGGAAATGTGCGCGGAACCCCTATTTGTTTATTTTTCTAAATACATTCAAATATGTATC
CGCTCATGAGACAATAACCCTGATAAATGCTTCAATAATATTGAAAAAGGAAGAGTATGAGTATTCAACATT
TCCGTGTCGCCCTTATTCCCTTTTTTGCGGCATTTTGCCTTCCTGTTTTTGCTCACCCAGAAACGCTGGTGA
AAGTAAAAGATGCTGAAGATCAGTTGGGTGCACGAGTGGGTTACATCGAACTGGATCTCAACAGCGGTAAGA
TCCTTGAGAGTTTTCGCCCCGAAGAACGTTTTCCAATGATGAGCACTTTTAAAGTTCTGCTATGTGGCGCGG
TATTATCCCGTATTGACGCCGGGCAAGAGCAACTCGGTCGCCGCATACACTATTCTCAGAATGACTTGGTTG
AGTACTCACCAGTCACAGAAAAGCATCTTACGGATGGCATGACAGTAAGAGAATTATGCAGTGCTGCCATAA
CCATGAGTGATAACACTGCGGCCAACTTACTTCTGACAACGATCGGAGGACCGAAGGAGCTAACCGCTTTTT
TGCACAACATGGGGGATCATGTAACTCGCCTTGATCGTTGGGAACCGGAGCTGAATGAAGCCATACCAAACG
ACGAGCGTGACACCACGATGCCTGTAGCAATGGCAACAACGTTGCGCAAACTATTAACTGGCGAACTACTTA
CTCTAGCTTCCCGGCAACAATTAATAGACTGGATGGAGGCGGATAAAGTTGCAGGACCACTTCTGCGCTCGG
CCCTTCCGGCTGGCTGGTTTATTGCTGATAAATCTGGAGCCGGTGAGCGTGGGTCACGCGGTATCATTGCAG
CACTGGGGCCAGATGGTAAGCCCTCCCGTATCGTAGTTATCTACACGACGGGGAGTCAGGCAACTATGGATG
AACGAAATAGACAGATCGCTGAGATAGGTGCCTCACTGATTAAGCATTGGTAACTGTCAGACCAAGTTTACT
CATATATACTTTAGATTGATTTAAAACTTCATTTTTAATTTAAAAGGATCTAGGTGAAGATCCTTTTTGATA
ATCTCATGACCAAAATCCCTTAACGTGAGTTTTCGTTCCACTGAGCGTCAGACCCCGTAGAAAAGATCAAAG
GATCTTCTTGAGATCCTTTTTTTCTGCGCGTAATCTGCTGCTTGCAAACAAAAAAACCACCGCTACCAGCGG
TGGTTTGTTTGCCGGATCAAGAGCTACCAACTCTTTTTCCGAAGGTAACTGGCTTCAGCAGAGCGCAGATAC
CAAATACTGTTCTTCTAGTGTAGCCGTAGTTAGGCCACCACTTCAAGAACTCTGTAGCACCGCCTACATACC
TCGCTCTGCTAATCCTGTTACCAGTGGCTGCTGCCAGTGGCGATAAGTCGTGTCTTACCGGGTTGGACTCAA
GACGATAGTTACCGGATAAGGCGCAGCGGTCGGGCTGAACGGGGGGTTCGTGCACACAGCCCAGCTTGGAGC
GAACGACCTACACCGAACTGAGATACCTACAGCGTGAGCTATGAGAAAGCGCCACGCTTCCCGAAGGGAGAA
AGGCGGACAGGTATCCGGTAAGCGGCAGGGTCGGAACAGGAGAGCGCACGAGGGAGCTTCCAGGGGGAAACG
CCTGGTATCTTTATAGTCCTGTCGGGTTTCGCCACCTCTGACTTGAGCGTCGATTTTTGTGATGCTCGTCAG
GGGGGCGGAGCCTATGGAAAAACGCCAGCAACGCGGCCTTTTTACGGTTCCTGGCCTTTTGCTGGCCTTTTG
CTCACATGTTCTTTCCTGCGTTATCCCCTGATTCTGTGGATAACCGTATTACCGCCTTTGAGTGAGCTGATA
CCGCTCGCCGCAGCCGAACGACCGAGCGCAGCGAGTCAGTGAGCGAGGAAGCGGAAGAGCGCCCAATACGCA
AACCGCCTCTCCCCGCGCGTTGGCCGATTCATTAATGCAGCTGGCACGACAGGTTTCCCGACTGGAAAGCGG
GCAGTGAGCGCAACGCAATTAATGTGAGTTAGCTCACTCATTAGGCACCCCAGGCTTTACACTTTATGCTTC
CGGCTCGTATGTTGTGTGGAATTGTGAGCGGATAACAATTTCACACAGGAAACAGCTATGACCATGATTACG
CCAAGCGCGAATTCTCCAGGCTTAGAATTCGCTCACTGGCCGTCGTTTTACACCATGATTACGCCAAGCGCG
AATTCTCCAGGCTTAGAATTCGCTCACTGGCCGTCGTTTTACAACGTCGTGACTGGGAAAACCCTGGCGTTA
CCCAACTTAATCGCCTTGCAGCACATCCCCCTTTCGCCAGCTGGCGTAATAGCGAAGAGGCCCGCACCGATC
GCCCTTCCCAACAGTTGCGCAGCCTGAATGGCGAATGGGACGCGCCCTGTAGCGGCGCATTAAGCGCGGCGG
GTGTGGTGGTTACGCGCAGCGTGACCGCTACACTTGCCAGCGCCCTAGCGCCCGCTCCTTTCGCTTTCTTCC
CTTCCTTTCTCGCCACGTTCGCCGGCTTTCCCCGTCAAGCTCTAAATCGGGGGCTCCCTTTAGGGTTCCGAT
TTAGTGCTTTACGGCACCTCGACCCCAAAAAACTTGATTAGGGTGATGGTTCACGTAGTGGGCCATCGCCCT
GATAGACGGTTTTTCGCCCTTTGACGTTGGAGTCCACGTTCTTTAATAGTGGACTCTTGTTCCAAACTGGAA
CAACACTCAACCCTATCTCGGTCTATTCTTTTGATTTATAAGGGATTTTGCCGATTTCGGCCTATTGGTTAA
AAAATGAGCTGATTTAACAAAAATTTAACGCGAATTTTAACAAAATATTAACGCTTACAATTTAG

Figure B.25 Sequence of the 2873 nt-long scaffold.

TGATAGACGGTTTTTCGCCCTTTGACGTTGGAGTCCACGTTCTTTAATAGTGGACTCTTGTTCCAAACTGGAACAACACTCAACCCTATCTCGGGCTATTCT
TTTGATTTATAAGGGATTTTGCCGATTTCGGAACCACCATCAAACAGGATTTTCGCCTGCTGGGGCAAACCAGCGTGGACCGCTTGCTGCAACTCTCTCAGG
GCCAGGCGGTGAAGGGCAATCAGCTGTTGCCCGTCTCACTGGTGAAAAGAAAAACCACCCTGGCGCCCAATACGCAAACCGCCTCTCCCCGCGCGTTGGCCG
ATTCATTAATGCAGCTGGCACGACAGGTTTCCCGACTGGAAAGCGGGCAGTGAGCGCAACGCAATTAATGTGAGTTAGCTCACTCATTAGGCACCCCAGGCT
TTACACTTTATGCTTCCGGCTCGTATGTTGTGTGGAATTGTGAGCGGATAACAATTTCACACAGGAAACAGCTATGACCATGATTACGAATTCGAGCTCGGT
ACCCGGGGATCCTCAACTGTGAGGAGGCTCACGGACGCGAAGAACAGGCACGCGTGCTGGCAGAAACCCCCGGTATGACCGTGAAAACGGCCCGCCGCATTC
TGGCCGCAGCACCACAGAGTGCACAGGCGCGCAGTGACACTGCGCTGGATCGTCTGATGCAGGGGGCACCGGCACCGCTGGCTGCAGGTAACCCGGCATCTG
ATGCCGTTAACGATTTGCTGAACACACCAGTGTAAGGGATGTTTATGACGAGCAAAGAAACCTTTACCCATTACCAGCCGCAGGGCAACAGTGACCCGGCTC
ATACCGCAACCGCGCCCGGCGGATTGAGTGCGAAAGCGCCTGCAATGACCCCGCTGATGCTGGACACCTCCAGCCGTAAGCTGGTTGCGTGGGATGGCACCA
CCGACGGTGCTGCCGTTGGCATTCTTGCGGTTGCTGCTGACCAGACCAGCACCACGCTGACGTTCTACAAGTCCGGCACGTTCCGTTATGAGGATGTGCTCT
GGCCGGAGGCTGCCAGCGACGAGACGAAAAAACGGACCGCGTTTGCCGGAACGGCAATCAGCATCGTTTAACTTTACCCTTCATCACTAAAGGCCGCCTGTG
CGGCTTTTTTTACGGGATTTTTTTATGTCGATGTACACAACCGCCCAACTGCTGGCGGCAAATGAGCAGAAATTTAAGTTTGATCCGCTGTTTCTGCGTCTC
TTTTTCCGTGAGAGCTATCCCTTCACCACGGAGAAAGTCTATCTCTCACAAATTCCGGGACTGGTAAACATGGCGCTGTACGTTTCGCCGATTGTTTCCGGT
GAGGTTATCCGTTCCGTGGCGGCTCCACCTCTGAAAGCTTGGCACTGGCCGTCGTTTTACAACGTCGTGACTGGGAAAACCCTGGCGTTACCCAACTTAAT
CGCCTTGCAGCACATCCCCCTTTCGCCAGCTGGCGTAATAGCGAAGAGGCCCGCACCGATCGCCCTTCCCAACAGTTGCGCAGCCTGAATGGCGAATGGCGC
TTTGCCTGGTTTCCGGCACCAGAAGCGGTGCCGGAAAGCTGGCTGGAGTGCGATCTTCCTGAGGCCGATACTGTCGTCGTCCCCTCAAACTGGCAGATGCAC
GGTTACGATGCGCCCATCTACACCAACGTGACCTATCCCATTACGGTCAATCCGCCGTTTGTTCCCACGGAGAATCCGACGGGTTGTTACTCGCTCACATTT
AATGTTGATGAAAGCTGGCTACAGGAAGGCCAGACGCGAATTATTTTTGATGGCGTTCCTATTGGTTAAAAAATGAGCTGATTTAACAAAAATTTAATGCGA
ATTTTAACAAAATATTAACGTTTACAATTTAAATATTTGCTTATACAATCTTCCTGTTTTTGGGGCTTTTCTGATTATCAACCGGGGTACATATGATTGACA
TGCTAGTTTTACGATTACCGTTCATCGATTCTCTTGTTTGCTCCAGACTCTCAGGCAATGACCTGATAGCCTTTGTAGATCTCTCAAAAATAGCTACCCTCT
CCGGCATTAATTTATCAGCTAGAACGGTTGAATATCATATTGATGGTGATTTGACTGTCTCCGGCCTTTCTCACCCTTTTGAATCTTTACCTACACATTACT
CAGGCATTGCATTTAAAATATATGAGGGTTCTAAAAATTTTTATCCTTGCGTTGAAATAAAGGCTTCTCCCGCAAAAGTATTACAGGGTCATAATGTTTTTG
GTACAACCGATTTAGCTTTATGCTCTGAGGCTTTATTGCTTAATTTTGCTAATTCTTTGCCTTGCCTGTATGATTTATTGGATGTTAATGCTACTACTATTA
GTAGAATTGATGCCACCTTTTCAGCTCGCGCCCCAAATGAAAATATAGCTAAACAGGTTATTGACCATTTGCGAAATGTATCTAATGGTCAAACTAAATCTA
CTCGTTCGCAGAATTGGGAATCAACTGTTATATGGAATGAAACTTCCAGACACCGTACTTTAGTTGCATATTTAAAACATGTTGAGCTACAGCATTATATTC
AGCAATTAAGCTCTAAGCCATCCGCAAAAATGACCTCTTATCAAAAGGAGCAATTAAAGGTACTCTCTAATCCTGACCTGTTGGAGTTTGCTTCCGGTCTGG
TTCGCTTTGAAGCTCGAATTAAAACGCGATATTTGAAGTCTTTCGGGCTTCCTCTTAATCTTTTTGATGCAATCCGCTTTGCTTCTGACTATAATAGTCAGG
GTAAAGACCTGATTTTTGATTTATGGTCATTCTCGTTTTCTGAACTGTTTAAAGCATTTGAGGGGGATTCAATGAATATTTATGACGATTCCGCAGTATTGG
ACGCTATCCAGTCTAAACATTTTACTATTACCCCCTCTGGCAAAACTTCTTTTGCAAAAGCCTCTCGCTATTTTGGTTTTTATCGTCGTCTGGTAAACGAGG
GTTATGATAGTGTTGCTCTTACTATGCCTCGTAATTCCTTTTGGCGTTATGTATCTGCATTAGTTGAATGTGGTATTCCTAAATCTCAACTGATGAATCTTT
CTACCTGTAATAATGTTGTTCCGTTAGTTCGTTTTATTAACGTAGATTTTTCTTCCCAACGTCCTGACTGGTATAATGAGCCAGTTCTTAAAATCGCATAAG
GTAATTCACAATGATTAAAGTTGAAATTAAACCATCTCAAGCCCAATTTACTACTCGTTCTGGTGTTTCTCGTCAGGGCAAGCCTTATTCACTGAATGAGCA
GCTTTGTTACGTTGATTTGGGTAATGAATATCCGGTTCTTGTCAAGATTACTCTTGATGAAGGTCAGCCAGCCTATGCGCCTGGTCTGTACACCGTTCATCT
GTCCTCTTTCAAAGTTGGTCAGTTCGGTTCCCTTATGATTGACCGTCTGCGCCTCGTTCCGGCTAAGTAACATGGAGCAGGTCGCGGATTTCGACACAATTT
ATCAGGCGATGATACAAATCTCCGTTGTACTTTGTTTCGCGCTTGGTATAATCGCTGGGGGTCAAAGATGAGTGTTTTAGTGTATTCTTTTGCCTCTTTCGT
TTTAGGTTGGTGCCTTCGTAGTGGCATTACGTATTTTACCCGTTTAATGGAAACTTCCTCATGAAAAAGTCTTTAGTCCTCAAAGCCTCTGTAGCCGTTGCT
ACCCTCGTTCCGATGCTGTCTTTCGCTGCTGAGGGTGACGATCCCGCAAAAGCGGCCTTTAACTCCCTGCAAGCCTCAGCGACCGAATATATCGGTTATGCG
TGGGCGATGGTTGTTGTCATTGTCGGCGCAACTATCGGTATCAAGCTGTTTAAGAAATTCACCTCGAAAGCAAGCTGATAAACCGATACAATTAAAGGCTCC
TTTTGGAGCCTTTTTTTTGGAGATTTTCAACGTGAAAAAATTATTATTCGCAATTCCTTTAGTTGTTCCTTTCTATTCTCACTCCGCTGAAACTGTTGAAAG
TTGTTTAGCAAAATCCCATACAGAAAATTCATTTACTAACGTCTGGAAAGACGACAAAACTTTAGATCGTTACGCTAACTATGAGGGCTGTCTGTGGAATGC
TACAGGCGTTGTAGTTTGTACTGGTGACGAAACTCAGTGTTACGGTACATGGGTTCCTATTGGGCTTGCTATCCCTGAAAATGAGGGTGGTGGCTCTGAGGG
TGGCGGTTCTGAGGGTGGCGGTTCTGAGGGTGGCGGTACTAAACCTCCTGAGTACGGTGATACACCTATTCCGGGCTATACTTATATCAACCCTCTCGACGG
CACTTATCCGCCTGGTACTGAGCAAAACCCGCTAATCCTTCTCTTGAGGAGTCTCAGCCTCTTAATACTTTCATGTTTCAGAATAATAGGTTCCG
AAATAGGCAGGGGGCATTAACTGTTTATACGGGCACTGTTACTCAAGGCACTGACCCCGTTAAAACTTATTACCAGTACACTCCTGTATCATCAAAAGCCAT
GTATGACGCTTACTGGAACGGTAAATTCAGAGACTGCGCTTTCCATTCTGGCTTTAATGAGGATTTATTTGTTTGTGAATATCAAGGCCAATCGTCTGACCT
GCCTCAACCTCCTGTCAATGCTGGCGGCGGCTCTGGTGGTGGTTCTGGTGGCGGCTCTGAGGGTGGTGGCTCTGAGGGTGGCGGTTCTGAGGGTGGCGGCTC
TGAGGGAGGCGGTTCCGGTGGTGGCTCTGGTTCCGGTGATTTTGATTATGAAAAGATGGCAAACGCTAATAAGGGGGCTATGACCGAAAATGCCGATGAAAA
CGCGCTACAGTCTGACGCTAAAGGCAAACTTGATTCTGTCGCTACTGATTACGGTGCTGCTATCGATGGTTTCATTGGTGACGTTTCCGGCCTTGCTAATGG
TAATGGTGCTACTGGTGATTTTGCTGGCTCTAATTCCCAAATGGCTCAAGTCGGTGACGGTGATAATTCACCTTTAATGAATAATTTCCGTCAATATTTACC
TTCCCTCCCTCAATCGGTTGAATGTCGCCCTTTTGTCTTTGGCGCTGGTAAACCATATGAATTTTCTATTGATTGTGACAAAATAAACTTATTCCGTGGTGT
CTTTGCGTTTCTTTTATATGTTGCCACCTTTATGTATGTATTTTCTACGTTTGCTAACATACTGCGTAATAAGGAGTCTTAATCATGCCAGTTCTTTTGGGT
ATTCCGTTATTATTGCGTTTCCTCGGTTTCCTTCTGGTAACTTTGTTCGGCTATCTGCTTACTTTTCTTAAAAAGGGCTTCGGTAAGATAGCTATTGCTATT
TCATTGTTTCTTGCTCTTATTATTGGGCTTAACTCAATTCTTGTGGGTTATCTCTCTGATATTAGCGCTCAATTACCCTCTGACTTTGTTCAGGGTGTTCAG
TTAATTCTCCCGTCTAATGCGCTTCCCTGTTTTTATGTTATTCTCTCTGTAAAGGCTGCTATTTTCATTTTTGACGTTAAACAAAAAATCGTTTCTTATTTG
GATTGGGATAAATAATATGGCTGTTTATTTTGTAACTGGCAAATTAGGCTCTGGAAAGACGCTCGTTAGCGTTGGTAAGATTCAGGATAAAATTGTAGCTGG
GTGCAAAAATAGCAACTAATCTTGATTTAAGGCTTCAAAACCTCCCGCAAGTCGGGAGGTTCGCTAAAACGCCTCGCGTTCTTAGAATACCGGATAAGCCTTC
TATATCTGATTTGCTTGCTATTGGGCGCGGTAATGATTCCTACGATGAAAATAAAAACGGCTTGCTTGTTCTCGATGAGTGCGGTACTTGGTTTAATACCCG
TTCTTGGAATGATAAGGAAAGACAGCCGATTATTGATTGGTTTCTACATGCTCGTAAATTAGGATGGGATATTATTTTTCTTGTTCAGGACTTATCTATTGT
TGATAAACAGGCGCGTTCTGCATTAGCTGAACATGTTGTTTATTGTCGTCGTCTGGACAGAATTACTTTACCTTTTGTCGGTACTTTATATTCTCTTATTAC
TGGCTCGAAAATGCCTCTGCCTAAATTACATGTTGGCGTTGTTAAATATGGCGATTCTCAATTAAGCCCTACTGTTGAGCGTTGGCTTTATACTGGTAAGAA
TTTGTATAACGCATATGATACTAAACAGGCTTTTTCTAGTAATTATGATTCCGGTGTTTATTCTTATTTAACGCCTTATTTATCACACGGTCGGTATTTCAA
ACCATTAAATTTAGGTCAGAAGATGAAATTAACTAAAATATATTTGAAAAAGTTTTCTCGCGTTCTTTGTCTTGCGATTGGATTTGCATCAGCATTTACATA
TAGTTATATAACCCAACCTAAGCCGGAGGTTAAAAAGGTAGTCTCTCAGACCTATGATTTTGATAAATTCACTATTGACTCTTCTCAGCGTCTTAATCTAAG
CTATCGCTATGTTTTCAAGGATTCTAAGGGAAAATTAATTAATAGCGACGATTTACAGAAGCAAGGTTATTCACTCACATATATTGATTTATGTACTGTTTC
CATTAAAAAAGGTAATTCAAATGAAATTGTTAAATGTAATTAATTTTGTTTTCTTGATGTTTGTTTCATCATCTTCTTTTGCTCAGGTAATTGAAATGAATA
ATTCGCCTCTGCGCGATTTTGTAACTTGGTATTCAAAGCAATCAGGCGAATCCGTTATTGTTTCTCCCGATGTAAAAGGTACTGTTACTGTATATTCATCTG
ACGTTAAACCTGAAAATCTACGCAATTTCTTTATTTCTGTTTTACGTGCAAATAATTTTGATATGGTAGGTTCTAACCCTTCCATTATTCAGAAGTATAATC
CAAACAATCAGGATTATATTGATGAATTGCCATCATCTGATAATCAGGAATATGATGATAATTCCGCTCCTTCTGGTGGTTTCTTTGTTCCGCAAAATGATA
ATGTTACTCAAACTTTTAAAATTAATAACGTTCGGGCAAAGGATTTAATACGAGTTGTCGAATTGTTTGTAAAGTCTAATACTTCTAAATCCTCAAATGTAT
TATCTATTGACGGCTCTAATCTATTAGTTGTTAGTGCTCCTAAAGATATTTTAGATAACCTTCCTCAATTCCTTTCAACTGTTGATTTGCCAACTGACCAGA
TATTGATTGAGGGTTTGATATTTGAGGTTCAGCAAGGTGATGCTTTAGATTTTTCATTTGCTGCTGGCTCTCAGCGTGGCACTGTTGCAGGCGGTGTTAATA
CTGACCGCCTCACCTCTGTTTTATCTTCTGCTGGTGGTTCGTTCGGTATTTTTAATGGCGATGTTTTAGGGCTATCAGTTCGCGCATTAAAGACTAATAGCC
ATTCAAAAATATTGTCTGTGCCACGTATTCTTACGCTTTCAGGTCAGAAGGGTTCTATCTCTGTTGGCCAGAATGTCCCTTTTATTACTGGTCGTGTGACTG
GTGAATCTGCCAATGTAAATAATCCATTTCAGACGATTGAGCGTCAAAATGTAGGTATTTCCATGAGCGTTTTTCCTGTTGCAATGGCTGGCGGTAATATTG
TTCTGGATATTACCAGCAAGGCCGATAGTTTGAGTTCTTCTACTCAGGCAAGTGATGTTATTACTAATCAAAGAAGTATTGCTACAACGGTTAATTTGCGTG
ATGGACAGACTCTTTTACTCGGTGGCCTCACTGATTATAAAAACACTTCTCAGGATTCTGGCGTACCGTTCCTGTCTAAAATCCCTTTAATCGGCCTCCTGT
TTAGCTCCCGCTCTGATTCTAACGAGGAAAGCACGTTATACGTGCTCGTCAAAGCAACCATAGTACGCGCCCTGTAGCGGCGCATTAAGCGCGGCGGGTGTG
GTGGTTACGCGCAGCGTGACCGCTACACTTGCCAGCGCCCTAGCGCCCGCTCCTTTCGCTTTCTTCCCTTCCTTTCTCGCCACGTTCGCCGGCTTTCCCCGT
CAAGCTCTAAATCGGGGGCTCCCTTTAGGGTTCCGATTTAGTGCTTTACGGCACCTCGACCCCAAAAAACTTGATTTGGGTGATGGTTCACGTAGTGGGCCA
TCGCCC

Figure B.26 Sequence of the 8064 nt**-long custom scaffold [83]**

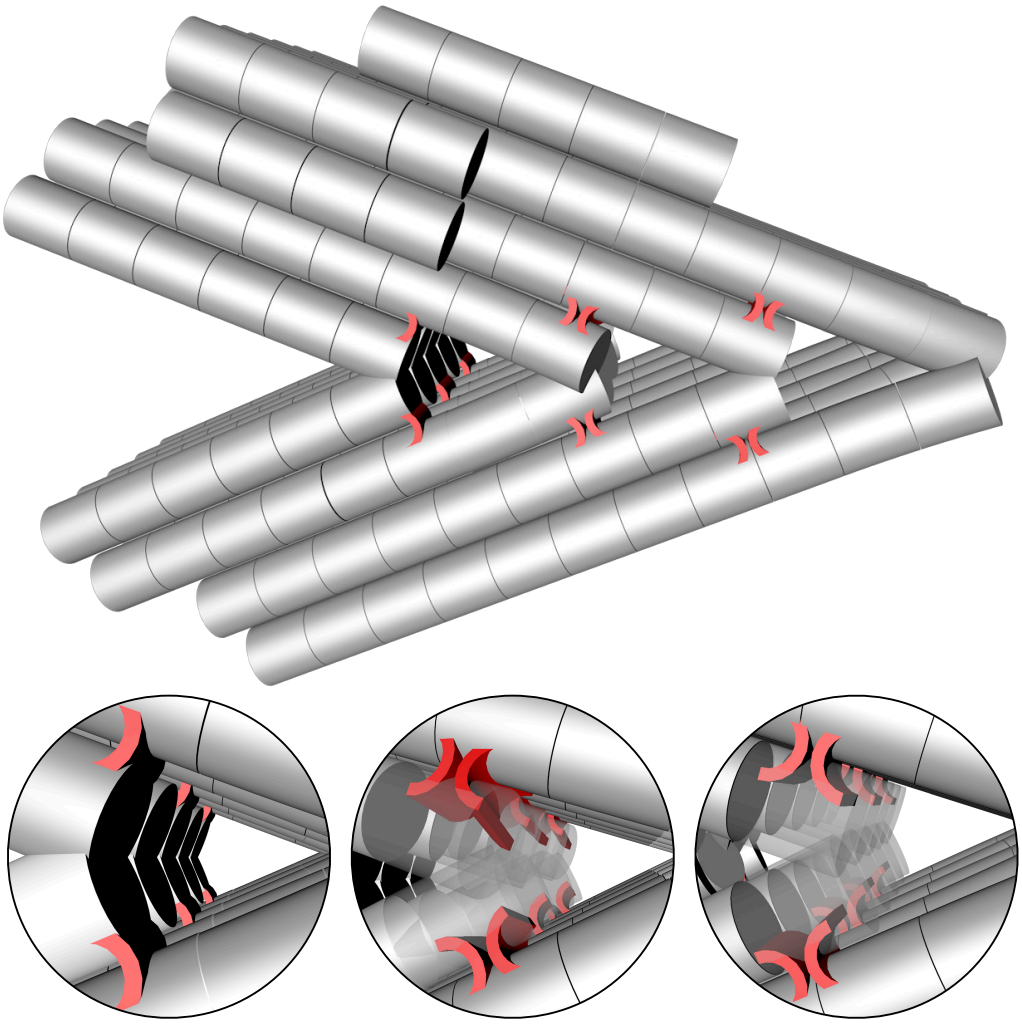

Figure B.27 Interlayer staple crossovers close to the corner sites. Staple crossovers are illustrated as red arcs. Full-crossovers connecting the outer and central helices of the first, second, and third layers are placed very close to the corner sites. Half-crossovers connecting the two outer and the central helices between the third and fourth layer are positioned directly at the corner site. In the three zoom-in views, parts of the helices are rendered transparent to make the crossovers visible.

Appendix C

Supporting information: gel electrophoresis

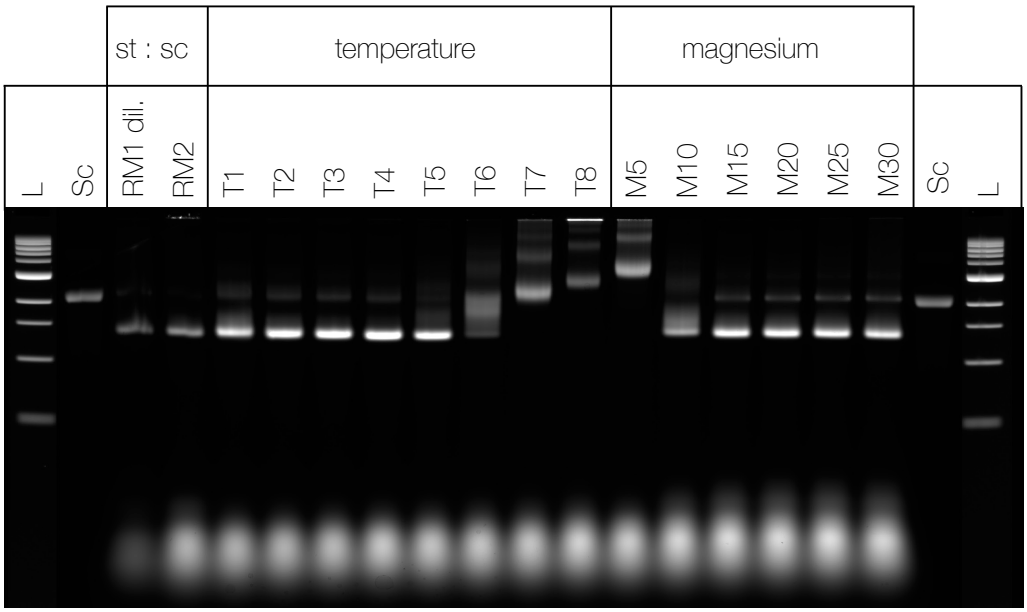

Figure C.1 Initial Folding Screen of the TwistTower. L = Ladder, Sc = scaffold, RM1 dil. = dilution 1:2.5 of Reaction Mixture 1 with FOB20, RM2 = Reaction Mixture 2, T1 to T8 = temperature screens, M5 to M30 = magnesium screens. A 1k base ladder and the 8064 nt scaffold were used as references. The reaction mixtures and annealing ramps were used as described in table A.1.

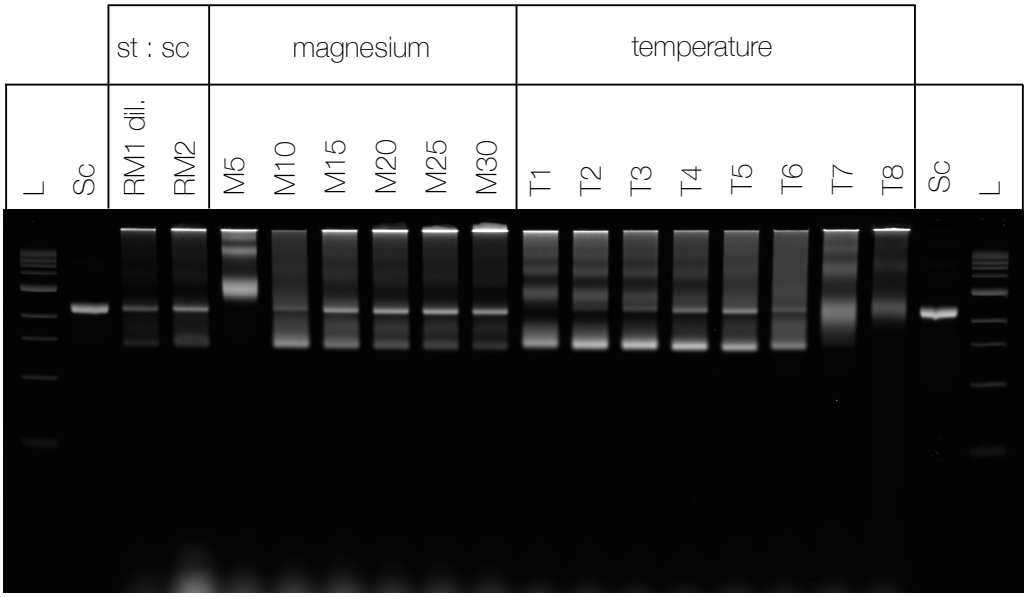

Figure C.2 Initial Folding Screen of CS-v1. L = Ladder, Sc = scaffold, RM1 dil. = dilution 1:2.5 of Reaction Mixture 1 with FOB20, RM2 = Reaction Mixture 2, T1 to T8 = temperature screens, M5 to M30 = magnesium screens. A 1k base ladder and the 2873 nt scaffold were used as references. The reaction mixtures and annealing ramps were used as described in table A.1.

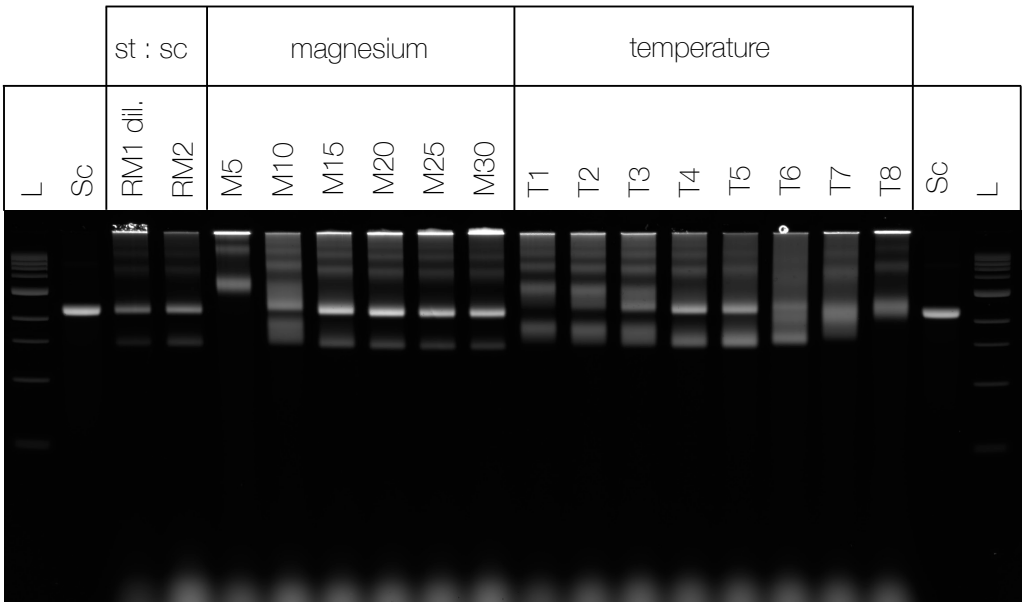

Figure C.3 Initial Folding Screen of CS-v2. L = Ladder, Sc = scaffold, RM1 dil. = dilution 1:2.5 of Reaction Mixture 1 with FOB20, RM2 = Reaction Mixture 2, T1 to T8 = temperature screens, M5 to M30 = magnesium screens. A 1k base ladder and the 2873 nt scaffold were used as references. The reaction mixtures and annealing ramps were used as described in table A.1.

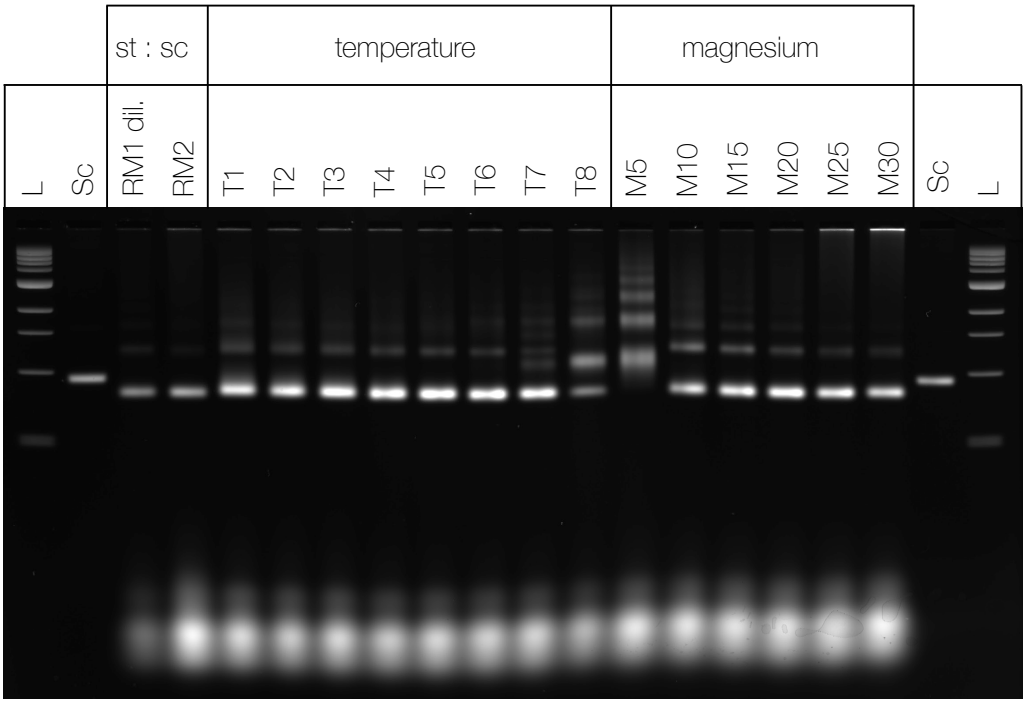

Figure C.4 Initial Folding Screen of CS-v3. L = Ladder, Sc = scaffold, RM1 dil. = dilution 1:2.5 of Reaction Mixture 1 with FOB20, RM2 = Reaction Mixture 2, T1 to T8 = temperature screens, M5 to M30 = magnesium screens. A 1k base ladder and the 2873 nt scaffold were used as references. The reaction mixtures and annealing ramps were used as described in table A.1.

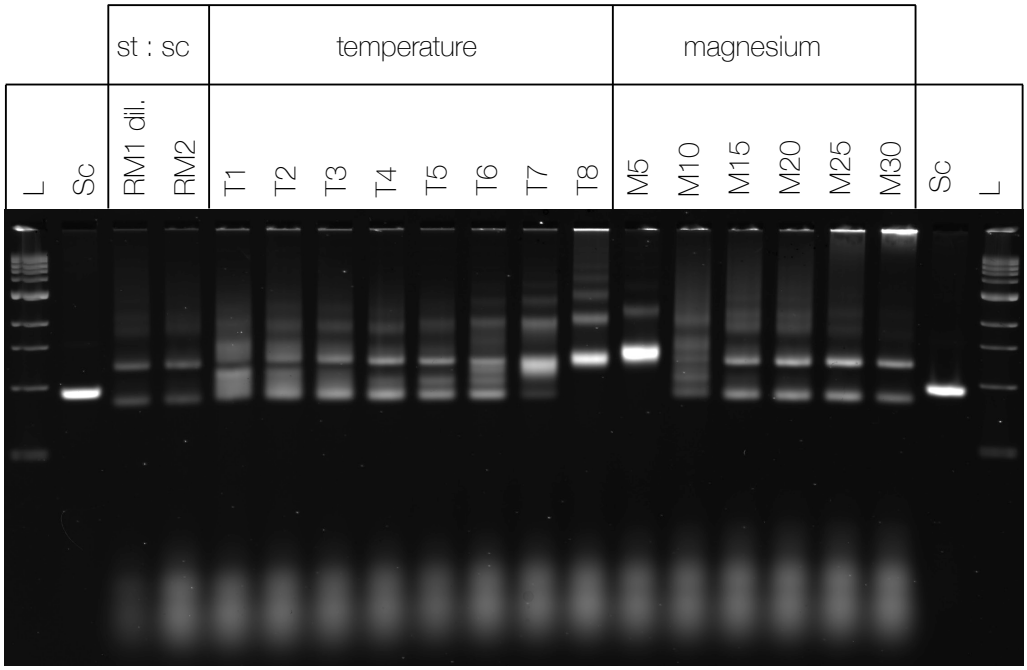

Figure C.5 Initial Folding Screen of CS-v4. L = Ladder, Sc = scaffold, RM1 dil. = dilution 1:2.5 of Reaction Mixture 1 with FOB20, RM2 = Reaction Mixture 2, T1 to T8 = temperature screens, M5 to M30 = magnesium screens. A 1k base ladder and the 2873 nt scaffold were used as references. The reaction mixtures and annealing ramps were used as described in table A.1.

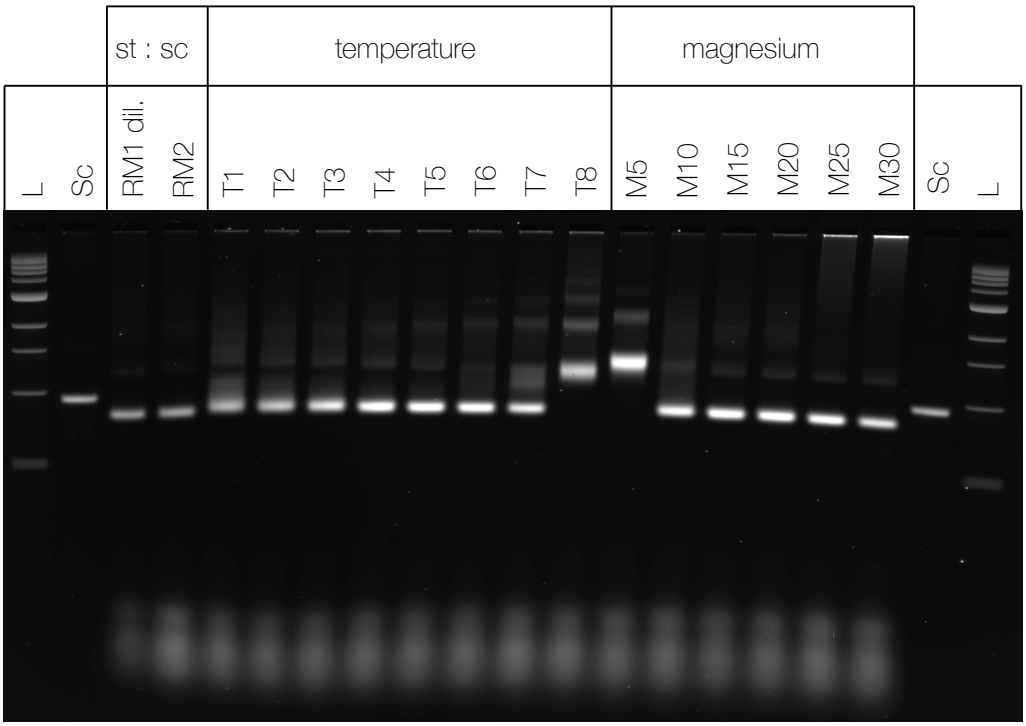

Figure C.6 Initial Folding Screen of CS-v4-2. L = Ladder, Sc = scaffold, RM1 dil. = dilution 1:2.5 of Reaction Mixture 1 with FOB20, RM2 = Reaction Mixture 2, T1 to T8 = temperature screens, M5 to M30 = magnesium screens. A 1k base ladder and the 2873 nt scaffold were used as references. The reaction mixtures and annealing ramps were used as described in table A.1.

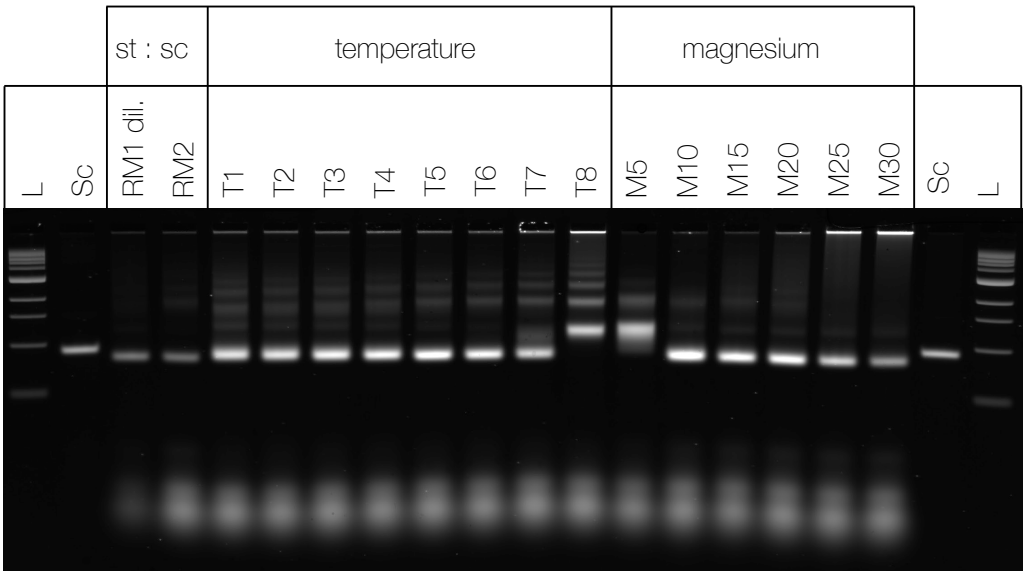

Figure C.7 Initial Folding Screen of CS-v5. L = Ladder, Sc = scaffold, RM1 dil. = dilution 1:2.5 of Reaction Mixture 1 with FOB20, RM2 = Reaction Mixture 2, T1 to T8 = temperature screens, M5 to M30 = magnesium screens. A 1k base ladder and the 2873 nt scaffold were used as references. The reaction mixtures and annealing ramps were used as described in table A.1. The reaction mixture did not contain the oligonucleotides which make the braces double stranded.

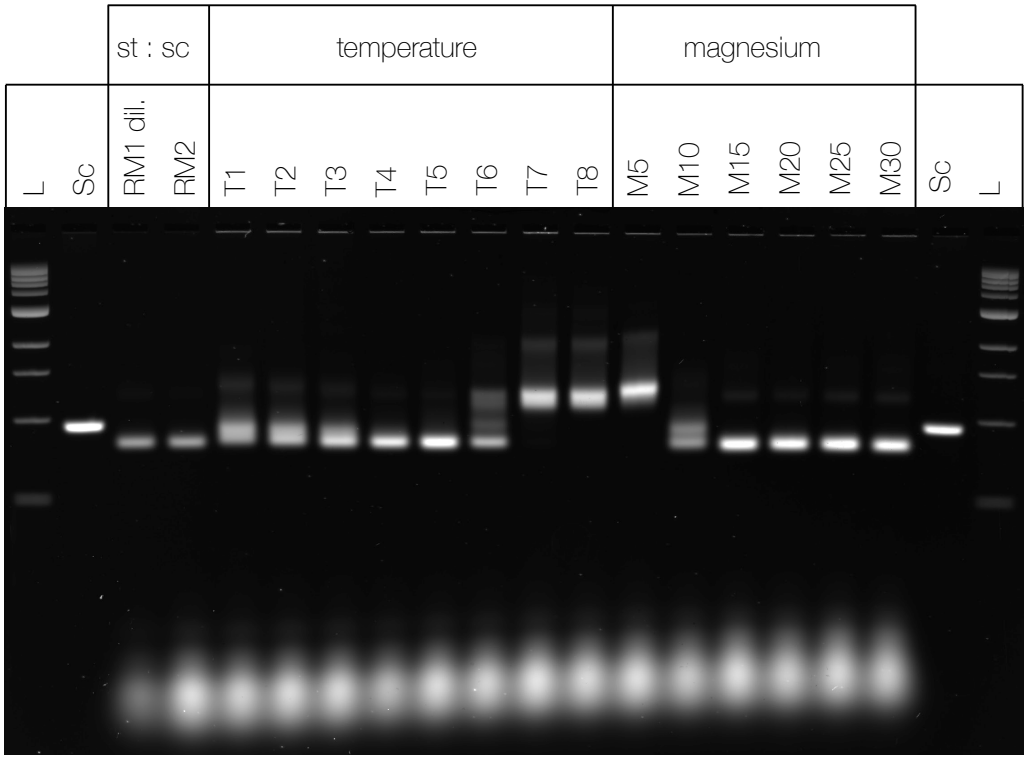

Figure C.8 Initial Folding Screen of CS-v6. L = Ladder, Sc = scaffold, RM1 dil. = dilution 1:2.5 of Reaction Mixture 1 with FOB20, RM2 = Reaction Mixture 2, T1 to T8 = temperature screens, M5 to M30 = magnesium screens. A 1k base ladder and the 2873 nt scaffold were used as references. The reaction mixtures and annealing ramps were used as described in table A.1. The reaction mixture did not contain the oligonucleotides which make the braces double stranded.

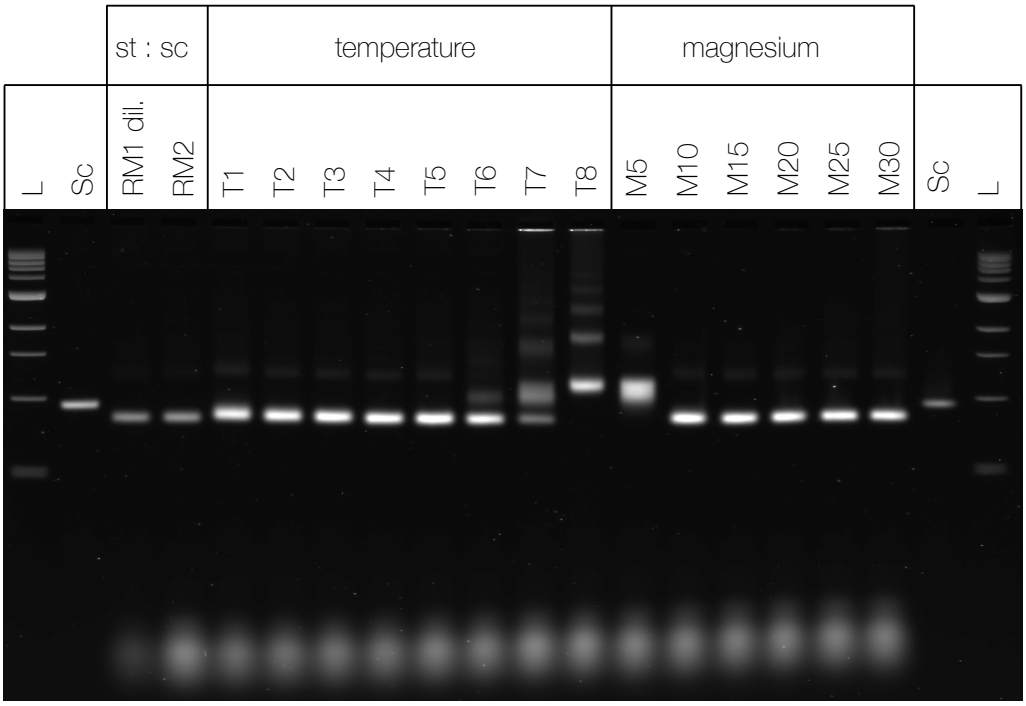

Figure C.9 Initial Folding Screen of CS-v7. L = Ladder, Sc = scaffold, RM1 dil. = dilution 1:2.5 of Reaction Mixture 1 with FOB20, RM2 = Reaction Mixture 2, T1 to T8 = temperature screens, M5 to M30 = magnesium screens. A 1k base ladder and the 2873 nt scaffold were used as references. The reaction mixtures and annealing ramps were used as described in table A.1.

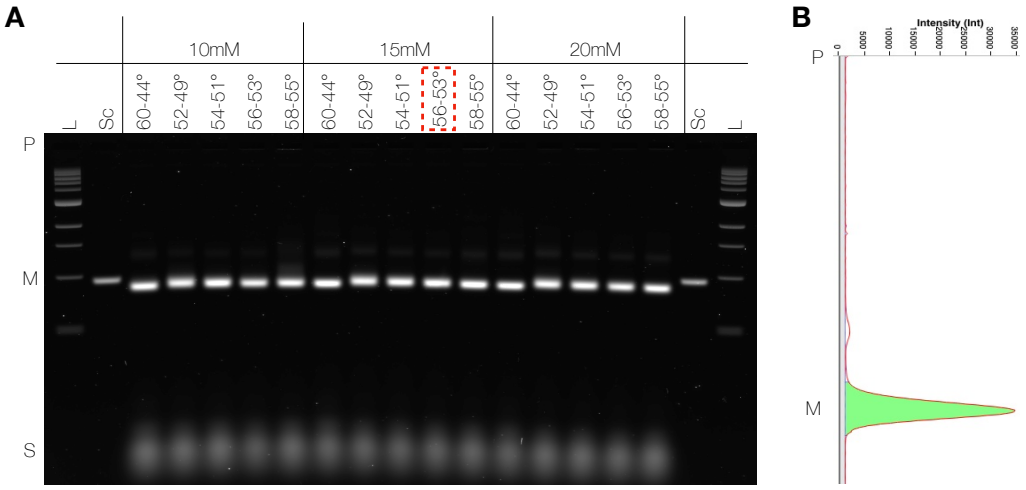

Figure C.10 Fine Folding Screen of CS-v7. A Gel scan. L = 1k-nt ladder, Sc = 2873-nt scaffold, P = gel pocket, M = approximate migration distance of monomers, P = excess staples. Samples were folded containing 50 nM scaffold and 200 nM staples, in folding buffers containing 10 mM to 20 mM $MgCl_2$ as indicated. Annealing ramps with 1 °C/h were applied using temperature ranges as indicated. The box indicates the folding condition used for preparing the cryo-EM sample. **(B)** Intensity profile of the folding condition highlighted in A. The monomer yield is 94 %.

Appendix D

Supporting information: reconstructions

D.1 Cryo-EM map determination

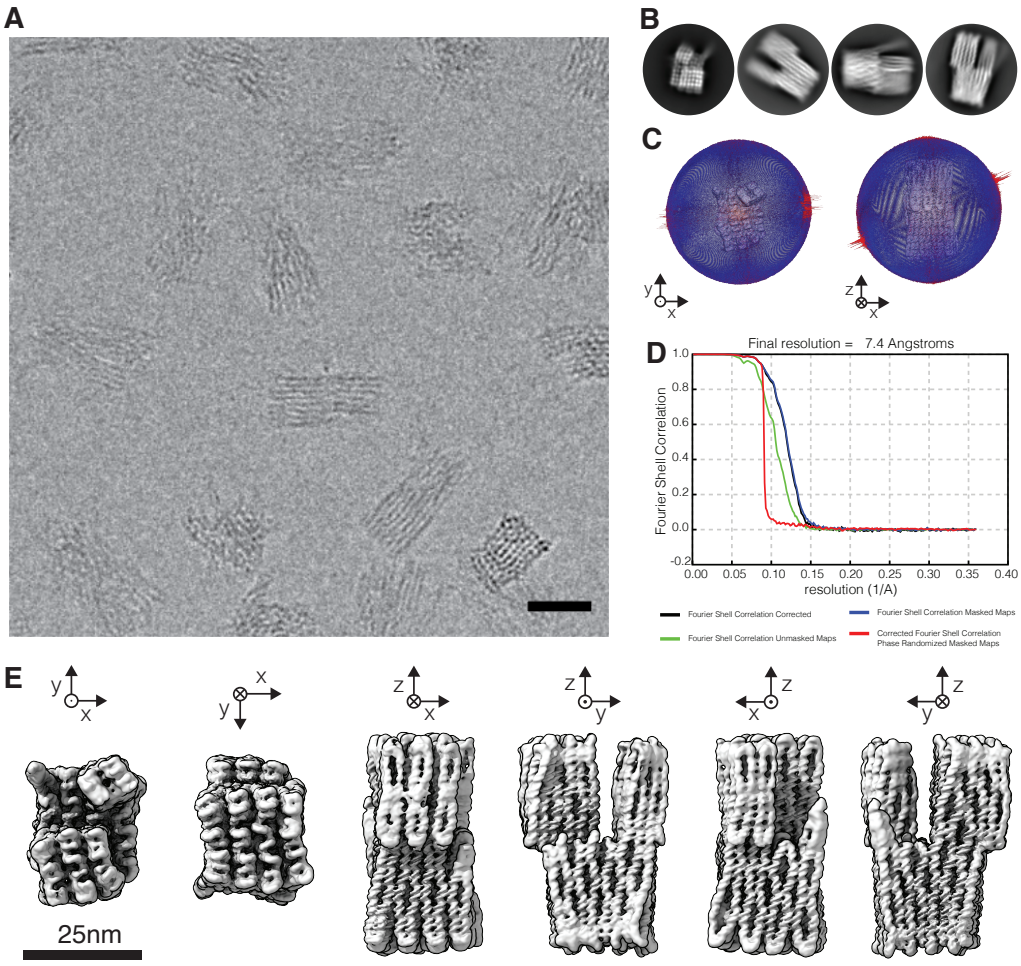

Figure D.1 Cryo-EM map determination of the TwistTower object. (A) Exemplary micrograph section. Scale bar is 25 nm **(B)** Representative 2D Class averages. **(C)** 3D Histogram representing the orientational distribution of particles. **(D)** FSC plots. **(E)** Six different views of the electron density map. Scale bar is 25 nm. Sample preparation and imaging conditions are listed in Tab. A.2 and Tab. A.3 [74].

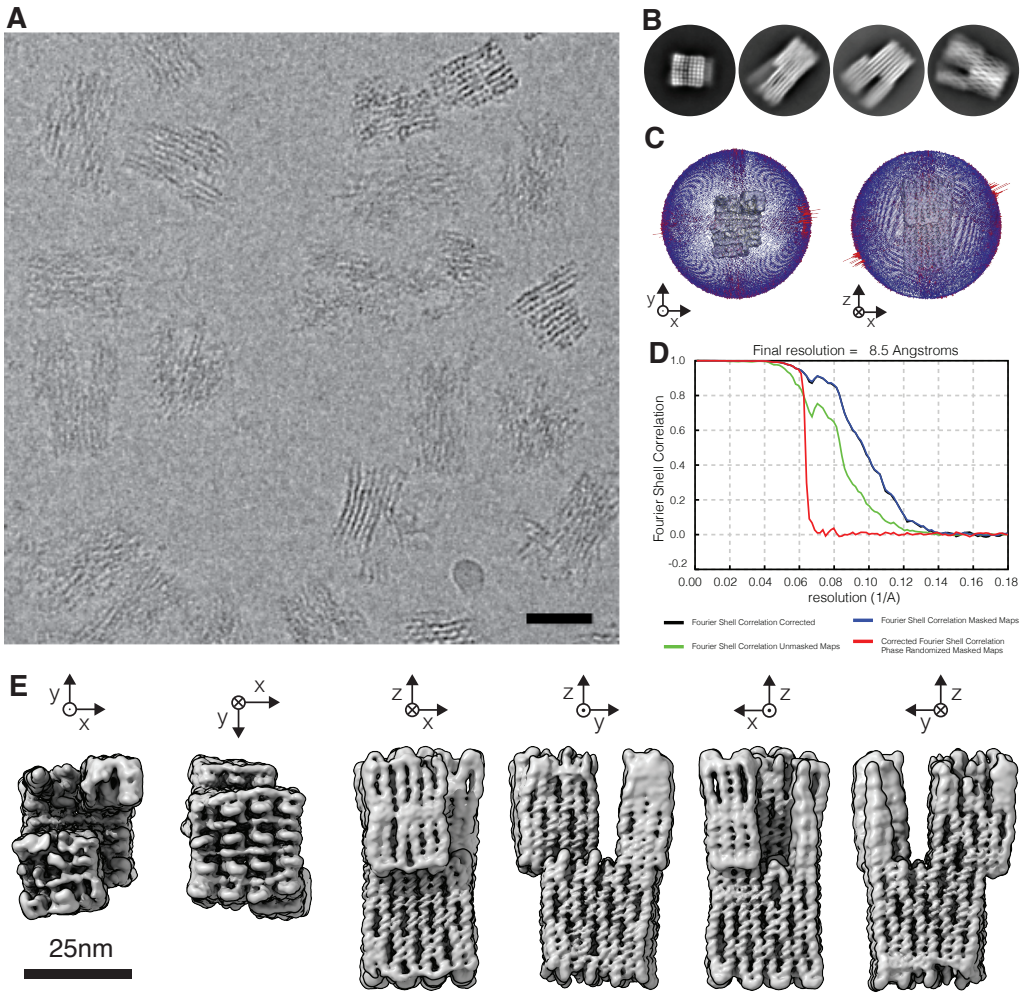

Figure D.2 Cryo-EM map determination of the TwistTower-v2 object. (A) Exemplary micrograph section. Scale bar is 25 nm **(B)** Representative 2D Class averages. **(C)** 3D Histogram representing the orientational distribution of particles. **(D)** FSC plots. **(E)** Six different views of the electron density map. Scale bar is 25 nm. Sample preparation and imaging conditions are listed in Tab. A.2 and Tab. A.3 [74].

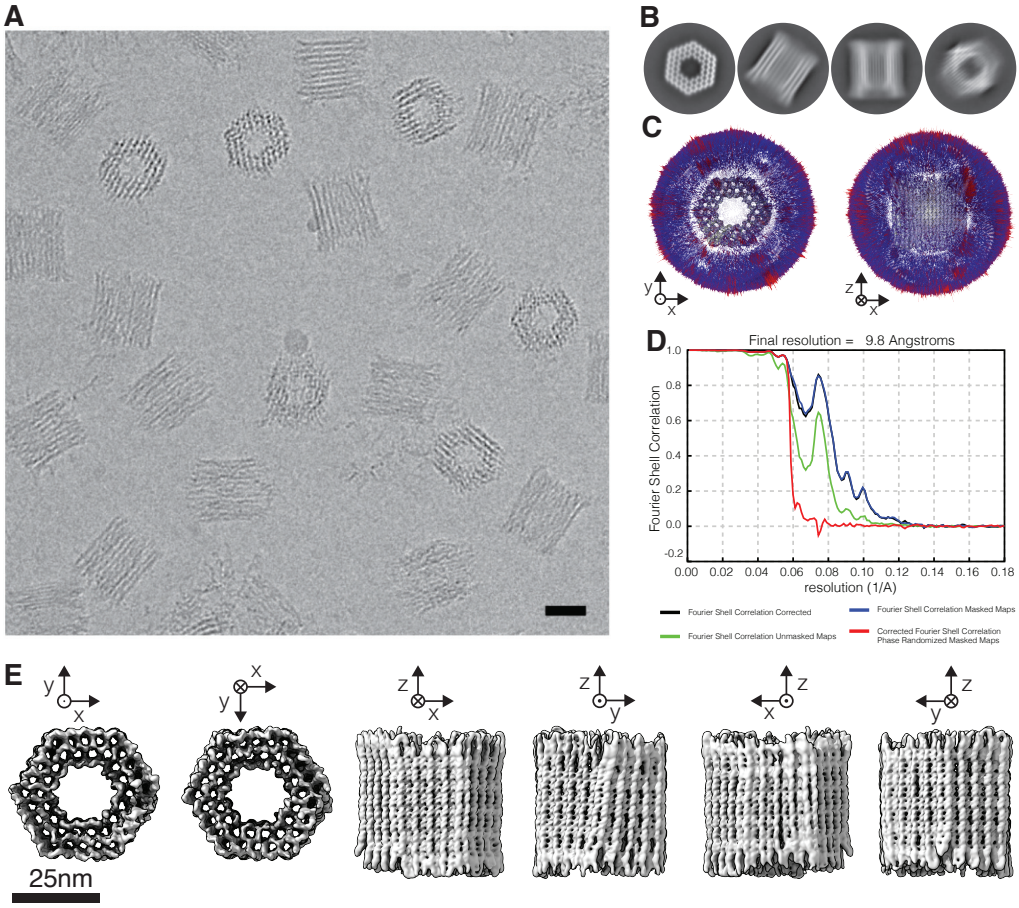

Figure D.3 Cryo-EM map determination of the 126 helix-bundle object. (A) Exemplary micrograph section. Scale bar is 25 nm **(B)** Representative 2D Class averages. **(C)** 3D Histogram representing the orientational distribution of particles. **(D)** FSC plots. **(E)** Six different views of the electron density map. Scale bar is 25 nm. Sample preparation and imaging conditions are listed in Tab. A.2 and Tab. A.3 [74].

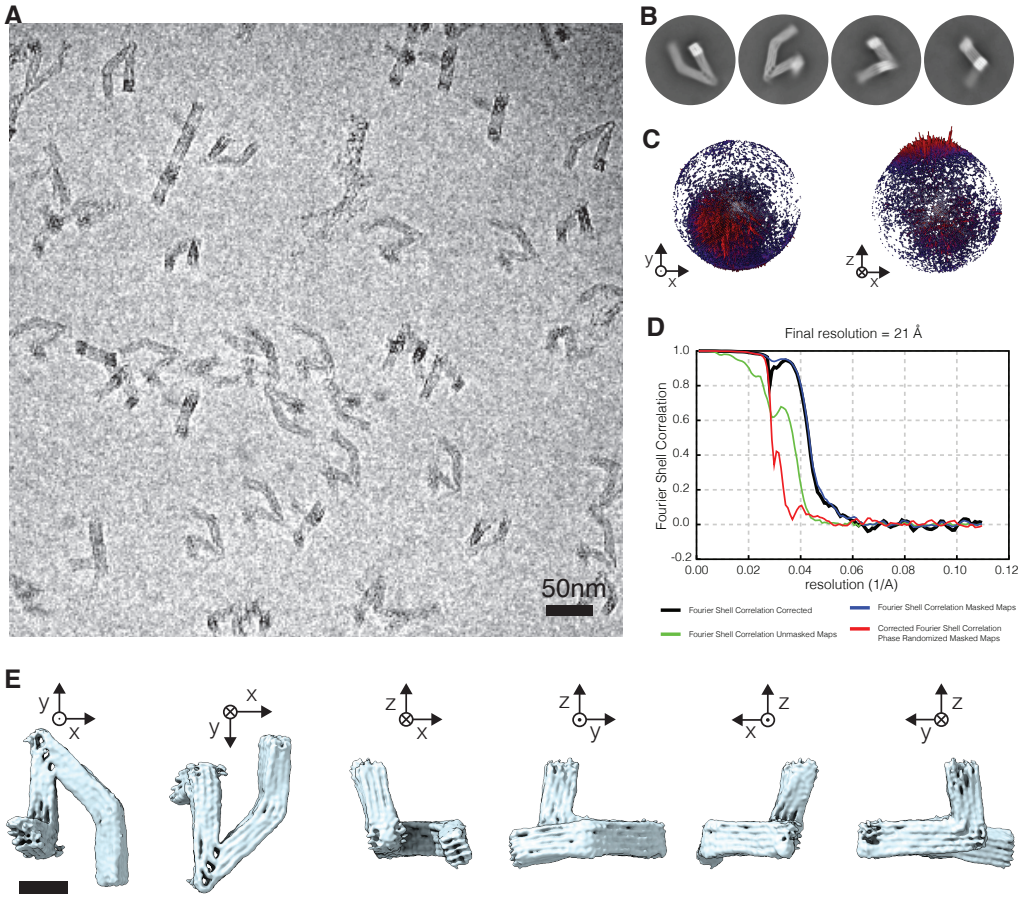

Figure D.4 Cryo-EM map determination of the CS-v1 object. (A) Exemplary micrograph. Scale bar is 50 nm **(B)** Representative 2D Class averages. **(C)** 3D Histogram representing the orientational distribution of particles. **(D)** FSC plots. **(E)** Six different views of the electron density map. Scale bar is 20 nm. Sample preparation and imaging conditions are listed in Tab. A.2 and Tab. A.3.

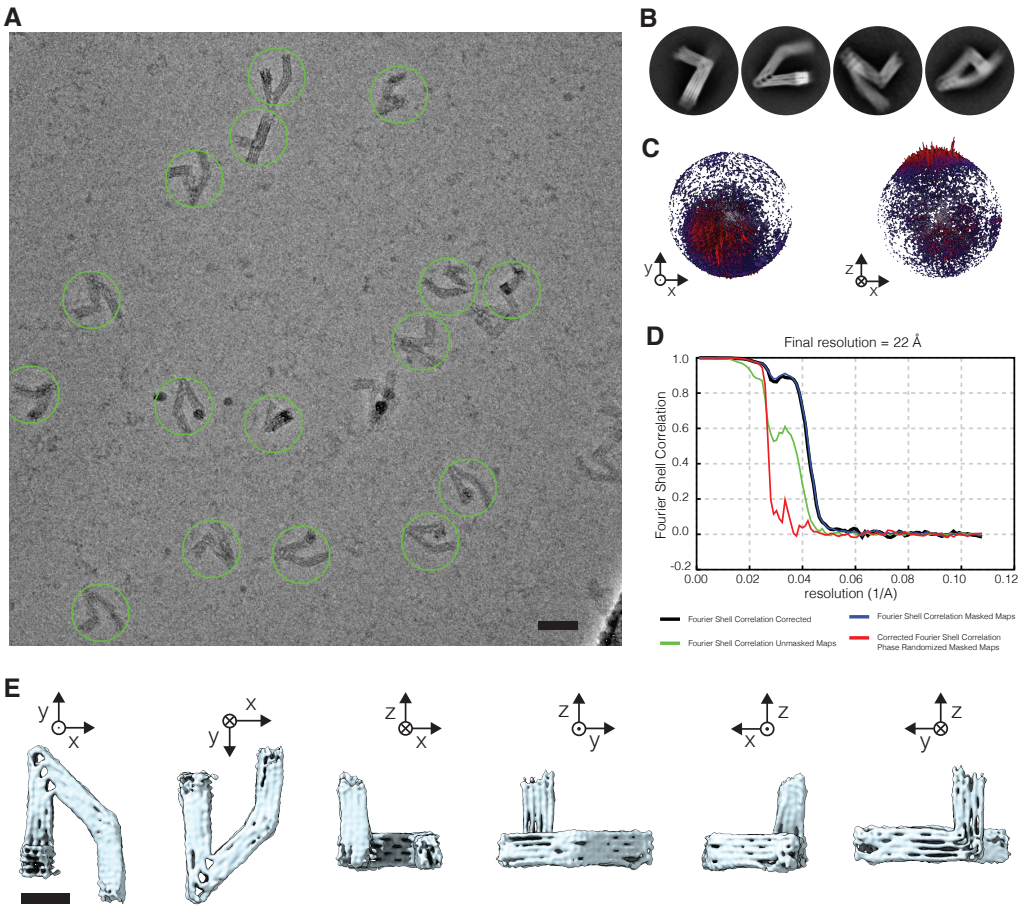

Figure D.5 Cryo-EM map determination of the CS-v1 object exposed to EtBr. **(A)** Exemplary micrograph. Scale bar is 50 nm **(B)** Representative 2D Class averages. **(C)** 3D Histogram representing the orientational distribution of particles. **(D)** FSC plots. **(E)** Six different views of the electron density map. Scale bar is 20 nm. Sample preparation and imaging conditions are listed in Tab. A.2 and Tab. A.3.

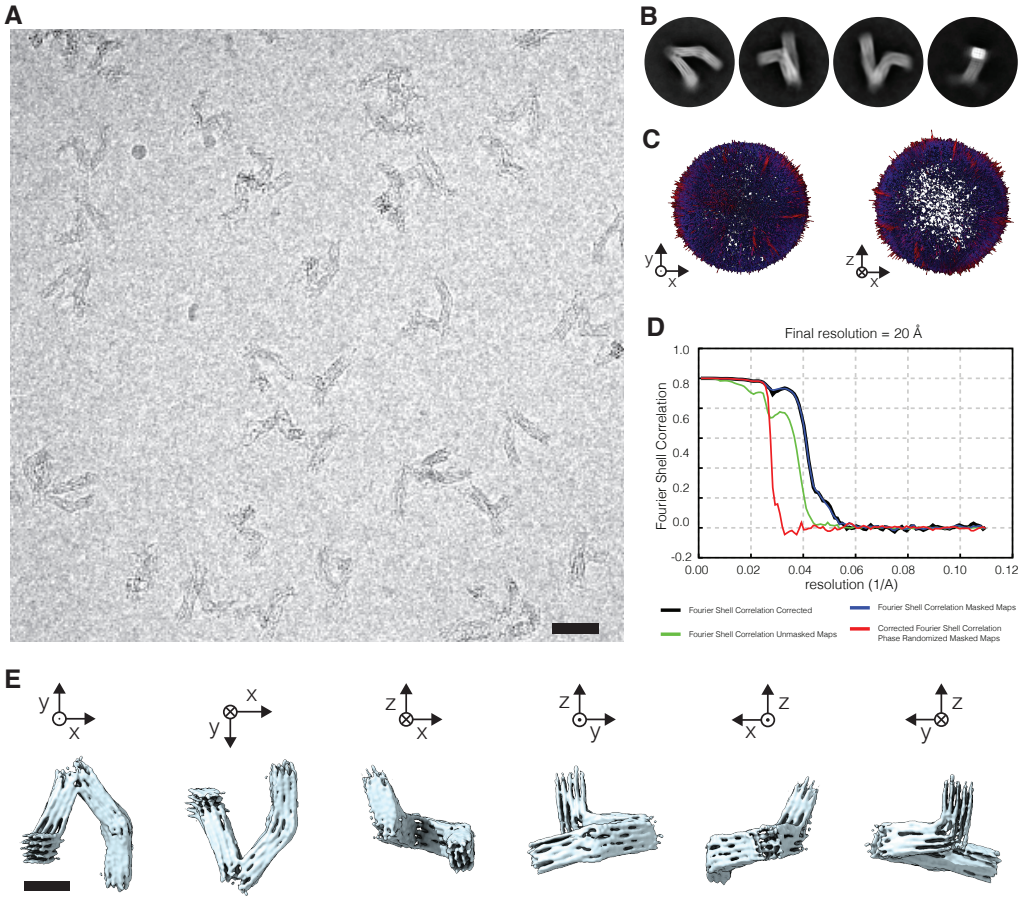

Figure D.6 Cryo-EM map determination of the CS-v2-1ss object. **(A)** Exemplary micrograph. Scale bar is 50 nm **(B)** Representative 2D Class averages. **(C)** 3D Histogram representing the orientational distribution of particles. **(D)** FSC plots. **(E)** Six different views of the electron density map. Scale bar is 20 nm. Sample preparation and imaging conditions are listed in Tab. A.2 and Tab. A.3.

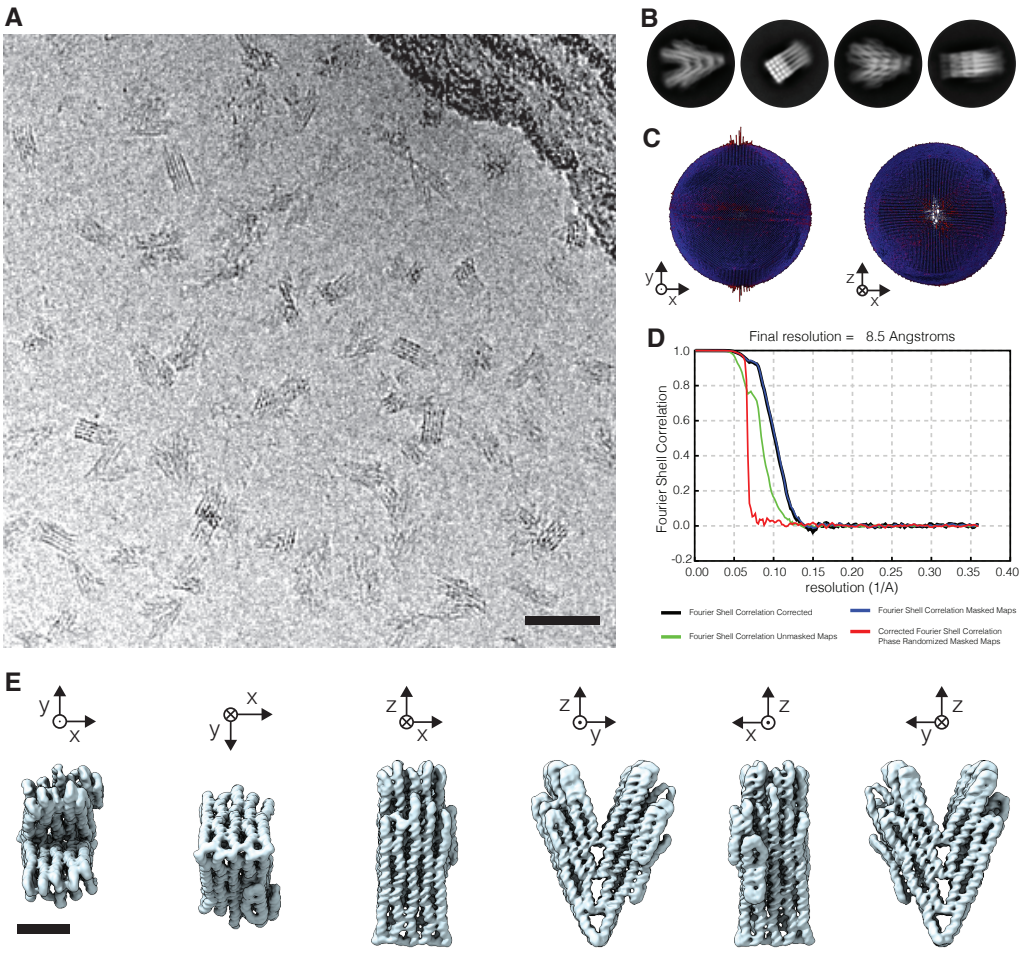

Figure D.7 Cryo-EM map determination of the CS-v3 object. **(A)** Exemplary micrograph. Scale bar is 50 nm **(B)** Representative 2D Class averages. **(C)** 3D Histogram representing the orientational distribution of particles. **(D)** FSC plots. **(E)** Six different views of the electron density map. Scale bar is 10 nm. Sample preparation and imaging conditions are listed in Tab. A.2 and Tab. A.3.

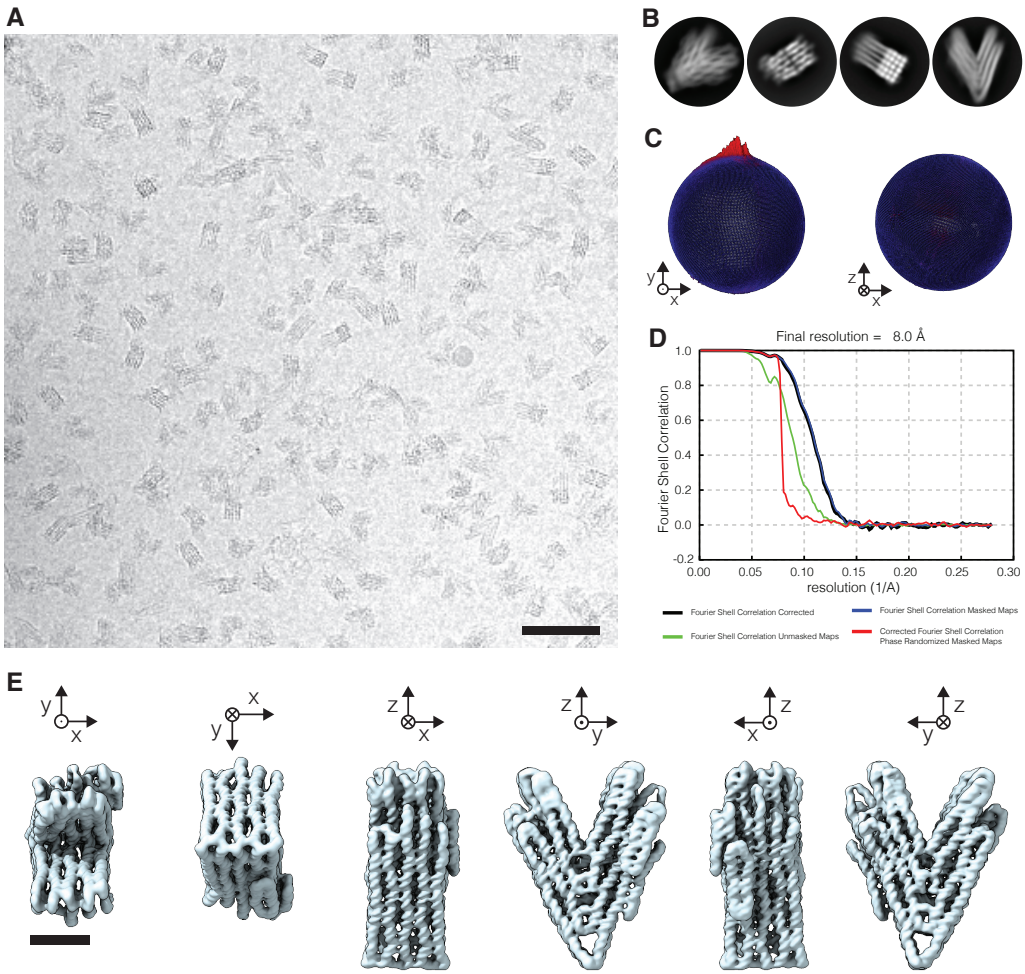

Figure D.8 Cryo-EM map determination of the CS-v4-2 object. **(A)** Exemplary micrograph. Scale bar is 50 nm **(B)** Representative 2D Class averages. **(C)** 3D Histogram representing the orientational distribution of particles. **(D)** FSC plots. **(E)** Six different views of the electron density map. Scale bar is 10 nm. Sample preparation and imaging conditions are listed in Tab. A.2 and Tab. A.3.

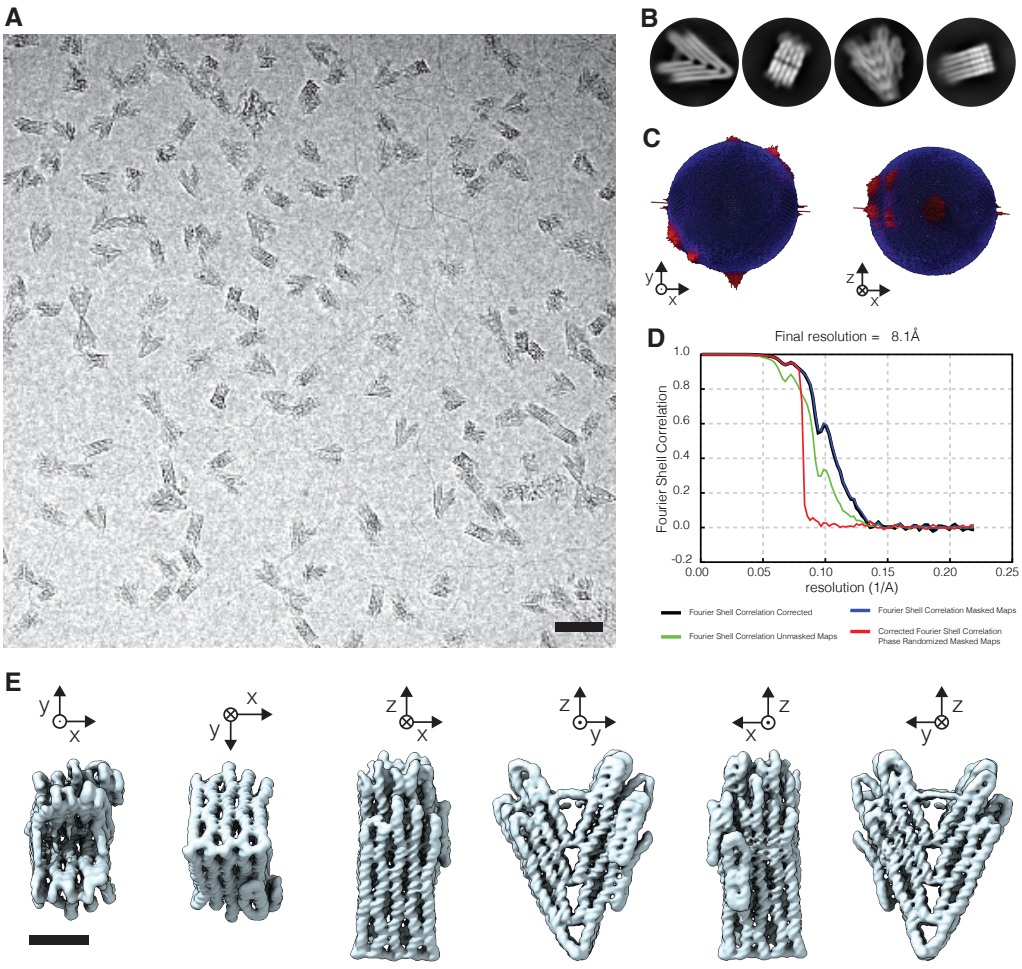

Figure D.9 Cryo-EM map determination of the CS-v5 object. **(A)** Exemplary micrograph. Scale bar is 50 nm **(B)** Representative 2D Class averages. **(C)** 3D Histogram representing the orientational distribution of particles. **(D)** FSC plots. **(E)** Six different views of the electron density map. Scale bar is 10 nm. Sample preparation and imaging conditions are listed in Tab. A.2 and Tab. A.3.

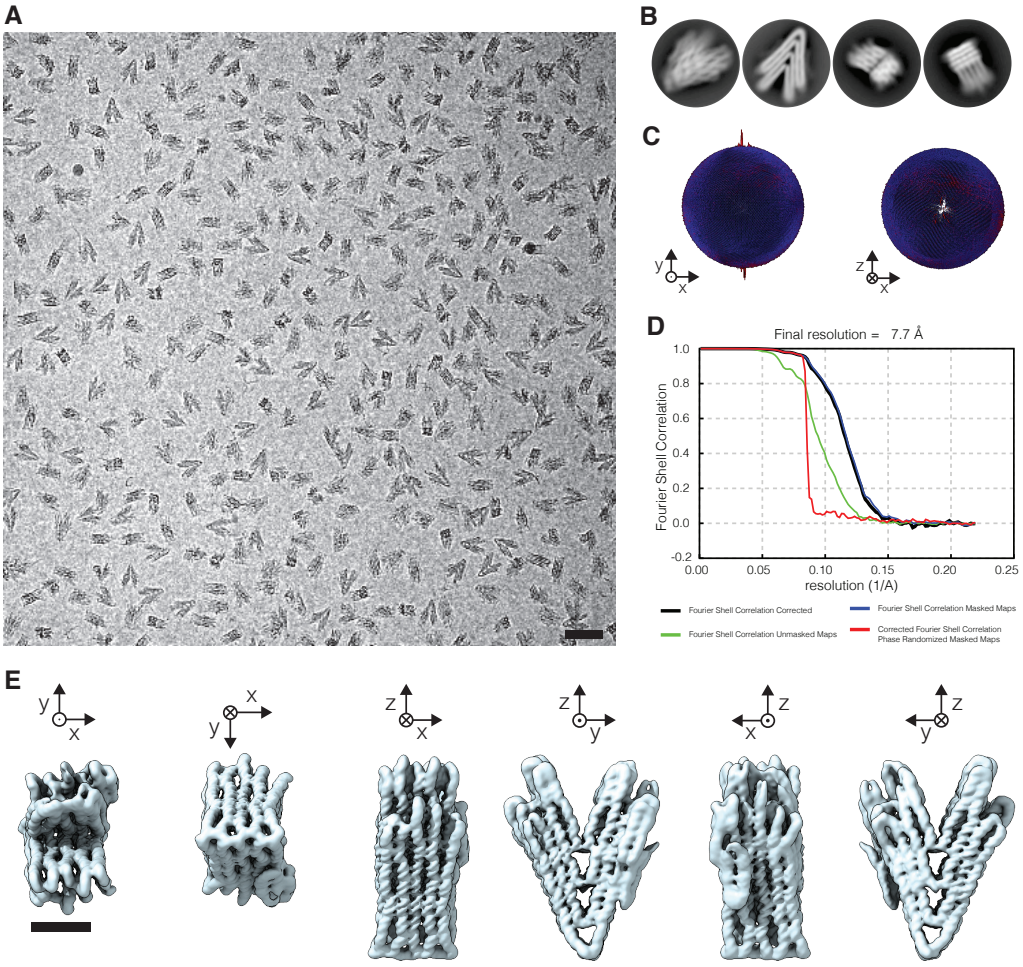

Figure D.10 Cryo-EM map determination of the CS-v6 object. **(A)** Exemplary micrograph. Scale bar is 50 nm **(B)** Representative 2D Class averages. **(C)** 3D Histogram representing the orientational distribution of particles. **(D)** FSC plots. **(E)** Six different views of the electron density map. Scale bar is 10 nm. Sample preparation and imaging conditions are listed in Tab. A.2 and Tab. A.3.

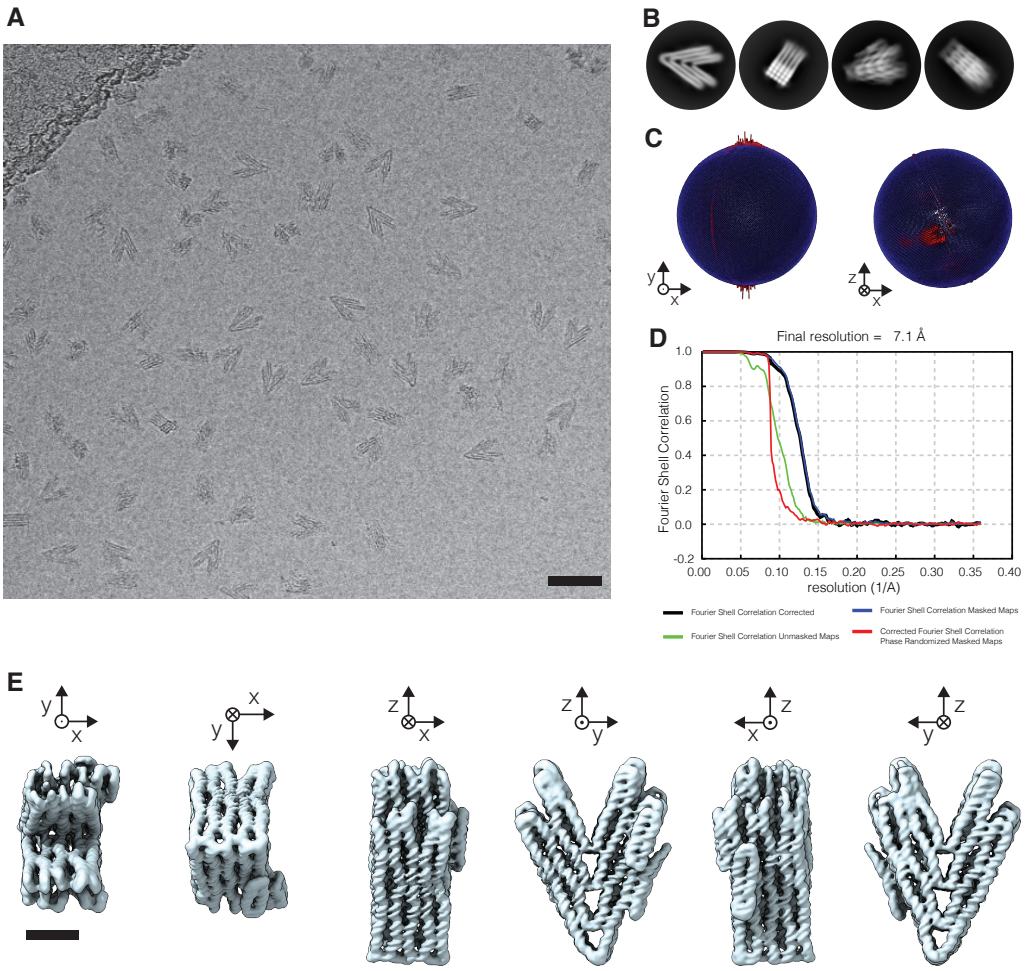

Figure D.11 Cryo-EM map determination of the CS-v7 object. **(A)** Exemplary micrograph. Scale bar is 50 nm **(B)** Representative 2D Class averages. **(C)** 3D Histogram representing the orientational distribution of particles. **(D)** FSC plots. **(E)** Six different views of the electron density map. Scale bar is 10 nm. Sample preparation and imaging conditions are listed in Tab. A.2 and Tab. A.3.

D.2 Multi-body refinements

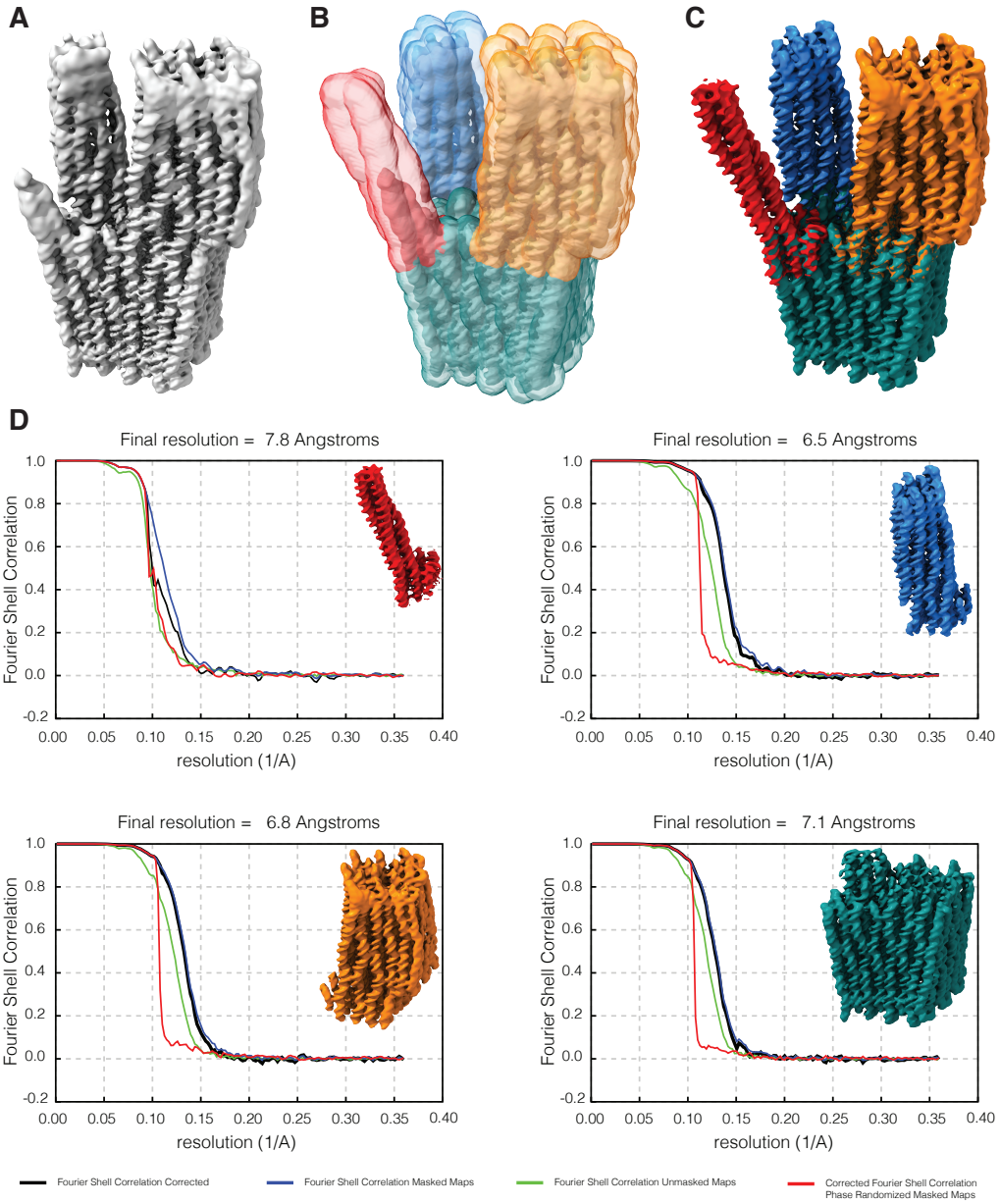

Figure D.12 Multi-body refinement of the TwistTower. **(A)** Consensus refinement. **(B)** Representation of masks used for multibody refinement. **(C)** Superposition of the multi-body refined parts. **(D)** FSC curves for the individual bodies [74].

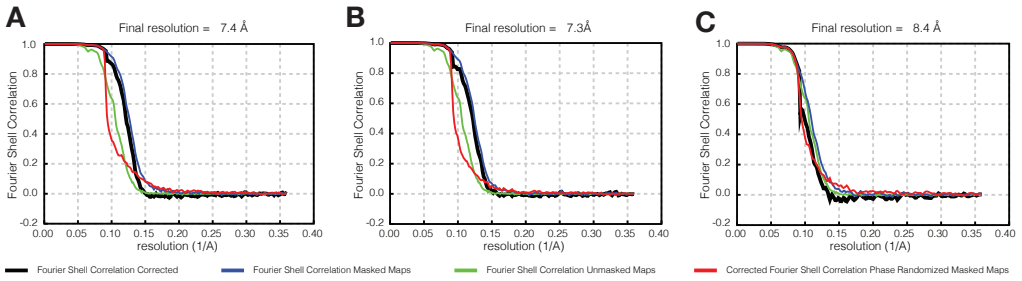

Figure D.13 Resolution estimation of domains in consensus refinement. (A) FSC curves of the 8 × 8 domain. The resolution of the region is estimated by masking of the consensus refined map using the separation of the multi-body refinement. **(B)** 6 × 6 domain.**(C)** 4 × 4 domain.

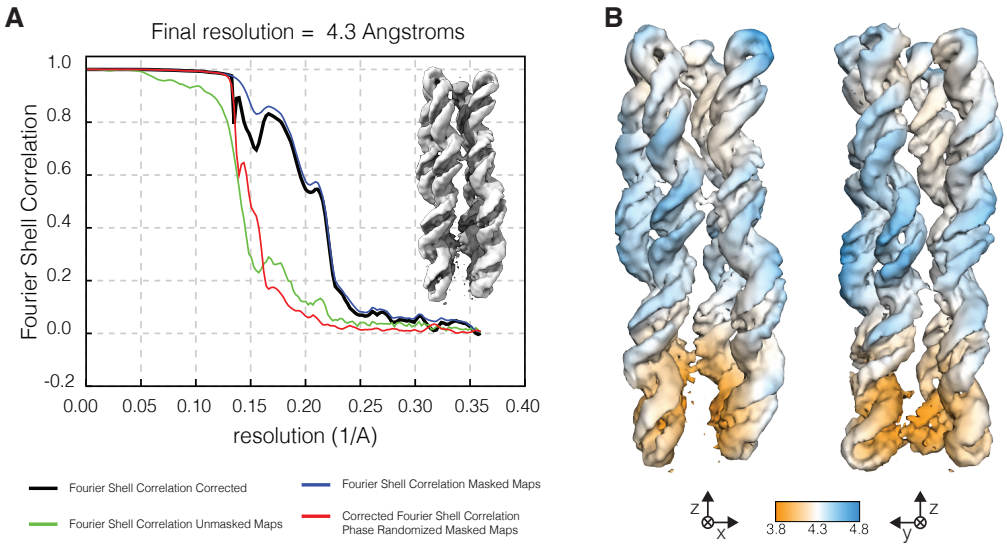

Figure D.14 Focused refinement of the central region of the 4 × 4 domain. (A) FSC curves for the focused refinement. **(B)** Local resolution estimation. [74].

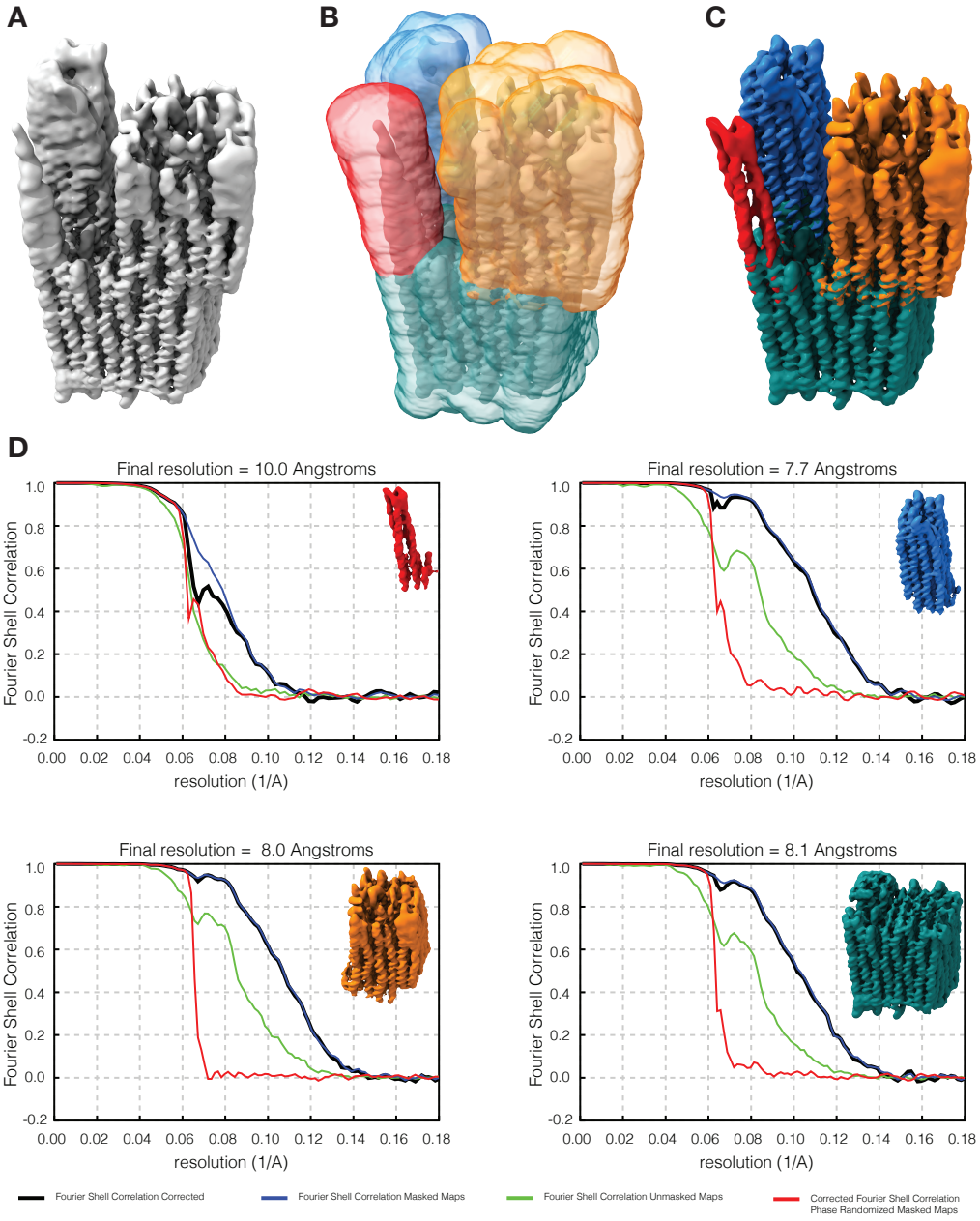

Figure D.15 Multi-body refinement of the TwistTower-v2. **(A)** Consensus refinement. **(B)** Representation of masks used for multibody refinement. **(C)** Superposition of the multi-body refined parts. **(D)** FSC curves for the individual bodies [74].

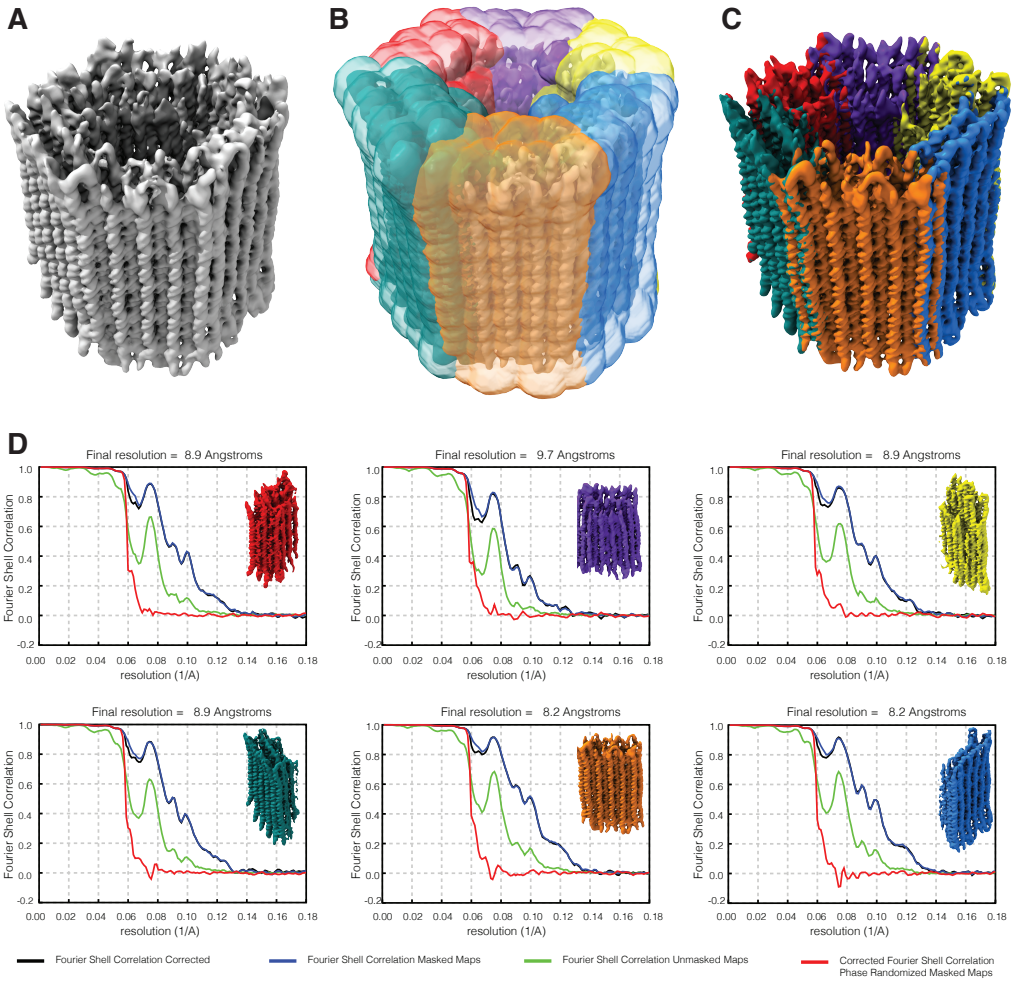

Figure D.16 Multi-body refinement of the 126 helix bundle. **(A)** Consensus refinement. **(B)** Representation of masks used for multibody refinement. **(C)** Superposition of the multi-body refined parts. **(D)** FSC curves for the individual bodies [74].

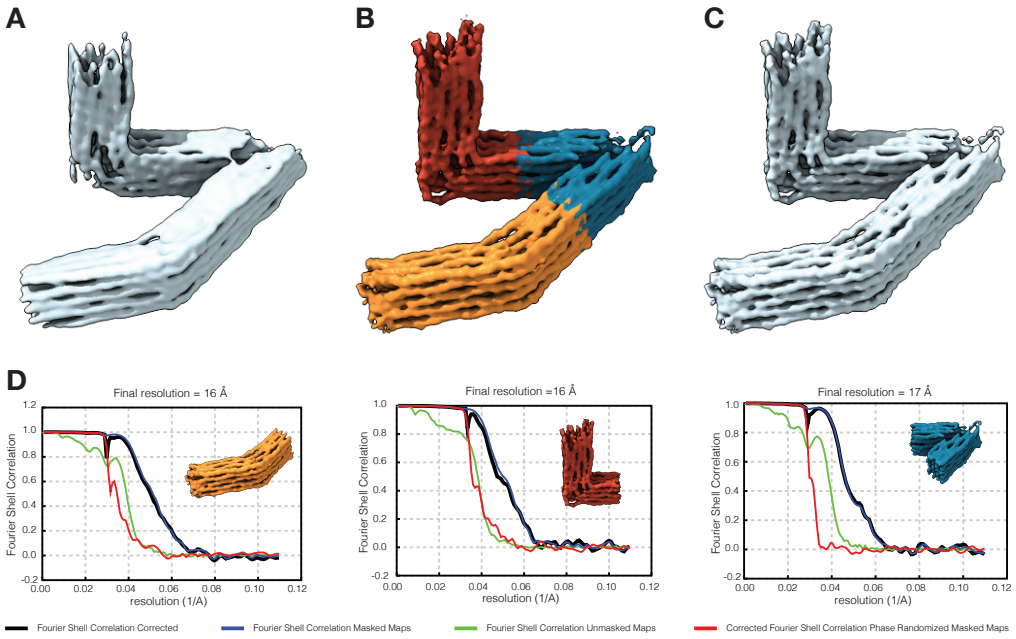

Figure D.17 Multi-body refinement of the CS-v1 object using three bodies. **(A)** Consensus refinement. **(B)** Superposition of the three multi-body refined parts. **(C)** Composite map. **(D)** FSC curves for the individual bodies.

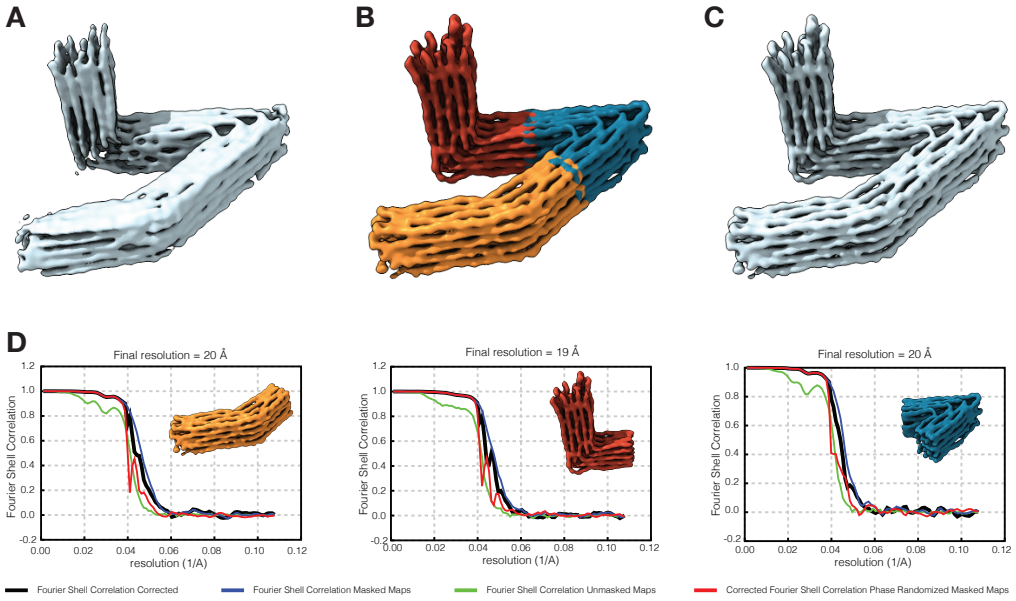

Figure D.18 Multi-body refinement of the CS-v1 object exposed to EtBr using three bodies. **(A)** Consensus refinement. **(B)** Superposition of the three multi-body refined parts. **(C)** Composite map. **(D)** FSC curves for the individual bodies.

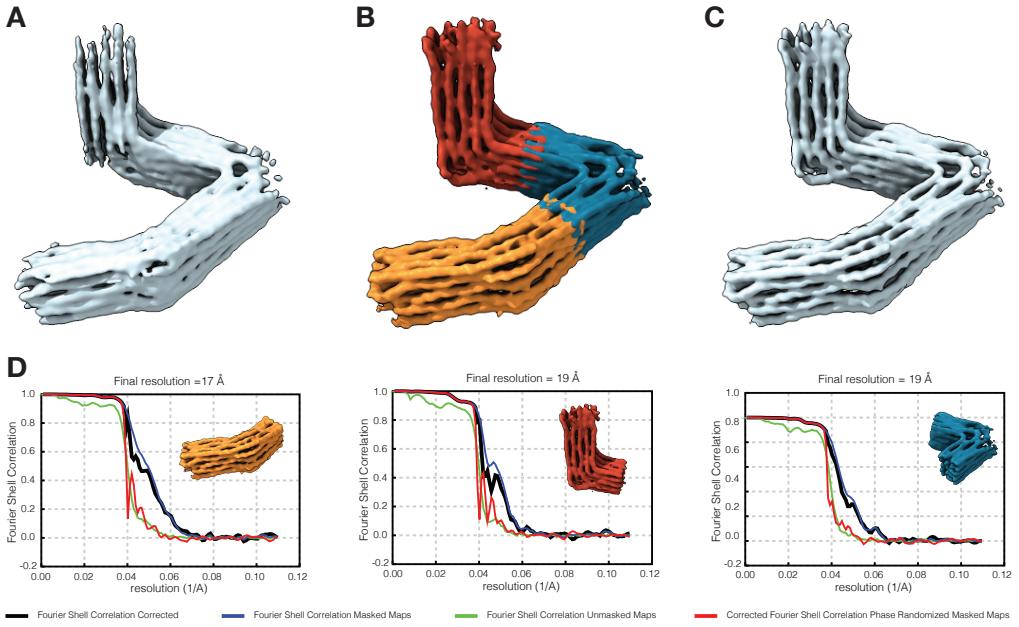

Figure D.19 Multi-body refinement of the CS-v2-1ss object using three bodies. **(A)** Consensus refinement. **(B)** Superposition of the three refined bodies. **(C)** Composite map. **(D)** FSC curves for the individual bodies.

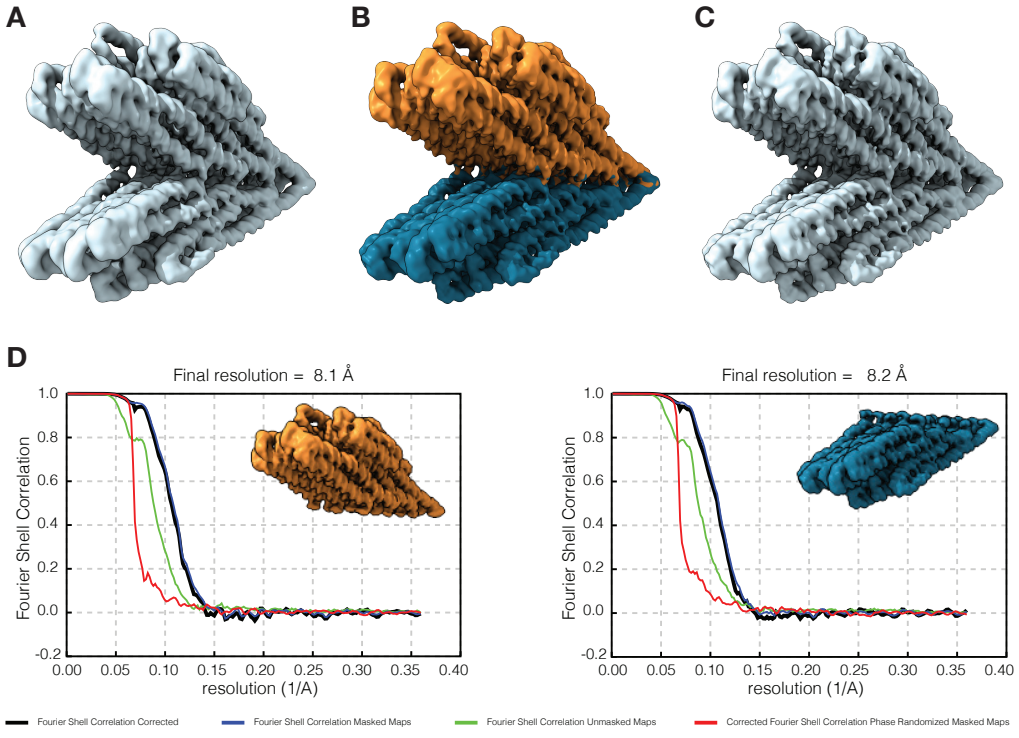

Figure D.20 Multi-body refinement of the CS-v3 object using two bodies. **(A)** Consensus refinement. **(B)** Superposition of the refined bodies. **(C)** Composite map. **(D)** FSC curves for the individual bodies.

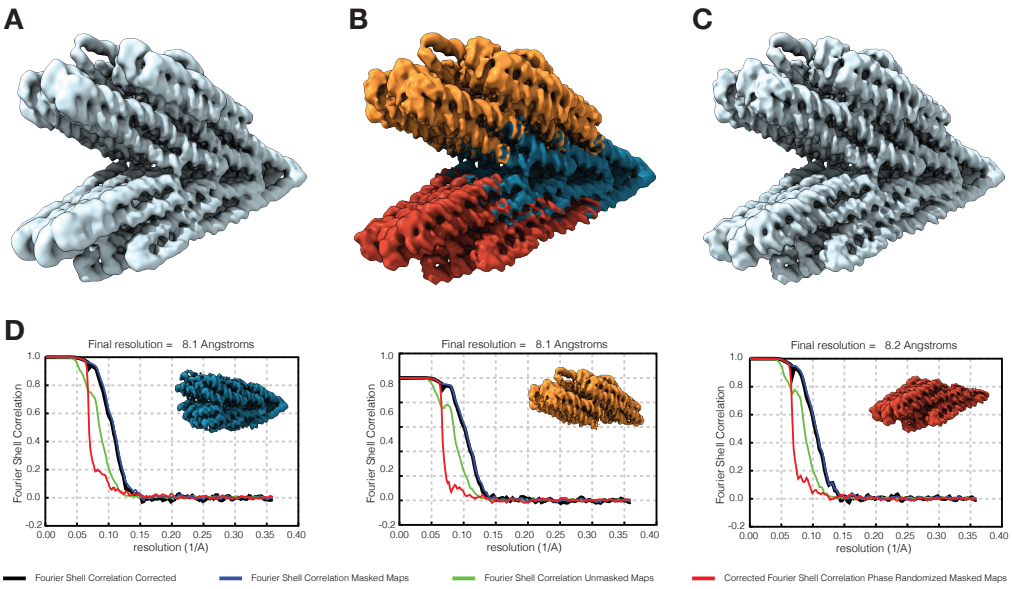

Figure D.21 Multi-body refinement of the CS-v3 object using three bodies. **(A)** Consensus refinement. **(B)** Superposition of the refined bodies. **(C)** Composite map. **(D)** FSC curves for the individual bodies.

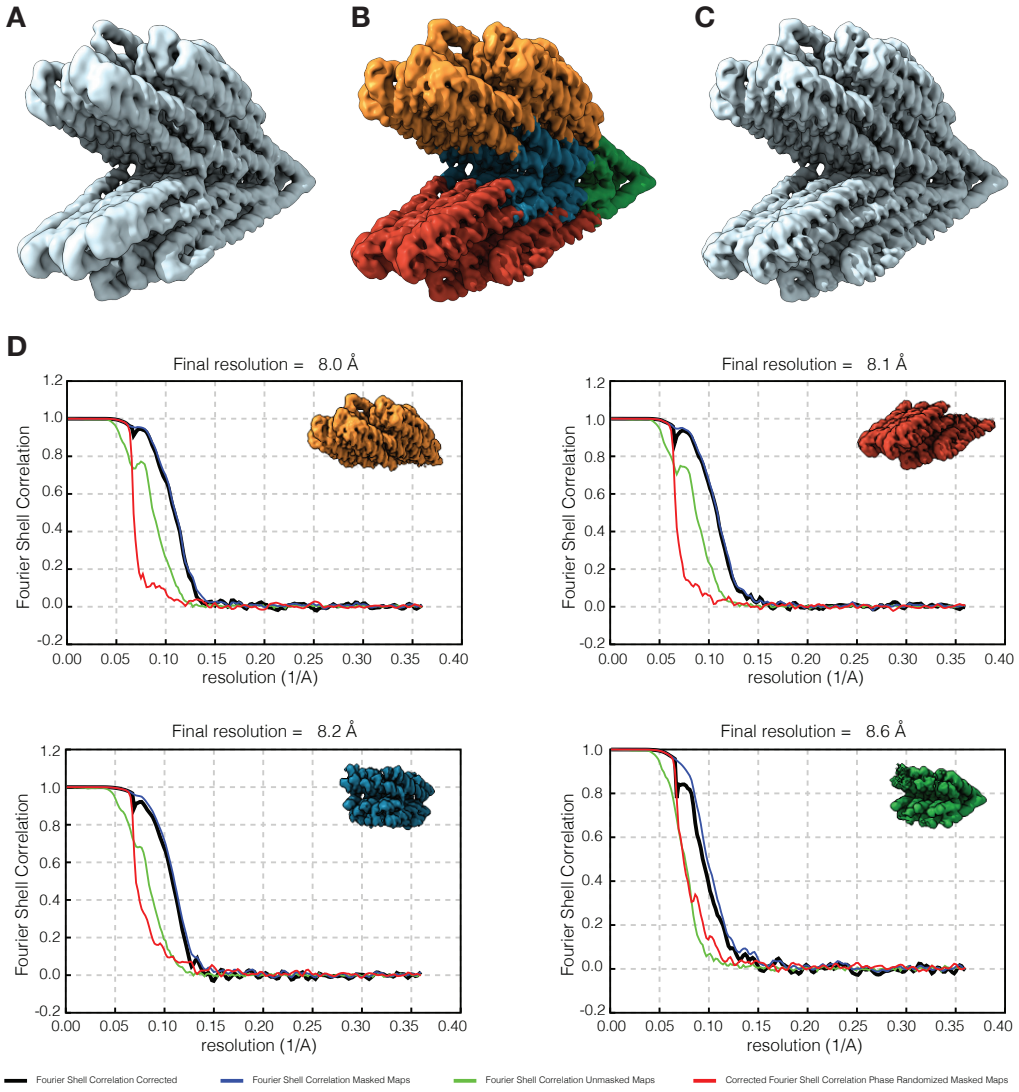

Figure D.22 Multi-body refinement of the CS-v3 object using four bodies. **(A)** Consensus refinement. **(B)** Superposition of the refined bodies. **(C)** Composite map. **(D)** FSC curves for the individual bodies.

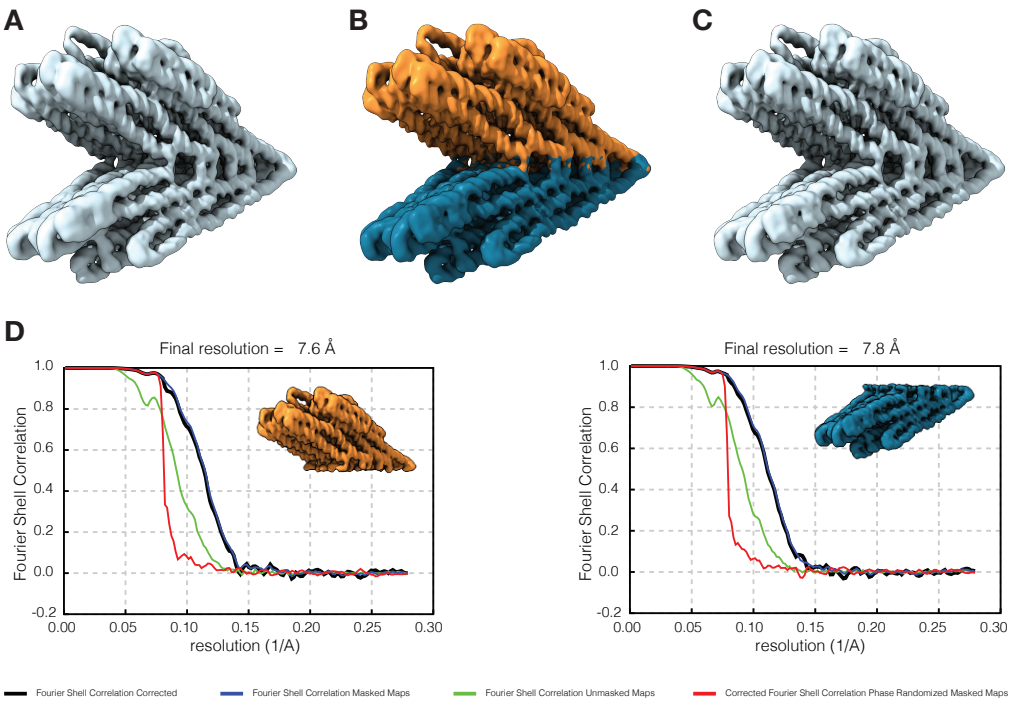

Figure D.23 Multi-body refinement of the CS-v4-2 object using two bodies. **(A)** Consensus refinement. **(B)** Superposition of the refined bodies. **(C)** Composite map. **(D)** FSC curves for the individual bodies.

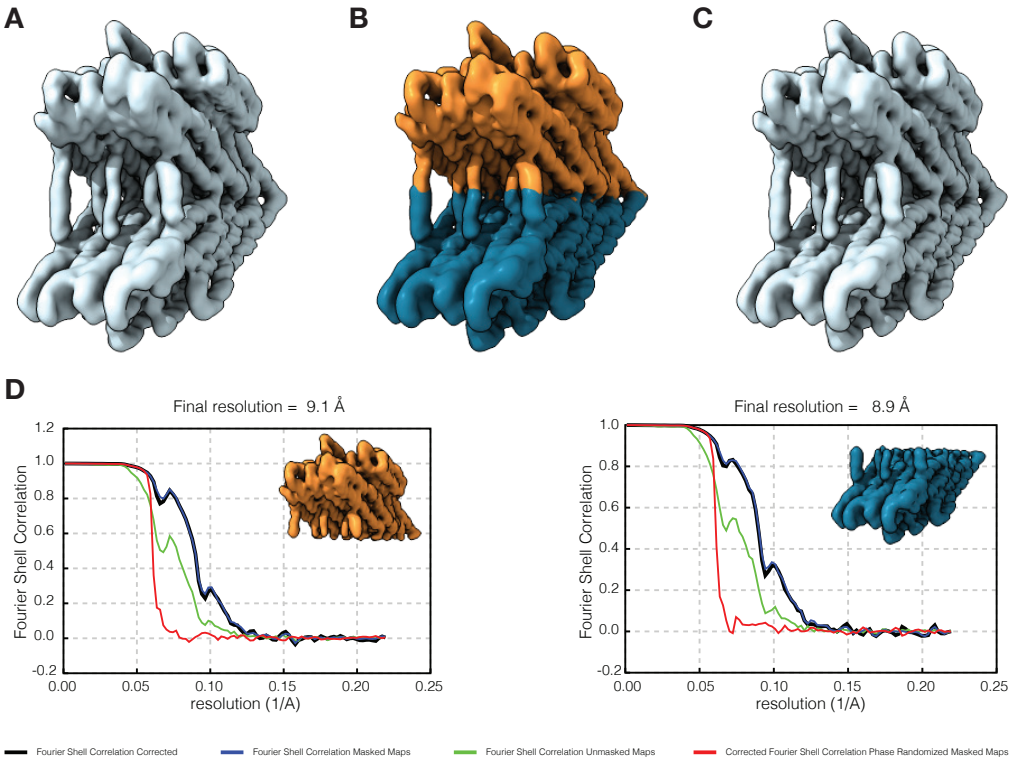

Figure D.24 Multi-body refinement of a 27k particle subset of the CS-v5 object using two bodies. **(A)** Consensus refinement. **(B)** Superposition of the refined bodies. **(C)** Composite map. **(D)** FSC curves for the individual bodies.

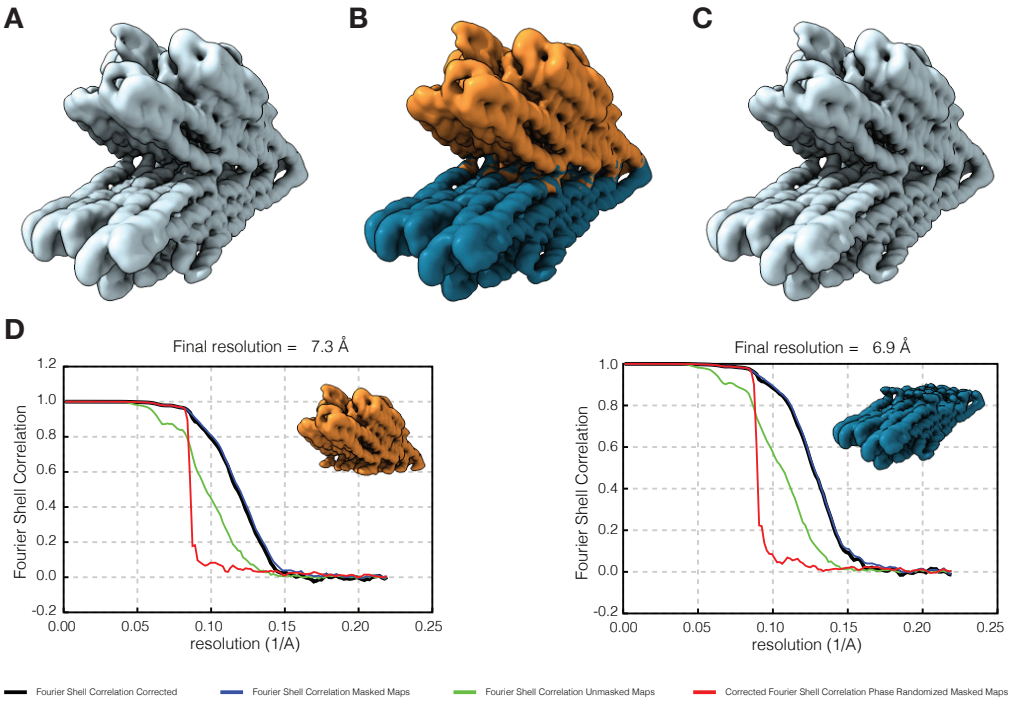

Figure D.25 Multi-body refinement of the CS-v6 object using two bodies. **(A)** Consensus refinement. **(B)** Superposition of the refined bodies. **(C)** Composite map. **(D)** FSC curves for the individual bodies.

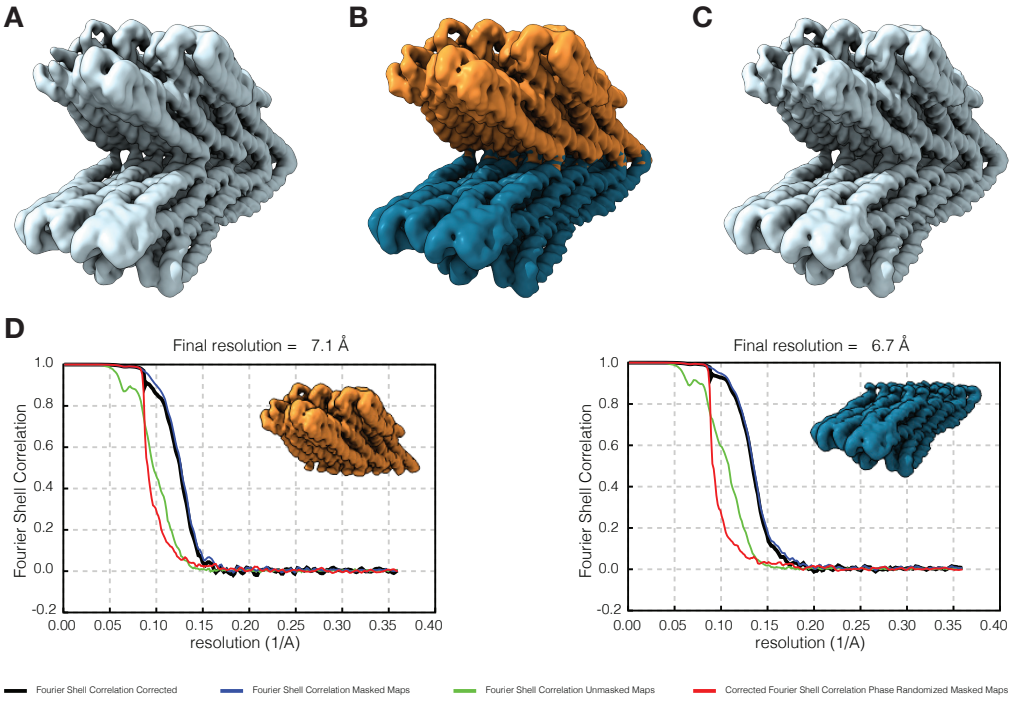

Figure D.26 Multi-body refinement of the CS-v7 object using two bodies. **(A)** Consensus refinement. **(B)** Superposition of the refined bodies. **(C)** Composite map. **(D)** FSC curves for the individual bodies.

Appendix E

Supporting Cryo-EM representations

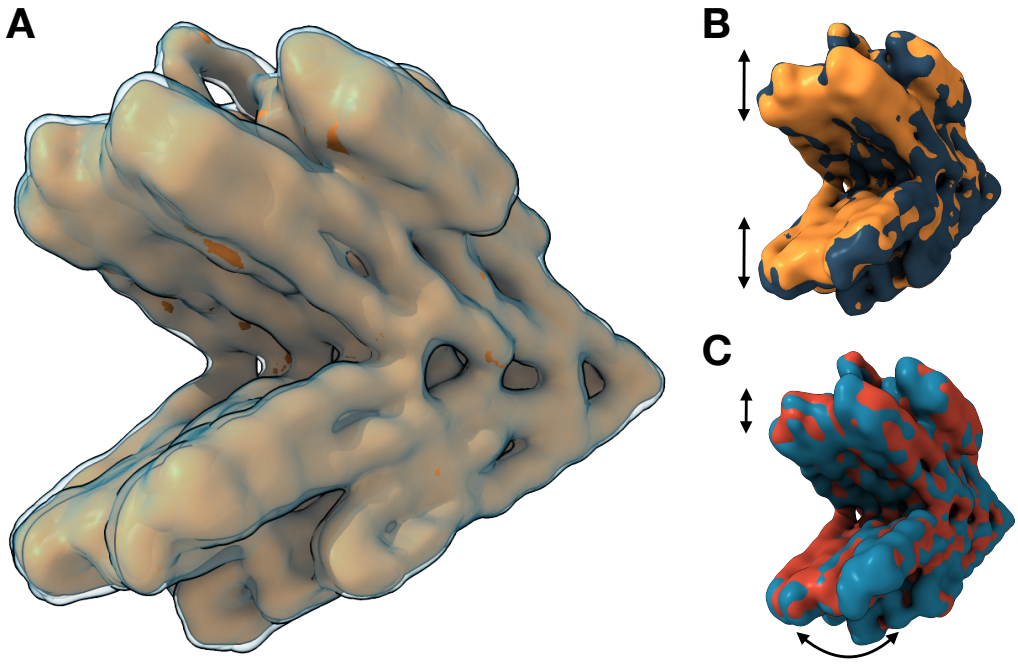

Figure E.1 Heterogeneity of 3D classes of CS-v3. **(A)** Superposition of the electron density maps of 29 classes. The most populated class is depicted in orange. The other classes are rendered in transparent blue. The classes are aligned to the consensus refinement. **(B)** Superpositions of the electron density maps of two selected exemplary 3D classes. Arrows indicate the approximate directions of the largest structural differences. **(C)** As in B, but for two different classes.

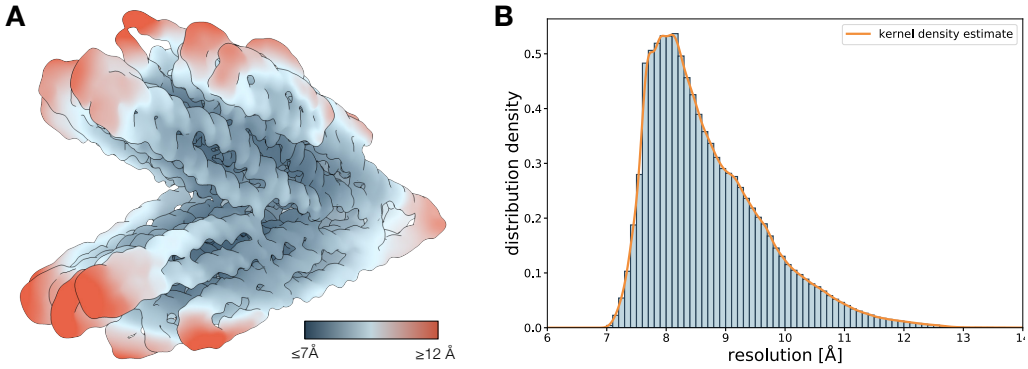

Figure E.2 Local resolution of CS-v3 consensus refinement. **(A)** The map locally colored according to the local in resolution as indicated by the color key. **(B)** Distributions of the resolution within the shown volume. The bin width of the histograms is 0.1 Å. The mean and standard deviation of the distribution is 0.70 Å and 0.97 Å. The distribution was fitted using a Gaussian kernel density estimation at a bin width of 0.01 Å.

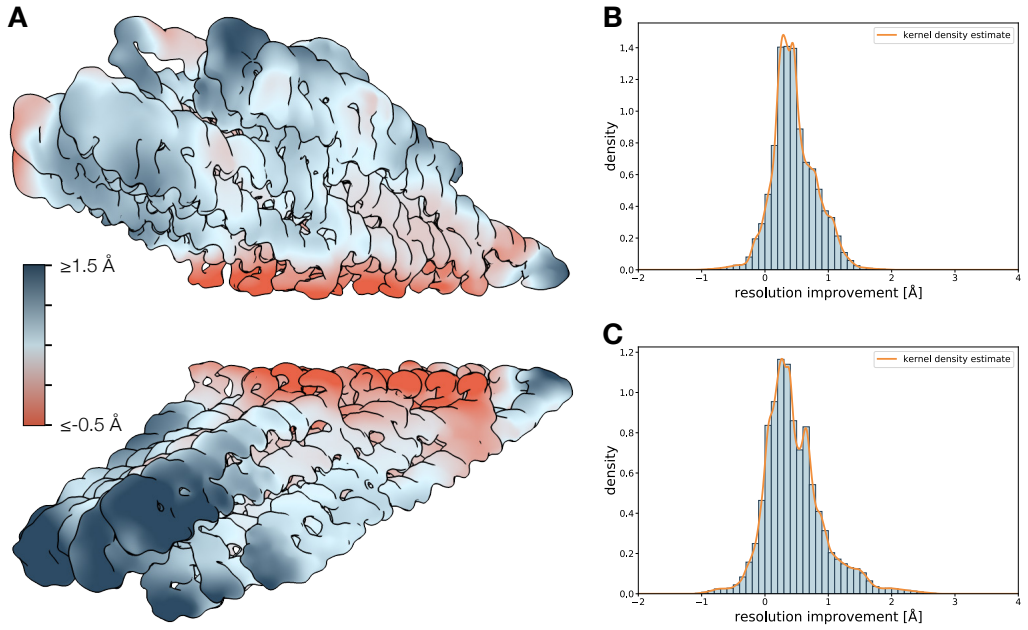

Figure E.3 Local resolution improvement of CS-v3 using a 2-body refinement. The improvement of the local resolution of the refined bodies was calculated as a difference of the local resolution of the respective body and the consensus map. **(A)** The two bodies locally colored according to the difference in resolution as indicated by the color key. Positive and negative values correspond to an improvement and deterioration, respectively. The biggest improvements can be found towards the ends of the arms and the most outer kink site. Except for this section the resolution of the pars at the interfaces between the two bodies has deteriorated. **(B)** Distributions of the resolution improvement of the upper arm. The bin width of the histograms is 0.1 Å. The mean and standard deviation of the distribution is 0.46 Å and 0.35 Å. The distribution was fitted using a Gaussian kernel density estimation at a bin width of 0.01 Å. **(C)** Distributions of the resolution improvement of the lower arm. The data are processed as in (B). The mean and standard deviation of the distribution is 0.46 Å and 0.47 Å.

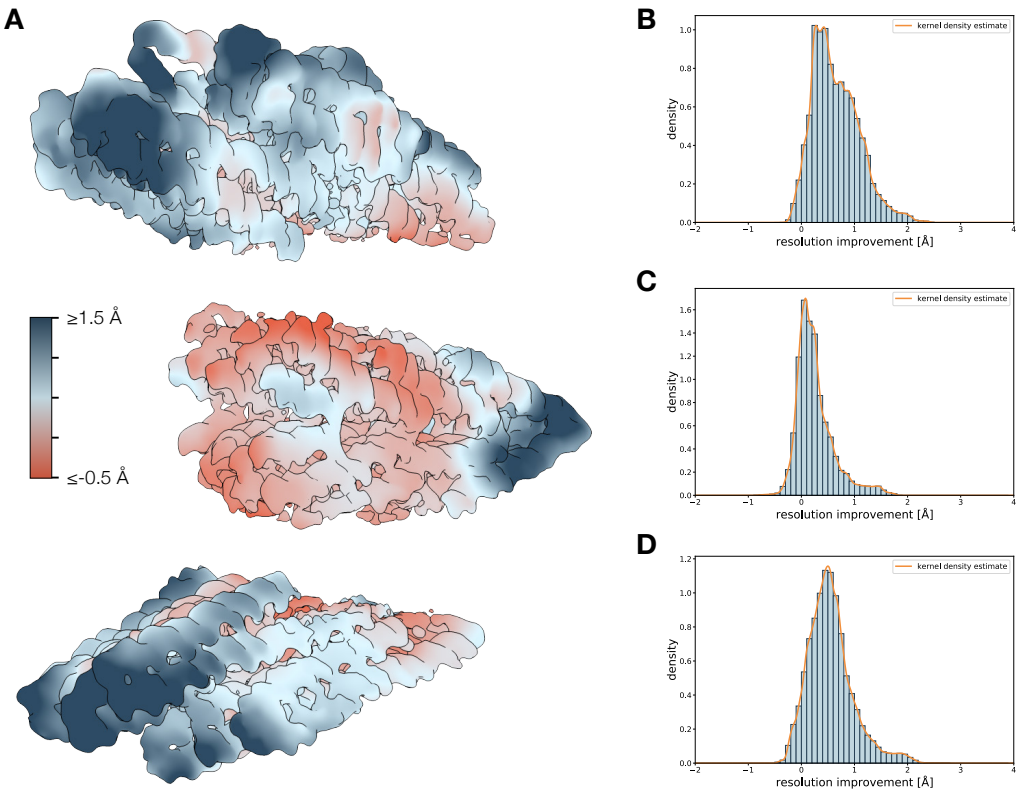

Figure E.4 Local resolution improvement of CS-v3 using a 3-body refinement. The improvement of the local resolution of the refined bodies was calculated as a difference of the local resolution of the respective body and the consensus map. **(A)** The three bodies locally colored according to the difference in resolution as indicated by the color key. Positive and negative values correspond to an improvement and deterioration, respectively. The biggest improvements can be found towards the ends of the arms and the most outer kink site. The resolution of the pars of the arms at the interfaces to the central part tends to have slightly deteriorated. The central part has a relatively low improvement compared to the parts of the arms (see distributions). **(B)** Distributions of the resolution improvement of the top part of the upper arm. The bin width of the histograms is 0.1 Å. The mean and standard deviation of the distribution is 0.65 Å and 0.44 Å. The distribution was fitted using a Gaussian kernel density estimation at a bin width of 0.01 Å. **(C)** Distributions of the resolution improvement of the central part. The data are processed as in (B). The mean and standard deviation of the distribution is 0.26 Å and 0.35 Å. **(D)** Distributions of the resolution improvement of the lower part of the lower arm. The data are processed as in (B). The mean and standard deviation of the distribution is 0.85 Å and 0.60 Å.

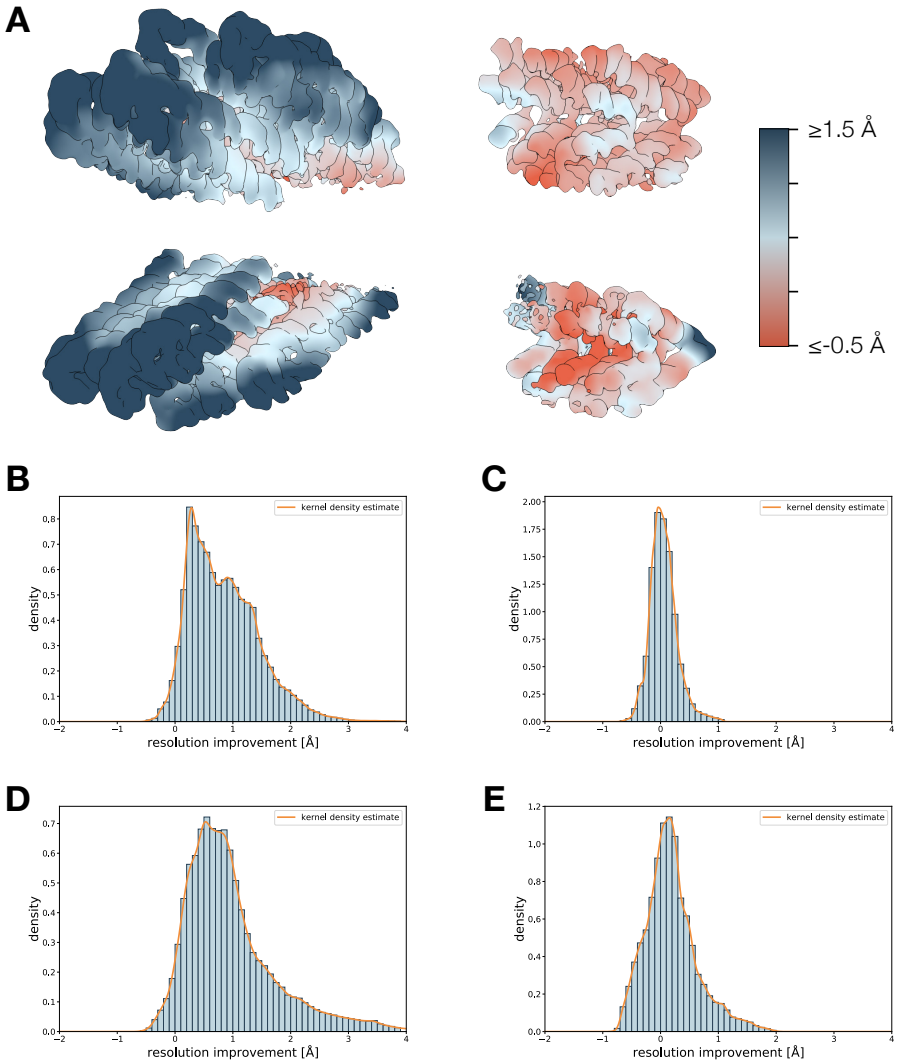

Figure E.5 Local resolution improvement of CS-v3 using a 4-body refinement. The improvement of the local resolution of the refined bodies was calculated as a difference of the local resolution of the respective body and the consensus map. **(A)** The four bodies locally colored according to the difference in resolution as indicated by the color key. Positive and negative values correspond to an improvement and deterioration, respectively. The biggest improvements can be found towards the ends of the arms. The two central part show relatively low improvements compared to the parts of the arms (see distributions). **(B)** - **(D)** Distributions of the resolution improvement. The bin width of the histograms is 0.1 Å. The distributions are fitted with Gaussian kernel density estimations using a bin width of 0.01 Å. **(B)** Distributions of the resolution improvement of the top part of the upper arm. The mean and standard deviation of the distribution is 0.85 Å and 0.60 Å. **(C)** Distributions of the resolution improvement of the left central part. The mean and standard deviation of the distribution is 0.05 Å and 0.24 Å. **(D)** Distributions of the resolution improvement of the lower part of the lower arm. The mean and standard deviation of the distribution is 0.97 Å and 0.80 Å. **(D)** Distributions of the resolution improvement of the right part of the central part. The mean and standard deviation of the distribution is 0.19 Å and 0.45 Å.

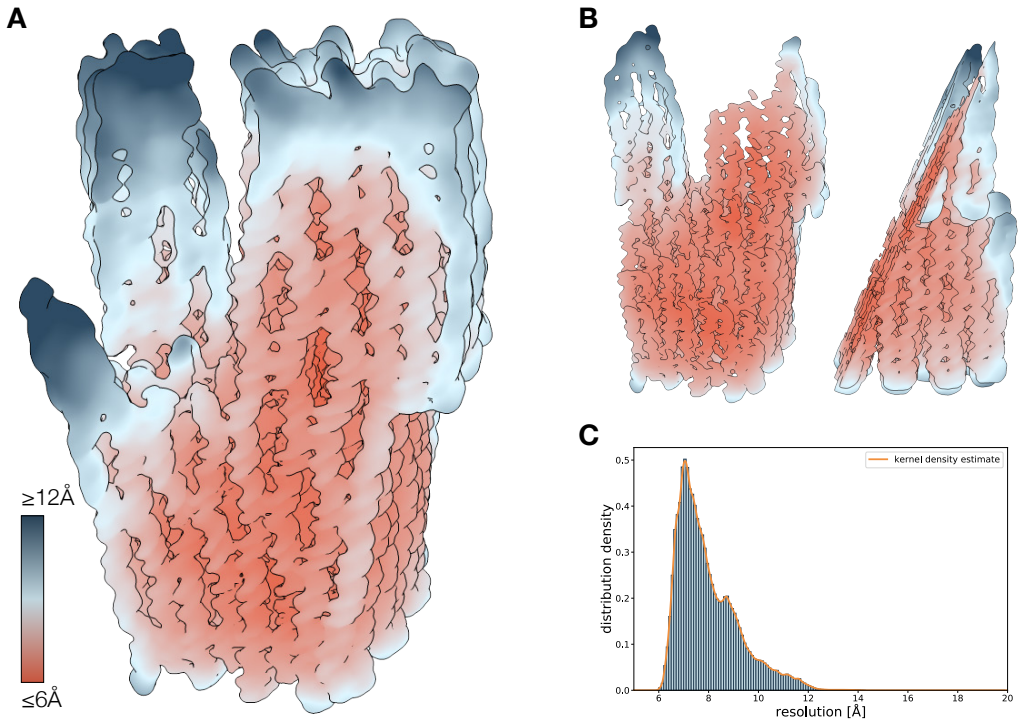

Figure E.6 Local resolution distribution of the consensus refinement of the Native Twist Tower. (A) Electron density map colored according to the resolution as indicated by the color key. **(B)** Front and side view of a slice through the resolution-colored map. **(C)**Distributions of the local resolution. The bin width of the histograms is 0.1 Å. The distributions are fitted with Gaussian kernel density estimations using a bin width of 0.01 Å. The mean and standard deviation of the distribution are 7.98 Å and 1.22 Å.

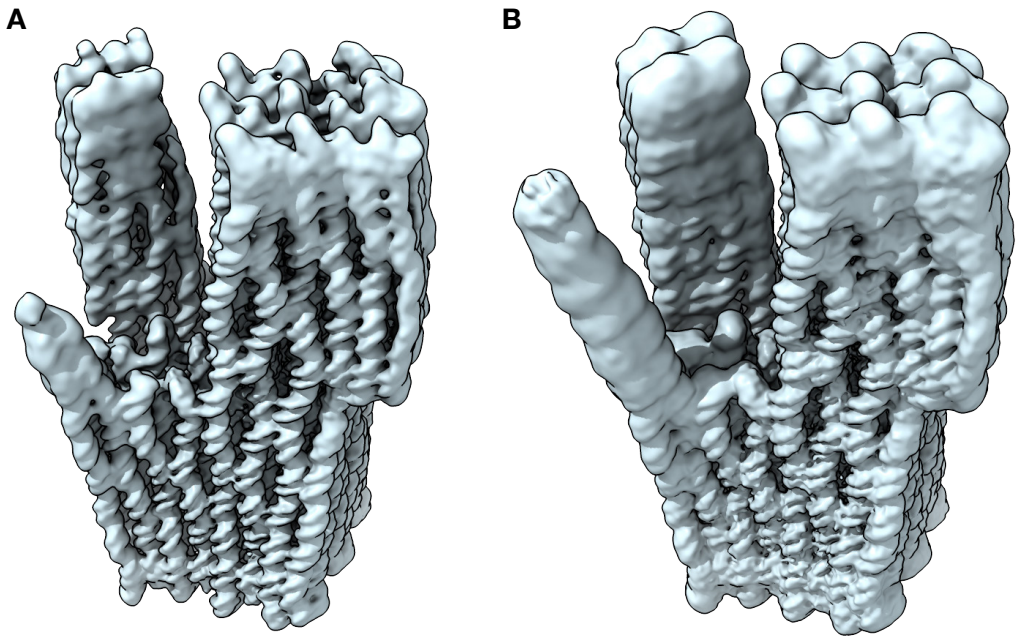

Figure E.7 Surface representations of the electron density map of the Twist-Tower. (A) Representation at a threshold of 0.05. Structural details of the helices in the well-resolved parts are resolved. Only the lower part of the 2x2 domain is visible. **(B)** Representation at a low threshold of 0.02. The structure is bloated and occupies a multiple of its actual volume. The global shape of the 2x2 domain can be recognized.

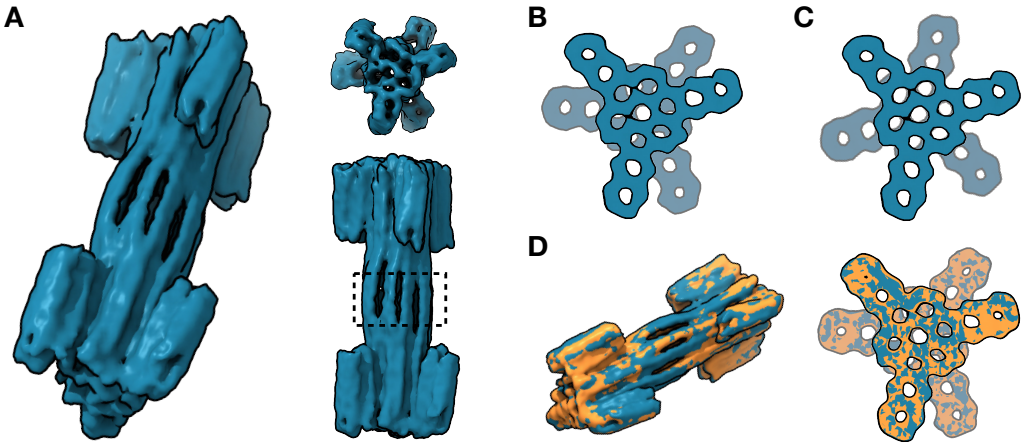

Figure E.8 The role of crossovers in twist correction. (A) Views of the electron density map of the dumbbell. In the central region of the handle (dashed box), the helices are not connected by crossovers. **(B)** Superposition of slices extracted from the front and the back. **(C)** In-silico twist correction. **(D)** Superposition of maps and slices of the variant with (blue) and without (orange) twist correction. Twist correction is implemented in the central region, where the helices are not connected by crossovers [74].

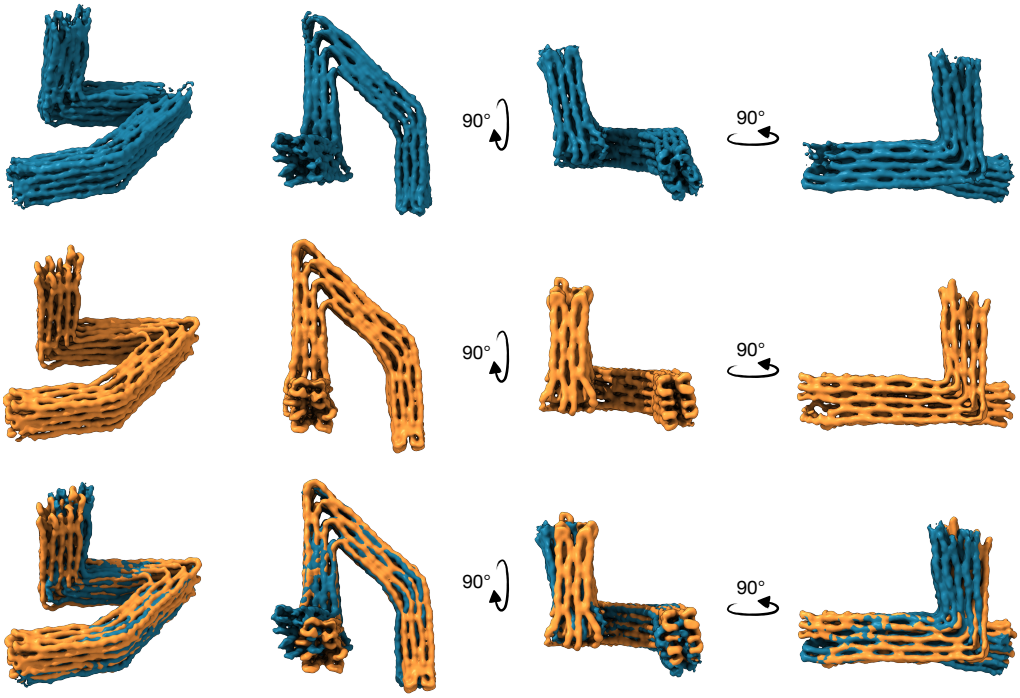

Figure E.9 Comparison of reconstructions of CS-v1 objects from EtBr-free PEG-and-HPLC-purified sample (blue) and EtBr exposed gel-purified sample (orange).

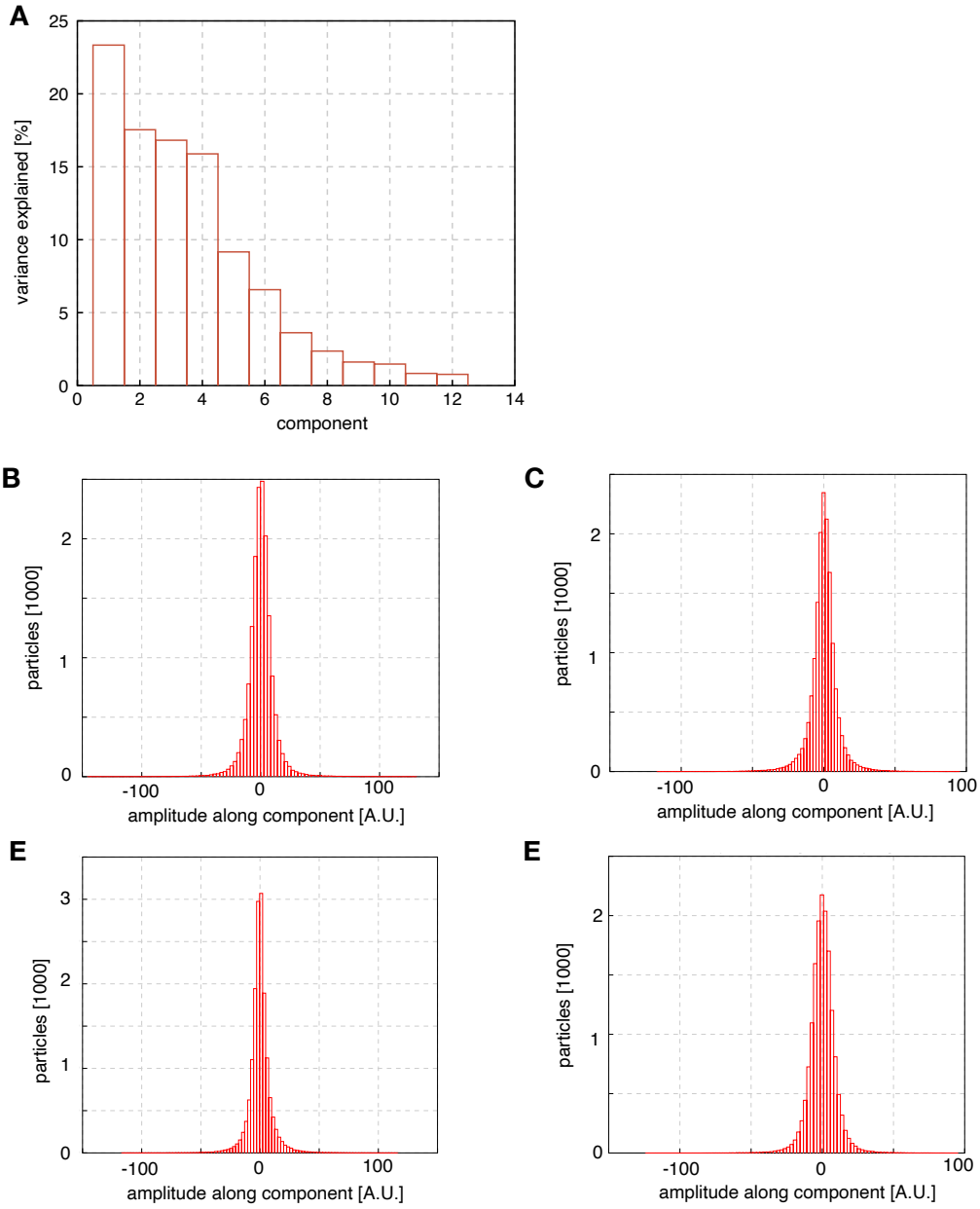

Figure E.10 PCA of the two-body refinement of CS-v3. **(A)** Percentages of total variance explained by the individual components. **(B)** - **(E)** Histograms of the distributions of the amplitudes along the first four components

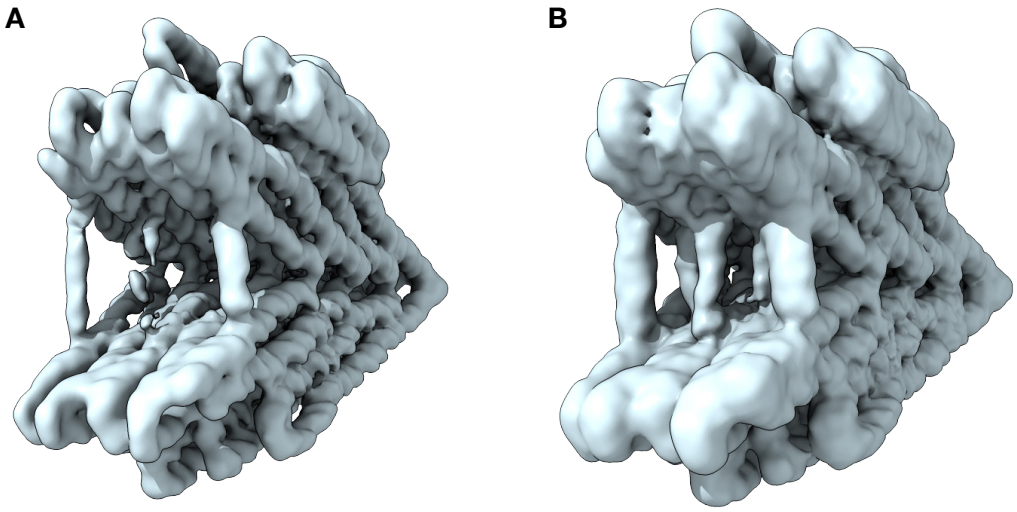

Figure E.11 Surface representation of the volume of CS-v5. **(A)** Representation at a reasonable threshold of 0.18. **(B)** Representation at a low threshold of 0.09.

Bibliography

[1] J. D. Watson and F. H. C. Crick, "Molecular Structure of Nucleic Acids: A Structure for Deoxyribose Nucleic Acid," *Nature*, vol. 171, no. 4356, pp. 737–738, 1953.

[2] N. C. Seeman, "Nucleic acid junctions and lattices," *Journal of Theoretical Biology*, vol. 99, no. 2, pp. 237–247, 1982.

[3] "Synthesis from DNA of a molecule with the connectivity of a cube," *Nature*, vol. 350, no. 6319, pp. 631–633, 1991.

[4] P. W. K. Rothemund, "Folding DNA to create nanoscale shapes and patterns," *Nature*, vol. 440, no. 7082, pp. 297–302, 2006.

[5] H. Gu, J. Chao, S.-J. Xiao, and N. C. Seeman, "A proximity-based programmable dna nanoscale assembly line," *Nature*, vol. 465, no. 7295, pp. 202–205, 2010.

[6] C. Zhou, X. Duan, and N. Liu, "A plasmonic nanorod that walks on DNA origami," *Nature Communications*, vol. 6, no. 1, p. 8102, 2015.

[7] "DNA-based self-assembly of chiral plasmonic nanostructures with tailored optical response," *Nature*, vol. 483, no. 7389, pp. 311–314, 2012.

[8] M. Dass, F. N. Gür, K. Kołątaj, M. J. Urban, and T. Liedl, "Dna origami-enabled plasmonic sensing," *The Journal of Physical Chemistry C*, vol. 125, no. 11, pp. 5969–5981, 2021.

[9] A. Gopinath, E. Miyazono, A. Faraon, and P. W. K. Rothemund, "Engineering and mapping nanocavity emission via precision placement of DNA origami," *Nature*, vol. 535, no. 7612, pp. 401–405, 2016.

[10] J. V. Le, Y. Luo, M. A. Darcy, C. R. Lucas, M. F. Goodwin, M. G. Poirier, and C. E. Castro, "Probing nucleosome stability with a dna origami nanocaliper," *ACS Nano*, vol. 10, no. 7, pp. 7073–7084, 2016.

[11] J. J. Funke, P. Ketterer, C. Lieleg, P. Korber, and H. Dietz, "Exploring Nucleosome Unwrapping Using DNA Origami," *Nano Letters*, vol. 16, no. 12, pp. 7891–7898, 2016.

[12] J. J. Funke, P. Ketterer, C. Lieleg, S. Schunter, P. Korber, and H. Dietz, "Uncovering the forces between nucleosomes using DNA origami," *Science Advances*, vol. 2, 2016.

[13] P. C. Nickels, B. Wünsch, P. Holzmeister, W. Bae, L. M. Kneer, D. Grohmann, P. Tinnefeld, and T. Liedl, "Molecular force spectroscopy with a dna origami–based nanoscopic force clamp," *Science*, vol. 354, no. 6310, pp. 305–307, 2016.

[14] F. Kilchherr, C. Wachauf, B. Pelz, M. Rief, M. Zacharias, and H. Dietz, "Single-molecule dissection of stacking forces in dna," *Science*, vol. 353, no. 6304, aaf5508, 2016.

[15] E. Silvester, B. Vollmer, V. Pražák, D. Vasishtan, E. A. Machala, C. Whittle, S. Black, J. Bath, A. J. Turberfield, K. Grünewald, and L. A. Baker, "DNA origami signposts for identifying proteins on cell membranes by electron cryotomography," *Cell*, vol. 184, no. 4, 1110–1121.e16, 2021.

[16] E. Pfitzner, C. Wachauf, F. Kilchherr, B. Pelz, W. M. Shih, M. Rief, and H. Dietz, "Rigid dna beams for high-resolution single-molecule mechanics," *Angewandte Chemie International Edition*, vol. 52, no. 30, pp. 7766–7771, 2013.

[17] J. J. Schmied, A. Gietl, P. Holzmeister, C. Forthmann, C. Steinhauer, T. Dammeyer, and P. Tinnefeld, "Fluorescence and super-resolution standards based on DNA origami," *Nature Methods*, vol. 9, no. 12, pp. 1133–1134, 2012.

[18] T. G. Martin, T. A. M. Bharat, A. C. Joerger, X.-c. Bai, F. Praetorius, A. R. Fersht, H. Dietz, and S. H. W. Scheres, "Design of a molecular support for cryo-em structure determination," *Proceedings of the National Academy of Sciences*, vol. 113, no. 47, E7456–E7463, 2016.

[19] "Molecular goniometers for single-particle cryo-electron microscopy of DNA-binding proteins," *Nature Biotechnology*, vol. 39, no. 3, pp. 378–386, 2021.

[20] K. F. Wagenbauer, C. Sigl, and H. Dietz, "Gigadalton-scale shape-programmable DNA assemblies," *Nature*, vol. 552, no. 7683, pp. 78–83, 2017.

[21] "Fractal assembly of micrometre-scale DNA origami arrays with arbitrary patterns," *Nature*, vol. 552, no. 7683, pp. 67–71, 2017.

[22] C. Sigl, E. M. Willner, W. Engelen, J. A. Kretzmann, K. Sachenbacher, A. Liedl, F. Kolbe, F. Wilsch, S. A. Aghvami, U. Protzer, M. F. Hagan, S. Fraden, and H. Dietz, "Programmable icosahedral shell system for virus trapping," *Nature Materials*, 2021. DOI: 10.1038/s41563-021-01020-4.

[23] P. Stömmer, H. Kiefer, E. Kopperger, M. N. Honemann, M. Kube, F. C. Simmel, R. R. Netz, and H. Dietz, "A synthetic tubular molecular transport system," *bioRxiv*, 2021. DOI: 10.1101/2021.03.22.436416.

[24] S. M. Douglas, I. Bachelet, and G. M. Church, "A logic-gated nanorobot for targeted transport of molecular payloads," *Science*, vol. 335, no. 6070, pp. 831–834, 2012.

[25] Q. Zhang, Q. Jiang, N. Li, L. Dai, Q. Liu, L. Song, J. Wang, Y. Li, J. Tian, B. Ding, and Y. Du, "Dna origami as an in vivo drug delivery vehicle for cancer therapy," *ACS Nano*, vol. 8, no. 7, pp. 6633–6643, 2014.

[26] P. Wang, M. A. Rahman, Z. Zhao, K. Weiss, C. Zhang, Z. Chen, S. J. Hurwitz, Z. G. Chen, D. M. Shin, and Y. Ke, "Visualization of the cellular uptake and trafficking of dna origami nanostructures in cancer cells," *Journal of the American Chemical Society*, vol. 140, no. 7, pp. 2478–2484, 2018.

[27] B. Yurke, A. J. Turberfield, A. P. Mills, F. C. Simmel, and J. L. Neumann, "A DNA-fuelled molecular machine made of DNA," *Nature*, vol. 406, no. 6796, pp. 604–608, 2000.

[28] P. Ketterer, E. M. Willner, and H. Dietz, "Nanoscale rotary apparatus formed from tight-fitting 3d dna components," vol. 2, no. 2, e1501209, 2016.

[29] E. Kopperger, J. List, S. Madhira, F. Rothfischer, D. C. Lamb, and F. C. Simmel, "A self-assembled nanoscale robotic arm controlled by electric fields," *Science*, vol. 359, no. 6373, pp. 296–301, 2018.

[30] J. Valero, N. Pal, S. Dhakal, N. G. Walter, and M. Famulok, "A bio-hybrid DNA rotor–stator nanoengine that moves along predefined tracks," *Nature Nanotechnology*, vol. 13, no. 6, pp. 496–503, 2018.

[31] A. E. Marras, L. Zhou, H.-J. Su, and C. E. Castro, "Programmable motion of dna origami mechanisms," *Proceedings of the National Academy of Sciences*, vol. 112, no. 1, pp. 713–718, 2015.

[32] A. J. Thubagere, W. Li, R. F. Johnson, Z. Chen, S. Doroudi, Y. L. Lee, G. Izatt, S. Wittman, N. Srinivas, D. Woods, E. Winfree, and L. Qian, "A cargo-sorting dna robot," *Science*, vol. 357, no. 6356, eaan6558, 2017.

[33] S. M. Douglas, A. H. Marblestone, S. Teerapittayanon, A. Vazquez, G. M. Church, and W. M. Shih, "Rapid prototyping of 3D DNA-origami shapes with caDNAno," *Nucleic Acids Research*, vol. 37, no. 29, pp. 5001–5006, 2009.

[34] C.-M. Huang, A. Kucinic, J. A. Johnson, H.-J. Su, and C. E. Castro, "Integrated computer-aided engineering and design for DNA assemblies," *Nature Materials*, 2021. DOI: 10.1038/s41563-021-00978-5.

[35] Y. Ke, S. M. Douglas, M. Liu, J. Sharma, A. Cheng, A. Leung, Y. Liu, W. M. Shih, and H. Yan, "Multilayer DNA origami packed on a square lattice," *Journal of the American Chemical Society*, vol. 131, no. 43, pp. 15 903–15 908, 2009.

[36] S. M. Douglas, H. Dietz, T. Liedl, B. Högberg, F. Graf, and W. M. Shih, "Self-assembly of DNA into nanoscale three-dimensional shapes," *Nature*, vol. 459, no. 7245, pp. 414–418, 2009.

[37] R. Holliday, "A mechanism for gene conversion in fungi," *Genetical Research*, vol. 5, no. 2, pp. 282–304, 1964.

[38] M. Karymov, D. Daniel, O. F. Sankey, and Y. L. Lyubchenko, "Holliday junction dynamics and branch migration: Single-molecule analysis," *Proceedings of the National Academy of Sciences*, vol. 102, no. 23, pp. 8186–8191, 2005.

[39] J.-P. J. Sobczak, T. G. Martin, T. Gerling, and H. Dietz, "Rapid folding of dna into nanoscale shapes at constant temperature," *Science*, vol. 338, no. 6113, pp. 1458–1461, 2012.

[40] T. G. Martin and H. Dietz, "Magnesium-free self-assembly of multi-layer DNA objects," *Nature Communications*, vol. 3, no. 1, pp. 1103–1109, 2012.

[41] F. Schneider, N. Möritz, and H. Dietz, "The sequence of events during folding of a DNA origami," *Science Advances*, vol. 5, no. 5, eaaw1412, 2019.

[42] A. E. Marras, Z. Shi, M. G. Lindell, R. A. Patton, C.-M. Huang, L. Zhou, H.-J. Su, G. Arya, and C. E. Castro, "Cation-activated avidity for rapid reconfiguration of dna nanodevices," *ACS Nano*, vol. 12, no. 9, pp. 9484–9494, 2018.

[43] C. Lee, J. Y. Lee, and D.-N. Kim, "Polymorphic design of DNA origami structures through mechanical control of modular components," *Nature Communications*, vol. 8, no. 1, p. 2067, 2017.

[44] "Self-assembly of a nanoscale DNA box with a controllable lid," *Nature*, vol. 459, no. 7243, pp. 73–76, 2009.

[45] K. F. Wagenbauer, F. A. S. Engelhardt, E. Stahl, V. K. Hechtl, P. Stömmer, F. Seebacher, L. Meregalli, P. Ketterer, T. Gerling, and H. Dietz, "How We Make DNA Origami," *ChemBioChem*, vol. 18, no. 19, pp. 1873–1885, 2017.

[46] R. Iinuma, Y. Ke, R. Jungmann, T. Schlichthaerle, J. B. Woehrstein, and P. Yin, "Polyhedra self-assembled from DNA tripods and characterized with 3D DNA-PAINT," *Science*, vol. 344, no. 6179, pp. 65–69, 2014.

[47] T. Gerling, K. F. Wagenbauer, A. M. Neuner, and H. Dietz, "Dynamic DNA devices and assemblies formed by shape-complementary, non-base pairing 3D components," *Science*, vol. 347, no. 6229, pp. 1446–1452, 2015.

[48] H. Dietz, S. M. Douglas, and W. M. Shih, "Folding DNA into Twisted and Curved Nanoscale Shapes," *Science*, vol. 325, no. 5941, pp. 725–730, 2009.

[49] D. Han, S. Pal, J. Nangreave, Z. Deng, Y. Liu, and H. Yan, "Dna origami with complex curvatures in three-dimensional space," *Science*, vol. 332, no. 6027, pp. 342–346, 2011.

[50] J. J. Funke and H. Dietz, "Placing molecules with Bohr radius resolution using DNA origami," *Nature Nanotechnology*, vol. 11, no. 1, pp. 47–52, 2016.

[51] I. Kaminska, J. Bohlen, S. Rocchetti, F. Selbach, G. P. Acuna, and P. Tinnefeld, "Distance dependence of single-molecule energy transfer to graphene measured with dna origami nanopositioners," *Nano Letters*, vol. 19, no. 7, pp. 4257–4262, 2019.

[52] M. Langecker, V. Arnaut, T. G. Martin, J. List, S. Renner, M. Mayer, H. Dietz, and F. C. Simmel, "Synthetic lipid membrane channels formed by designed dna nanostructures," *Science*, vol. 338, no. 6109, pp. 932–936, 2012.

[53] S. Dey, C. Fan, K. V. Gothelf, J. Li, C. Lin, L. Liu, N. Liu, M. A. D. Nijenhuis, B. Saccà, F. C. Simmel, H. Yan, and P. Zhan, "DNA origami," *Nature Reviews Methods Primers*, vol. 1, no. 1, pp. 1–24, 2021.

[54] C. E. Castro, F. Kilchherr, D. N. Kim, E. L. Shiao, T. Wauer, P. Wortmann, M. Bathe, and H. Dietz, "A primer to scaffolded DNA origami," *Nature Methods*, vol. 8, no. 3, pp. 221–229, 2011.

[55] P.-S. Huang, S. E. Boyken, and D. Baker, "The coming of age of de novo protein design," *Nature*, vol. 537, no. 7620, pp. 320–327, 2016.

[56] S. E. Boyken, Z. Chen, B. Groves, R. A. Langan, G. Oberdorfer, A. Ford, J. M. Gilmore, C. Xu, F. DiMaio, J. H. Pereira, B. Sankaran, G. Seelig, P. H. Zwart, and D. Baker, "De novo design of protein homo-oligomers with modular hydrogen-bond network–mediated specificity," *Science*, vol. 352, no. 6286, pp. 680–687, 2016.

[57] A. Chevalier, D.-A. Silva, G. J. Rocklin, D. R. Hicks, R. Vergara, P. Murapa, S. M. Bernard, L. Zhang, K.-H. Lam, G. Yao, C. D. Bahl, S.-I. Miyashita, I. Goreshnik, J. T. Fuller, M. T. Koday, C. M. Jenkins, T. Colvin, L. Carter, A. Bohn, C. M. Bryan, D. A. Fernández-Velasco, L. Stewart, M. Dong, X. Huang, R. Jin, I. A. Wilson, D. H. Fuller, and D. Baker, "Massively parallel de novo protein design for targeted therapeutics," *Nature*, vol. 550, no. 7674, pp. 74–79, 2017.

[58] A. Merk, A. Bartesaghi, S. Banerjee, V. Falconieri, P. Rao, M. I. Davis, R. Pragani, M. B. Boxer, L. A. Earl, J. L. Milne, and S. Subramaniam, "Breaking Cryo-EM Resolution Barriers to Facilitate Drug Discovery," *Cell*, vol. 165, no. 7, pp. 1698–1707, 2016.

[59] A. Bartesaghi, A. Merk, S. Banerjee, D. Matthies, X. Wu, J. L. S. Milne, and S. Subramaniam, "2.2 Å resolution cryo-em structure of β-galactosidase in complex with a cell-permeant inhibitor," *Science*, vol. 348, no. 6239, pp. 1147–1151, 2015.

[60] X. C. Bai, I. S. Fernandez, G. McMullan, and S. H. W. Scheres, "Ribosome structures to near-atomic resolution from thirty thousand cryo-EM particles," *eLife*, vol. 2, e00461, 2013.

[61] A. Amunts, A. Brown, J. Toots, S. H. W. Scheres, and V. Ramakrishnan, "The structure of the human mitochondrial ribosome," *Science*, vol. 348, no. 6230, pp. 95–98, 2015.

[62] Y. Liu, S. Gonen, T. Gonen, and T. O. Yeates, "Near-atomic cryo-EM imaging of a small protein displayed on a designed scaffolding system," *Proceedings of the National Academy of Sciences*, vol. 115, no. 13, pp. 3362–3367, 2018.

[63] A. Boland, T. G. Martin, Z. Zhang, J. Yang, X. C. Bai, L. Chang, S. H. Scheres, and D. Barford, "Cryo-EM structure of a metazoan separase-securin complex at near-atomic resolution," *Nature Structural and Molecular Biology*, vol. 24, no. 4, pp. 414–418, 2017.

[64] N. Fischer, P. Neumann, A. L. Konevega, L. V. Bock, R. Ficner, M. V. Rodnina, and H. Stark, "Structure of the E. coli ribosome-EF-Tu complex at <3 Å resolution by C_s-corrected cryo-EM," *Nature*, vol. 520, no. 7548, pp. 567–570, 2015.

[65] T. H. D. Nguyen, W. P. Galej, X. C. Bai, C. Oubridge, A. J. Newman, S. H. Scheres, and K. Nagai, "Cryo-EM structure of the yeast U4/U6.U5 tri-snRNP at 3.7 Å resolution," *Nature*, vol. 530, no. 7590, pp. 298–302, 2016.

[66] Z. Ke, J. Oton, K. Qu, M. Cortese, V. Zila, L. McKeane, T. Nakane, J. Zivanov, C. J. Neufeldt, B. Cerikan, J. M. Lu, J. Peukes, X. Xiong, H.-G. Kräusslich, S. H. W. Scheres, R. Bartenschlager, and J. A. G. Briggs, "Structures and distributions of SARS-CoV-2 spike proteins on intact virions," vol. 588, no. 7838, pp. 498–502, 2020.

[67] D. Wrapp, N. Wang, K. S. Corbett, J. A. Goldsmith, C.-L. Hsieh, O. Abiona, B. S. Graham, and J. S. McLellan, "Cryo-EM structure of the 2019-nCoV spike in the prefusion conformation," *Science*, vol. 1263, no. 6483, pp. 1260–1263, 2020.

[68] X.-c. Bai, T. G. Martin, S. H. W. Scheres, and H. Dietz, "Cryo-em structure of a 3d dna-origami object," *Proceedings of the National Academy of Sciences*, vol. 109, no. 49, pp. 20 012–20 017, 2012.

[69] Y. Dong, S. Chen, S. Zhang, J. Sodroski, Z. Yang, D. Liu, and Y. Mao, "Folding DNA into a Lipid-Conjugated Nanobarrel for Controlled Reconstitution of Membrane Proteins," *Angewandte Chemie - International Edition*, vol. 57, no. 8, pp. 2072–2076, 2018.

[70] Y. Ahmadi, A. L. Nord, A. J. Wilson, C. Hütter, F. Schroeder, M. Beeby, and I. Barišić, "The Brownian and Flow-Driven Rotational Dynamics of a Multicomponent DNA Origami-Based Rotor," *Small*, vol. 16, no. 22, pp. 1–7, 2020.

[71] R. Veneziano, S. Ratanalert, K. Zhang, F. Zhang, H. Yan, W. Chiu, and M. Bathe, "Designer nanoscale DNA assemblies programmed from the top down," *Science*, vol. 352, no. 6293, p. 1534, 2016.

[72] J. R. Gallagher, A. J. Kim, N. M. Gulati, and A. K. Harris, "Negative-Stain Transmission Electron Microscopy of Molecular Complexes for Image Analysis by 2D Class Averaging," *Current Protocols in Microbiology*, vol. 54, no. 1, pp. 1–29, 2019.

[73] J. Frank, *Three-Dimensional Electron Microscopy Of Macromolecular Assemblies: Visualization Of Biological Molecules In Their Native State*. Oxford University Press, 2006.

[74] M. Kube, F. Kohler, E. Feigl, B. Nagel-Yüksel, E. M. Willner, J. J. Funke, T. Gerling, P. Stömmer, M. N. Honemann, T. G. Martin, S. H. Scheres, and H. Dietz, "Revealing the structures of megadalton-scale DNA complexes with nucleotide resolution," *Nature Communications*, vol. 11, no. 1, pp. 6229–6239, 2020.

[75] D. Kimanius, B. Forsberg, S. H. W. Scheres, and E. Lindahl, "Accelerated cryo-EM structure determination with parallelisation using GPUs in RELION-2," *eLife*, vol. 5, e18722, 2016.

[76] S. H. Scheres, "RELION: Implementation of a Bayesian approach to cryo-EM structure determination," *Journal of Structural Biology*, vol. 180, no. 3, pp. 519–530, 2012.

[77] S. H. Scheres, "A bayesian view on cryo-EM structure determination," *Journal of Molecular Biology*, vol. 415, no. 2, pp. 406–418, 2012.

[78] T. Nakane, D. Kimanius, E. Lindahl, and S. H. Scheres, "Characterisation of molecular motions in cryo-EM single-particle data by multi-body refinement in RELION," *eLife*, vol. 7, e36861, 2018.

[79] J. Zivanov, T. Nakane, B. O. Forsberg, D. Kimanius, W. J. Hagen, E. Lindahl, and S. H. Scheres, "New tools for automated high-resolution cryo-EM structure determination in RELION-3," *eLife*, vol. 7, pp. 1–38, 2018.

[80] A. Punjani, J. L. Rubinstein, D. J. Fleet, and M. A. Brubaker, "CryoSPARC: Algorithms for rapid unsupervised cryo-EM structure determination," *Nature Methods*, vol. 14, pp. 290–296, 2017.

[81] A. Punjani and D. J. Fleet, "3D variability analysis: Resolving continuous flexibility and discrete heterogeneity from single particle cryo-EM," *Journal of Structural Biology*, vol. 213, no. 2, p. 107 702, 2021.

[82] B. Wei, M. Dai, and P. Yin, "Complex shapes self-assembled from single-stranded DNA tiles," *Nature*, vol. 485, no. 7400, pp. 623–626, 2012.

[83] F. A. Engelhardt, F. Praetorius, C. H. Wachauf, G. Brüggenthies, F. Kohler, B. Kick, K. L. Kadletz, P. N. Pham, K. L. Behler, T. Gerling, and H. Dietz, "Custom-Size, Functional, and Durable DNA Origami with Design-Specific Scaffolds," *ACS Nano*, vol. 13, no. 5, pp. 5015–5027, 2019.

[84] A. N. Marchi, I. Saaem, B. N. Vogen, S. Brown, and T. H. LaBean, "Toward larger dna origami," *Nano Letters*, vol. 14, no. 10, pp. 5740–5747, 2014.

[85] X. Chen, Q. Wang, J. Peng, Q. Long, H. Yu, and Z. Li, "Self-assembly of large dna origami with custom-designed scaffolds," *ACS Applied Materials & Interfaces*, vol. 10, no. 29, pp. 24 344–24 348, 2018.

[86] L. L. Ong, N. Hanikel, O. K. Yaghi, C. Grun, M. T. Strauss, P. Bron, J. Lai-Kee-Him, F. Schueder, B. Wang, P. Wang, J. Y. Kishi, C. Myhrvold, A. Zhu, R. Jungmann, G. Bellot, Y. Ke, and P. Yin, "Programmable self-assembly of three-dimensional nanostructures from 10,000 unique components," *Nature*, vol. 552, no. 7683, pp. 72–77, 2017.

[87] H. Liu, X. Zhang, S. Ning, Y. Xiao, and J. Zhang, "The electronic structure and work functions of single crystal lab6 typical crystal surfaces," *Vacuum*, vol. 143, pp. 245–250, 2017.

[88] D. Williams, "Electron microscopy: Transmission," in *Encyclopedia of Materials: Science and Technology*, Oxford: Elsevier, 2001, pp. 2577–2584.

[89] A. Ilitchev. (2019). "How do you make an electron beam?" [Online]. Available: `https://www.thermofisher.com/blog/microscopy/electron-source-fundamentals/`. accessed: 03.05.2021.

[90] S. De Carlo and J. R. Harris, "Negative staining and cryo-negative staining of macromolecules and viruses for TEM," *Micron*, vol. 42, no. 2, pp. 117–131, 2011.

[91] K. W. Urban, "Studying atomic structures by aberration-corrected transmission electron microscopy," *Science*, vol. 321, no. 5888, pp. 506–510, 2008.

[92] O. Scherzer, "über einige Fehler von Elektronenlinsen (some defects of electron lenses)," *Optik*, vol. 101, no. 9, pp. 593–603, 1936.

[93] O. Scherzer, "The theoretical resolution limit of the electron microscope," *Journal of Applied Physics*, vol. 20, no. 1, pp. 20–29, 1949.

[94] G. McMullan, A. R. Faruqi, and R. Henderson, "Direct Electron Detectors," *Methods in Enzymology*, vol. 579, pp. 1–17, 2016.

[95] (). "Basics - phase contrast," [Online]. Available: https://www.ceos-gmbh.de/en/basics/phasecontrast. (accessed: 03.05.2021).

[96] A. Ilitchev. (2019). "Seeing with electrons: The anatomy of an electron microscope," [Online]. Available: https://www.thermofisher.com/blog/microscopy/seeing-with-electrons-the-anatomy-of-an-electron-microscope/. accessed: 16.06.2021.

[97] H.-W. Wang and X. Fan, "Challenges and opportunities in cryo-em with phase plate," *Current Opinion in Structural Biology*, vol. 58, pp. 175–182, 2019.

[98] P. A. Penczek, "Image restoration in cryo-electron microscopy," *Methods in Enzymology*, vol. 482, pp. 35–72, 2010.

[99] E. Nogales and S. H. Scheres, "Cryo-em: A unique tool for the visualization of macromolecular complexity," *Molecular Cell*, vol. 58, no. 4, pp. 677–689, 2015.

[100] A. Suma, E. Poppleton, M. Matthies, P. Šulc, F. Romano, A. A. Louis, J. P. K. Doye, C. Micheletti, and L. Rovigatti, "Tacoxdna: A user-friendly web server for simulations of complex dna structures, from single strands to origami," *Journal of Computational Chemistry*, vol. 40, pp. 2586–2595, 2019.

[101] J.-P. Sobczak, "Investigations of the dna origami folding process," Dissertation, Technische Universität München, München, 2018.

[102] B. Kick, F. Praetorius, H. Dietz, and D. Weuster-Botz, "Efficient production of single-stranded phage dna as scaffolds for dna origami," *Nano Letters*, vol. 15, no. 7, pp. 4672–4676, 2015.

[103] E. Stahl, T. G. Martin, F. Praetorius, and H. Dietz, "Facile and scalable preparation of pure and dense dna origami solutions," *Angewandte Chemie International Edition*, vol. 53, no. 47, pp. 12 735–12 740, 2014.

[104] S. Woo and P. W. K. Rothemund, "Programmable molecular recognition based on the geometry of DNA nanostructures," vol. 3, no. 8, pp. 620–627, 2011.

[105] M. A. B. Baker, A. J. Tuckwell, J. F. Berengut, J. Bath, F. Benn, A. P. Duff, A. E. Whitten, K. E. Dunn, R. M. Hynson, A. J. Turberfield, and L. K. Lee, "Dimensions and Global Twist of Single-Layer DNA Origami Measured by Small-Angle X-ray Scattering," *ACS Nano*, vol. 12, no. 6, pp. 5791–5799, 2018.

[106] E. Bertosin, P. Stömmer, E. Feigl, M. Wenig, M. N. Honemann, and H. Dietz, "Cryo-Electron Microscopy and Mass Analysis of Oligolysine-Coated DNA Nanostructures," *ACS Nano*, vol. 15, no. 6, pp. 9391–9403, 2021.

[107] D. N. Kim, F. Kilchherr, H. Dietz, and M. Bathe, "Quantitative prediction of 3D solution shape and flexibility of nucleic acid nanostructures," *Nucleic Acids Research*, vol. 40, no. 11, pp. 2862–2868, 2012.

[108] H. Chen, H. Zhang, J. Pan, T. G. Cha, S. Li, J. Andréasson, and J. H. Choi, "Dynamic and Progressive Control of DNA Origami Conformation by Modulating DNA Helicity with Chemical Adducts," *ACS Nano*, vol. 10, no. 5, pp. 4989–4996, 2016.

[109] C. L. Lawson, M. L. Baker, C. Best, C. Bi, M. Dougherty, P. Feng, G. Van Ginkel, B. Devkota, I. Lagerstedt, S. J. Ludtke, R. H. Newman, T. J. Oldfield, I. Rees, G. Sahni, R. Sala, S. Velankar, J. Warren, J. D. Westbrook, K. Henrick, G. J. Kleywegt, H. M. Berman, and W. Chiu, "EMDataBank.org: Unified data resource for CryoEM," *Nucleic Acids Research*, vol. 39, no. suppl1, pp. 456–464, 2011.

[110] P. Emsley, B. Lohkamp, W. G. Scott, and K. Cowtan, "Features and development of coot," *Acta Crystallographica Section D - Biological Crystallography*, vol. 66, no. 4, pp. 486–501, 2010.

[111] L. G. Trabuco, E. Villa, K. Mitra, J. Frank, and K. Schulten, "Flexible Fitting of Atomic Structures into Electron Microscopy Maps Using Molecular Dynamics," *Structure*, vol. 16, no. 5, pp. 673–683, 2008.

[112] C. Maffeo and A. Aksimentiev, "MrDNA: A multi-resolution model for predicting the structure and dynamics of DNA systems," *Nucleic Acids Research*, vol. 48, no. 9, pp. 5135–5146, 2020.

[113] C. Maffeo, J. Yoo, and A. Aksimentiev, "De novo reconstruction of DNA origami structures through atomistic molecular dynamics simulation," *Nucleic Acids Research*, vol. 44, no. 7, pp. 3013–3019, 2016.

[114] J. Y. Lee, J. G. Lee, G. Yun, C. Lee, Y. J. Kim, K. S. Kim, T. H. Kim, and D. N. Kim, "Rapid Computational Analysis of DNA Origami Assemblies at Near-Atomic Resolution," *ACS Nano*, vol. 15, no. 1, pp. 1002–1015, 2021.

[115] B. E. Snodin, J. S. Schreck, F. Romano, A. A. Louis, and J. P. Doye, "Coarse-grained modelling of the structural properties of DNA origami," *Nucleic Acids Research*, vol. 47, no. 3, pp. 1585–1597, 2019.

[116] R. V. Reshetnikov, A. V. Stolyarova, A. O. Zalevsky, D. Y. Panteleev, G. V. Pavlova, D. V. Klinov, A. V. Golovin, and A. D. Protopopova, "A coarse-grained model for DNA origami," *Nucleic Acids Research*, vol. 46, no. 3, pp. 1102–1112, 2018.

[117] S. Q. Zheng, E. Palovcak, J. P. Armache, K. A. Verba, Y. Cheng, and D. A. Agard, "MotionCor2: Anisotropic correction of beam-induced motion for improved cryo-electron microscopy," *Nature Methods*, vol. 14, no. 4, pp. 331–332, 2017.

[118] A. Rohou and N. Grigorieff, "CTFFIND4: Fast and accurate defocus estimation from electron micrographs," *Journal of Structural Biology*, vol. 192, no. 2, pp. 216–221, 2015.

[119] T. Wagner, F. Merino, M. Stabrin, T. Moriya, C. Antoni, A. Apelbaum, P. Hagel, O. Sitsel, T. Raisch, D. Prumbaum, D. Quentin, D. Roderer, S. Tacke, B. Siebolds, E. Schubert, T. R. Shaikh, P. Lill, C. Gatsogiannis, and S. Raunser, "SPHIRE-crYOLO is a fast and accurate fully automated particle picker for cryo-EM," *Communications Biology*, vol. 2, no. 1, pp. 218–231, 2019.

[120] T. Bepler, A. Morin, M. Rapp, J. Brasch, L. Shapiro, A. J. Noble, and B. Berger, "Positive-unlabeled convolutional neural networks for particle picking in cryo-electron micrographs," *Nature Methods*, vol. 16, no. 11, pp. 1153–1160, 2019.

[121] T. D. Pettersen Ef Fau - Goddard, C. C. Goddard Td Fau - Huang, G. S. Huang Cc Fau - Couch, D. M. Couch Gs Fau - Greenblatt, E. C. Greenblatt Dm Fau - Meng, T. E. Meng Ec Fau - Ferrin, T. E. Ferrin, and J. C. Chem, "UCSF Chimera–a visualization system for exploratory research and analysis," *Journal of Computational Chemistry*, vol. 25, no. 13, pp. 1605–1612, 2004.

[122] T. D. Goddard, C. C. Huang, E. C. Meng, E. F. Pettersen, G. S. Couch, J. H. Morris, and T. E. Ferrin, "UCSF ChimeraX: Meeting modern challenges in visualization and analysis," *Protein Science*, vol. 27, no. 1, pp. 14–25, 2018.

[123] P. Virtanen, R. Gommers, T. E. Oliphant, M. Haberland, T. Reddy, D. Cournapeau, E. Burovski, P. Peterson, W. Weckesser, J. Bright, S. J. van der Walt, M. Brett, J. Wilson, K. J. Millman, N. Mayorov, A. R. J. Nelson, E. Jones, R. Kern, E. Larson, C. J. Carey, İ. Polat, Y. Feng, E. W. Moore, J. VanderPlas, D. Laxalde, J. Perktold, R. Cimrman, I. Henriksen, E. A. Quintero, C. R. Harris, A. M. Archibald, A. H. Ribeiro, F. Pedregosa, P. van Mulbregt, and SciPy 1.0 Contributors, "SciPy 1.0: Fundamental Algorithms for Scientific Computing in Python," *Nature Methods*, vol. 17, no. 3, pp. 261–272, 2020.

[124] C. R. Harris, K. J. Millman, S. J. van der Walt, R. Gommers, P. Virtanen, D. Cournapeau, E. Wieser, J. Taylor, S. Berg, N. J. Smith, R. Kern, M. Picus, S. Hoyer, M. H. van Kerkwijk, M. Brett, A. Haldane, J. F. del Río, M. Wiebe, P. Peterson, P. Gérard-Marchant, K. Sheppard, T. Reddy, W. Weckesser, H. Abbasi, C. Gohlke, and T. E. Oliphant, "Array programming with numpy," *Nature*, vol. 585, no. 7825, pp. 357–362, 2020.

[125] T. Kluyver, B. Ragan-Kelley, F. Pérez, B. Granger, M. Bussonnier, J. Frederic, K. Kelley, J. Hamrick, J. Grout, S. Corlay, P. Ivanov, D. Avila, S. Abdalla, and C. Willing, "Jupyter Notebooks - a publishing format for reproducible computational workflows," in *Positioning and Power in Academic Publishing: Players, Agents and Agendas*, IOS Press, 2016, pp. 87–90.

[126] T. Burnley, C. M. Palmer, and M. Winn, "Recent developments in the CCP-EM software suite," *Acta Crystallographica Section D: Structural Biology*, vol. 73, no. 6, pp. 469–477, 2017.

Danksagung

Lieber Hendrik, ich möchte mich ganz herzlich bei dir für die Gelegenheit meine Doktorarbeit an deinem Lehrstuhl anfertigen zu dürfen bedanken. Vielen Dank für die motivierende Arbeitsatmosphäre sowie konstruktive Diskussionen und Ratschläge. Vielen Dank für die Möglichkeit an verschiedenen Projekten zu arbeiten, in denen ich mich explorativ entfalten konnte. Vielen Dank für die unschlagbaren Mittel und die Laborausstattung, die du bereitstellt hast, allen voran die state-of-the-art Elektronenmikroskope. Vielen Dank für das entgegengebrachte Vertrauen mir die Verantwortung für die Betreuung dieser Geräte zu übergeben.

Vielen Dank Elija und Massimo für die tolle Zusammenarbeit im Projekt Frozen-Gulasch. Ich möchte auch allen anderen danken, mit denen ich in gemeinsamen Projekten zusammenarbeiten durfte, insbesondere bei meinen Studenten Anna, Baki und MaxW.

Mein großer Dank geht an Dario, Elija, Jessica, Klaus, Matthias, MaxH, Ryan, und Siggi für das Korrekturlesen dieses Schriftstücks.

Danke auch an das gesamte Dietzlab der vergangenen Jahre für tolle Gespräche und Diskussionen, die unvergesslichen Feiern und Grillabende, sowie Saunabesuche (mehr Teer) und Radtouren (tatsächlich führen auch Radwege nach Rom).

Mein besonderer Dank gilt meinen Eltern für die stetige Unterstützung. Dass ihr immer für mich da wart und ich immer nach Hause kommen konnte, hat mir große Sicherheit gegeben.

Liebe Jana, ich möchte dir von ganzen Herzen danken. Danke für dein Verständnis und die Unterstützung, wenn besonders viel Arbeit anstand. Danke für die gespendete Kraft und Aufmunterung wenn es einmal nicht so gut lief. Danke aber auch für geteilte Freude über Erfolge.